



REPORT ON COPPER – NIOB RESEARCH AT THE MAX-PLANCK-INSTITUT DÜSSELDORF

– SIMULATIONS AND EXPERIMENTS

MAX-PLANCK PROJECT REPORT

Dierk Raabe, Andika Pramono

*Max-Planck-Institut für Eisenforschung
Max-Planck-Str. 1
40237 Düsseldorf
Germany*

März 2004, Max-Planck-Society

<http://www.mpg.de> <http://www.mpie.de> <http://edoc.mpg.de/>



KEYWORDS: *copper, niobium, silver, in-situ, drawing, composites, conductivity,
strength, rule- of mixtures*



Project References

F. Heringhaus, D. Raabe, L. Kaul, G. Gottstein: *Metall* 47 (1993) 558–561, „Schmelzmetallurgische Herstellung eines Kupfer-Niob-Verbundwerkstoffes“

F. Heringhaus, D. Raabe, G. Gottstein: *Metall* 48 (1994) 287–294, „Eigenschaften und Anwendungen von Kupfer-Niob in-situ Faserverbundwerkstoffen“

D. Raabe, F. Heringhaus: *physica status solidi (a)* 142 (1994) 473–481, „Correlation of superconductivity and microstructure in an in-situ formed Cu-20%Nb composite“

F. Heringhaus, D. Raabe, G. Gottstein: *Acta Metall.* 43 (1995) 1467–1476, „On the correlation of microstructure and electromagnetic properties of heavily cold worked Cu-20 wt.% Nb wires“

F. Heringhaus, D. Raabe: *Journal of Materials Processing Technology* 59 (1996) 367–372, „Recent advances in the manufacturing of copper–base composites“

D. Raabe, F. Heringhaus, U. Hangen, G. Gottstein: *Zeitschrift für Metallkunde* 86 (1995) 405–422, „Investigation of a Cu-20mass%Nb in situ Composite, Part I: Fabrication, Microstructure and Mechanical Properties, Part II: Electromagnetic Properties and Application“

D. Mattissen, D. Raabe, F. Heringhaus: *Acta Materialia* 47 (1999) 1627–1634, „Experimental investigation and modeling of the influence of microstructure on the resistive conductivity of a Cu–Ag–Nb in situ composite“

F. Heringhaus, U. Hangen, D. Raabe, G. Gottstein: *Materials Science Forum* 157–162 (1994) 709–714., „Textures of rolled and wire drawn Cu-20% Nb“

U. Hangen, D. Raabe: *physica status solidi (a)* 147 (1995) 515–527, „Experimental investigation and simulation of the normal conducting properties of a heavily cold rolled Cu-20mass% Nb in situ composite“

D. Raabe, U. Hangen: *Materials Letters* 22 (1995) 155–161, „Observation of amorphous areas in a heavily cold rolled Cu-20wt.% Nb composite“



U. Hangen, D. Raabe: Acta Metall 43 (1995) 4075–4082, „Modelling of the yield strength of a heavily wire drawn Cu-20%Nb composite by use of a modified linear rule of mixtures“

D. Raabe, U. Hangen: Journal of Materials Research 12 (1995) 3050–3061, „Investigation of structurally less ordered areas in the Nb filaments of a heavily cold rolled Cu-20wt.% Nb in-situ composite“

D. Raabe, U. Hangen: Acta metall. 44 (1996) 953–961, „Correlation of microstructure and type II superconductivity of a heavily cold rolled Cu-20mass% Nb in situ composite“

D. Raabe, U. Hangen: Computational Materials Science 5 (1996) 195–202, „Simulation of the yield strength of wire drawn Cu-based in situ composites“

D. Raabe, U. Hangen: physica status solidi (a) 154 (1996) 715–726, „On the anisotropy of the superconducting properties of a heavily cold rolled Cu-20 mass% Nb in situ composite“

D. Raabe, D. Mattissen: Acta Materialia 46 (1998) 5973–5984, „Microstructure and mechanical properties of a cast and wire drawn ternary Cu-Ag-Nb in situ composite“

D. Raabe, D. Mattissen: Acta Materialia 47 (1999) 769–777, „Experimental investigation and Ginzburg–Landau modeling of the microstructure dependence of superconductivity in Cu–Ag–Nb wires“

K. Miyake, N. Hanzawa, H. Takahara, S. Kobayashi, D. Raabe: Japanese Journal of Applied Physics 39 (2000) 119-121, „Application of In Situ-Formed Metallic-Fiber-Reinforced Copper Matrix Composites to Cables Used for Robots “

D. Raabe, K. Miyake, H. Takahara: Material Science and Engineering, A 291 (2000) 186-197, „Processing, microstructure, and properties of ternary high–strength Cu–Cr–Ag in situ composites“



CHAPTER ONE

INTRODUCTION

Among many *in-situ* metal matrix composites (MMCs) niobium-reinforced copper is a scientifically, technically and commercially interesting material. In the aspect of scientific investigations, Cu-20mass%Nb is a very challenging material since it possesses a very high tensile strength after deformation, which particularly exceeds that expected from the rule of mixtures (ROM) [1-12]. It is also of particular interest since niobium is not a strong metal and therefore unlikely acts as a reinforcing element when considering ROM. In fact, for sufficiently high values of deformation (η), the strength of copper-niobium composites as a whole surpasses the strength of heavily cold-worked niobium and that of most materials from which reinforcing fibers are usually made [4].

From technical and commercial point of view, copper-niobium MMCs play an important role as highly potential candidate materials for the production of mechanically stressed electrical devices, such as application in long pulse high-field resistive magnets and rotating electrical machinery, since they have a good combination of high strength and good electrical conductivity [1,4,13,14]. In fact, both the mechanical properties and the electrical conductivity of copper-niobium considerably exceed those of competitive alloys like copper-beryllium, copper-nickel, copper-nickel-manganese, copper-tantalum or copper-chromium as plotted in figure 1.1. In this case, the potential properties of copper-niobium often justify the high cost. In figure 1.1 an alloy containing 18 to 20 mass% of niobium seems to have optimum electrical and mechanical properties, since reducing the niobium content causes the composite to lose its strength and increasing the niobium content results in degradation of ductility and electrical conductivity [2-7].

Due to the high cost of fiber material, it is highly considered to maintain the fiber volume fraction as low as possible in the production of metal matrix composites. With a low fiber volume fraction some desirable physical characteristics in the matrix such as low density or high electrical and thermal conductivity can also be retained. Recently, the

mechanical properties of filamentary composites with a dense distribution of sub-micron filaments are in the enormous interest. These composites are usually fabricated *in-situ* using two-phase alloys prepared either by powder metallurgy (PM) or by quenching a liquid solution of two mutually insoluble components. The next possibility is the cast or directionally solidified eutectic composites. Considering both phases are ductile, such two phase alloys can then be mechanically processed to large reduction in cross sectional area (by rolling or drawing) until the *in-situ* formed filaments are sufficiently small [4].

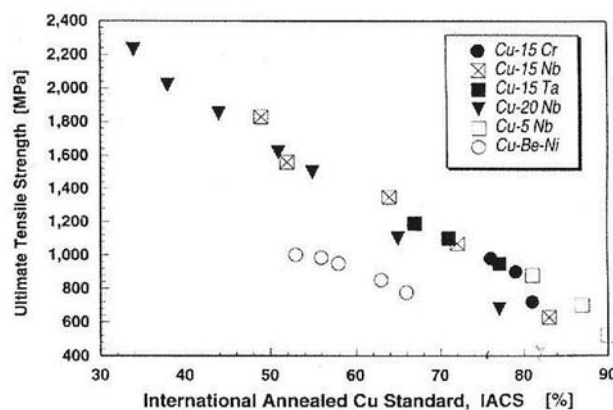


Figure 1.1 The ultimate tensile strength versus international annealed copper-standard (IACS) of various copper-based alloys [1].

The objective in designing a pulse magnet is to maximize the generated field [15]. In application with large electrical currents, it is required that the material has a good conductivity in order to minimize ohmic heating during operation. In a generation of very high magnetic fields, two main problems must be avoided in the coil material : coil melting and coil expansion due to hoop stress generated by the Lorentz force. In order to avoid the coil melting, the highest magnetic fields are generated for fractions of a second in pulsed magnets. In order to minimize the coil expansion, the high mechanical strength is necessary for the winding material.

In selecting materials for high-field magnetic design, the ultimate tensile strength versus conductivity (such as that in figure 1.1) is commonly used to determine the appropriate materials. Another option to select and compare the appropriate magnetic materials is to use a graphic of $(\sigma_y)^{1/2}$ versus $(C_p \rho / \rho_e)^{1/2}$, where σ_y is the yield strength, C_p is the specific heat, ρ is the density, and ρ_e is the electrical resistivity of the wire. Such graphic is called *the materials selection chart* (MSC) and plotted in figure 1.2. In figure



1.2, material M_1 is excellent for short pulses of very high field application. M_3 is the best choice for long pulses at lower field, and M_2 for intermediate fields and pulse lengths. Material M_4 is less qualified than all the others under all conditions. The best materials for maximizing field strength and pulse time will always be found in the upper right portion of the chart.

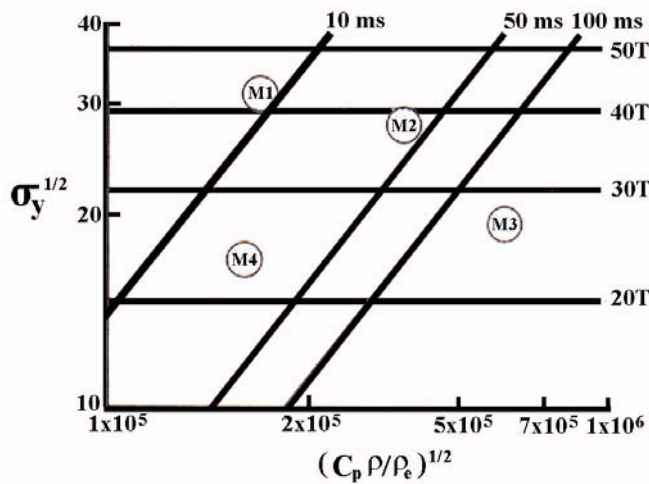


Figure 1.2 The materials selection chart (MSC) for high-field, pulsed magnet coils [15].

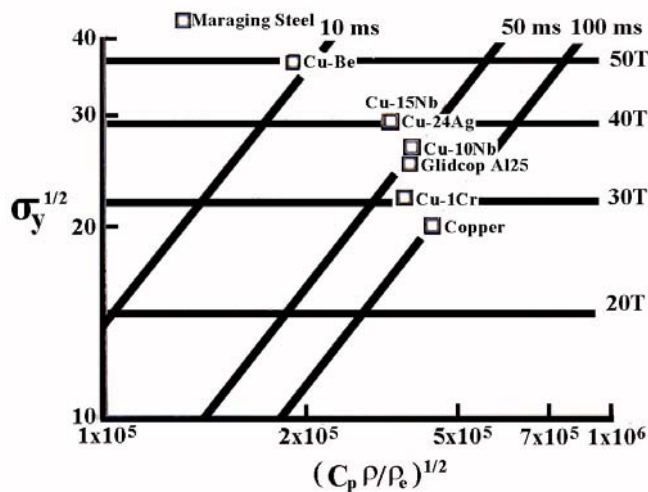


Figure 1.3 The materials selection chart with relative positions of various candidate materials [15].

MSC for various candidate materials for high magnetic field is shown in figure 1.3. Here one observes that Cu-15%Nb is located in the intermediate region of MSC. One could also then expect that Cu-18%Nb and Cu-20%Nb lie in M_2 region close to M_1 . Interesting to note is the relative position of copper, which is located between M_2 and M_3 .



Despite its low strength, copper has very good thermal performance which would allow longer pulse time. In order to generate high magnetic field, the strength should be increase against Lorentz force by solid solution strengthening which, however, reduces the electrical conductivity. To maintain solute-free copper matrix (i.e. maintain optimum electrical conductivity), a precipitation hardening material having little or negligible solid solubility with copper (e.g. beryllium, chromium, or niobium) is added. As these *in-situ* composite systems are further deformed, the second phase fiber or particle can provide great strengthening.

This doctoral research is aimed to explore some new aspects in studying the behavior of copper-niobium *in-situ* metal matrix composite, which cover :

- the macrotexture evolution of both phases after heat treatment at temperatures close to the critical temperature, T_c , of 1080°C;
- the morphological changes of niobium filaments and their quantitative measurement (i.e. the change in filament thickness and interfilament spacing) after heat treatment at temperatures close to T_c ;
- the changes in hardness and strength of the wire after heat treatment at temperatures close to T_c ;
- the likely mutual interactions among the macrotexture evolution, the morphological changes of niobium, and the changes in hardness and strength after heat treatment at temperatures close to T_c ;
- the computer simulation of niobium evolution in copper matrix at temperatures close to T_c .

These five objectives can be summarized as the observations of *thermomechanical instability* of copper-niobium *in-situ* composites. Such stability can reflect the ability of material to simultaneously overcome the problems of coil melting and coil expansion of a pulse magnet at highly generated field while maintaining the optimum, potential mechanical and electrical properties. These objectives are then elaborated to include observations in :

- The change of macrotexture orientation of deformed samples due the application of high temperatures ($T = 800^\circ\text{C}$ and 1000°C). X-ray measurement by means of the Goniometer will be utilized to investigate the change in copper and niobium orientations. The results will be manifested in the form of inverse pole figures with respect to rolling direction (RD).



- The change of morphology or microstructure evolution at high temperatures. Elevated temperature use of metal matrix composites entails the risk of microstructural coarsening and/or shape instability of the reinforcement, if the latter is in the form of plates or fibers [16]. At $T = 800^{\circ}\text{C}$ and 1000°C it is highly expected that the coarsening and/or the shape instability of niobium filaments occurs much more significantly than at $T = 500^{\circ}\text{C}$ from previous study by Hong et al. [17]. According to copper-niobium phase diagram with pure constituents (no oxygen, nitrogen, sulphur, and carbon), the Cu-18%Nb system is stable up to 1080°C . Just above 1080°C , the copper in the system will melt leaving a solid α -niobium. Hence, the observation of microstructure evolution at 800°C and 1000°C will provide valuable descriptions regarding the thermal stability of the system at the final frontier. The appropriate instability mechanisms in niobium filaments will be observed using mainly the light/optical microscope and the scanning electron microscope (SEM). The measurement in the change of filament thickness and matrix spacing with respect to deformation (η) and annealing time (t) will be conducted based upon mainly SEM micrographs. The investigations will be focused on low deformations of $0 < \eta < 5$. Previous study by Verhoeven et al. [18] on copper-niobium wires shows that there is no significant or tremendous difference between niobium filament thickness, up to $\eta = 4$ or 5 , measured by the SEM and the transmission electron microscope (TEM). The TEM analysis will be used mainly to qualitatively investigate the thermal instability of copper matrix substructure and at some extent of niobium filament at the higher resolution. The x-ray energy dispersive spectrometer (EDS) analysis will be additionally applied in TEM observations to ensure : the region of copper and niobium and whether or not interstitial impurities such as oxygen or carbon exist. The selected area diffraction (SAD) will be aided to clarify some important phenomena in the TEM substructure, such as : twinning, orientations of grains in copper matrix, orientations of niobium filaments.
- The softening of Cu-18%Nb wire due to the application of high temperatures ($T = 800^{\circ}\text{C}$ and 1000°C). After annealing, the Cu-18%Nb wire may soften, lose its strength and thereby increase its ductility. To ensure the softening of wire, microhardness testing will be applied. To observe the declining strength and the increasing ductility, tensile testing will be implemented.



- The computer simulation of niobium evolution at high temperatures using the Cahn-Hilliard equation (CHE). This equation will be implemented into a C-language based program, to depict the morphological changes in niobium filaments at high temperatures. The first and ideal assumption in developing correlation between the Gibbs free energy and the concentration needed for the Cahn-Hilliard equation is the negligible mutual solid solubility of the copper-niobium system with no interstitial impurities.

This dissertation consists of seven main chapters. *Chapter One* introduces the role of metal matrix composites, their fabrication processes, and their design objective and the materials selections for high field magnetic applications. The objectives of this research study and their elaboration are also presented in this chapter. *Chapter Two* reviews the previous and recent works in studying the copper-niobium *in-situ* metal matrix composites. *Chapter Three* discusses some underlining theories behind the knowledge of metal matrix composites and the Cahn-Hilliard theory. *Chapter Four* focuses on the experimental procedures conducted in this study and the application of Cahn-Hilliard equation in simulating phase evolution of the heat-treated copper-niobium composite. *Chapter Five* presents the results of experiments and the Cahn-Hilliard simulation. *Chapter Six* contains the scientific discussion of the results given in Chapter Five. *Chapter Seven* summarizes the substantial aspects obtained in this research work.



References

1. Raabe, D.; Heringhaus, F.; Hangen, U.; and Gottstein, G. : Z. Metallkd. **86** (1995) 405.
2. Frommeyer, G.I. : "Verbundwerkstoffe", DGM-Verlag (1981).
3. Karasek, K.R.; and Bevk, J. : J. Appl. Phys. **52** (1981) 1370.
4. Bevk, J.; Harbison, J.P.; and Bell, J.L. : J. Appl. Phys. **49** (1978) 6031.
5. Bevk, J.; and Karasek, K.R. : in : D. Kuhlmann-Wilsdorf, W.C. Harrigan (eds.) : "New Developments and Applications in Composites", AIME Warrendale-PA (1979) 101.
6. Spitzig, W.A.; and Krotz, P. : Scripta metall. **21** (1987) 1143.
7. Spitzig, W.A. : Acta metall. **39** (1991) 1085.
8. Trybus, C.; and Spitzig, W.A. : Acta metall. **37** (1989) 1971.
9. Spitzig, W.A.; Pelton, A.R.; and Laabs, F.C. : Acta metall. **35** (1987) 2427.
10. Frommeyer, G.; and Wassermann, G. : Acta metall. **23** (1975) 1353.
11. Funkenbusch, P.D.; and Courtney, T.H. : Acta metall. **33** (1985) 913.
12. Bevk, J.; Sunder, W.A.; Dublon, G.; and Cohen, E. : in : F.D. Lemkey, H.E. Cline, M. McLean (eds.) : "In Situ Composites IV", Elsevier, Amsterdam (1982) 121.
13. Embury, J.D.; Hill, M.A.; Spitzig, W.A.; and Sakai, Y. : MRS Bull. **8** (1993) 57.
14. Schneider-Muntau, H.J. : IEEE Trans. Magn. **18** (1982) 32.
15. Wood, J.T.; Embury, J.D.; and Ashby, M.F. : Acta mater. **45** (1997) 1099.
16. Courtney, T.H. : in : N. Hansen (ed.) : "Metal Matrix Composites Processing, Microstructure and Properties", 12th Risø International Symposium on Materials Science (1991) 17.
17. Hong, S.I.; Hill, M.A.; Sakai, Y.; Wood, J.T.; and Embury, J.D. : Acta metall. **43** (1995) 3317.
18. Verhoeven, J.D.; Chumbley, L.S.; Laabs, F.C.; and Spitzig, W.A. : Acta metall. **39** (1991) 2827.



CHAPTER TWO

LITERATURE REVIEW

Numerous studies have been conducted to investigate microstructures and properties of metal matrix composites. Chapter Two is intended to acknowledge, appreciate and review numerous valuable efforts and results of previous works concerning the copper base composites and their related topics, with more focus on the copper-niobium *in-situ* MMC. The important data and figures will also be here presented.

2.1 Introduction

Composites have been categorized as one of the four basic structural materials other than : metals, polymers and ceramics. The relative importance of the four basic materials in a historical scope has been presented schematically by Ashby [1] as shown in figure 2.1. Figure 2.1 clearly shows the steadily increasing importance of polymers, composites, and ceramics and the decreasing role of metals.

It is difficult to certainly say when or where humans first learned about fibrous composites, in which reinforcing fibers embedded in a binder, or matrix material. However mother nature provides us with numerous examples. Wood consists mainly of fibrous cellulose in a matrix of lignin, whereas most mammalian bone is made up of layered and oriented collagen fibrils in a protein-calcium phosphate matrix [2]. The apparently first examples of man-made fibrous composites were produced by the ancient Israelites and Egyptians, who used the straw-reinforced clay bricks to build pyramids. The early natives of South and Central America used plant fibers in their pottery. The early purpose of using fibrous reinforcement was probably based on the desire to keep clay from cracking during drying rather than on structural reinforcement.

Composite can be defined as a material consisting of two or more physically and/or chemically distinct, suitably arranged or distributed phases [3,4]. The composite desirable properties or characteristics are not represented by any of its constituents acting alone. Reinforcement, matrix and interface become the entities that determine the characteristics of a composite. Over the years, many scientists have realized that the matrix microstructure



and its mechanical properties can considerably affect the overall performance of a composite. In metal matrix composites, for instance, incorporation of a reinforcement (fiber, whisker, or particle) can lead to changes in the metallic matrix microstructure, and consequently, in some structure-sensitive properties such as strength and toughness.

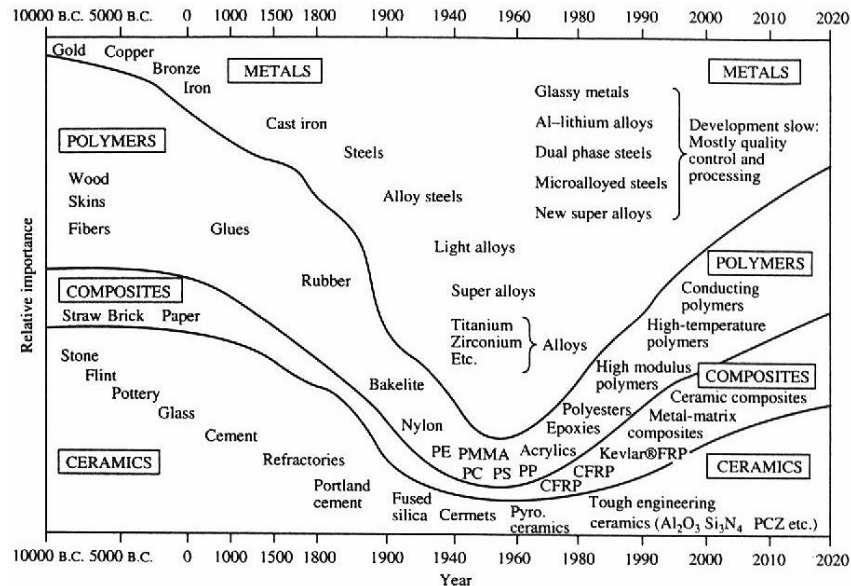


Figure 2.1 The relative importance of metals, polymers, composites and ceramics as a function of time. The diagram shows a schematic description, and neither tonnage nor value is used. The time scale is nonlinear [1].

2.2 Metal Matrix Composites

2.2.1 General Types of Metal Matrix Composites

Metal matrix composites entail continuous metal matrix with reinforcing materials. According to the kind of reinforcement, there are generally three types of metal matrix composites [3,5]:

Continuous-fiber-reinforced composites. In this type of MMCs, continuous filaments greatly improve the stiffness (tensile modulus) and the strength. A good example of continuous-fiber MMCs is aluminum alloy matrix reinforced with boron fiber. By adding 51vol% of boron fibers, the tensile strength of aluminum alloy 6061 is increased from 310 to 1417 MPa, and its tensile modulus is increased from 69 to 231 GPa. The fabrication of Al-B composite takes place by hot pressing layers of B fibers between Al foils so that the foils deform around the fibers and bond to each other. The application of Al-B composite includes the structural members in the midfuselage of the space shuttle orbiter.



Discontinuous-fiber-reinforced composites. This type of MMCs has been produced mainly by powder metallurgy and melt infiltration process. An example of discontinuous-fiber composite is Al 6061-T6 (20% SiC). Here needle-like silicon carbide whiskers about 1 to 3 μm in diameter and 50 to 200 μm long are mixed with Al powders, and then consolidated by hot pressing and extruded or forged into desired shapes. By adding 20% SiC, the ultimate tensile strength of Al alloy 6061 is increased from 310 to 480 MPa, and the tensile modulus is raised from 69 to 115 GPa. Missile guidance parts and high-performance automobile pistons use this type of MMC.

Particulate-reinforced composites. Unlike discontinuous-fiber composite, the shapes of alumina and silicon carbide are irregular with size of about 3 to 200 μm in diameter. The particulate is mixed with molten aluminum alloy and cast into ingots or extrusion billets for further fabrication. By adding 20% SiC, the ultimate tensile strength of Al alloy 6061 can be raised from 310 to 496 MPa, and the tensile modulus is increased from 69 to 103 GPa. Many sporting equipment and automobile engine parts are fabricated from this type of MMC.

2.2.2 Roles of Discontinuously-Reinforced MMCs

The discontinuous-fiber and particulate-reinforced composites (discontinuously-reinforced MMCs) have assumed special importance [3]. Compared to the continuously-reinforced composites, they are less expensive. It is particularly true for large volume usage, since cost is an important and essential item. The discontinuously reinforced MMCs allow the use of conventional metallurgical processes such as casting or powder metallurgy, followed by conventional secondary processing techniques of rolling, forging, and extrusion. In addition to higher temperature use, discontinuously-reinforced MMCs have potential combined advantages such as enhanced modulus and strength, increased thermal stability, better wear resistance and most importantly isotropic properties. Nevertheless, many continuously reinforced MMCs feature higher modulus and strength, as shown by the previous example of Al-B composite.



2.2.3 In-situ Metal Matrix Composites

The *in-situ* composite microstructure features relatively small alternate layer structure of reinforcements and matrix, either in regular or random fashion, which is not synthetically arranged. In this composite, which is also considered as a microcomposite [6], only a small part of the advantages comes from the combination of the properties of its constituents. It is rather the interaction of the structural phases, in microscopic level, that determines the properties of such composites [6,7]. The *in-situ* composite material is generally produced in one step processing from an appropriate starting alloy, thus avoiding the difficulties inherent in combining the separate components as typically done in macrocomposite processing.

The production of an *in-situ* composite material can be typically achieved either by the melting metallurgy [8-10] or the powder metallurgy [11-13]. Within the scope of discontinuously reinforced composites, the latter process is considered to be more expensive than the first one. In the melting metallurgy process, the thermodynamic mixing ratio of co-existing phases enables a two-phase microstructure in different systems to be produced. It is possible firstly via a eutectic system, in which lamellar microstructure is developed from a melt during simultaneous solidification of the two phases. Lamellar microstructure (figure 2.2) takes place as the result of concentration exchange that is driven by the diffusion during rapid solidification of the phases over short distances [14]. In non-eutectic composition the primary mixed crystal will precipitate out usually in the form of dendrites until the rest of melt reaches the eutectic composition and solidifies in lamellar form. As the cooling rate increases the lamellar spacing decreases. A controlled unidirectional solidification of a eutectic alloy can also yield one phase being distributed as fibers or ribbon in the other. The fine distribution of reinforcement phase can be obtained by controlling the solidification rate. Secondly, the *in-situ* composite microstructure can be obtained via a precipitation hardening system, in which finely dispersed second phase of the crystal precipitates out during aging. Thirdly, a monotectic system can be utilized, in which the two metals exhibit no mutual solid solubility.

Powder metallurgy methods (cold pressing-hot pressing or cold pressing-sintering combination) can also be used to fabricate *in-situ* metal matrix composites. In this case the mutual solid solubility of the constituents plays no role. Some certain amount of matrix and reinforcing powders is blended together to produce a homogeneous distribution. The blend is then cold pressed to produce a *green body*, which has approximately 80% relative

density. The purpose of external pressure in cold pressing is to shape the powder and promote higher packing densities [15,16]. Higher pressure then leads to a higher density through plastic deformation or cold welding, which originates the so called *green strength* of the compact. This cold-pressed green body is then sealed in a container and degassed to remove any absorbed moisture from the particle surfaces. The final step is to hot press the green body (either uniaxially or isostatically) until a fully dense composite is achieved. The hot pressing temperature can be either below or above the matrix alloy solidus. Cold pressing followed by sintering is a less desirable process since either the high pressure needed to achieve the required density may break the fibers or the sintering process may degrade the fibers.

As the material with *in-situ* composite microstructure is deformed (i.e. drawing or extrusion), the interphase boundaries are arranged parallel to deformation direction which yields a unidirectional lamellar structure (filament structure) in a matrix. These filaments act as strengthening material for the matrix.

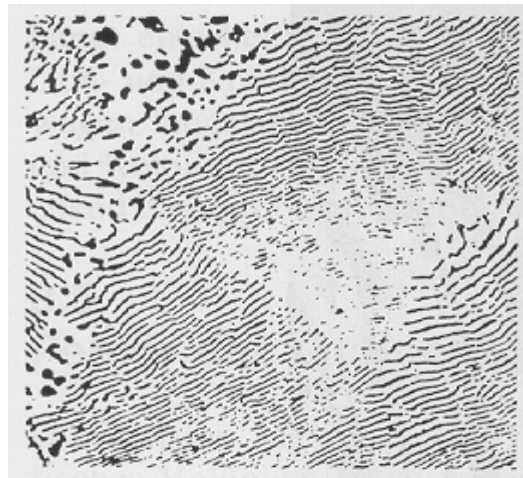


Figure 2.2 The irregular lamellar structure of as-cast Cd-18%Zn [14].

2.3 Copper-Niobium Metal Matrix Composite

Copper has a face center cubic (fcc) structure. Its use as an electrical conductor is quite widespread due to its good thermal conductivity. Copper and some body center cubic (bcc) transition metals (e.g. niobium, molybdenum, vanadium, tungsten, or chromium) have relatively small mutual solubility. The MMCs made of these copper-bcc metals exhibit simultaneously high tensile strength and good electrical conductivity [17-20]. The



rest of sections in this chapter will be mainly focused on some achievements-to-date regarding the copper-niobium metal matrix composite.

2.3.1 Fabrication

The preparation of some large initial ingots of Cu-18to20%Nb by consumable arc casting had been conducted by Spitzig and Krotz [21] and Trybus and Spitzig [35]. In the first study [21] the billet was prepared by casting into a water cooled copper mold, while in the second study [35] the graphite liner was implemented in the mold. The graphite liner had been plasma sprayed with a thin layer of yttria stabilized zirconia and some little pick-up of carbon from the liner was observed. The main difference in the result between the two studies is an average as-cast niobium dendrite size of 3.8 μm in the unlined billet versus 6.2 μm for the graphite lined billet. Details of the arc casting process was presented by Verhoeven et al. [9].

Another method known as the medium frequency induction melting technique was also applied [18,22-24] in order to produce Cu-20%Nb ingot. For this purpose an induction frequency of 10 kHz, a maximum coil voltage of 250 V and a maximum generator power of 30 kW were used. The important aspect regarding this induction melting is the complete dissolution of the niobium which can be achieved by raising temperature up to about 2125 K. Insufficient melting temperatures can allow the survival of small niobium crystals, which may cause the material failure during wire drawing [25].

Wires and sheets are then manufactured from the as-cast ingot. These can be achieved through rotary swaging and subsequent drawing through hard metal drawing bench without intermediate annealing [8], cold rolling [18,35], or combination of cold rolling and drawing [21,29]. Sakai et al. [26] have shown that interrupting the drawing process after 40% reduction in area and annealing at 450°C for 1 hr prior to redrawing results in a higher final strength. For the drawn wire, the reduction ratio (η_d) can be determined as the logarithmic ratio of initial cross sectional area (A_0) and final cross sectional area (A_f) :

$$\eta_d = \ln\left(\frac{A_0}{A_f}\right) \quad \text{Equation 2-1}$$



The reduction in area (ϵ_d) for a drawn wire is defined as :

$$\epsilon_d = \frac{A_0 - A_f}{A_0} \quad \text{Equation 2-2}$$

The correlation between η_d and ϵ_d can then be determined as :

$$\eta_d = \ln \frac{1}{(1 - \epsilon_d)} \quad \text{Equation 2-3}$$

For the cold-rolled sample, the reduction ratio or the true strain (η_r) has been defined as the logarithmic ratio of initial plate thickness (d_0) and final plate thickness (d_f) :

$$\eta_r = \ln \left(\frac{d_0}{d_f} \right) \quad \text{Equation 2-4}$$

Any increase in the wire strength during drawing is accompanied by a reduction in cross sectional area. Hence, no wires with strengths on the order of at least 1.5 GPa have been produced with relatively large enough cross sections to be used in magnetic applications. Renaud, et al. [27,85] tried to rebundle fine, high strength copper-niobium wires. These wires were clad in copper, then restacked, coextruded and redrawn. Despite the wire strength of 1.2 GPa, the process was labor intensive and the resulting wire was relatively expensive. Another disadvantage was the limited achieved strength due to the introduction of copper cladding and the required extrusion temperatures.

An equal channel angular extrusion (ECAE) is an innovative method which refines the as-cast ingot structure without reduction in the cross sectional dimensions [28-31]. All samples, processed by ECAE prior to wire drawing, have significantly higher strengths than their as-cast and as-drawn counterparts (at a given wire diameter). ECAE process enables the production of high-strength conductors with adequately large cross sections for pulse magnets.

2.3.2 Microstructure

2.3.2.1 Phase Diagram

There are essentially two types of copper-niobium phase diagram : The phase diagram without miscibility gap and impurities, as shown in figure 2.3 [32], and the phase diagram with miscibility gap due to impurity effects, as shown in figure 2.4 [33]. The two diagrams show the negligible mutual solubility of both phases in solid. The phase diagram in figure 2.3 indicates a complete miscibility in melt and a separation of the both phases in solid state. By going down and passing the liquidus line, niobium solidifies first leaving a nearly pure copper melt. Further cooling below 1080°C results in the solidification of copper. Regardless of any cooling condition, niobium solidifies as finely distributed dendrites in the copper matrix. The liquidus temperature of some very well known compositions of Cu-18 wt%Nb and Cu-20 wt%Nb is about 1720°C.

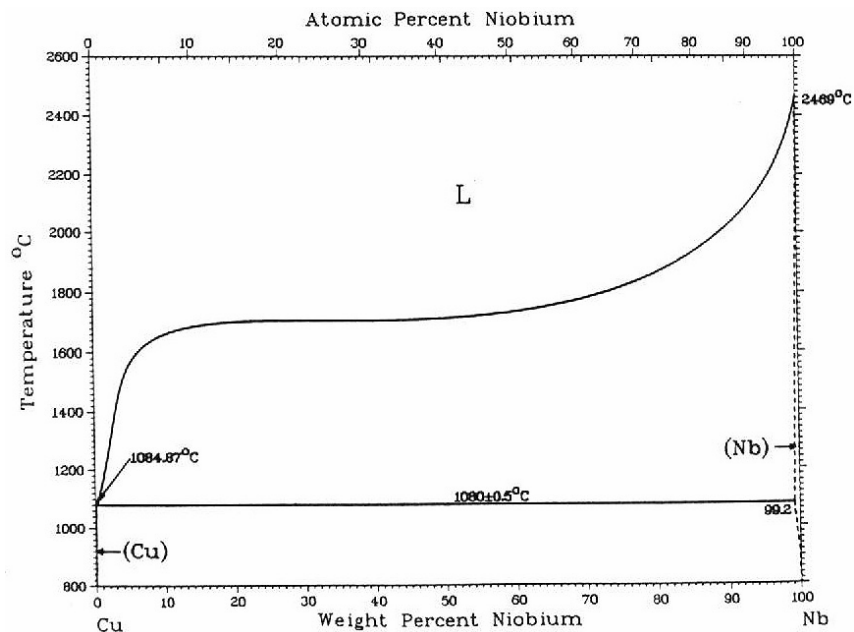


Figure 2.3 The phase diagram of copper-niobium system without miscibility gap and impurities [32].

In figure 2.4 one can see the miscibility gap which lies close below 1800°C. Interstitial impurities (such as oxygen, nitrogen, sulphur, and carbon) are of major importance for deviations from the equilibrium phase diagram, among which oxygen is supposed to have the strongest impact [33].

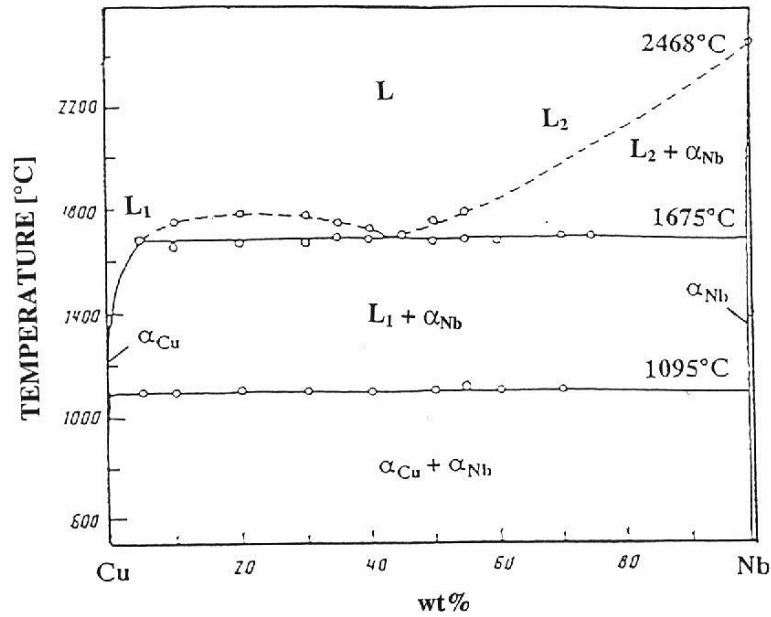


Figure 2.4 The phase diagram of copper-niobium system with miscibility gap due to impurity effects [33].

2.3.2.2 As-Cast Microstructure

Many attempts have been conducted in order to examine the sub-structure of copper phase [34-37] and the microstructure of niobium filaments [8,18,25]. The typical microstructure of as-cast Cu-20%Nb is shown in figures 2.5a,b [18].

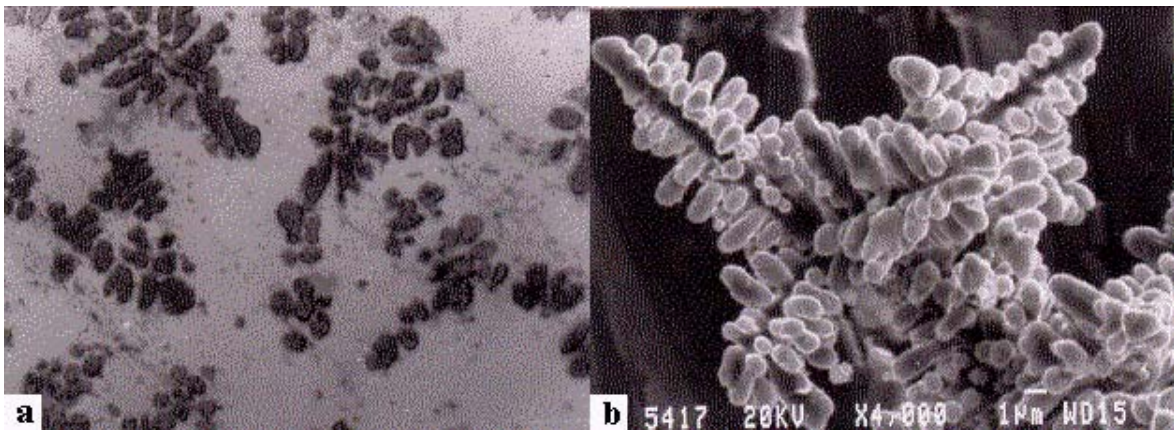


Figure 2.5 a) The typical as-cast microstructure of Cu-20%Nb; 1000x, b) Emerging niobium-dendrites in HNO₃-etched copper matrix; 4000x, [18].

Figure 2.5a shows the microstructure of as-cast Cu-20%Nb under an optical microscope. As the copper matrix is etched away, the emerging niobium-dendrites can be more clearly observed under SEM (figure 2.5b). From figure 2.5b it is obvious that the dendrites grow up to the third generation. The orientations of the primary dendrites are randomly



distributed in the as-cast samples. However, the dendritic arms are commonly aligned parallel to the crystallographic $\langle 100 \rangle$ directions. The result of Heringhaus' work [8], also emphasized by Raabe et al. [25], indicates the average diameter of secondary dendrites to be $D = 2.2 \pm 0.4 \mu\text{m}$. Thus, the previously mentioned casting processes (i.e. the arc casting process with unlined billet [21] and the medium frequency induction melting technique [8,18,22-24] with high cooling rate) can produce small dendrite diameters, namely about $3.8 \mu\text{m}$ and $2.2 \mu\text{m}$ respectively. In addition, the latter process also yields higher density of the second and the third generation dendrites. These relatively small diameters of the secondary dendrites can lead to a high tensile strength after heavy deformation.

2.3.2.3 As-Drawn and Cold-Rolled Microstructures

As-Drawn SEM Observations

As the cast copper-niobium is heavily deformed, the niobium-dendrites are elongated into the form of fibers parallel to the deformation direction (figure 2.6a) which depicts the adoption of filamentary morphology [22,34,37]. The morphology of niobium filaments appears inhomogeneous at small extent of deformation (figure 2.7a), while higher amounts of deformation yields a more uniform shape in filaments (figure 2.7b) [8]. The strong bending in isolated niobium filaments in figure 2.7b indicates the presence of strong residual elastic stresses. A simple estimate of these stresses may be made by applying elastic beam theory [38] :

$$\sigma = \frac{E y}{r} \quad \text{Equation 2-5}$$

where E is Young's modulus, y is the distance from the neutral axis, and r is the radius of curvature.

The origin of inhomogeneity of niobium morphology at lower deformation comes mainly from the non-uniform strain distribution across the wire diameter during drawing. Due to the deformation incompatibility between fcc copper and bcc niobium, more ductile copper matrix must experience a higher deformation locally as a result of unequal distribution of niobium, which modifies the stress distribution within the wire [25]. Further, for $\eta < 6$ most initially randomly oriented niobium dendrites are just rotated to

the wire axis orientation, while a massive cross sectional reduction of the aligned niobium dendrites predominantly occurs at $\eta \geq 6$ [25,34].

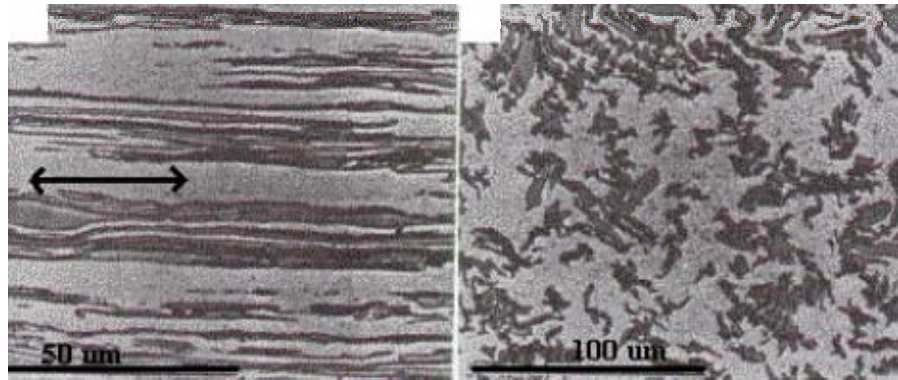


Figure 2.6 The optical micrographs of drawn Cu-20%Nb, deformation $\eta = 5.3$, in : a) Longitudinal section with arrow indicating the deformation axis, b) cross-section [34].

The irregular shape of the filaments in the cross-section (figure 2.6b) reflects the mode of deformation in niobium. The niobium filaments do not maintain circular shapes with increasing deformation. Instead, they are folded or twisted resulting in the so called niobium flat and curled morphology. Hosford [77] analyzed the reason of this phenomena as the result of plane strain deformation of the filaments. With increasing deformation, bcc metals develop a $\langle 110 \rangle$ fiber texture. This texture allows only two of the four $\langle 111 \rangle$ bcc slip directions to allow plastic deformation parallel to the wire axis. Since only two slip directions are active, a local plane strain deformation occurs yielding bent and curled niobium shapes.

Cold-Rolled SEM Observations

In cold rolled Cu-20%Nb samples, Hangen [18], Raabe et al. [25] and Trybus and Spitzig [35] found out that the fiber morphology in the transverse section appeared quite inhomogeneous even after heavy deformation ($\varepsilon = 99.4\%$), as shown in figure 2.8. As some dendrites experienced considerable flattening, some others appeared less deformed.

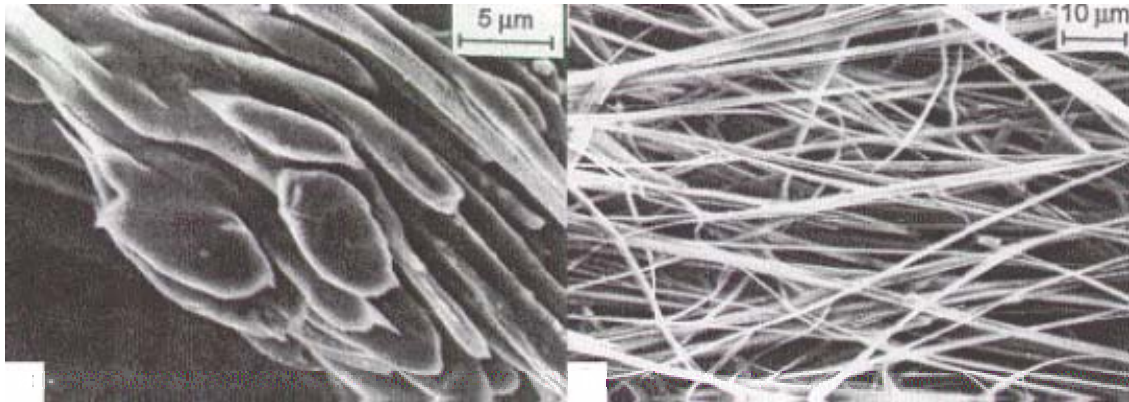


Figure 2.7 The SEM micrographs of drawn niobium filaments after dissolving the copper matrix at a) $\varepsilon = 88.9\%$, b) $\varepsilon = 94.8\%$ [8]. The degree of uniformity of the filaments increases with the degree of cold working.

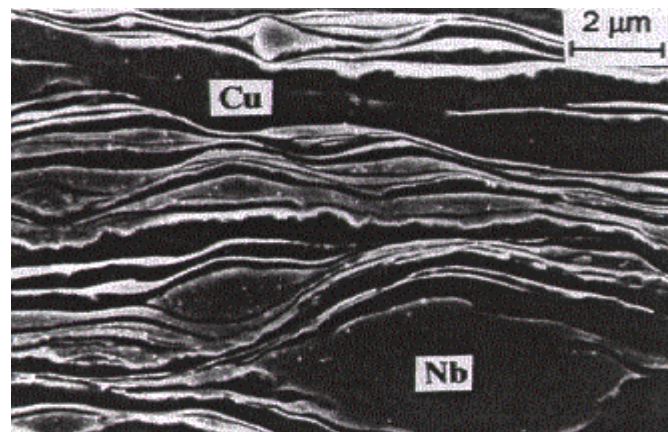


Figure 2.8 The transverse section of cold rolled Cu-20%Nb, $\varepsilon = 99.4\%$ [25].

As-Drawn TEM Observations

TEM investigations [34] in the transverse section Cu-20%Nb wire reveal that, at low draw ratio ($\eta = 3.1$), the dislocations form cells within grains (figure 2.9a). Further reduction to $\eta = 5.3$ results in the coarsening of the cell walls and the reduction of the cell size (figure 2.9b). There are low interior dislocation densities within the cells. In other regions of this composite, some high angle grain boundaries are observed. As the size of copper grains is getting smaller, the distribution of the niobium filaments in the transverse section of the wire at $\eta = 10.3$ is not uniform and tends to form clusters. At $\eta = 11.9$ the selected area diffraction pattern (SADP) results surely reveal the highly textured niobium filaments with $\langle 110 \rangle$ orientation and copper grains with $\langle 100 \rangle$ and $\langle 111 \rangle$ orientations.

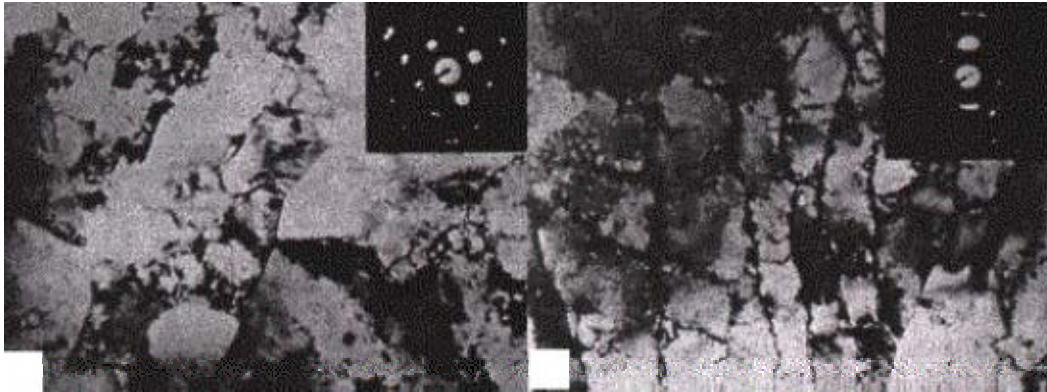


Figure 2.9 The TEM images of Cu-20%Nb wire in the transverse sections with a) $\eta = 3.1$, b) $\eta = 5.3$ [34].

Cold-Rolled TEM Observations

For cold-rolled samples, Trybus and Spitzig [35] observed the substructure of Cu-20%Nb sheet using TEM and explained the results in three different stages of deformation :

■ Low deformation ($\eta = 3.6$)

In this stage, the transverse substructure is characterized predominantly by elongated copper grains in some areas and mainly small grains and heavily dislocated cell walls in the others. The dynamic recovery and recrystallization processes are indicated by a large equiaxed copper grain along with smaller equiaxed cells and grains (figure 2.10). The two copper rolling textures, frequently observed in transverse section, are $\{110\}\langle 112\rangle$ and $\{100\}\langle 001\rangle$. The longitudinal substructure is characterized by elongated copper grains, high angle grain boundaries, heavily dislocated boundaries and some deformation twinning. Much greater texturing takes place here than in the transverse section, with $\langle 111\rangle$ copper parallel with $\langle 110\rangle$ niobium.

■ Intermediate deformation ($\eta = 6.0$).

In the transverse substructure, single and multiple blocks of copper separate the adjacent niobium filaments. Small equiaxed strain free grains are observed. Cell structures are not common. The average dislocation density of copper is $5.0 \times 10^{10}/\text{cm}^2$. The texture in the transverse section shows many rational and irrational orientations, and no obvious copper orientation trend is observed. In the longitudinal substructure, niobium is slightly curved unlike its straight feature in the transverse section. Small twins are observed in the longitudinal substructure. SADP in this section reveals $\langle 110\rangle_{\text{Nb}} \parallel \langle 111\rangle_{\text{Cu}}$.



Figure 2.10 The transverse section of $\eta = 3.6$ sheet [35].

■ High deformation ($\eta = 6.9$)

Figure 2.11 shows the substructure in transverse section of cold-rolled Cu-20%Nb. Unlike at $\eta = 6.0$, the copper phase is now predominated by single grains and neither cells nor equiaxed grains appear. At solely this deformation, twinings in copper take place plentifully. The dislocation density of copper reaches $4.3 \times 10^{10}/\text{cm}^2$. Strong texturing of $\langle 110 \rangle_{\text{Nb}} \parallel \langle 111 \rangle_{\text{Cu}}$ is observed.

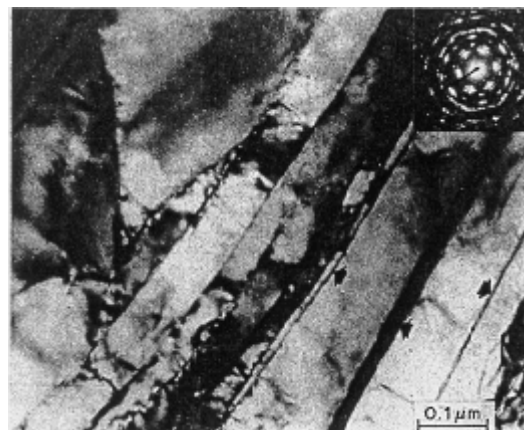


Figure 2.11 The typical transverse section of $\eta = 6.9$ sheet [35].

In TEM of cold-rolled Cu-20%Nb, dislocation cells and tangles are the dominant elements of the substructure in the longitudinal section [18,25]. The dislocation densities of a sample with $\eta = 99.4\%$ reaches as high as 10^{16} m^{-2} . The most interesting result of Hangen's TEM study [18] is the discovery of structurally less ordered or amorphous, glassy areas in many niobium filaments extracted from cold rolled samples. Copper content is enhanced in this glassy as well as in the adjacent crystalline areas. The enhanced impurity contents (e.g. nitrogen, carbon, and sulphur) may provoke the development of this metallic glass, since very pure metals never transform into the amorphous state. Previous studies by Luborsky [39], Güntherodt and Beck [40], Wang et al. [41], and Iwasaki and Wang [42] underline this glassy areas observation, i.e., niobium tends to potentially undergo phase transformation into a structurally less ordered area.

2.3.2.4 As-Drawn/Annealed SEM/TEM Observations

Hong et al. [38] have examined the microstructural instability of copper-niobium wires (up to $\varepsilon = 99.9\%$), annealed at various temperatures between 300 and 500°C for 1 hr under SEM and TEM. After annealing at 500°C, the previously bent niobium-fibers become essentially straight indicating that the elastic stresses (equation 2-5) in the fibers are removed. It is observed that the rate of spheroidization varies with position in the microstructure leading to the difficulty in the quantitative analysis of the kinetics of spheroidization. The onset of spheroidization in niobium-filaments under SEM is shown in figure 2.12. Hong et al. also predicted the time (t_s) of the entire spheroidization process for copper-niobium and copper-Ag of various structural scales. The results are plotted in figure 2.13.

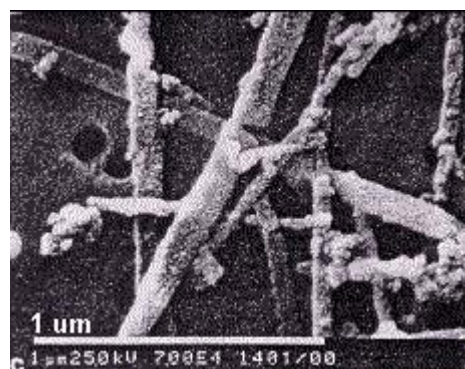


Figure 2.12 The onset of spheroidization of niobium-filaments after annealing at 500°C for 1 hr under SEM [38].

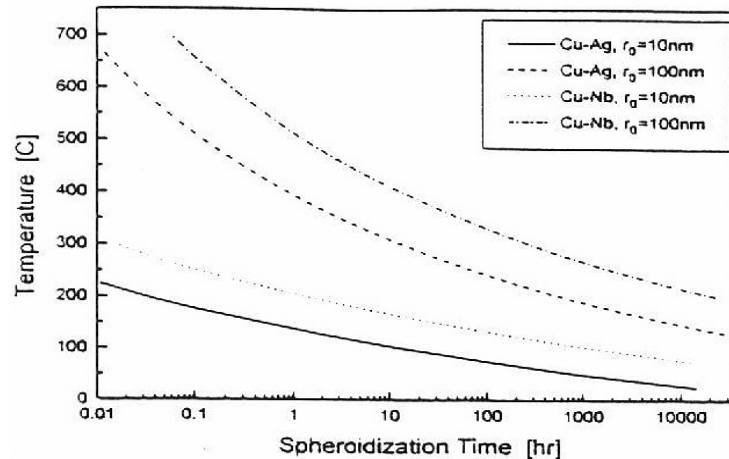


Figure 2.13 The predicted spheroidization times for niobium and silver cylinders of various initial sizes in a copper matrix [38].

2.3.3 Filament Thickness and Spacing

The thickness of niobium filaments decreases much more rapidly with increasing degree of rolling as compared to wire drawing (figure 2.14) [35]. Verhoeven et al. [43] compared their measurements of filament thickness and spacing with those of Spitzig and Krotz [21] and Spitzig et al. [34], for Cu-20%Nb wires cast in a copper mold with and without graphite liner. At $\eta \geq 6$ (cast in the lined copper mold) and at $\eta > 4$ (cast in the unlined copper mold) large discrepancies take place, of which TEM data of filament thickness are much lower than those of SEM. These discrepancies may arise from an under estimation of the filament spacings/thickness using TEM, an over estimation of the spacings/thickness using optical and SEM, or a combination of the both possibilities [43].

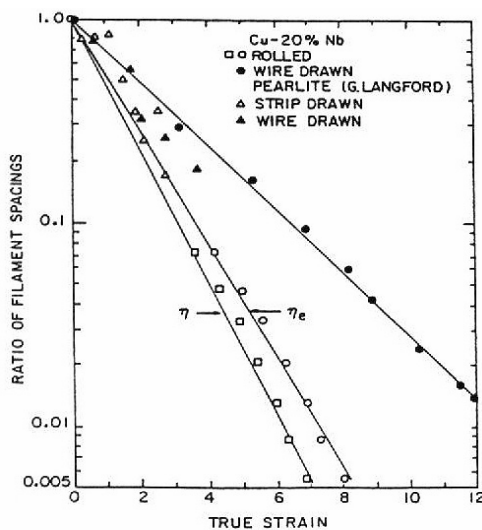


Figure 2.14 The effect of rolling reduction or wire draw ratio on the spacing of niobium filaments in Cu-20%Nb. For direct comparison with the results for wire drawn material, effective strain (η_e) for the rolled specimen is also plotted [35].

2.3.4 Crystallographic Textures

Crystallographic texture is defined as the distribution of the lattice orientations of a polycrystal. Numerous papers had been written to investigate the textures of copper and niobium in drawn wire and cold rolled specimens. Hong et al. [38] determined the textures of the materials (with unspecified degrees of deformation) from views along the fiber axis. Raabe und Gottstein [22], Heringhaus et al. [24], Raabe [44], Raabe et al. [45], and Heringhaus et al. [46] conducted the measurements of such specimens from various degrees of deformation. The Fourier type series expansion method [47] was implemented in order to compute the orientation distribution functions (ODFs) from the incomplete X-ray pole figures [48]. The microtexture of specimens, i.e. the single grain orientation measurements, was carried out using the electron back scattering (EBSD) technique [36,44,45]. From the results, presented as RD (rolling direction) inverse pole figures in figure 2.15, it is clear that copper in MMC exhibits mainly two texture orientations after heavy deformations : $\langle 111 \rangle$ and $\langle 100 \rangle$ directions parallel to the drawing axis. The increasing maximum intensities indicate that the copper is getting textured mainly in such orientation as deformation increases. Figure 2.16 shows the RD inverse pole figures of niobium phase in drawn MMC featuring a texture of $\langle 110 \rangle$ orientation parallel to the drawing axis after heavy deformation.

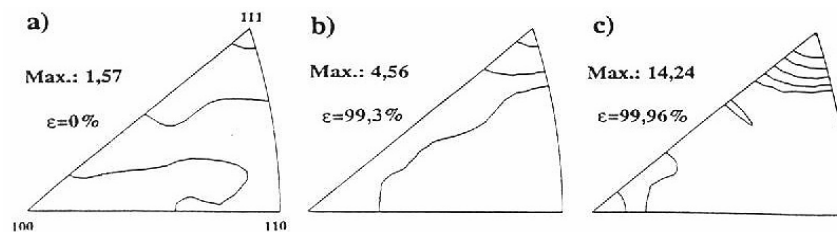


Figure 2.15 The texture of the copper phase in the drawn metal matrix composite, a) $\eta = 0$, b) $\eta = 4.3$, c) $\eta = 8.6$ [25].

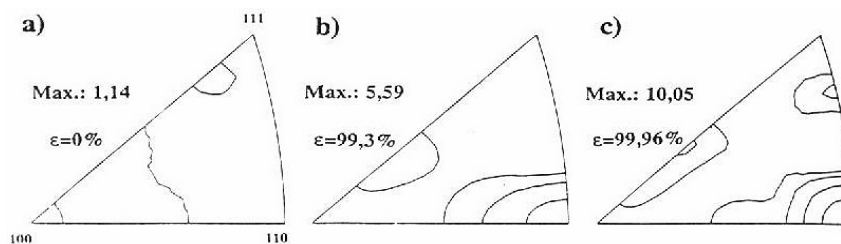


Figure 2.16 The texture of the niobium phase in the drawn metal matrix composite, a) $\eta = 0$, b) $\eta = 4.3$, c) $\eta = 8.6$ [25].



2.3.5 Physical Properties of Copper and Niobium

There is apparently no better way than to summarize in a table (table 2.1) what previous studies have already presented regarding the basic physical properties of copper and niobium.

| Properties | Copper | Niobium |
|--|-------------------|---------|
| Lattice structure [8,17,18] | fcc | bcc |
| Melting temperature [°C] [8,17,18] | 1083 | 2468 |
| Atomic radius [Å] [8,17] | 1.28 | 1.46 |
| Lattice constant [Å] [8,17,18] | 3.61 | 3.30 |
| Density [kg/dm ³] [8,17,18] | 8.93 | 8.58 |
| Young's modulus [GPa] [8,17,18] | 128 | 105 |
| Shear modulus [GPa] [8,17,18] | 48 | 38 |
| Poisson's ratio [8,17,18] | 0.34 | 0.38 |
| Stacking fault energy [J/m ²] [8] | 0.07 | |
| Specific resistance [μΩ.mm] [49,52] | 1.7 | 16 |
| Debye temperature [K] [50] | 343 | 275 |
| Ductile-to-brittle transition temperature [K] [51] | | 147 |
| Transition temperature for superconductivity [K] [49,52] | <10 ⁻⁴ | 9.2 |

Table 2.1 The physical properties of copper and niobium [8,17,18,49-52].

2.3.6 Copper-Niobium Diffusion Coefficient

2.3.6.1 ⁹⁵Nb→Cu

The impurity diffusion of ⁹⁵Nb into pure polycrystalline copper (99.999%) was studied over the temperature range of 807°C to 906°C [53]. The diffusion coefficients are listed in table 2.2. The employed analysis was residual activity method to determine the concentration profile of the diffused isotope. The specimen was sectioned by grinding, and the thickness of the removed layer was estimated by weight difference.



| Temperature (°C) | ⁹⁵ D (cm ² /sec) |
|------------------|--|
| 807 | 1.56 x 10 ⁻¹² |
| 827 | 2.21 x 10 ⁻¹² |
| 856 | 4.17 x 10 ⁻¹² |
| 865 | 5.63 x 10 ⁻¹² |
| 906 | 1.46 x 10 ⁻¹¹ |

Table 2.2 The niobium-95 tracer diffusion coefficients in copper [53].

Butrymowicz et al. [54] plotted the temperature dependence of the data in table 2.2. The following relationship was then found from the best fit data of the plot :

$$D^* = 2.04 \exp \left[\frac{-60.060 \frac{\text{kcal}}{\text{mol}}}{RT} \right] \left(\frac{\text{cm}^2}{\text{sec}} \right) \quad \text{Equation 2-6}$$

The accuracy of the frequency factor ($D_0 = 2.04 \text{ cm}^2/\text{sec}$) is within $\pm 30\%$, whereas that of the activation energy ($Q = 60.060 \text{ kcal/mol}$) is within $\pm 2\%$.

2.3.6.2 Copper-Niobium Interdiffusion

The interdiffusion taking place between a niobium-coated wire covering a copper core was investigated in the temperature range of 800 to 907°C [55]. The degree of interdiffusion occurring in such bimetallic wire was detected with electrical resistance measurements, which was previously employed by Ceresara et al. [56] and calculated by Bokshtein et al. [57]. By assuming the concentration-dependent of interdiffusion over a narrow temperature range of the study, the two main parameters for Arrhenius expression have been derived as :

$$D_0 = 4.91 \pm 0.22 \text{ cm}^2/\text{sec}$$

$$Q = 52.6 \pm 10.3 \text{ kcal/mol}$$

No individual interdiffusion coefficients were reported.



Schelle [58] conducted the interdiffusion investigations at somewhat higher temperature (1100 to 1740°C) which only yielded very qualitative data without calculation of interdiffusion coefficients. Solid state diffusion couples of pure copper and niobium annealed at 1000°C for as long as 14 days showed little or no interdiffusion [58].

2.3.7 Thermomechanical Properties of Copper-Niobium Composites

2.3.7.1 Strength of Copper-Niobium

The interesting copper-niobium composites feature very high strengths which are greater than those predicted by rule of mixture or ROM [19-21,34,35,59,60,64-70], as shown in figure 2.17. It is clear from figure 2.17 that the strength of copper-niobium *in-situ* composites depends on the draw ratio (η) and the initial niobium dendrite size (t_0). The combination of fcc and bcc phases in the *in-situ* composites exhibits greater tensile strength than when they are both fcc [34,65,69,70].

The stress-strain curves for Cu-18.2%Nb with different diameters were presented by Bevk et al. [19], as shown in figure 2.18. Some interesting points from figure 2.18 are :

- the total strain to failure does not vary appreciably with reduction;
- the degree of plastic deformation decreases gradually with increasing reduction in cross-sectional area;
- for the wire with smallest diameter, most of strain appears to be elastic leaving little room for further strengthening.

For sufficiently high values of η , the strength of composites as a whole surpasses the strength of heavily deformed niobium and copper, as shown in figure 2.19 [19]. In figure 2.19 the solid line connects the ultimate tensile strengths of heat treated bulk copper and niobium, whereas the dashed line connects the strength values of both cold worked copper and niobium.

Spitzig and Krotz [21] derived an equation describing the effect of deformation (η) on the filament thickness and spacing in the composites. Such equation, which is expressed in exponential term, acknowledges the initial condition of composite microstructure :

$$\frac{\bar{\lambda}}{\lambda_0} = \frac{\bar{t}}{t_0} = \exp(-0.37\eta) \quad \text{Equation 2-7}$$



where :

$\bar{\lambda}$ = average copper matrix spacing after deformation

$\bar{\lambda}_0$ = average initial copper matrix spacing

\bar{t} = average niobium filament thickness after deformation

\bar{t}_0 = average initial niobium dendrite size

Equation 2-7 was derived based upon the experimental measurement data of : Cu-20%Nb wires with two different initial niobium dendrite sizes, and Pearlite [83].

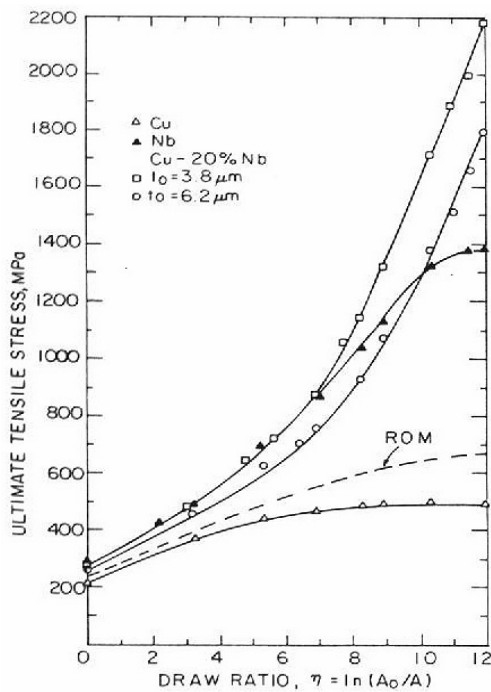


Figure 2.17 The effect of draw ratio on the ultimate tensile stress of copper, niobium, and Cu-20%Nb composites [21].

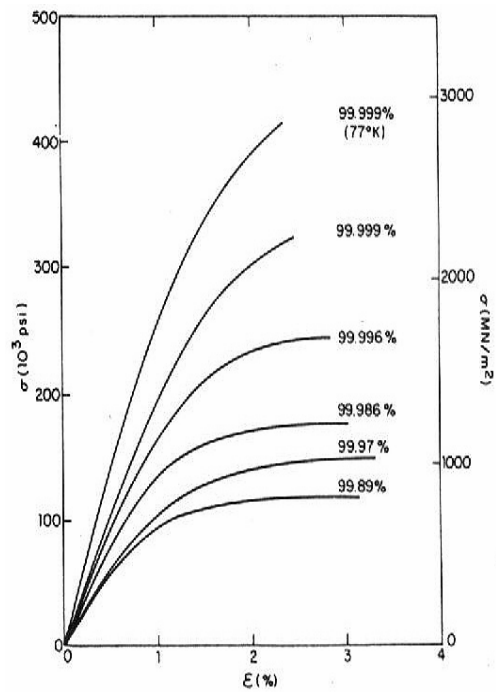


Figure 2.18 Stress-strain curves for a series of Cu-18.2%Nb composite wires with different extents of deformation [19].

Further, Spitzig and Krotz also obtained a relationship among the ultimate tensile strength (σ_{uts}), the draw ratio and the average initial niobium dendrite size as :

$$\sigma_{\text{uts}} = 82 + 459 (t_0)^{-0.5} \exp\left(\frac{\eta}{5.4}\right) \quad \text{Equation 2-8}$$

where σ_{uts} is in MPa and t_0 in μm .

Experimental data of Cu-20%Nb with the average initial niobium dendrite sizes of $t_0 = 3.8 \mu\text{m}$ and $6.2 \mu\text{m}$ show a good correlation with equation 2-8. It is concluded that a higher tensile strength can be achieved by reducing the initial niobium dendrite size through more rapid cooling process.

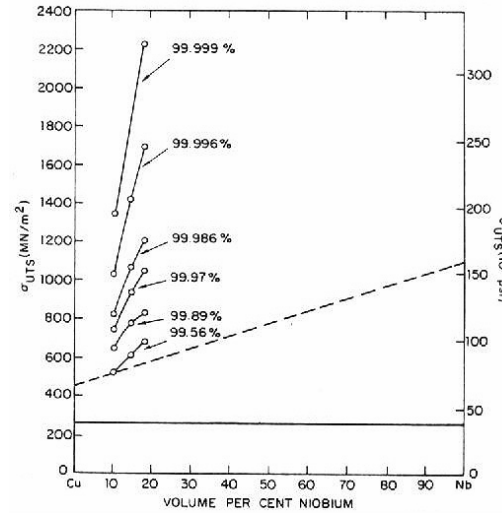


Figure 2.19 The ultimate tensile strength of *in-situ* copper-niobium composites as a function of niobium concentration. The area between the solid and the dashed lines represents the rule of mixture (ROM) prediction of σ_{uts} [19].

Recently Hangen [18] and Raabe et al. [25] simulated and discussed the yield strength of copper-niobium MMC. The simulation model accounts essentially for wire drawn specimens. Nevertheless, most of underlying assumptions behind the model are also applicable to rolled samples. The model includes firstly the contribution of the fiber morphology to the yield strength ($\Delta\sigma$) of the composite, which is :

$$\Delta\sigma = (0.8 + 0.2 \cdot R) \cdot \left(-\frac{4.25\text{MPa}}{M_{\text{Nb}}} \cdot R + \sqrt{\left(\frac{4.25\text{MPa}}{M_{\text{Nb}}}\right)^2 + 5.9\text{MPa}^2 \cdot \left(9.25 - \frac{\eta}{2}\right)} \right) \cdot \exp\left(\frac{\eta}{2}\right) \quad \text{Equation 2-9}$$

in this case :

$$\frac{\sigma_{\text{ROM}}^{\text{Nb}}}{\sigma_{\text{ROM}}^{\text{Cu}}} = \frac{\Delta\sigma^{\text{Nb}}}{\Delta\sigma^{\text{Cu}}} \equiv R \quad \text{Equation 2-10}$$

where :

$\sigma_{\text{ROM}}^{\text{Nb}}$ = the yield strength of pure niobium

$\sigma_{\text{ROM}}^{\text{Cu}}$ = the yield strength of pure copper

$\Delta\sigma^{\text{Nb}}$, $\Delta\sigma^{\text{Cu}}$ = the additional strength contributions, attributed to the impact of the filaments

M_{Nb} = the Taylor factor of the niobium phase

Equation 2-9 is then added to the ROM-based strength (σ_{ROM}) yielding a model of :

$$\sigma_{\text{p}0.2} = \sigma_{\text{ROM}} + \Delta\sigma = \text{ROM} + \text{MMC} \quad \text{Equation 2-11}$$

As equation 2-11 is plotted (figure 2.20), it reveals a very good correspondence to the experimental results (Exp). The experimental data were taken from Spitzig and Krotz [21].

The model, however, does not apply for low strains where $\sigma_{\text{UTS}} > R_{\text{p}0.2}$.

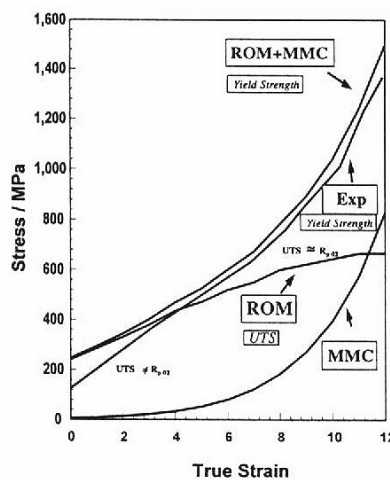


Figure 2.20 The resulted simulation (ROM+MMC) of the copper-niobium MMC wire based on the equation 2-11 [45]. The experimental data were taken from Spitzig and Krotz [21].

Bevk and Karasek [61] discussed the strength of copper-niobium composites both at room temperature and high temperatures (figures 2.21 and 2.22). Using the specific example of Cu-14.8%Nb, they found out that the strength increased with the overall composite reduction at room temperature and high temperatures (figure 2.22). Further they also



observed that the strength decreased by approximately 60% between room temperature and 768 K, with the lowest strength achieved by the wire with smallest diameter.

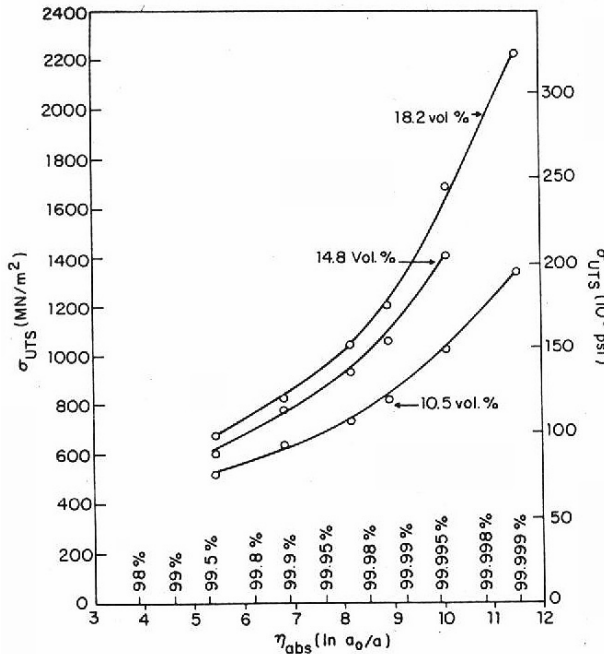


Figure 2.21 The ultimate tensile strength, σ_{UTS} , of in-situ formed copper-niobium composites (with different niobium contents) as a function of cross-sectional area reduction, η_{abs} [61].

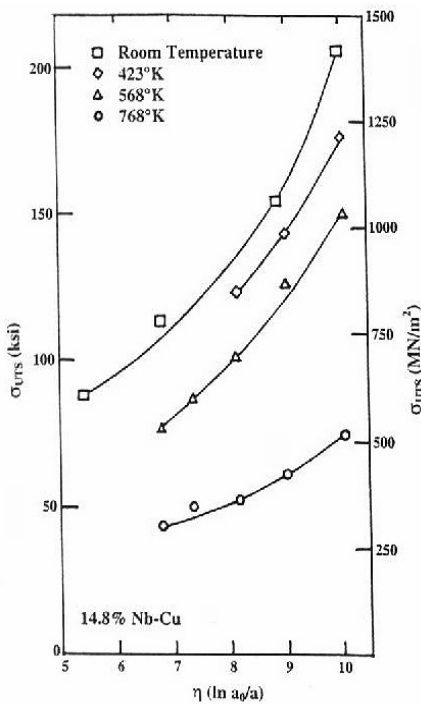


Figure 2.22 The ultimate tensile strength of Cu-14.8%Nb wire as a function of true strain at various temperatures [61].

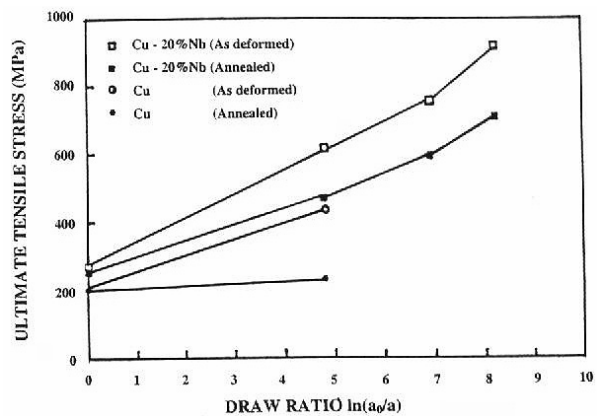


Figure 2.23 The variation in the ultimate tensile strength of Cu-20%Nb and copper with draw ratio, before and after annealing at 650°C for 24 hr [65].



Biner and Spitzig [65] compared the ultimate tensile strength of Cu-20%Nb and copper (deformed and annealed) as a function of draw ratio (figure 2.23). For a given η , the strength of annealed material is lower than that of the deformed one. As a whole, Cu-20%Nb has the higher tensile strength than copper alone.

2.3.7.2 Strengthening Mechanisms

There are primarily six models introduced to explain the strengthening mechanisms in the *in-situ* composites :

- Rule of Mixture (ROM) Model [66] and its modifications to account for plasticity effects as the both phases undergo extensive plastic deformation [67-69].
- Barrier Model [70,71,76].
- Nonhomogeneous Deformation Model [72].
- Dislocation Propagation Model [35,73].
- Modified Dislocation Strengthening Model [63,74].
- Lamellar Structures Model [75].

These mechanisms will be treated in more detail in Chapter 3 : Background Theories.

2.3.7.3 Creep Characteristics

Again, recently Biner and Spitzig [65] investigated the creep deformation and rupture characteristics of Cu-20%Nb wire and compared them with the results from pure copper. The main results show that the creep rupture strength (σ) and the stress exponent (n) of the Norton's power law (equation 2-12) is considerably higher in Cu-20%Nb than in pure copper. This phenomenon is predominantly caused by the introduction of constraint on the creep flow of the copper matrix by niobium filaments, and the increase in diffusion type creep damage produced by the easy diffusion paths along the elongated niobium filaments and the reduced matrix grain size as the draw ratio increases.

$$\dot{\epsilon} = B\sigma^n \quad \text{Equation 2-12}$$

where :

$\dot{\epsilon}$ = the steady state creep strain rate
 B = the creep coefficient

σ = the creep rupture stress
 n = the stress exponent

For Cu-20%Nb, the value of n is in the range of 6.6-8.1, while for pure copper it is 2.75. These creep experiments for pure copper and Cu-20%Nb (with different draw ratios) were performed at $T = 500^\circ\text{C}$.

2.3.7.4 Hardness

The hardness measurement for the as-cast and as-drawn Cu-20%Nb had been conducted by Heringhaus [8]. In as-cast condition, the result of 200 g Vickers indicates HV80, while measurement by Hangen [18] of the Vickers hardness (100 g) shows HV130. The results of 200 g Vickers hardness of the drawn wires show a plateau of approximately HV150 within the range $2 \leq \eta \leq 6$ (figure 2.24). Above $\eta = 6$, the hardness strongly increases reaching an average maximum value of HV325 at $\eta = 10$. Raabe et al. [25] discussed the existence of such hardness plateau as the range in which the initially randomly oriented dendrites rotate towards an orientation parallel to the wire axis.

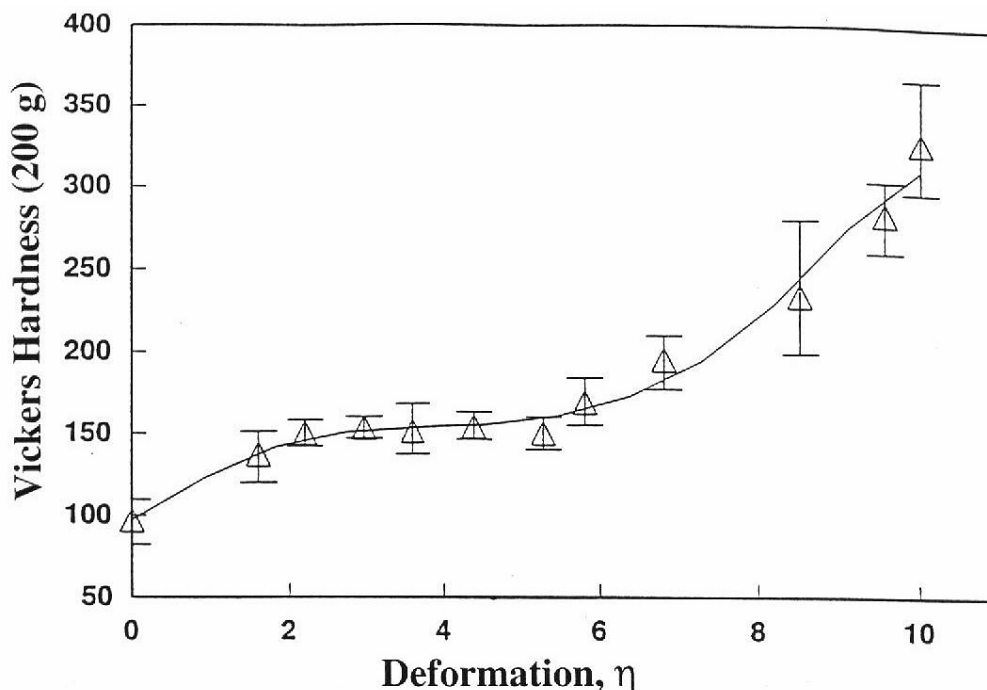


Figure 2.24 The average Vickers hardness (200 g) of Cu-20%Nb wire [8].

Hangen [18] examined the hardness of cold rolled Cu-20%Nb sheets in two ways :

- along the ND/RD plane (figure 2.25 a), and
- along the TD/RD plane (figure 2.25 b)

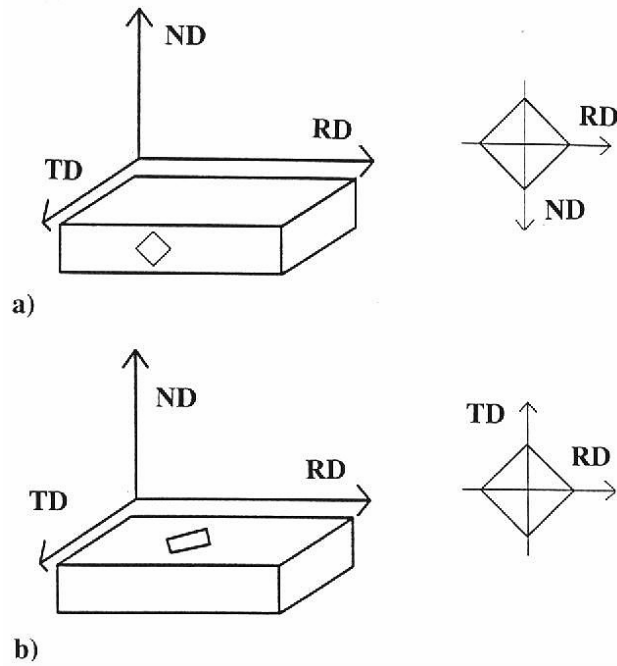


Figure 2.25 a) The hardness measurement along the ND/RD plane, and b) along the TD/RD plane [18]. ND = normal direction, TD = transverse direction, and RD = rolling direction.

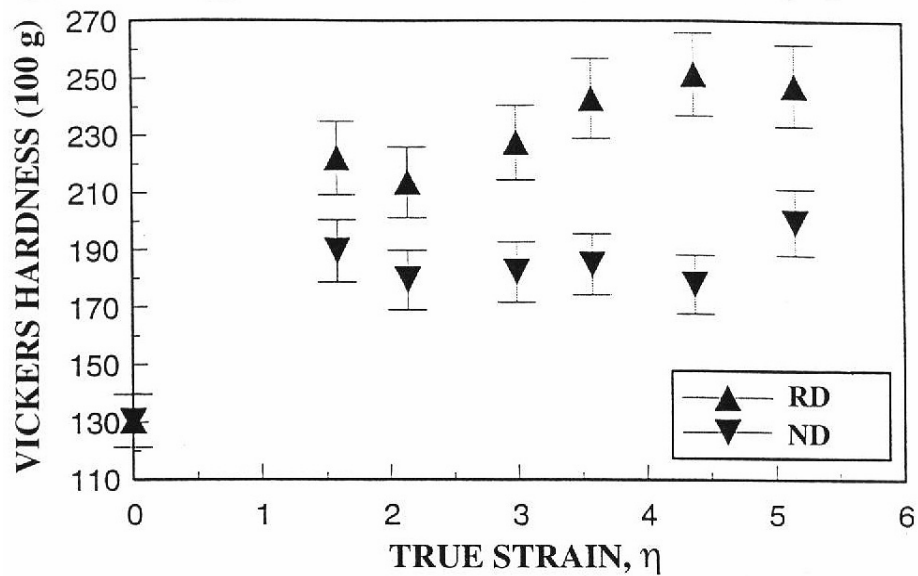


Figure 2.26 The Vickers Hardness (100 g) of the Cu-20%Nb sheet in the ND/RD plane. The hardness in the RD is higher than that in the ND [18].

For the measurement along the ND/RD plane, it is found that the hardness in the rolling direction (RD) is higher than that in the normal direction (ND) (figure 2.26). However there is no significant difference between the hardness in the TD and that in the RD (figure 2.27).

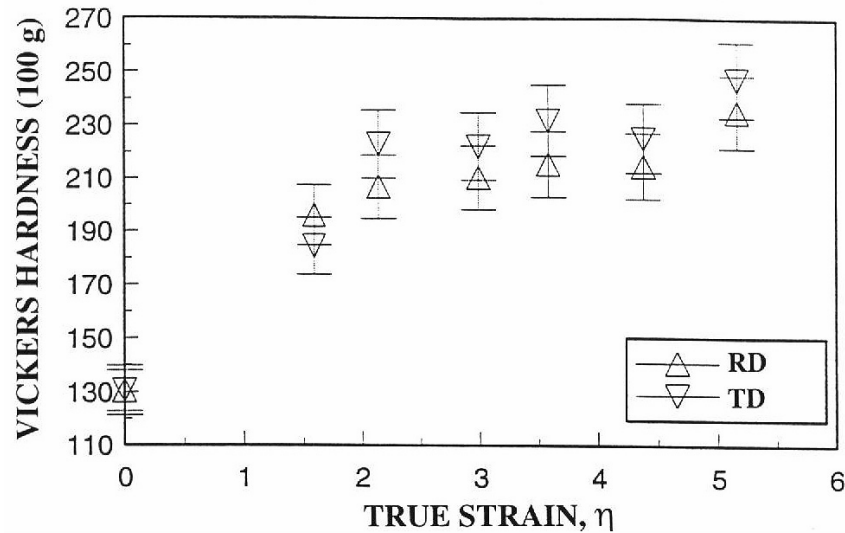


Figure 2.27 The Vickers Hardness (100 g) of the Cu-20%Nb sheet in the TD/RD plane [18].

2.3.8 Electrical/Electromagnetic Properties of Copper-Niobium Composites

The electrical conductivity of copper-niobium MMCs has been the subject of many works and discussions [19,21-24,34,35,46,62,63,78-82,87]. Karasek and Bevk [78] worked out a typical resistivity-vs-temperature plot for a copper-niobium composite wire, with diameter of 61 μm over the temperature range of 293-823 K (figure 2-28). Here, it is clearly shown that the resistivity of such wire increases with the temperature. The upper curve represents the data obtained for the initial temperature increase from the as drawn state.

Gielisse und Bai [83] showed that when ultimate tensile strength vs. conductivity data for the copper-niobium and copper-silver systems were together plotted (similar to figure 1.1), a linear relationship was obtained (equation 2-13). This conclusion was reached after collecting data from various sources [19,26,27,84-86].

$$\sigma_{\text{UTS}} = -35\sigma_{\text{COND}} + 3760$$

Equation 2-13

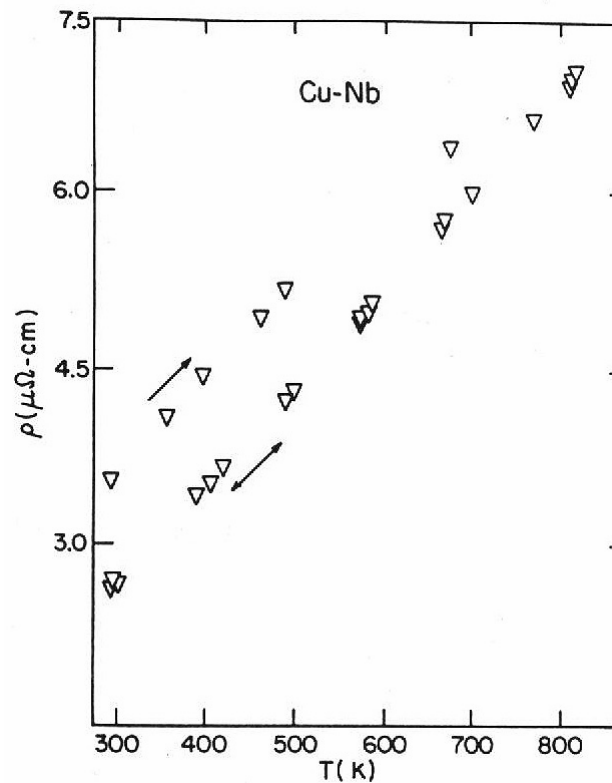


Figure 2.28 The typical resistivity-vs-temperature behavior of a 61 μm copper-niobium composite wire [78].

Heringhaus [8] and Raabe et al. [87] investigated and reported the electromagnetic properties and application of Cu-20mass%Nb wire. The measurement temperatures of the electrical resistivity were : 77 K, 198 K and 295 K. The important results and discussions cover those such as :

- The resistivity of pure copper apparently does not depend on the degree of deformation.
- The resistivity of Cu-20mass%Nb is always higher than that of pure copper. It increases for $\eta > 6$ ($\varepsilon = 99.75\%$) in wires and for $\eta > 3$ ($\varepsilon = 95\%$) in sheet materials.
- Annealing at 823 K for 5 hr does not much affect the resistivity of pure copper, but noticeably decreases that of Cu-20mass%Nb. This drop of the resistivity becomes more significant for $\eta > 6$ in case of wires and for $\eta > 3$ in case of sheets. At low deformation the general drop of resistivity takes place probably due to the segregation of solute atoms (e.g. sulfur from graphite crucible) into internal boundaries which serve as good sinks. At higher deformation, such drop exists due to the coarsening of the niobium filaments since, for the diffusion controlled coarsening of the ribbons, mass transport



can take place along the copper-niobium phase boundaries with a much lower energy of activation than for bulk diffusion [88].

- The presence of external magnetic field B increases the resistivity of both copper and Cu-20mass%Nb wires. For Cu-20mass%Nb, the transition temperature from the normal into the superconducting state takes place at about 8 K. Such temperature appears to be decreased with increasing magnetic field (figure 2-29). Such phenomenon is also observed in rolled specimens.
- The transition of the superconducting state of Cu-20mass%Nb wire depends upon the degree of deformation, i.e. on the microstructure (figure 2-30). In the absence and the presence of external magnetic field, the sample with larger deformation (i.e. larger thickness reduction) features the higher resistivity (in normal conducting state). However the onsets of transition temperatures of both samples stay approximately the same .
- An external transverse magnetic field on wires causes a decrease in the transition temperatures for both levels of deformation and a change of their relative positions with respect to each other (figure 2-30b). In this case, the more strongly deformed wire has the higher onset of transition temperature than the less deformed one. The difference between T_{onset} and T_{offset} is larger in the presence of external magnetic field. The same behaviors are also observed in rolled specimens.
- At $T = 4.3$ K, a Cu-20mass%Nb wire sample with $\eta = 6.8$ ($\varepsilon = 99.89\%$) requires $B = 1.3$ T for superconducting transition state, while the one with $\eta = 10$ ($\varepsilon = 99.995\%$) needs $B = 2$ T.
- By assuming *only inelastic scattering* of conduction electrons at internal phase boundaries as primary contribution, a resistivity simulation yields :

$$\rho(\mathbf{d}, T) = \rho_0(T) \cdot \left(1 + \frac{3}{4} \cdot \left(\frac{l(T)}{d} \right) \right) \quad \text{Equation 2-14}$$

where :

$\rho(\mathbf{d}, T)$ = the resistivities of copper or niobium as a function of fiber diameter and temperature $\rho_0(T)$ = the resistivities of copper or niobium without scattering at the phase boundary

$l(T)$ = the mean free path of a conduction electron d = the thickness of the fiber; $d > l$

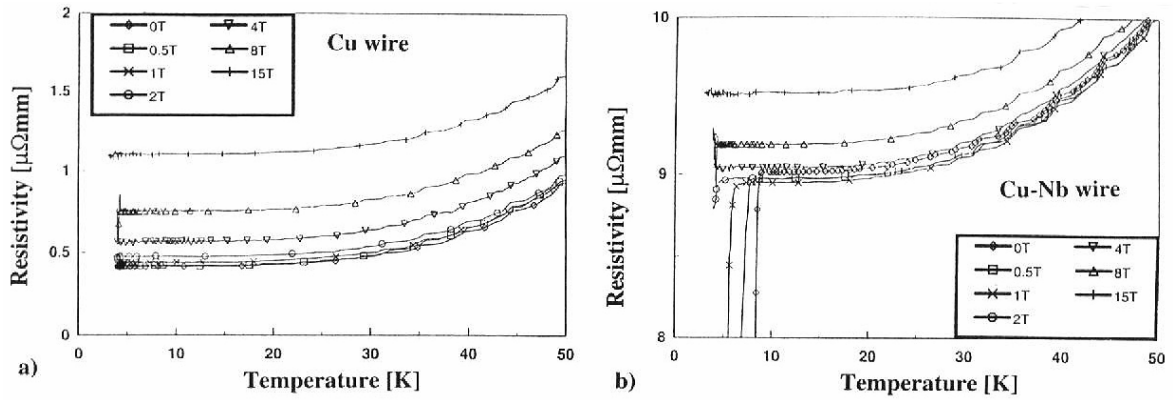


Figure 2.29 a) copper, and b) Cu-20%Nb. The temperature dependence of the resistivity of drawn copper and Cu-20%Nb wires ($\eta = 10$, $\varepsilon = 99.995\%$) in the presence of different external magnetic fields [8].

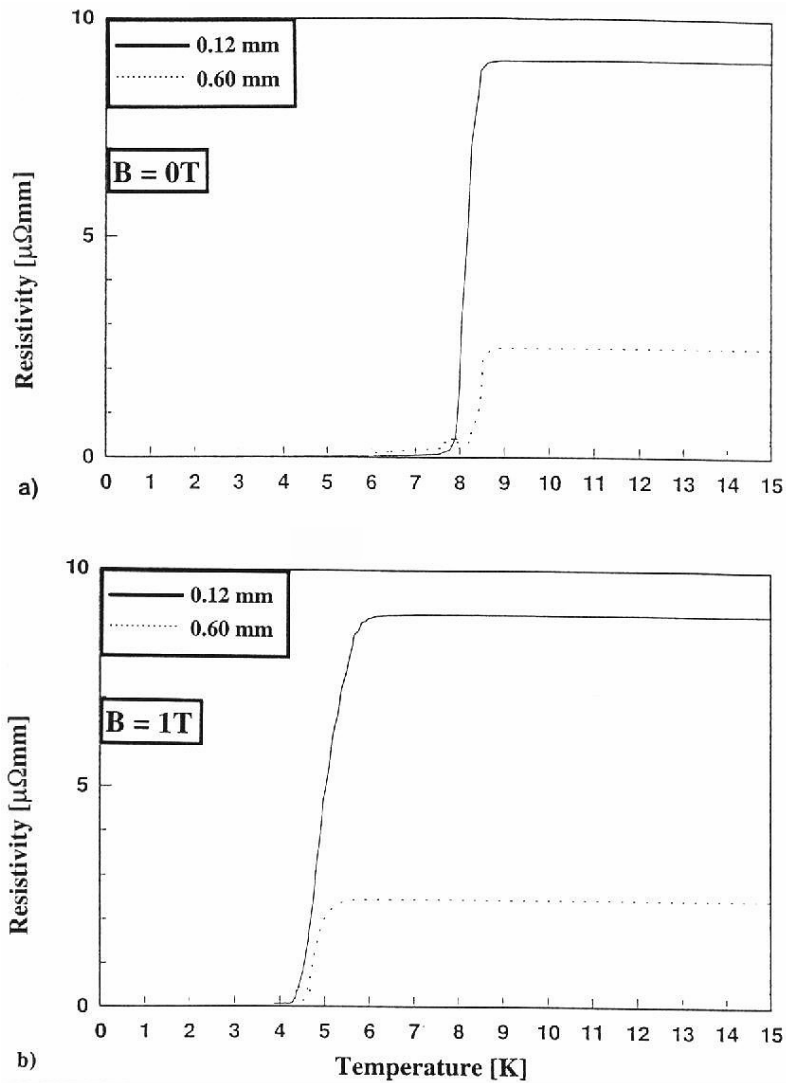


Figure 2.30 a) B = 0 T, and b) B = 1 T. The resistivity of wire drawn Cu-20mass%Nb as a function of the temperature for two different degrees of deformation ($d = 0.6$ mm [$\eta = 6.8$, $\varepsilon = 99.89\%$]; $d = 0.12$ mm [$\eta = 10$, $\varepsilon = 99.995\%$]) [87].



- It is known that after heavy deformation, the morphology of copper and niobium is no longer cylindrical, but curled. In order to account for the curled morphology, a correction term has been inserted into equation 2-14, yielding :

$$\rho(\mathbf{d}, \mathbf{T}) = \rho_0(\mathbf{T}) \cdot \left(1 + \frac{3}{4} \cdot \left(\frac{l(\mathbf{T})}{\mathbf{d} \cdot \left(1 - 0.44 \cdot \left(\frac{\eta}{\eta_{\max}} \right) \right)} \right) \right) \quad \text{Equation 2-15}$$

- By taking into account the increasing influence of dislocation density ($\Delta\Lambda$) in both phases, equation 2-15 can then be modified as :

$$\rho(\mathbf{d}, \mathbf{T}) = \rho_0(\mathbf{T}) \cdot \left(1 + \frac{3}{4} \cdot \left(\frac{l(\mathbf{T})}{\mathbf{d} \cdot \left(1 - 0.44 \cdot \left(\frac{\eta}{\eta_{\max}} \right) \right)} \right) \right) + \Delta\Lambda \cdot \rho_{\text{Disloc}} \quad \text{Equation 2-16}$$

where : $\rho_{\text{CuDisloc}} = 2 \cdot 10^{-26} \Omega\text{m}^3$

$\rho_{\text{NbDisloc}} = 25 \cdot 10^{-24} \Omega\text{m}^3$

Λ is assumed to increase linearly with the technical strain, ε

- The comparison of experimental data and simulation of resistivity is shown in figure 2-31 at $T = 298 \text{ K}$. In figure 2-31, the calculated resistivities are somewhat lower than the experimental data. This deviation may likely appear from the microstructural data. In this case, transmission electron microscopy (TEM) should be implemented in order to measure filament diameter and spacing especially for heavily deformed copper-niobium MMCs (24).
- The next deviation in figure 2-31, which is the resistivity drop in the range $5 < \eta < 7$ ($\varepsilon = 99.33\%$ to $\varepsilon = 99.91\%$), is caused by the initial rotation of the niobium dendrites. Within the range, these dendrites primarily rotate parallel to the drawing axis rather than experiencing large thickness reduction [25].

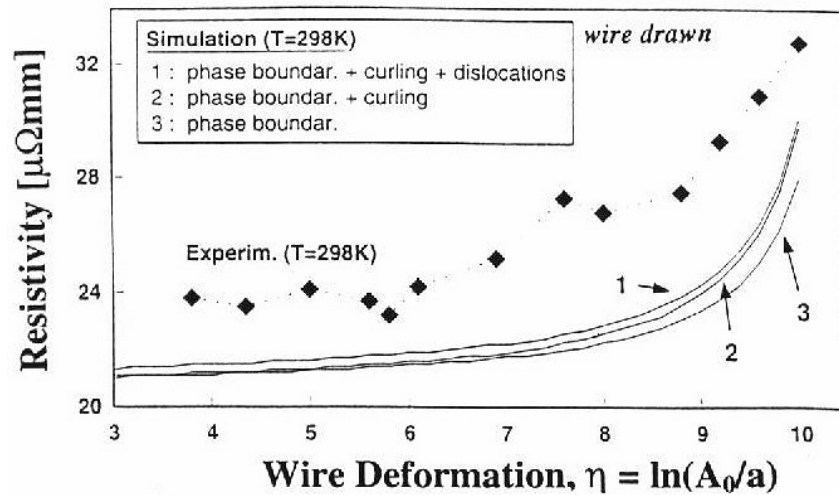


Figure 2.31 The resistivity of wire drawn Cu-20mass%Nb as a function of deformation at $T = 298$ K. (1) Inelastic scattering at phase boundaries + curled filament geometry + dislocations, i.e. Equation 2-16; (2) inelastic scattering at phase boundaries + curled geometry, i.e. Equation 2-15; (3) inelastic scattering at phase boundaries only, i.e. Equation 2-14 [87].

- It is concluded from figure 2-31 that the calculated resistivities are lower than the experimental ones. Such deviation occurs likely due to the utilized average fiber data which are too large. The enhancement of such microstructural data plays more significant role in adjusting experimental resistivity values with those of simulated ones by employing TEM instead of SEM. The inelastic scattering with the increase of dislocation density (curve 1) and the curled morphology (curve 2) has indeed minor effect on the total normal-state resistivity.
- Based upon the analogy of parallel connected resistors, the total resistivity ρ of copper-niobium wire depends on ρ_{Cu} and ρ_{Nb} according to :

$$\frac{1}{\rho} = \frac{0.8}{\rho_{\text{Cu}}} + \frac{0.2}{\rho_{\text{Nb}}} \quad \text{Equation 2-17}$$



References

1. *Ashby, M.F.* : Phil. Trans. Royal Soc. London **A322** (1987) 393.
2. *Wainwright, S.A.; Biggs, W.D.; Currey, J.D.; and Gosline, J.M.* : "Mechanical Design in Organisms", Princeton University Press (1976).
3. *Chawla, K.K.* : in : R.W. Cahn, P. Haasen, and E.J. Kramer (eds.) : "Materials Science and Technology", **13** (1993) 125.
4. *Chawla, K.K.* : "Composite Materials : Science and Engineering", Springer, NY (1987).
5. *Smith, W.F.* : "Principles of Materials Science and Engineering", McGraw-Hill **3** (1996) 814.
6. *Heringhaus, F.* : Dissertation, Fakultät für Bergbau, Hüttenwesen und Geowissenschaften, RWTH Aachen-Germany (1998).
7. *Gibson, R.F.* : "Principles of Composites Material Mechanics", McGraw-Hill (1994) 1.
8. *Heringhaus, F.* : Diplomarbeit, Fakultät für Bergbau, Hüttenwesen und Geowissenschaften, RWTH Aachen-Germany (1994).
9. *Verhoeven, J.D.; Spitzig, W.A.; Schmidt, F.A.; Krotz, P.D.; and Gibson, E.D.* : J. Mater. Sci. **24** (1989) 1015.
10. *Heringhaus, F.; and Raabe, D.* : J. Mat. Proc. Tech. **59** (1996) 367.
11. *Kolb-Telieps, A.* : Dissertation, Fakultät für Bergbau, Hüttenwesen und Maschinenbau, Technische Universität Clausthal-Germany (1984).
12. *Dew-Hughes, D.; Quincey, P.G.; and Upadhyay, P.L.* : Mat. Sci. Tech. **3** (1987) 936.
13. *Benghalem, A.; and Morris, D.G.* : Mat. Sci. Eng. **A161(2)** (1993) 255.
14. *Gottstein, G.* : "Physikalische Grundlagen der Materialkunde", Springer-Verlag (1998) 356-357.
15. *German, R.M.* : "Powder Metallurgy Science", Metal Powder Industries Federation (1984).
16. *Pramono, A.W.* : Senior Project, Department of Materials Science and Engineering Wayne State University, Detroit-USA (1993).
17. *Mattisen, D.* : Diplomarbeit, Fakultät für Bergbau, Hüttenwesen und Geowissenschaften, RWTH Aachen-Germany (1997).
18. *Hangen, U.D.* : Diplomarbeit, Mathematisch-Naturwissenschaftlichen Fakultät, RWTH Aachen-Germany (1994).
19. *Bevk, J.; Harbison, J.P.; and Bell, J.L.* : J. Appl. Phys. **49** (1978) 6031.
20. *Karasek, K.R.; and Bevk, J.* : Amer. Inst. Phys. **52** (1981) 1370.



21. Spitzig, W.A.; and Krotz, P.D. : Scripta metall. **21** (1987) 1143.
22. Raabe, D.; and Gottstein, G. : J. de Phys. IV, col. C7, sup. J. de Phys. III **3** (1993) 1727.
23. Heringhaus, F.; Raabe, D.; Kaul, L.; and Gottstein, G. : Zeitschrift Metall **6** (1993) 558.
24. Heringhaus, F.; Raabe, D.; and Gottstein, G. : Metall **48** (1994) 287.
25. Raabe, D.; Heringhaus, F.; Hangen, U.; and Gottstein, G. : Z. Metallkd. **86** (1995) 405.
26. Sakai, Y.; Inoue, K.; Asano, T.; Wada, H.; and Maeda, H. : Appl. Phys. Lett. **59** (1991) 2965.
27. Renaud, C.V.; Gregory, E.; and Wong, J. : Adv. Cry. Eng. **32** (1986) 443.
28. Segal, V.M.; Reznikov, V.I.; Drobyshevski, A.E.; and Kopylov, V.J. : Russian Metallurgy **1** (1981) 115.
29. Summers, T.S.E.; Segal, V.M.; Hartwig, K.T., Goforth, R.E.; Walsh, R.P.; and Pernambuco-Wise, P. : Adv. Cry. Eng. **42A** (1996) 499.
30. Ferrasse, S.; Segal, V.M.; Hartwig, K.T.; and Goforth : Metall. Mater. Trans. **28A** (1997) 1047.
31. Ferrasse, S.; Segal, V.M.; Hartwig, K.T.; and Goforth : J. Mater. Res. **12(5)** (1997) 1253.
32. Chakrabarti, D.J.; and Laughlin, D.E. : in : T.B. Massalski, H. Okamoto, P.R. Subramanian, L. Kacprzak (eds.) : "Binary Alloy Phase Diagrams", ASM International **2** (1990) 1440-1441.
33. Terekhov, G.I.; and Aleksandrova, L.N. : Izv. Akad. Nauk SSSR. Met. **4** (1984) 210.
34. Spitzig, W.A.; Pelton, A.R.; and Laabs, F.C. : Acta metall. **35** (1987) 2427.
35. Trybus, C.; and Spitzig, W.A. : Acta metall. **37** (1989) 1971.
36. Engler, O.; and Gottstein, G. : Steel Research **63** (1992) 413.
37. Pelton, A.R.; Laabs, F.C.; Spitzig, W.A.; and Cheng, C.C. : Ultramicroscopy **22** (1987) 251.
38. Hong, S.I.; Hill, M.A.; Sakai, Y.; Wood, J.T.; and Embury, J.D. : Acta metall. Mater. **43(9)** (1995) 3313.
39. Luborsky, F.E. : "Amorphous Metallic Alloys", Butterworths-London (1983).
40. Güntherodt, H.J.; and Beck, H. : "Glassy Metals", Springer Verlag-Berlin **1** (1981), **2** (1982).
41. Wang, W.K.; Iwasaki, H.; Suryanarayana, G.; Masumoto, T.; Fukamichi, F.; Syono, Y.; and Togo, T. : in : T. Masumoto, K. Suzuki (eds.) : "Proceedings of the 4th



- International Conference on Rapidly Quenched Metals", Japan Institute of Metals-Sendai **RQ4** (1984) 663.
42. *Iwasaki, H.; and Wang, W.K.* : Sci. Rep. of Res. Inst. of the Tohoku Univ. **29A** (1981) 195.
 43. *Verhoeven, J.D.; Chumbley, L.S.; Laabs, F.C.; and Spitzig, W.A.* : Acta metall. Mater. **39(11)** (1991) 2827.
 44. *Raabe, D.* : Dissertation, Fakultät für Bergbau, Hüttenwesen und Geowissenschaften, RWTH Aachen-Germany (1992).
 45. *Raabe, D.; Ball, J.; and Gottstein, G.* : Scripta metall. **27** (1992) 211.
 46. *Heringhaus, F.; Hangen, U.; Raabe, D.; and Gottstein, G.* : Mat. Sci. Forum **157-162** (1994) 709.
 47. *Bunge, H.J.* : Z. Metallkd. **56** (1965) 872.
 48. *Schulz, L.G.* : Appl. Phys. **20** (1949) 1030.
 49. *Brandes, E.A. (ed.)* : "Smithells Metals Reference Book", **6** (1983) 14.1-14.5.
 50. *Kohlrausch, F.* : in : G. Lautz, R. Taubert (eds.) : "Praktische Physik", Teubner-Verlag (1968).
 51. *Balliett, R.W.; Coscia, M.; and Hunkeler, F.J.* : J. Metals (1986) 25.
 52. *Jones, L.L.; Spitzig, W.A.; Verhoeven, J.D.; Schmidt, F.A.; Gibson, E.D.; Downing, H.L.; Laabs, F.C.; and Chumbley, L.S.* : Ames Lab., U.S. Dep. of Energy Metallurgy and Ceramic Division, Iowa State University, Ames, Iowa 50011.
 53. *Saxena, M.C.; and Sharma, B.D.* : Trans. Indian Inst. Met. **23** (1970) 16.
 54. *Butrymowicz, D.B.; Manning, J.R.; and Read, M.E.* : "Diffusion Rate Data and Mass Transport Phenomena for Copper Systems", Diffusion in Metals Data Center, Metallurgy Division, Institute for Materials Research, National Bureau of Standards, Washington, D.C. **20234** (1977) 144-145.
 55. *Borukhin, L.M.; and Shpichinetskii, E.S.* : Zavod. Lab. **37** (1971) 1196 [Ind. Lab. (USSR) **37** (1972) 1530].
 56. *Ceresara, S.; Feredighi, T.; and Pieragostini, F.* : Phys. Stat. Sol. **16** (1996) 439.
 57. *Bokshstein, B.S.; Zhukovitskii, A.A.; and Surmava, G.G.* : Zavod. Lab. **32** (1966) 438 [Ind. Lab. (USSR) **32** (1966) 540].
 58. *Schelle, R.F.* : M.S. Thesis, Iowa State University (1971).
 59. *Frommeyer, G.; and Wassermann, G.* : Acta metall. **23** (1975) 1353.
 60. *Frommeyer, G.* : "Verbundwerkstoffe", DGM-Verlag (1981).
 61. *Bevk, J.; and Karasek, K.R.* : in : D. Kuhlmann-Wilsdorf, W.C. Harrigan (eds.) : "New Developments and Applications in Composites", AIME Warrendale-PA (1979) 101.



62. Spitzig, W.A. : Acta metall. **39** (1991) 1085.
63. Funkenbusch, P.D.; and Courtney, T.H. : Acta metall. **33** (1985) 913.
64. Bevk, J.; Sunder, W.A.; Dublon, G.; and Cohen, E. : in : F.D. Lemkey, H.E. Cline, M. McLean (eds.) : "In-situ Composites IV", Elsevier-Amsterdam (1982) 121.
65. Biner, S.B.; and Spitzig, W.A. : Mat. Sci. Eng. **A150** (1992) 213.
66. Kelly, A.; and Tyson, W.R. : in : V.F. Zackay (ed.) : "High Strength Materials", John Wiley&Sons (1965) 578.
67. Mileiko, S.T. : J. Mat. Sci. **4** (1969) 974.
68. Garmong, G.; and Thompson, R.B. : Metall. Trans. **4** (1973) 863.
69. Cho, K.; and Gurland, J. : Metall. Trans. **19A** (1988) 2027.
70. Li, J.C.; and Chou, Y. : Metall. Trans. **1** (1970) 1145.
71. Li, J.C. : Trans. Amer. Inst. Min. Eng. **227** (1963) 239.
72. Ashby, M.F. : "Strengthening Methods in Crystals", Wiley-NY (1971) 137.
73. Sevillano, J.G. : in : P. Haasen, V. Gerold, G. Kostorz (eds.) : "Strength of Metals and Alloys", Proc. ICSMA 5, Pergamon Press-Oxford (1980) 819.
74. Funkenbusch, P.D.; and Courtney, T.H. : Metall. Trans. **18A** (1987) 1249.
75. Koehler, J.S. : Phys. Rev. **2(2)** (1970) 547.
76. Embury, J.D.; and Fisher, R.M. : Acta metall. **14** (1966) 147.
77. Hosford, W.F. Jr. : Trans. TMS AIME **230** (1964) 12.
78. Karasek, K.R.; and Bevk, J. : J. Appl. Phys. **52** (1981) 1370.
79. Raabe, D.; and Hangen, U. : in : S.I. Andersen, J.B. Bilde-Sorensen, T. Lorentzen, O.B. Pedersen, N.J. Sorensen (eds.) : "Proc. 15th Risø Int. Symp. on Mater. Sci. on Num. Prediction of Def. Proc. and the Behav. of Real Mater.", RISØ Nat. Lab. Roskilde-Denmark (1994) 487.
80. Embury, J.D.; Hill, M.A.; Spitzig, W.A.; and Sakai, Y. : MRS Bull. **8** (1993) 57.
81. Schneider-Muntau, H.J. : IEEE Trans. Mag. **18** (1982) 32.
82. Raabe, D.; and Heringhaus, F. : Phys. Stat. Sol. (a) **142** (1994) 473.
83. Gielisse, P.J.; and Bai, N.Z. : "Deformation-Processed High-Strength High-Conductivity Microcomposite Conductors", National High Magnetic Field Laboratory-Florida State University , **1** (1992).
84. Spitzig, W.A.; and Krotz, P.D. : Acta metall. **36** (1988) 1709.
85. Renaud, C.V.; Gregory, E.; and Wong, J. : Adv. Cry. Eng. **34** (1988) 435.



86. Verhoeven, J.D.; Schmidt, F.A.; Gibson, E.D.; and Spitzig, W.A. : J. Metals **20** (1986) 20.
87. Raabe, D.; Heringhaus, F.; Hangen, U.; and Gottstein, G. : Z. Metallkd. **86** (1995) 416.
88. Courtney, T.H. : in : D. Kuhlmann-Wilsdorf, W.C. Harrigan (eds.) : "New Developments and Applications in Composites", AIME Warrendale-PA (1979) 6.



CHAPTER THREE

BACKGROUND THEORIES

Deliberating and understanding the fundamental theories behind the knowledge of metal matrix composites (MMCs), especially *in-situ* copper-niobium system, will be necessary in order to aid assessing the observed phenomena in such materials, i.e. microstructure evolution and thermomechanical properties.

3.1 Wire Drawing

Wire drawing is an important metal forming process. In this method, a starting rod or wire stock is drawn through one or more tapered wire-drawing dies. It is very important to make the surface of the stock clean and properly lubricated. As the drawn wire work hardens during processes, it is necessary to perform intermediate softening heat treatments in order to ease the way. Such process of deformation is schematically depicted in figure 3.1a [1], whereas the material flow during the process is shown in figure 3.1b [2].

Although wire drawing appears to be one of the simplest metal working processes, a complete analysis that enables calculation of the draw force to better than ± 20 percent of the observed value is a rather difficult problem [3]. Wistreich [4] derived an equation describing the drawing stress (σ_{xa}) with the existence of friction (μ) between the strip and the die as :

$$\sigma_{xa} = \frac{P_d}{A_a} = \bar{\sigma}_0 \ln \frac{A_b}{A_a} (1 + \mu \cot \alpha) \quad \text{Equation 3-1}$$

where :

P_d = the applied force

A_a = the cross sectional area before drawing

A_b = the cross sectional area after drawing

$\bar{\sigma}_0$ = the flow stress

α = semi-die angle

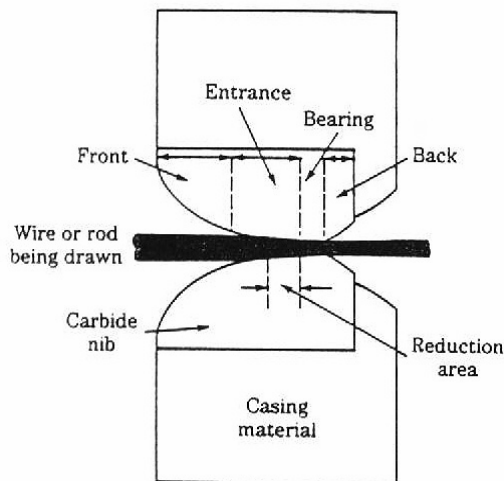


Figure 3.1a The section through a wire drawing die [1].

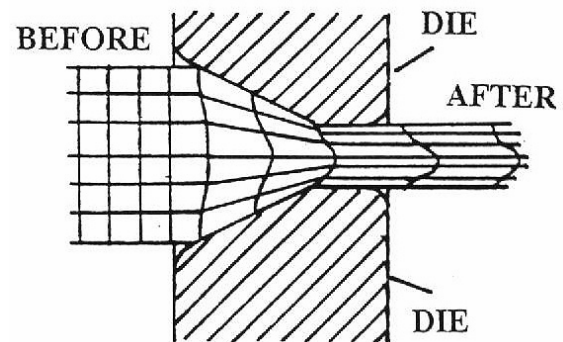


Figure 3.1b The material flow during wire drawing [2].

Two distinct types of residual stress patterns are found in cold drawn rod and wire, depending on the amount of reduction [3]. For reductions per pass of less than about 1 percent the longitudinal and circumferential residual stresses are compressive at the surface and tensile at the axis, while the radial stresses are tensile at the axis and become zero at the free surface. This type of residual stress pattern is characteristic of forming operations, of which the deformation is localized in the surface layers. For larger reductions of commercial purpose the residual stress distribution is completely reversed from the first type of stress pattern. In this case the longitudinal and circumferential stresses are tensile at the surface and compressive at the axis of the rod or wire, whereas the radial stresses are compressive at the axis.

Linicus and Sachs [5] investigated the effect of die angle and the amount of reduction per pass on the longitudinal residual stress in cold drawn brass wire, and their results were also emphasized by Wright [6]. For a given reduction, the longitudinal residual stress increases with the semi-die angle. In this case the maximum values of longitudinal residual stresses are obtained for reductions in the region of 15 to 35 percent.



3.2 Curling Phenomena in Drawn bcc Metals

This section highlights and summarizes the quantitative theory behind the existence of curled grain shapes found in the microstructures of drawn wires of bcc metals, proposed earlier by Hosford [7]. As previously mentioned in Chapter 2 (figure 2.6b), such phenomenon takes place in the niobium of drawn copper-niobium MMC.

A simple quantitative argument will be presented based on the reality that the macroscopic strains of a crystal resulting from slip are given by :

$$\begin{aligned}
 d\epsilon_x &= m_{xa} d\gamma_a + m_{xb} d\gamma_b + m_{xc} d\gamma_c + \dots \\
 d\epsilon_y &= m_{ya} d\gamma_a + m_{yb} d\gamma_b + m_{yc} d\gamma_c + \dots \\
 d\epsilon_z &= m_{za} d\gamma_a + m_{zb} d\gamma_b + m_{zc} d\gamma_c + \dots
 \end{aligned}
 \tag{Equation 3-2}$$

where :

$d\epsilon_x, d\epsilon_y, d\epsilon_z$ = normal strain increments parallel to x, y, and z axes

$d\gamma_a, d\gamma_b, d\gamma_c, \dots$ = crystallographic shear-strain increments on slip systems
a, b, c, ...

$m_{xa}, m_{xb}, m_{xc}, \dots$ = Schmid's factors of a, b, c, ... slip systems with respect to
x axis

$m_{ya}, m_{yb}, m_{yc}, \dots$ = Schmid's factors of a, b, c, ... slip systems with respect to
y axis

$m_{za}, m_{zb}, m_{zc}, \dots$ = Schmid's factors of a, b, c, ... slip systems with respect to
z axis

In a bcc metal drawn parallel to $[011]$ axis (figure 3.2), the following situations take place concerning the slip systems :

- Only $[111]$ and $[\bar{1}\bar{1}1]$ slip directions are oriented favorably to accommodate extension parallel to $[011]$ and contraction parallel to $[100]$. No expansion or contraction occurs along $[0\bar{1}1]$ which leads to one of plane strains.
- For axially symmetric flow, $[\bar{1}\bar{1}1]$ and $[1\bar{1}1]$ slip directions would have to operate in such a way as to increase the $[100]$ diameter while decreasing the $[0\bar{1}1]$ diameter. Slips in $[\bar{1}\bar{1}1]$ and $[1\bar{1}1]$, however, do not contribute to the elongation.

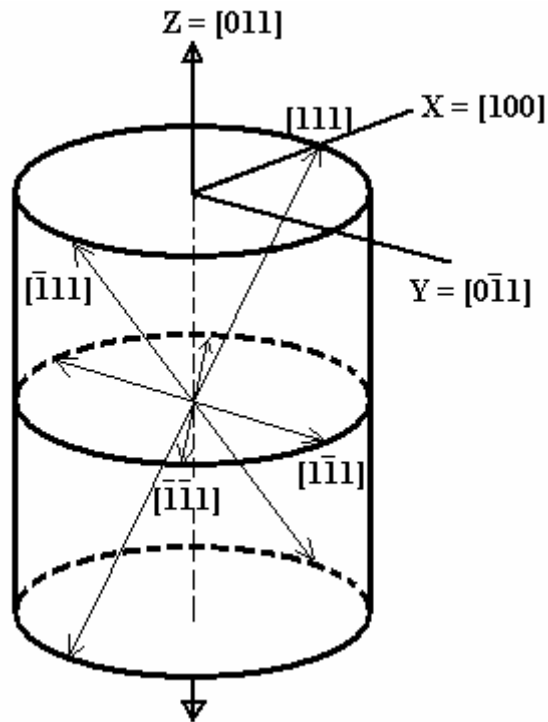


Figure 3.2 The representation of the position of the $\langle 111 \rangle$ slip directions in a bcc crystal drawn parallel to $[011]$ axis [7].

- By assuming the most highly stressed slip plane is $\{112\}$ and the xyz axes are shown in figure 3.2, equation 3-2 becomes :

$$d\epsilon_x = \frac{\sqrt{2}}{3} (-d\gamma_I + d\gamma_{II})$$

$$d\epsilon_y = \frac{\sqrt{2}}{3} (-d\gamma_{II})$$

$$d\epsilon_z = \frac{\sqrt{2}}{3} d\gamma_I$$

Equation 3-3

where :

$$d\gamma_I = d\gamma_{[111](\bar{2}11)} + d\gamma_{[\bar{1}\bar{1}1](211)}$$

$$d\gamma_{II} = d\gamma_{[1\bar{1}1](\bar{2}\bar{1}1)} + d\gamma_{[\bar{1}\bar{1}\bar{1}](2\bar{1}1)}$$

For *plane strain flow*, $d\epsilon_y = 0$ and $d\epsilon_x = -d\epsilon_z$. Implementing such condition into equation 3-3 yields $d\gamma_{II} = 0$ and the total amount of slip $d\gamma_T$ per unit axial strain $d\epsilon_z$ is



$$\frac{d\gamma_{\text{T}}}{d\varepsilon_z} = \frac{d\gamma_{\text{I}}}{d\varepsilon_z} = \frac{3\sqrt{2}}{2} \quad \text{Equation 3-4}$$

For *axially symmetric flow*, $d\varepsilon_x = d\varepsilon_y = -\frac{1}{2}d\varepsilon_z$. Implementing such criterion into equation

3-3 yields $d\gamma_{\text{II}} = \frac{1}{2}d\gamma_{\text{I}}$. Hence, according to Hosford [7] :

$$\frac{d\gamma_{\text{T}}}{d\varepsilon_z} = \frac{d\gamma_{\text{I}}}{d\varepsilon_z} + \frac{d\gamma_{\text{II}}}{d\varepsilon_z} = \frac{9\sqrt{2}}{4} \quad \text{Equation 3-5}$$

Thus the amount of slip required to facilitate axially symmetric flow (equation 3-5) is 3/2 of that required for plane strain flow (equation 3-4). In fact, such ratio of 3/2 is also valid for the other active slip planes of {110} and {123} in bcc metals.

This quantitative analysis concludes that the applied stress σ_z required for axially symmetric flow of individual grains must be 3/2 of that required for plane strain flow. Consequently, grains in a [011] fiber textured wire strongly deform by plane strain elongation, which would develop elliptical cross sections normal to the fiber axis. To keep the compatibility, neighboring grains with different orientations would have to arc around one another. The additional slip required for such bending could probably be lower than the difference between the slip requirements of axial symmetry and plane strain.

3.3 Strengthening Mechanisms in *in-situ* Metal Matrix Composites

3.3.1 Rule of Mixtures (ROM)

3.3.1.1 Fundamentals

The basic knowledge of rule of mixtures originates from what so called *elementary mechanics of materials models*, as discussed by Gibson [8]. In this model the fiber packing geometry is not specified, so that representative volume element (RVE) may be a generic composite block consisting of fiber material bonded to matrix material, as shown in figure 3.3a. The constituent volume fractions in the RVE are assumed to be the same as those in the actual composite. Since it is assumed that the fibers remain parallel and that the dimensions do not change along the length of the element, the area fractions must be equal to the volume fractions. Assuming perfect bonding at the interface, no slip occurs between

fiber and matrix materials. The fiber and matrix materials are assumed to be linearly elastic and homogeneous. The matrix is assumed to be isotropic, however the fiber can be either isotropic or orthotropic. Orthotropic material is the one that has three mutually orthogonal planes of material property symmetry (i.e. the 12, 23, and 13 planes). Following the concept of the RVE, the lamina is assumed to be macroscopically homogeneous, linearly elastic, and orthotropic. Further, the mechanics of materials approach does not require the specification of the stresses, strains, and displacements at each point; hence only volume-averaged or area-averaged quantities are taken into account.

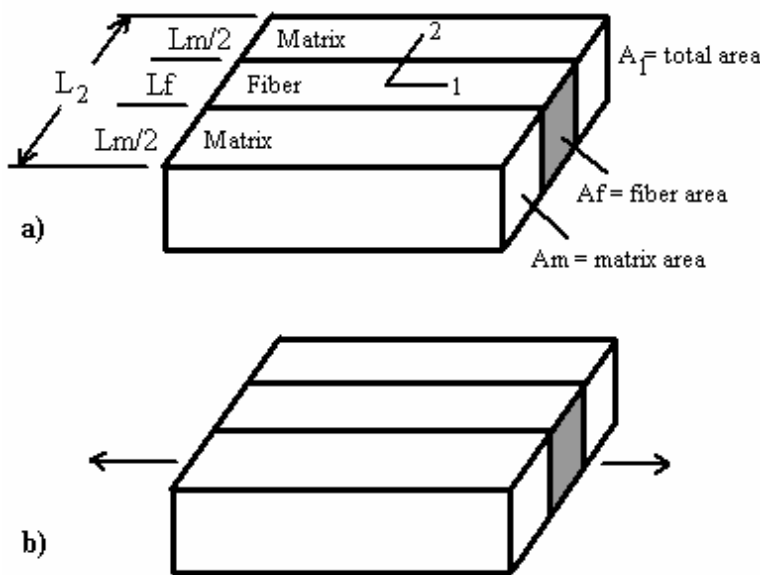


Figure 3.3 a) The representative volume element (RVE), b) simple longitudinal stress state used in elementary mechanics of materials models [8].

Finally, since it is assumed that the stresses, strains, displacements, and RVE dimensions do not change along the length, volume or area averages can then be defined as :

$$\bar{\sigma} = \frac{1}{V} \int \sigma dV = \frac{1}{A} \int \sigma dA \quad \text{Equation 3-6}$$

$$\bar{\epsilon} = \frac{1}{V} \int \epsilon dV = \frac{1}{A} \int \epsilon dA \quad \text{Equation 3-7}$$

$$\bar{\delta} = \frac{1}{V} \int \delta dV = \frac{1}{A} \int \delta dA \quad \text{Equation 3-8}$$

where :



the overbar denotes an averaged quantity, and

σ = stress

ε = strain

δ = displacement

V = volume

A = cross sectional area of the face on which loading is applied

Now if the RVE in figure 3.3a is subjected to a longitudinal normal stress, as shown in figure 3.3b, the response is governed by the effective longitudinal modulus, E_1 . Static equilibrium criterion requires that the total resultant force on the element must equal the sum of the forces acting on the fiber and matrix. Combining such condition with equation 3.6, one gets :

$$\bar{\sigma}_{c1} A_1 = \bar{\sigma}_{f1} A_f + \bar{\sigma}_{m1} A_m \quad \text{Equation 3-9}$$

where :

c, f, and m refer to composite, fiber, and matrix respectively
the second subscript refers to the direction

Since area fractions are equal to the corresponding volume fractions (v), equation 3-9 can be rearranged to give *the rule of mixtures for longitudinal stress* :

$$\bar{\sigma}_{c1} = \bar{\sigma}_{f1} v_f + \bar{\sigma}_{m1} v_m \quad \text{Equation 3-10}$$

Under the assumptions that the matrix is isotropic, the fiber is orthotropic, and the material follows a one dimensional Hooke's law (i.e. Poisson strains are neglected) in which :

$$\bar{\sigma}_{c1} = E_1 \bar{\varepsilon}_{c1}; \quad \bar{\sigma}_{f1} = E_{f1} \bar{\varepsilon}_{f1}; \quad \bar{\sigma}_{m1} = E_{m1} \bar{\varepsilon}_{m1}; \quad \text{Equation 3-11}$$

equation 3-10 becomes :

$$E_1 \bar{\varepsilon}_{c1} = E_{f1} \bar{\varepsilon}_{f1} v_f + E_{m1} \bar{\varepsilon}_{m1} v_m \quad \text{Equation 3-12}$$



Double subscripts are utilized for the fiber modulus since the fiber is assumed to be orthotropic. It means, the longitudinal fiber modulus (E_{f1}), is not necessarily equal to the transverse fiber modulus (E_{f2}). Since the matrix is assumed to be isotropic, the matrix modulus (E_m) does not need a second subscript.

The next key assumption is that the average strains in the composite, fiber, and matrix along the 1 direction are equal, which is known as the strain compatibility :

$$\bar{\epsilon}_{c1} = \bar{\epsilon}_{f1} = \bar{\epsilon}_{m1} \tag{Equation 3-13}$$

The validity of this assumption has been examined using a strain energy approach. Substitution of equation 3-13 to equation 3-12 yields *the rule of mixture for the longitudinal modulus* :

$$E_1 = E_{f1}v_f + E_mv_m \tag{Equation 3-14}$$

which predicts a linear variation of the longitudinal modulus with fiber volume fraction. This linear variation agrees well with the experimental data from Adams [9], as shown in figure 3.4.

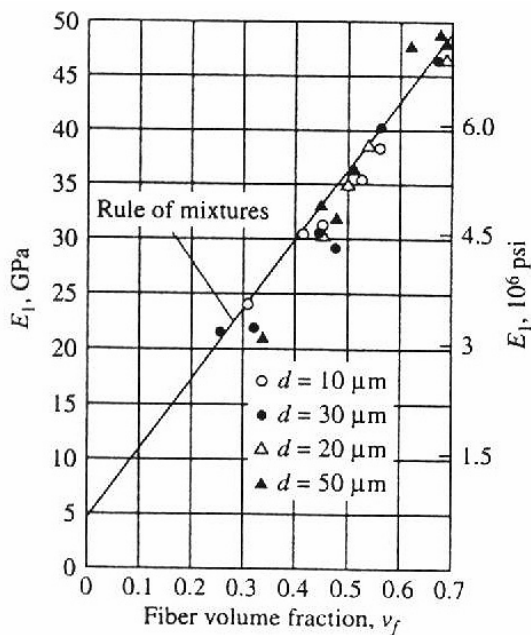


Figure 3.4 The comparison of predicted and measured E_1 for E-glass/polyester [9].



3.3.1.2 Rule of Mixtures at Ultimate Loading

This section deals with the strain, ultimate strength, and work during uniform strain to ultimate loading of metal matrix composites deformed in tension parallel to the reinforcement, according to the work of Garmong and Thompson [10]. The approach is based on the systematic application of a macroscopic principle generally used to predict the ultimate strength of ductile monolithic materials, in which necking occurs when the load borne by the material is maximized. For ductile monolithic materials, a theory of ultimate tensile strength (at necking) has been well developed by Dieter [3]. The necking event, assuming constant volume during plastic flow, is predicted as :

$$0 = \frac{d\sigma}{d\varepsilon} - \sigma \quad \text{Equation 3-15}$$

where : σ is true stress and ε is true strain

Similar to equation 3-9, a basic rule of mixture has been used by Garmong and Thompson [10] to determine the force (F) borne during tensile loading parallel to the fibers in a composite, i.e. :

$$F_c = \sigma_f A_f + \sigma_m A_m \quad \text{Equation 3-16}$$

where :

A = physical area of each phase present in a transverse section
c,f,m refer to composite, fiber, and matrix respectively

The stress in each phase at the composite maximum load is found by taking a total differential of equation 3-16. Further, the differential area obtained in the derived equation may be eliminated from the expression by recalling that the Poisson's contraction under uniaxial stress is given by :

$$\frac{dA_{f,m}}{A_{f,m}} = -2\nu_{f,m} d\varepsilon \quad \text{Equation 3-17}$$

where : ν is Poisson's ratio



By using the assumptions that ε is constant across any cross section and the volume fraction V (area of a phase divided by the total area in transverse section) is constant during elastic deformation and plastic flow, one gets :

$$\mathbf{0} = V_f \left(\frac{d\sigma_f}{d\varepsilon} - 2\nu_f \sigma_f \right) + V_m \left(\frac{d\sigma_m}{d\varepsilon} - 2\nu_m \sigma_m \right) \quad \text{Equation 3-18}$$

where :

$V_{f,m}$ = volume fraction of fiber and matrix respectively

Equation 3-18 provides the basis for calculation of stress components at composite ultimate strength in the same manner as stress at necking is predicted for a monolithic material (equation 3-15).

Application in Ductile Fibers

By implementing equation 3-18 together with a reasonable stress-strain equation of the form :

$$\sigma_{f,m}(\varepsilon) = \sigma_{0f,m} + K_{f,m} \varepsilon^{n_{f,m}} \quad \text{Equation 3-19}$$

where :

K, n = constants describing subsequent work hardening

σ_0 = yield stress

f, m indicate fiber and matrix respectively,

one can derive the following quantities at ultimate loading:

- *the composite uniform strain*

$$\varepsilon_c = \frac{V_f n_f (\sigma_f - \sigma_{0f}) + V_m n_m (\sigma_m - \sigma_{0m})}{V_f \sigma_f + V_m \sigma_m} \quad \text{Equation 3-20}$$

- *the composite stress*

$$\sigma_c = V_f \sigma_f + V_m \sigma_m \quad \text{Equation 3-21}$$



- *the work to necking*

$$\mathbf{W}_c = L_0 A_0 \int_0^{\varepsilon_c} [\mathbf{V}_f \sigma_f(\varepsilon) + \mathbf{V}_m \sigma_m(\varepsilon)] d\varepsilon \quad \text{Equation 3-22}$$

Equations 3-20 to 3-22 have been reported to be in a reasonably good agreement with the experimental data conducted by Piehler [11], Kelly and Tyson [12], and Ahmad and Barranco [13] for ductile materials.

Application in Brittle Fibers

When applied force of a brittle fiber-ductile matrix composite is plotted schematically against strain, a curve shown in figure 3.5 is obtained. Three crucial values of extrema R_1 , R_2 , and R_3 are observed. These three values of R represent the solutions for equation 3-18. Failure commencing at a strain $\varepsilon = R_1$ may be identified as composite failure due to brittle fiber failure. The solution $\varepsilon = R_2$ represents a local minimum in the force-strain curve and may be ignored. Failure commencing at a strain $\varepsilon = R_3$ corresponds to ultimate strength at matrix necking, after all the fibers have previously failed.

The solution of equation 3-18 for composite ultimate stress at $\varepsilon = R_1$ is :

$$\sigma_c = \mathbf{V}_f \sigma_f(\varepsilon = R_1) + \mathbf{V}_m \sigma_m(\varepsilon = R_1) \quad \text{Equation 3-23}$$

For the solution $\varepsilon = R_3$, composite ultimate stress is given by :

$$\sigma_c = \mathbf{V}_m \sigma_m(\varepsilon = R_3) \quad \text{Equation 3-24}$$

The term involving $\mathbf{V}_f \sigma_f(\varepsilon = R_3)$ is not present in equation 3-24, as the fibers have failed previously. This analysis of failure of a brittle fiber-ductile matrix composite by Garmon and Thompson [10] yields the same result when σ_c is engineering stress as previously presented by Kelly and Davies [14].

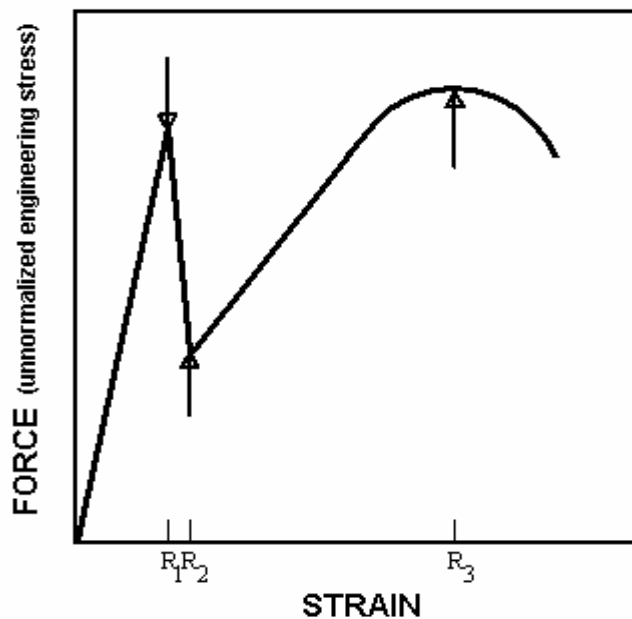


Figure 3.5 The schematic drawing of force (unnormalized engineering stress) vs. strain curve for a brittle fiber-ductile matrix composite [10].

3.3.1.3 Modified Rule of Mixtures

A number of studies of two-phase alloy systems have considered the plastic properties of the alloys in terms of the states of deformation or flow properties of the constituent phases [15-24]. Several forms of the law of mixtures have been used to correlate the deformations or properties of the constituents with the properties of the composite alloy. First among these is the classical linear law of mixtures, which shows the yield strength of a bulk, σ_y , as :

$$\sigma_y = \sigma_\alpha^0 V_\alpha + \sigma_\beta^0 V_\beta \quad \text{Equation 3-25}$$

where :

$\sigma_\alpha^0, \sigma_\beta^0$ = the yield strengths of the constituents as measured in bulk
 V_α, V_β = their volume fractions

However, the yield strengths and flow stresses of most particulate two-phase alloys of technical interest do not follow a linear law of mixtures based on bulk strengths. The properties and stress states of the *in-situ* phases are affected by the microstructure, i.e., size, shape, orientation, and connectivity, and are modified by interaction between the



phases. An alteration for the purpose of accounting for microstructural and interaction effects has been proposed by Ankem and Margolin [25], which has the following form :

$$\sigma_y = \sigma_{y\alpha}^c V_\alpha + \sigma_{y\beta}^c V_\beta + I_{\alpha\beta}^y \quad \text{Equation 3-26}$$

where :

$\sigma_{y\alpha}^c, \sigma_{y\beta}^c$ = the bulk yield strengths of α and β phases corrected for variations in grain size and texture

$I_{\alpha\beta}^y$ = the interaction between α and β phases

The interaction term may be additive or subtractive depending on microstructure, alloy system, and composition. In principle, its sign and magnitude as a function of composition could account for the shapes of the yield strength curve as function of the volume fraction. Equation 3-26 has the advantage of featuring explicitly the interaction term, but it does not directly identify the separate contribution of each phase to the alloy strength.

A more general form of the law of mixtures relating to average stresses and strains in each phase has been suggested for empirical purpose by Tamura, Tomota, and Ozawa [26] and further discussed by Fischmeister and Karlsson [27]. This form is called a "modified" law of mixtures because the relevant average stresses and average strains of each phase are *in-situ* values, and neither generally bulk flow properties nor necessarily *in-situ* flow properties. For an aggregate or alloy consisting of two phases (α and β) under uniaxial loading, the modified law of mixtures for stress and strains is given by :

$$\sigma_c = \bar{\sigma}_\alpha V_\alpha + \bar{\sigma}_\beta V_\beta \quad \text{Equation 3-27}$$

$$\varepsilon_c = \bar{\varepsilon}_\alpha V_\alpha + \bar{\varepsilon}_\beta V_\beta \quad \text{Equation 3-28}$$

where :

$\bar{\sigma}, \bar{\varepsilon}$ = the average values, respectively, of the directional components of stress and strain parallel to the direction of the applied load. They are averaged on planes normal to the load direction (for stress) or along lines parallel to the load direction (for strains).

These equations apply to any direction of loading and to all possible structural arrangements of the two-phase mixtures, including the limiting cases of parallel and series arrangements of the constituents.



The modified law of mixtures, based on average *in-situ* stress and strain, is valid for small deformations (for both "engineering" and "true" stress and strain) [28]. In general, this theory identifies the contribution of each of the phases to the strength and deformation of two-phase alloy. The plastic deformation behavior of two-phase alloys can be understood comprehensively by combining the law of mixtures with the dislocation-continuum strain hardening theory, as suggested previously by Embury and Duncan [29]. Empirical use of the modified law of mixtures for stress and/or strain has indicated good agreement with experiment [19,22,27,30], theoretical modeling [21,24], and finite element analysis [17,30,31]. The existence of nonhomogeneous deformation in the same phase does not limit the applicability of the modified law of mixtures. However, it restricts the application of constitutive equations relating average stress to average strain. The stress and strain values ($\bar{\sigma}_{\alpha,\beta}$ and $\bar{\varepsilon}_{\alpha,\beta}$) in equation 3-27 and 3-28 represent strictly the average values of stress and strain in each phase, without reference to the flow properties of the phase, at a particular condition of deformation of the alloy with flow stress σ_c and flow strain ε_c . However, uniform deformation is often implicitly assumed and the average stress of a plastically deforming phase is then assumed to be equal to the *in-situ* flow stress of that phase. Hence, solely with the assumption of uniform deformation, the flow stress and flow strain could be constitutively related within a phase.

In the modified law of mixtures, the interaction effects are already incorporated into the stress and strain values associated with each phase. Consider the schematic diagram of figure 3.6 representing the idealized tensile deformation of a composite alloy consisting of phases α and β [21,27]. In this case, the two-phase system is simplified as :

- there is strong bonding between the phases, with no interfacial debonding or other void formation;
- both phases have the same elastic modulus, and elastic interaction effects are neglected.
- the hard phase deforms only elastically; and
- the soft phase deforms in the elastic, perfectly-plastic mode.

The composite alloy, which consists of particles or grains of α and β , deforms in two levels : elastic from points O to Y, and elastic-plastic beyond Y, along line YF. For a given state of deformation of the alloy indicated by point F, the average *in-situ* stresses and strains of the constituents are given by points A and B. The line AFB is a graphic representation of the modified law of mixtures (equation 3-27 and 3-28).

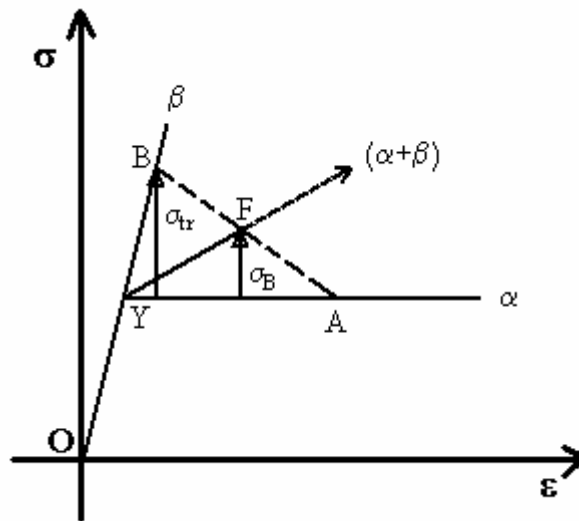


Figure 3.6 The simplified schematic stress-strain curves of two-phase alloy and its constituents : α and β . OY = elastic region, YF = elastic-plastic. AFB = modified law of mixtures [21,27].

Equation 3-27 is then equivalent to a lever rule, such that :

$$\frac{\sigma_f - \bar{\sigma}_\alpha}{\bar{\sigma}_\beta - \bar{\sigma}_\alpha} = \frac{FA}{BA} = V_\beta \quad \text{Equation 3-29}$$

where :

σ_f , $\bar{\sigma}_\alpha$, $\bar{\sigma}_\beta$ = the stresses at points F, A, and B respectively

Since strain hardening of the soft phase is not included in this simplified model, the only work hardening of the alloy to be considered is that due to the load transfer hardening which arises from interaction effects which cause the hard phase to carry a higher stress than the softer phase. The load transfer, σ_{tr} , is shown in figure 3.6 as the difference between the average stresses in α and β . The difference between the flow stress of the alloy (σ_f) and the average stress in the softer phase ($\bar{\sigma}_\alpha$) is indicated as σ_B in this figure. It represents the strength of the alloy with reference to that of the α phase. In dispersion hardening theory it is sometimes called as *the back stress*. From the geometry it follows that :



$$\sigma_B = \sigma_{tr} V_\beta \quad \text{Equation 3-30}$$

In terms of σ_B and σ_f , the partition of stress is given by :

$$\bar{\sigma}_\alpha = \sigma_f - \sigma_B \quad \text{Equation 3-31}$$

$$\bar{\sigma}_\beta = \sigma_f + \sigma_B \frac{V_\alpha}{V_\beta} \quad \text{Equation 3-32}$$

The two significant interaction effects between soft and hard phases in plastically deforming two-phase alloys are : (1) the load transfer represented by the interaction stress σ_B , and the geometrically induced strain hardening of the soft phase which affects the magnitude of $\bar{\sigma}_\alpha$. Both have their origins in the local strain difference at the interface of soft and hard phases. From equation 3-31, the alloy flow stress for two-phase alloys with non-deformable hard phase is given as :

$$\sigma_f = \bar{\sigma}_\alpha + \sigma_B \quad \text{Equation 3-33}$$

Cho and Gurland [28] shows that the modified rule of mixtures, represented by equation 3-33, is compatible with the strength theories of : continuum theory [32], shear-lag theory [33], and dispersion hardening theory [34-36].

3.3.2 Barrier Model

The basic idea of the barrier model is the Hall-Petch type of equation developed by Hall [37] and greatly extended by Petch [38].

$$\sigma_0 = \sigma_i + kD^{-1/2} \quad \text{Equation 3-34}$$

where :

σ_0 = the yield stress

σ_i = the "friction stress" representing the overall resistance of the crystal lattice to dislocation movement

k = the "locking parameter" which measures the relative hardening contribution of the grain boundaries

D = the grain diameter



This equation has also been found to apply not only to grain boundaries, but to other kinds of boundaries such as ferrite-cementite in pearlite, mechanical twins, and martensite plates [3].

The growing realization of the importance of grain boundaries as dislocation sources, however, has cast considerable doubt on the dislocation pile-up model for the Hall-Petch equation. Li [39] has proposed a more general model to avoid the description of the stresses at grain boundaries and instead to concentrate on the influence of grain size on the dislocation density. This model has been also discussed by Li and Chou [40], and Embury and Fisher [41]. In this case, the flow stress of a single phase polycrystal is given in terms of dislocation density by :

$$\sigma_0 = \sigma_i + \alpha G b \rho^{1/2} \quad \text{Equation 3-35}$$

where :

σ_i has the same meaning as in equation 3-34

α = a numerical constant generally between 0.3 and 0.6, and often modified by M, the Taylor factor

ρ = dislocation density

The correlation between dislocation density and grain size lies on the experimental observation that ρ is an inverse function of the grain size. Thus :

$$\sigma_0 = \sigma_i + \alpha G b D^{-1/2} = \sigma_i + k' D^{-1/2} \quad \text{Equation 3-36}$$

The analogy of grain boundaries as dislocation sources in the single phase polycrystal can be applied to a metal matrix composite. In metal matrix composites the interfaces act as sources of dislocations, which control plastic flow across the interface and thus affecting the yielding characteristics of the composite [42]. The number of dislocation per unit of deformation is proportional to the interfacial surface area per unit volume (S_v), as shown by Spitzig [43]. For aligned structures :

$$S_v = \frac{2}{(\lambda + t)} \quad \text{Equation 3-37}$$



where :

λ , t = the spacing and the thickness of filaments, respectively

By defining the dislocation density (ρ) as mS_v , where m is the density of dislocation sources in the interfaces (number per unit length), the combination of equation 3-35 and 3-37 yields :

$$\sigma_0 = \sigma_i + (2m)^{1/2} \alpha G b (\lambda + t)^{-1/2} \quad \text{Equation 3-38}$$

In the Cu-20%Nb system, S_v (equation 3-37) has the value of $1.6/\lambda$. By substituting it into equation 3-38, one gets :

$$\sigma_0 = \sigma_i + (1.6m)^{1/2} \alpha M G b (\lambda)^{-1/2} \quad \text{Equation 3-39}$$

where :

M is again the Taylor factor, which is often used to modify equation 3-35

A good correlation of the results from equation 3-39 and the experimental data for drawn and rolled Cu-20%Nb system has been shown by Spitzig [43].

3.3.3 Non-homogeneous Deformation Model

Ashby [44] discussed this model based on the concept of dislocation generation from the inter-region of two phases. However, it derives its increasing dislocation density from non-homogeneous deformation processes. It is treated as the two phase alloys deform plastically in a non uniform behavior. Differences in behavior between the phases result in gradients of deformation, the extent of which is determined by the particle or phase spacing in these plastically non-homogeneous alloys. During deformation, the alloy has to store an increasingly dense array of geometrically necessary dislocations to compensate the gradients of deformation and thus allows compatible deformation.

Empirical expression of the flow stress of the composite (equation 3-35) again becomes the starting point for the development of the parametric equation of this model. The geometrically necessary dislocation density, ρ_g , required to ensure compatible deformation of the two phases is given by :



$$\rho_g = \frac{4\gamma}{b\lambda} \quad \text{Equation 3-40}$$

where :

γ = the shear strain

λ = the spacing between the harder phase fibers (particles)

Spitzig [43] worked out a slightly different expression for such dislocation density, of which :

$$\rho_g = \frac{4\theta}{b\lambda} \quad \text{Equation 3-41}$$

where :

θ = the angle of rotation between a nondeforming plate in a deforming matrix

λ = the spacing of the harder phase

If it is assumed that no plastic deformation occurs in the plane of the interface between the plate and the matrix, the angle θ can be accounted as $\tan^{-1}\gamma$, where γ is shear strain.

In case of Cu-20%Nb, the filaments deform along with the matrix [42]. It significantly reduces θ at a given strain, so that θ can be taken equivalent to $K.\tan^{-1}\gamma$, where K is a compatibility constant accounting for the plastic deformation of the niobium filaments. Based on this condition, equation 3-40 can be modified to yield the average density of the geometry necessary dislocation as :

$$\rho_g = \frac{4K \tan^{-1} \gamma}{b\lambda} \quad \text{Equation 3-42}$$

By substituting equation 3-42 to equation 3-35, one gets :

$$\sigma = \sigma_0 + 2\alpha MG(bK)^{1/2} \left\{ \frac{\tan^{-1} 2(\eta + \varepsilon)}{\lambda} \right\}^{1/2} \quad \text{Equation 3-43}$$

where :

η = the wire drawing or rolling strain

ε = the plastic tensile test strain

$\gamma = 2(\eta + \varepsilon)$



Similar to the barrier model, the non-homogeneous deformation model (equation 3-43) has shown a very good correlation with the observed strengths of Cu-20%Nb wire and sheet data as conducted by Spitzig [43].

3.3.4 Dislocation Propagation Model

Unlike in wire drawn composites, dislocations in rolled sheets can propagate relatively unimpeded parallel to the filaments. Thus, an alternate strengthening is required. A strengthening model used to explain such behavior is based on an approach originally calculated by Sevillano [45] to explain strengthening in pearlite, in which the dislocations are thought to shift, at a certain critical stress, between the cementite plates in the iron matrix. The model was also emphasized by Trybus and Spitzig [46]. According to this model, the critical stress necessary to propagate dislocations between lamellae is given by :

$$\sigma_c = \sigma_0 + \frac{MAGb}{2\pi\Lambda} \ln\left(\frac{\Lambda}{b}\right) \quad \text{Equation 3-44}$$

where :

G = the shear modulus

b = the Burgers vector

Λ = the lamellae spacing

σ_0 = the friction stress

M = the Taylor factor (taken as 2 for bcc and 3 for fcc materials [47])

A = a constant depending on the dislocation character (taken as 1.21 for mixed dislocations [48])

Equation 3-44 gives an approximation of the inverse correlation between strength and lamellae spacing corrected by a logarithmic factor. Unlike in pearlite, in which cementite plates is not considered to be plastically deformed, both copper and niobium in copper-niobium system are both plastically deformed during tensile testing. Hence, equation 3-44 should be applied to both components.

Since both copper and niobium contribute to the flow stress of the Cu-20%Nb composite, a rule of mixture criterion is used to predict the composite strength (σ_c). The composite strength would be then :

$$\sigma_c = \sigma_{Cu} V_{Cu} + \sigma_{Nb} V_{Nb} \quad \text{Equation 3-45}$$



where :

σ_{Cu} and σ_{Nb} are calculated from equation 3-44
 V_{Cu} and V_{Nb} are 0.8 and 0.2, respectively

The calculated and observed values of the ultimate tensile stress show very good agreement [46] and give confidence to the proposal that the increased difficulty in propagating dislocations in copper and niobium with increasing structure refinement is primarily responsible for strengthening in rolled Cu-20%Nb. It means the propagation of dislocations occurs parallel to the aligned filaments. This model, however, cannot be used to explain the strengthening observed in wire drawn copper-niobium composites. It is mainly because the filament spacings and thicknesses in the wire drawn composite are much larger than those in rolled composite. Apparently, the difficulty in transmitting plastic deformation between the copper and niobium phases in wire is the major source of strengthening, since the highly kinked morphology of the niobium filaments makes them more effective obstructions to dislocation motion than the aligned planar niobium filaments in the rolled composite [46].

3.3.5 Modified Dislocation Strengthening Model

This model introduced by Funkenbusch and Courtney [19,49] has been originally developed to explain : the (indirect) importance of the interphase spacing on composite strength, the presence of high dislocation densities in the *in-situ* composite, and the long range (greater than atomic scale) nature of the forces responsible for the strengths of these materials. The model begins with the concept of geometrical dislocation strengthening in which geometrically necessary dislocations ($\bar{\rho}_g$) exist. As function of interphase spacing (D) and true deformation strain (ϵ_T), such dislocation can be expressed as :

$$\bar{\rho}_g = 2K \left[1 - \exp\left(\frac{\epsilon_T}{2}\right) \right] D^{-1} \quad \text{Equation 3-46}$$

where :

K = a "geometrical constant" which presumably takes into account the relative degree of mismatch among the grains

At low strains ($\epsilon_T \ll 1$) equation 3-46 is equivalent to Ashby's formulation [50] of $\bar{\rho}_g \approx K(\epsilon/D)$, where ϵ is the strain. At high strain ($\epsilon_T \gg 1$), it reduces to :



$$\bar{\rho}_g \approx \frac{2K}{D} \quad \text{Equation 3-47}$$

However, the density of geometrical dislocations predicted by equation 3-46 represents an average value. There are apt to be differences in the relative extent to which each of the phases acts to accommodate mismatch. This situation leads us to expect the dislocation densities within each of the phases to differ. The geometrically necessary dislocation densities in the two phases A and B can then be written as :

$$\rho_g = P_{A,B} \frac{\bar{\rho}_g}{V_{A,B}} \quad \text{Equation 3-48}$$

where :

$V_{A,B}$ = the respective volume fractions of A and B
 P 's = partition coefficients with values between zero and one such that
 $P_A + P_B = 1$

The flow strengths of the individual phases are similar to equation 3-35. Unfortunately an equally simple equation expressing the "statistical" dislocation density (ρ_s) as a function of strain is unavailable. In contrast to geometrical dislocations, which are the result of strain inhomogeneities, statistical dislocations arise as a result of essentially random dislocation-dislocation interactions within the crystal lattice. As a first approximation, the variation of ρ_s with strain and total dislocation density in each phase ($\rho_T = \rho_s + \rho_g$) may be written as :

$$d\rho_s \approx [C_1 \sqrt{\rho_T} - C_2 \rho_T] d\varepsilon_T \quad \text{Equation 3-49}$$

where :

C_1, C_2 = proportionality constants

The first term in the brackets on the right side of equation 3-49 predicts dislocation multiplication proportional to dislocation spacing, while the second term is consistent with the assumption that the loss of dislocation line length per increment of strain is proportional to the total line length present [49].



Since the constants C_1 and C_2 of equation 3-49 reflect random processes within the crystal lattice, their values should be independent of the presence (or absence) of phase boundaries. Hence an equation for the total dislocation density in phase A of an *in-situ* composite material may be obtained merely by adding equation 3-49 to a suitable (i.e. derivative) version of equation 3-46. With appropriate consideration for partitioning of the geometrical dislocations (equation 3-35 but for each phase), one can obtain :

$$\frac{d\rho_{T_A}}{d\varepsilon_T} = C_{1_A} \sqrt{\rho_{T_A}} - C_{2_A} \rho_{T_A} + P_A K \exp\left(\frac{\varepsilon_T}{2V_A D_0}\right) \quad \text{Equation 3-50}$$

where :

D_0 = the interphase spacing at zero strain. The correlation between D and D_0 is :
 $D \approx D_0 \exp(-\varepsilon_T/2)$

The first term on the right side accounts for dislocation multiplication, the second for annihilation processes, whereas the third one represents the geometrically necessary dislocations. Equation 3-50, known also as statistical/geometrical interaction, may take two general forms. If statistical dislocation annihilation dominates dislocation multiplication at high strains and statistical processes serve to eliminate dislocations generated on geometrical effects, composite strengths will not be much greater than those predicted by the rule of mixtures. On the other hand, if $C_2 \approx 0$, statistical processes act to magnify dislocation multiplication catalyzed by geometrical processes and it will lead to strengths greater than predicted by ROM. The agreement between the model developed and the experimental results in silver-nickel and copper-iron composites is good [49].

3.3.6 Lamellar Structures Model

This model was derived originally by Koehler [51]. It is proposed that strengthening in solids could be accomplished with the development of a composite consisting of alternating ultra thin layers of two materials A and B, which can be achieved essentially by epitaxial growth. In such composite, the following criteria are required :

- the lattice parameters of the two crystals at the operating temperature are nearly equal;
- their thermal expansions should be as nearly equal as possible so that changes in temperature will not destroy the lattice fit at the interface;
- their elastic constants should differ as much as possible;



- the bonding between A atoms and B atoms should be large, i.e., of the same order as the bonding between two A atoms or between two B atoms; and
- the thicknesses of the A and B layers must be small, so that a Frank Read source dislocation generation cannot operate inside the low elastic constant material.

In this model the stress (σ) necessary to penetrate the interface between the two components is given by :

$$\sigma = \frac{RG_A}{8\pi} \quad \text{Equation 3-51}$$

where :

G_A = the shear modulus in the low elastic constant material A
 $R = (G_B - G_A)/(G_B + G_A)$, with G_B is the shear modulus of the high elastic constant material

The stress required to initiate the Frank Read source in metal A is given by :

$$\sigma_{S(A)} = \frac{4G_A b_A}{t_A} \quad \text{Equation 3-52}$$

where :

b_A = the Burgers vector
 t_A = the distance between two pinning points of the Frank Read source

If the penetrating force (equation 3-51) is in equilibrium with the Frank Read source (equation 3-52), then one finds :

$$t_A = \frac{32\pi b_A}{R} \quad \text{Equation 3-53}$$

Equation 3-53 informs that the Frank Read source dislocation multiplication can operate in metal A with low elastic constant, when the available space for dislocation pinning is at least equal to $32\pi b_A/R$. However for the purpose of the composite strengthening (i.e. the Koehler type strengthening), Frank Read phenomena should not occur or at least is minimized. The only way to attain this is by reducing the thickness of metal A (t) to be less than t_A as the critical value, which means :



$$t < \frac{32\pi b_A}{R} \quad \text{Equation 3-54}$$

3.4 Recovery and Recrystallization of Deformed Metals

3.4.1 Introduction

In industry, it is sometimes necessary to reheat a cold worked metal or alloy in order to soften it and thus increase its ductility. If the metal is reheated to a sufficiently high temperature for a long enough time, the cold worked structure will go through a series of changes of recovery, recrystallization, and grain growth. Such structural changes along with the corresponding changes in mechanical properties are schematically drawn in figure 3.7, as proposed by Jastrzebski [52]. According to figure 3.7 the internal residual stresses, the strength and the hardness of the reheated material decrease in different ways with increasing temperature. This reheating treatment which softens a cold worked metal is called *annealing*, and the terms *partial anneal* and *full anneal* are often used to refer to degrees of softening. The ductility, however, increases with the heat treatment temperatures. The size of newly developed grains steadily increases from the temperature range of which recrystallization process takes place. As shown by Gottstein [53], the electrical conductivity of heat treated Cu-35%Zn alloy, for instance, increases slightly around $T = 100^\circ\text{C}$ and then stays relatively constant.

A small percentage of the energy expended in plastically deforming a metal remains stored in the metal causing an increase in internal energy. This increment in internal energy is associated with the defects generated during deformation and provides the driving force for recovery and recrystallization. The concept of the release of energy (and changes in other properties) between recovery and recrystallization is based on the definition that recovery includes all annealing phenomena that occur before the appearance of recrystallized grains, whether these are detected by conventional or transmission electron microscopy [54]. The recrystallized grains are taken as those virtually strain-free grains which grow in the deformed matrix by the movement of large angle grain boundaries.

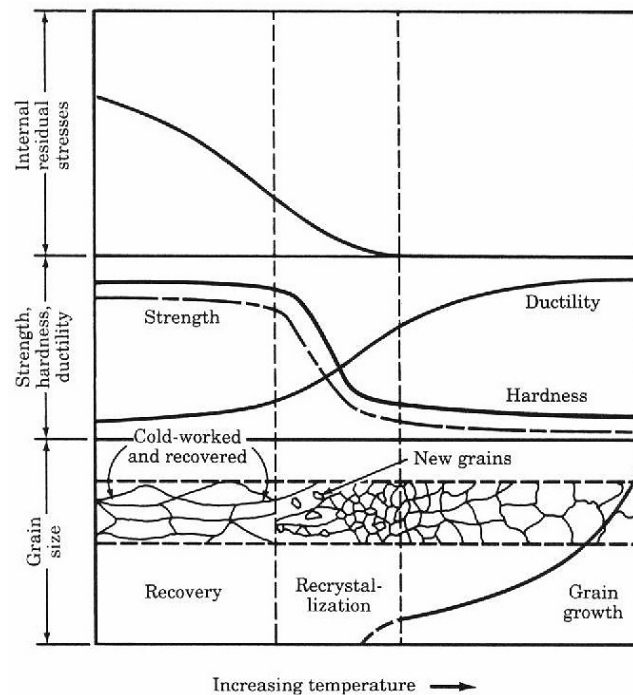


Figure 3.7 The effect of heat treatment on the structure and mechanical property changes of a cold worked metal [52].

3.4.2 Recovery

3.4.2.1 Introduction

When a cold worked metal is heated in the recovery temperature range (just below the recrystallization temperature range) internal stresses in the metal are relieved (see figure 3.7). During recovery, sufficient thermal energy is added to allow dislocations to rearrange themselves into lower energy configurations. Recovery of many cold worked metals yields a subgrain structure with low angle grain boundaries. This recovery process is called polygonization, and is often defined as a structural change which precedes recrystallization (figure 3.8). The internal energy of the recovered metal is lower than that of the cold worked condition, since many dislocations are annihilated or transferred into lower energy configurations. Recovery can also occur during deformation, and such recovery has been called *dynamic recovery*. It can clearly be observed through the reduction of work (or strain) hardening rate and is the reason for the rearrangement of dislocations in cell walls or in sub-grain boundaries (for strong dynamic recovery).

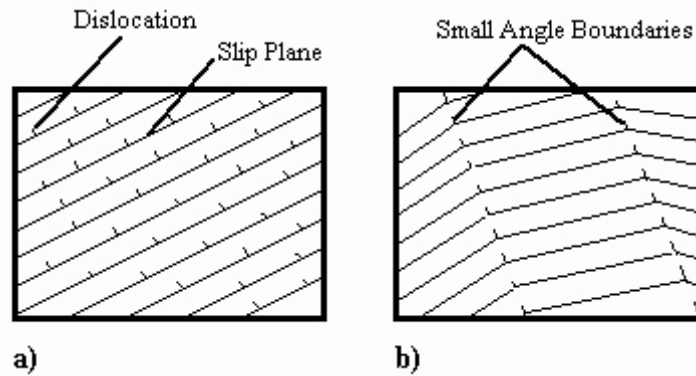


Figure 3.8 The schematic representation of polygonization in a deformed metal. a) Deformed metal crystal with dislocations piled up on slip planes. b) After recovery heat treatment, dislocations rearrange to form small angle grain boundaries [55].

3.4.2.2 Recovery Mechanisms

As discussed by Gottstein [53], recovery is based on interaction of dislocations due to their wide stress field. The corresponding interaction force between an edge dislocation with Burgers vector b_1 and another parallel dislocation with Burgers vector b_2 is :

$$F = \frac{Gb_1b_2}{2\pi r_v(1-\nu)} \cos \Phi \cos 2\Phi \quad \text{Equation 3-55}$$

where :

G = the shear modulus

r_v = the spacing between the two dislocations

Φ = the angular coordinate ($\Phi = 0^\circ$ when they are on the same slip plane)

ν = the Poisson's ratio

Dislocations of opposite sign on the same slip plane will attract each other, run together, and annihilate each other. On the other hand, dislocations of like sign on the same slip plane will repel each other. Further, when the two dislocations are wide apart by several slip planes, the annihilation occurs through repel action and multiple dislocation climb. The dislocations of the same sign repel each other when $\Phi < 45^\circ$ and attract each other when $\Phi > 45^\circ$. The reverse is true for dislocations of opposite sign. The interaction force (equation 3-55) then will be zero when the two dislocations are in an equilibrium position. Such position exists when $\Phi = 90^\circ$, of which these edge dislocations lie vertically above one another.



Recovery takes place via dislocation climb and cross-slip. These mechanisms depend on stacking fault energy, i.e., more climb and cross-slip occurs with the increasing of stacking fault energy. Material with the high stacking fault energy exhibits strong recovery. Aluminum and most bcc metals have such high stacking fault energy; while silver, copper, and fcc alloys have low stacking fault energy and show little tendency to do recovery. Dislocation climb occurs as an edge dislocation moves out of the slip plane onto a parallel plane directly above or below its slip plane. Dislocation climb is a diffusion-controlled mechanism, in which vacancies or interstitials diffuse to or away from the site of the dislocation. Since it is diffusion-controlled, dislocation climb is thermally activated and takes place readily at elevated temperature. In cross-slip process, a screw dislocation changes its slip plane. Usually a screw dislocation move in its own slip plane, of which it experiences larger shear stress. As it faces an obstruction in this primary slip plane, it can alternate the course into another slip plane, i.e. the cross-slip plane.

3.4.3 Recrystallization

3.4.3.1 Introduction

Upon heating a cold worked metal to a sufficiently high temperature, new strain-free grains are nucleated in the recovered metal structure and start to develop, forming a recrystallized structure. After a long-enough time at this recrystallization temperature, the cold worked structure is completely replaced with a recrystallized grain structure

According to Dieter [3] and Smith [56], important factors which affect the recrystallization process in metals and alloys are : (1) amount of prior deformation of the metal, (2) temperature, (3) time, (4) initial grain size, (5) composition of the metal or alloy, and (6) amount of recovery or polygonization prior to the start of recrystallization. The recrystallization of a metal can take place over a range of temperatures, and this range depends on some extent of the above variables.

3.4.3.2 Driving Force and Kinetics of Recrystallization

The driving force for the primary recrystallization is the deformation energy stored in dislocations. This driving force, p , is given as function of dislocation density according to :



$$p = \rho E_v = \frac{1}{2} \rho G b^2 \quad \text{Equation 3-56}$$

where :

E_v = the energy of dislocation per unit length

ρ = the dislocation density

G = the shear modulus

b = the Burgers vector

To measure the release of stored energy and subsequently to follow the kinetics of recrystallization process, the experimental data are usually analyzed with reference to an equation of the type :

$$x = 1 - \exp(-Bt^k) \quad \text{Equation 3-57}$$

where :

x = the recrystallization fraction after time t , at constant temperature

B, k = constants

The temperature dependence of B is of the form :

$$B = B_0 \exp(-kQ / RT) \quad \text{Equation 3-58}$$

where :

Q = the activation energy of the process

The kinetics of recrystallization is determined from the thermal activation of recrystallization mechanisms, namely nucleation and nucleation growth. Hence, one defines the nucleation rate \dot{N} and the growth rate v as :

$$\dot{N} = \frac{dz_k}{dt} (1-x)^{-1} \quad \text{Equation 3-59}$$

$$v = \frac{dR}{dt} \quad \text{Equation 3-60}$$

where :

x = the recrystallization volume fraction (equation 3-57)

t = the time

R = the radius of primary recrystallized grain

z_K = the number of the observed nucleus per unit volume



Another expression (similar to equation 3-57) has been defined to determine the recrystallization volume fraction, which is called the Avrami-Johnson-Mehl-Kolmogorov equation [57-59] :

$$x = 1 - \exp\left\{-\left(\frac{t}{t_R}\right)^q\right\} \quad \text{Equation 3-61}$$

where :

q = the time exponential

t_R = the recrystallization time defined as the elapsed time until the whole structure is recrystallized

The recrystallization time (t_R), and the primary recrystallized grain size (R) can be defined as function of nucleation rate and growth rate according to :

$$t_R = \left(\frac{\pi}{3} \dot{N} v^3\right)^{-1/4} \quad \text{Equation 3-62}$$

$$R = 2vt_R \cong 2\left(\frac{3}{\pi} \frac{v}{\dot{N}}\right)^{1/4} \quad \text{Equation 3-63}$$

Further, recrystallization time and recrystallized grain size can also be defined as function of temperature, since recrystallization is a thermally activated process. Thereby, one has to firstly define the activation energies of Q_v and Q_N , which are respectively related to the grain growth and the nucleation rate according to :

$$v = v_0 \exp\left(-\frac{Q_v}{kT}\right) \quad \text{Equation 3-64}$$

$$\dot{N} = \dot{N}_0 \exp\left(-\frac{Q_N}{kT}\right) \quad \text{Equation 3-65}$$

where :

v_0, \dot{N}_0 = factors that independent of temperature

Now one can determine the recrystallization time and the recrystallized grain size as exponential function of temperature :



$$t_R = \left(\frac{3}{\pi \dot{N}_0 v_0^3} \right)^{1/4} \exp\left(\frac{Q_N + 3Q_v}{4kT} \right) \quad \text{Equation 3-66}$$

$$R = \left(\frac{48v_0}{\pi \dot{N}_0} \right)^{1/4} \exp\left(\frac{Q_N - Q_v}{4kT} \right) \quad \text{Equation 3-67}$$

3.4.3.3 Primary Recrystallization Mechanisms

Primary recrystallization occurs by two principal mechanisms : (1) an expansion of isolated nucleus within a deformed grain or (2) a migration of original high angle grain boundary into a more highly deformed region of a metal. In either case, the structure on the concave side of the shifting boundary is strain-free and features a relatively low internal energy, whereas the structure on the convex side of the moving interface is highly strained with a high dislocation density and high internal energy. In this case, grain boundary movement is away from the boundary's center of curvature. Thus the growth of an expanding new grain during primary recrystallization results in overall decrease in the internal energy of the metal by substituting strain-free regions into deformed regions.

Nucleation

There are three instability criteria for nucleation to occur [53] :

- (1) **Thermodynamic instability.** A nucleus must have critical size to develop, of which its growth must lead to the reduction of free enthalpy. This critical radius is given as :

$$r_c = \frac{2\gamma}{p} = \frac{4\gamma}{\rho G b^2} \quad \text{Equation 3-68}$$

where :

γ = the grain boundary energy [J/m²]

The other parameters in equation 3-68 have been defined previously in equation 3-56.

- (2) **Mechanical instability.** An unequally distributed driving force should exist, so that the grain boundaries have a defined direction to move. This requirement can be fulfilled through inhomogeneous distribution of dislocations or through local large sub-grains that grow during recovery.

(3) **Kinetic instability.** The interface of nuclei must be mobile. This condition is possible, however, for large angle grain boundaries. The mobile development of these boundaries from a deformed structure is the most difficult step in the recrystallization nucleation.

Grain Boundary Movement

At sufficiently high temperatures, the grain boundaries in a recrystallized specimen will migrate as to reduce the total number of grains and thereby increase the mean grain diameter. According to Gottstein and Shvindlerman [60], the velocity of grain boundary can be defined as the difference of the thermally activated diffusional jogs from shrinking to growing grains and vice versa, as shown in figure 3.9 :

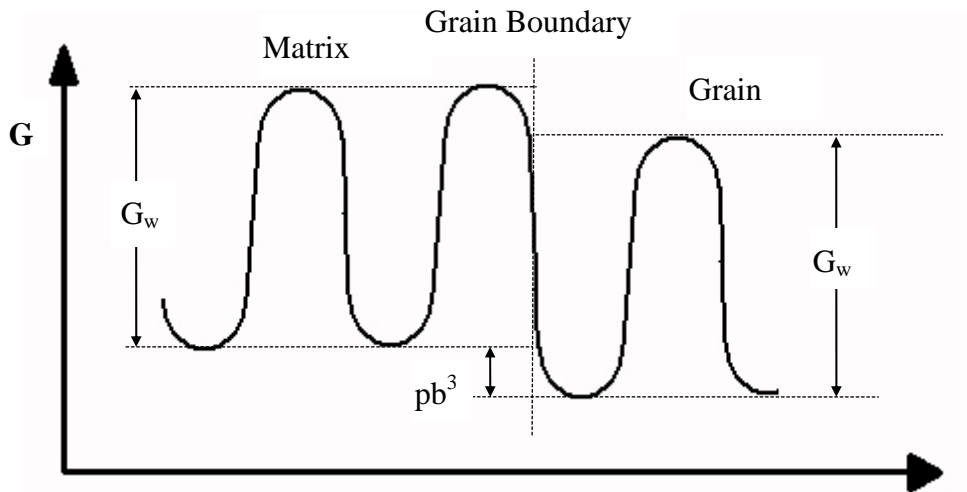


Figure 3.9 The schematic representation of the free enthalpy around the grain boundary under the influence of a driving force p [60].

For all driving force of the recrystallization, it is always valid that :

$$pb^3 \ll kT \quad \text{Equation 3-69}$$

where :

pb^3 = the free enthalpy
 b^3 = the atomic volume

The velocity of grain boundary (v) can be expressed as :



$$v = b^4 v_0 c_{LG} \frac{1}{kT} \exp\left(-\frac{G_w}{kT}\right) p \quad \text{Equation 3-70}$$

or

$$v = mp \quad \text{Equation 3-71}$$

where :

v_0 = the atomistic vibrational frequency ($\approx 10^{13}$ /sec)

G_w = the free activation enthalpy for a diffusional jump through the grain boundary

c_{LG} = the concentration of vacancy in the grain boundary

m = the mobility

The correlation between the mobility, m , and diffusion coefficient, D_m , for jumps through the grain boundaries with activation energy, Q_m , can be defined from Nernst-Einstein equation as :

$$m = \frac{b^2 D_m}{kT} = \frac{b^2 D_0}{kT} \exp\left(-\frac{Q_m}{kT}\right) = m_0 e^{-\frac{Q_m}{kT}} \quad \text{Equation 3-72}$$

Further, the mobility of grain boundaries can be strongly influenced by the impurities in material that present in grain boundary and perform a reverse driving force to the grain boundary. In this case, a very high activation energy, Q_m , can take place. The mobility of grain boundary also depends on the orientation relationship of crystal :

$$m = m(\omega < hkl >) \quad \text{Equation 3-73}$$

where :

ω = the rotation angle

$<hkl>$ = the rotation axis

The orientation-dependency of grain boundary movement or mobility, especially from the rotation axis, is normally explained through *the coincidence grain boundaries* that occur by high mobility. The coincidence grain boundaries are defined as the grain boundaries between crystallites (with rotational relationship between each other) that yield a high number of coincident points [53]. These coincident grain boundaries take very few foreign atoms. With increasing content of foreign atoms the mobility of grain boundaries lowers.



With very high purity, the orientation-dependency of grain boundary movement is vanished.

3.4.3.4 Important Points of Recrystallization

According to Mehl [61], the following aspects can be summarized as the important points in the recrystallization process :

1. A minimum amount of deformation is necessary for recrystallization to be possible.
2. The smaller the degree of deformation (above the minimum), the higher the temperature needed to cause the recrystallization.
3. Increasing the temperature for recrystallization decreases the time necessary to complete it. In this case, the temperature is far more important than time. Doubling the annealing time is roughly equivalent to increasing the annealing temperature by 10°C.
4. The final grain size depends mainly on the degree of deformation and to a lesser extent on the annealing temperature. The greater the degree of deformation and the lower the annealing temperature, the smaller the recrystallized grain size.
5. The larger the original grain size, the greater the amount of deformation required to produce an equivalent amount of recrystallization.
6. The recrystallization temperature decreases with increasing purity of the metal. Solid solution strengthening or alloying always raises the recrystallization temperature.
7. The amount of deformation required to produce equivalent recrystallization behavior increases with increased temperature of working.
8. For a given reduction in cross section, different metal working processes (e.g. : rolling, drawing, etc) yield somewhat different effective deformations. Hence, identical recrystallization behavior from such different processes may not be observed.

3.4.4 Grain Growth

As discussed in 3.4.1, the grain growth occurs subsequent to the complete primary recrystallization process. The driving force for grain growth is appreciably lower than the driving force for recrystallization. It means, at a temperature of which recrystallization takes place readily grain growth will occur slowly. On the other hand, grain growth depends strongly on temperature, and a grain-growing region will soon be reached in which the grain size increases very rapidly. The presence of a fine dispersion of second-phase particles inhibits considerably the grain growth, by restricting the grain boundary



movement. *Exaggerated* or *abnormal grain growth* occurs, in which some of the finely recrystallized grains will begin to grow rapidly at the expense of the other grains at a high temperature. The driving force for the abnormal grain growth is the decrease in surface energy, instead of stored energy. However, such process features kinetics similar to those of primary recrystallization, hence, it is called *secondary recrystallization*.

3.5 Microstructural Instabilities in Metallurgical Systems

3.5.1 Introduction

The changes in the size and shape distributions of the constituent phases occurring at elevated temperatures by diffusional processes can be either advantageous or detrimental depending on whether they are deliberately induced during material processing or occur in service, respectively.

According to McLean [62], there are two broad categories of sources of the instability driving forces :

1. The reduction in free energy as an isolated alloy tends towards thermodynamic equilibrium. Such phenomenon results in *intrinsic* instabilities. Here, the interfacial energies make an important contribution to such process, leading to particle coarsening and spheroidization.
2. The interaction between the alloy and an externally applied potential field, which results in *extrinsic* instabilities. In this case, there is no stable equilibrium form. However a progressive reduction in energy is manifested as phase migration, coarsening, and shape changes provoked by diffusion along the applied potential field.

In intrinsic instabilities, the microstructural changes leading to a reduced free energy take a variety of forms. Such instabilities are associated with the energy reduction attained by removing defects from the alloy. In this discussion, the emphasis will be placed strongly on the evolution of microstructure of existing phases, instead of phase changes and deposition of new phases. The most important aspect in the intrinsic instabilities is the reduction of the various interfaces area, which can be manifested as :

- grain or precipitate coarsening (e.g. : grain growth, Ostwald ripening),
- shape changes of grains or precipitates (e.g. : spheroidization, faceting, agglomeration, etc.), and
- interaction of phase or grain boundaries.



In extrinsic instabilities, the diffusional flow can be induced in a material by a variety of externally applied potential fields such as temperature, stress, and electric potential gradients. As in the case of intrinsic instabilities, such mass transport in a polyphase material can be manifested as changes in shape, size, and position of the constituent phases. By far, the largest contribution to the extrinsic instabilities comes from temperature gradients.

The rest of discussion will deal with some aspects of microstructural instabilities (i.e. : intrinsic, extrinsic, or combination of both) which are likely pertinent to describe the phase evolution in heat treated *in-situ* metal matrix composites. Again, the corresponding external field taken into account will be the temperature.

3.5.2 Morphological Thermal-Instabilities in Metal Matrix Composites

3.5.2.1 Coarsening Mechanisms in Duplex Microstructures

In the duplex microstructures (either rod - or plate-like structures), there are basically two mechanisms involved in the coarsening of the lamellae :

1. **Fault migration**, proposed by Cline [64] and Graham and Kraft [65]. Such mechanism is associated with a flux of A atoms from the α phase to the β phase, as shown in figure 3.10a.
2. **Boundary migration**, proposed by Livingston and Cahn [66]. This mechanism involves the diffusion of solute atoms from the finely spaced (λ_1) lamellae along a migrating boundary (with rate V) to the widely spaced (λ_2) lamellae on the other side of the interface as shown in figure 3.10b.

The coarsening rate increases with increasing temperature and decreasing spacing of the lamellae as both effects minimize the required diffusion times. Coarsening by the boundary migration becomes expectedly more prevalent than that by fault migration at low temperatures, since at such temperatures short-circuit diffusion along grain boundaries is dominant. Further, coarsening by boundary migration becomes more important at finer spacings of the lamellae.

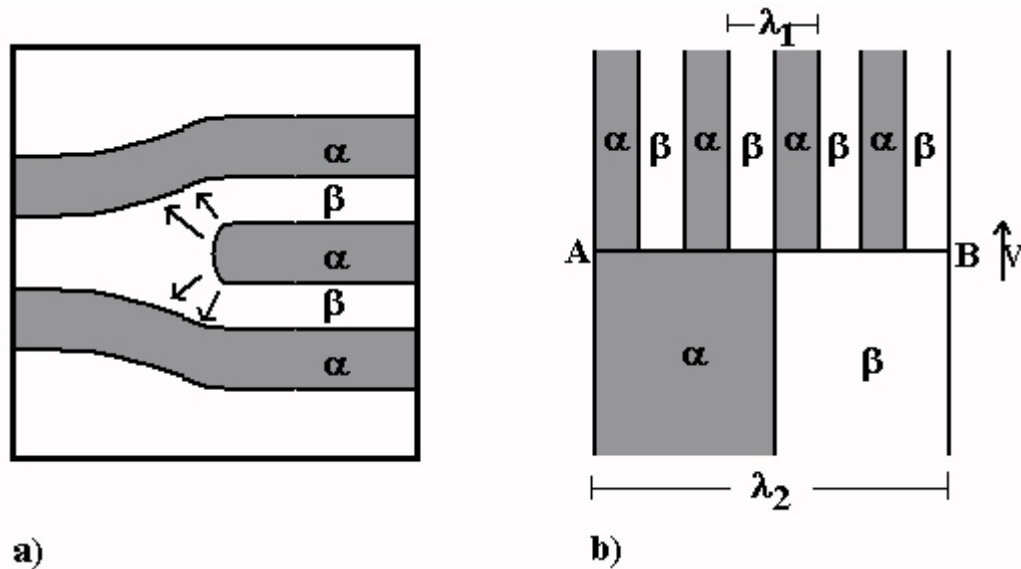


Figure 3.10 a) The schematic of mass flux in the vicinity of a lamellar termination (fault). As the termination recedes, the adjacent filaments thicken [64]. b) An idealized model of discontinuous coarsening process or boundary migration. As the boundary moves, spacing λ_1 is consumed and spacing λ_2 is generated [66].

3.5.2.2 Shape Instabilities in Rod-Shaped Duplex Structures

The growth of a shape perturbation on a cylinder was firstly analyzed a century ago by Rayleigh [67]. The quantitative models for spheroidization of cylindrical precipitates have been recently developed by Ho and Weatherly [63], Cline [64], and Nichols [68]. Theoretically, Rayleigh instability can dominate in infinite fibers (figure 3.11a), whereas the drop detachment at the end of the fibers should be the faster process (figure 3.11c). A long fiber with length l and radius d ($l/d > 7.2$) is eventually transformed into a string of spheres, of which the sphere radii and spacing, λ , depend on the active kinetic processes (figure 3.11c). In this case, the transformation of the fiber into spheres is called *Rayleigh instability*. On the contrary, when the aspect ratio (l/d) is less than 7.2, shape relaxation to a single sphere may occur (figure 3.11b). Another mechanism of spheroidization, which applies to both fibrous and lamellar inclusions, exists when grain boundaries in either phase intersect phase boundaries between the fibers and matrix. At the intersection points, grooves will develop and progressively deepen with time to establish a local equilibrium configuration, which finally cause a division of one phase and result in spheroidization (figure 3.11d).

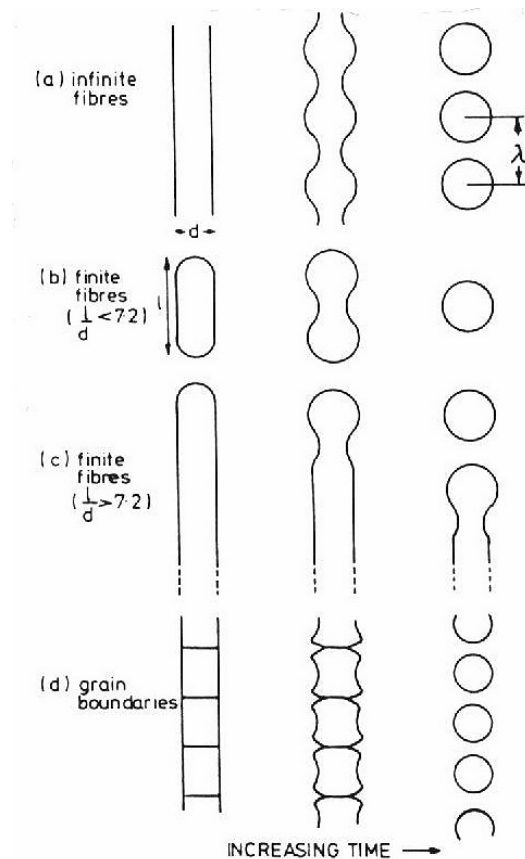


Figure 3.11 The schematic representation of different modes of spheroidization of cylindrical inclusions [62].

3.5.2.3 Shape Instabilities in Plate-Like Duplex Structures

A plate-like structure requires the presence of plate terminations to instigate microstructural evolution, as discussed by Courtney [69]. Figure 3.12 shows schematically the types of shape instability that can be observed to occur when mass transfer is intraplate (in the plate). In figure 3.12a, the mass is transferred from terminations to the flat surfaces of the plate. The transfer may be affected by volume or surface diffusion, and it eventually produces a cylindrical particle. Such process is then called cylinderization. Following cylinderization the cylinder decomposes into a row of spheres via Rayleigh instability process, if intrafiber transport is the only viable transport route. Otherwise, the resulting cylinder can coarsen via two-dimensional Ostwald ripening among other cylinder formed similarly.

Edge spheroidization, illustrated in figure 3.12b, may interrupt the cylinderization process. Such process is "nucleated" during the initial stages of cylinderization. The plate forms a bulge in the termination vicinity due to rapid diffusion to the adjacent flat faces of the plate. This "pseudocylinder" or partial cylinder can then decompose into spheres in much the same manner an isolated cylinder does. Clearly edge spheroidization should



occur more rapidly than cylinderization for plates with large aspect ratios (w/t) and vice versa.

The final instability is associated with the presence of internal boundaries running parallel to the long axis of the plate (figure 3.12c), and is called boundary splitting. The dihedral angle (2ϕ) at the triple point of the internal-external boundary juncture is determined by the relative boundary energies ($2 \cos \phi = \gamma_B/\gamma_S$, with γ_B = internal boundary surface energy and γ_S = interphase surface energy). If γ_B is relatively large, i.e. $2\phi \ll 180^\circ$, the groove deepens and the boundary splitting takes place. Boundary splitting will occur in preference to edge spheroidization/cylinderization for plates having small thicknesses and/or low dihedral angles [70].

From these three main instability mechanisms, the important geometrical variables are the plate aspect ratio and the dihedral angle developed at the internal-interphase boundary. Courtney and Malzahn Kampe [70] approximated the diffusion geometries and rate equations for the involved mass transport. The dominant mechanism has been defined as the one requiring the least time to complete. Results of this analysis are manifested in diagrams, which are called *shape instability diagrams*. Figure 3.13a shows the shape instability diagram for volume diffusion control of the process, whereas figure 3.13b illustrates the one for surface diffusion control. Such diagrams have axes of the plate aspect ratio and the cosine of the junction dihedral angle. Contours of the time are expressed in terms of a normalized time $\tau' = t^3 kT / Dc_0 \gamma_s \Omega^2$, where : k = Boltzmann constant, T = absolute temperature, D = operative diffusivity, c_0 = equilibrium solubility of dispersed phase in matrix, γ_s = interphase surface energy, and Ω = atomic volume). In this case, τ is the time required to complete each process.

3.5.2.4 Termination Migration in Plate-Like Duplex Structures

When volume diffusion controls the mass transport, a various structural evolution paths can be clearly followed. Such shape instability diagrams can then be extended to include complexities arising from inter- and intraplate diffusion and take into account the concept of *termination migration*.

By termination migration process, the dominant mechanism is the one that yields the greatest rate of volume transport, dV/dt . The edge spheroidization is likely not observable when volume diffusion controls microstructural evolution, since the value of

dV/dt associated with edge spheroidization is much less than that for termination migration. Thus, the termination recession overcomes the development and growth of unstable perturbations along the long axis of the plate. Further, termination migration may be considered as an alternative cylinderization route through deposition of mass onto the broad face of an adjacent lamella as the termination recedes. Even, a plate with receding ends may have in some extents thickening of its broad faces due to mass deposition from a termination of an adjacent lamella. Figure 3.14 illustrates schematically microstructural evolution when termination migration controls the coarsening of lamellar structures [71]. An extended shape instability diagram for volume diffusion controlled coarsening of plate-like structures is shown in figure 3.15. It is clearly seen that termination migration replaces edge spheroidization as the dominant process for plate with large aspect ratios. In this case, the boundaries on the map depend on the coarsening phase volume fraction, V_α .

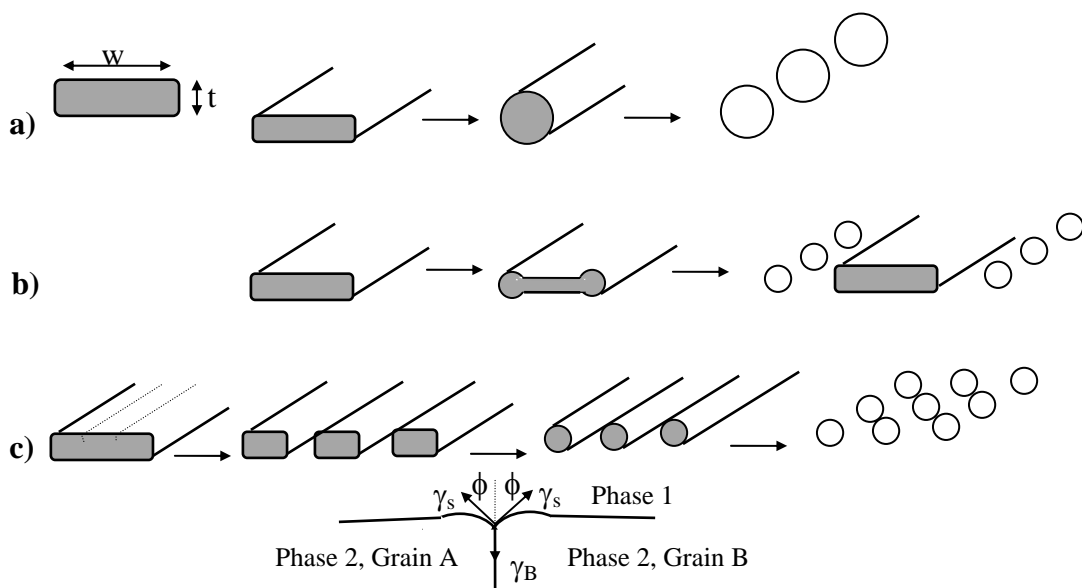


Figure 3.12 The termination instigated instabilities in isolated plate-like structure : a) cylinderization, b) edge spheroidization c) boundary splitting with the definition of dihedral angle (ϕ) of the triple junction during grooving [70].

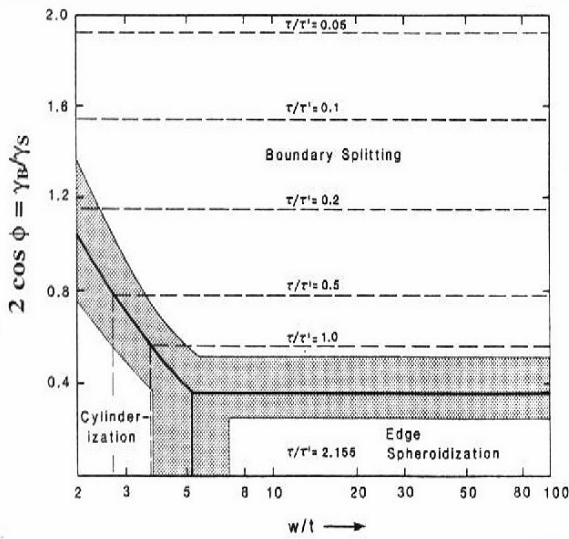


Figure 3.13a The shape instability diagram that is based on volume diffusion control. The shaded regions represent the estimated uncertainties [70].

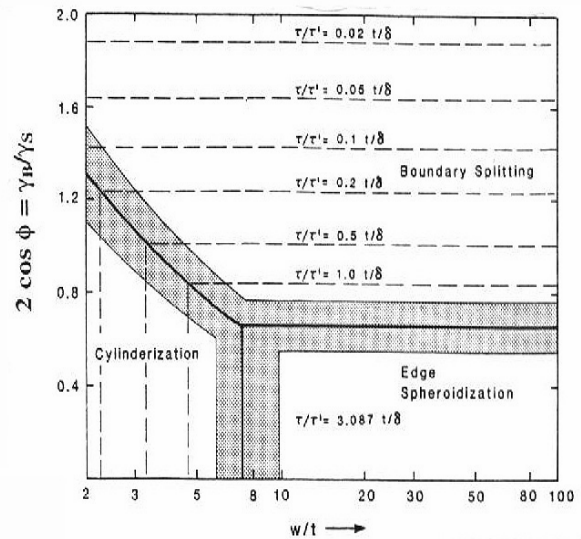


Figure 3.13b The shape instability diagram when the instability is controlled by surface diffusion [70].

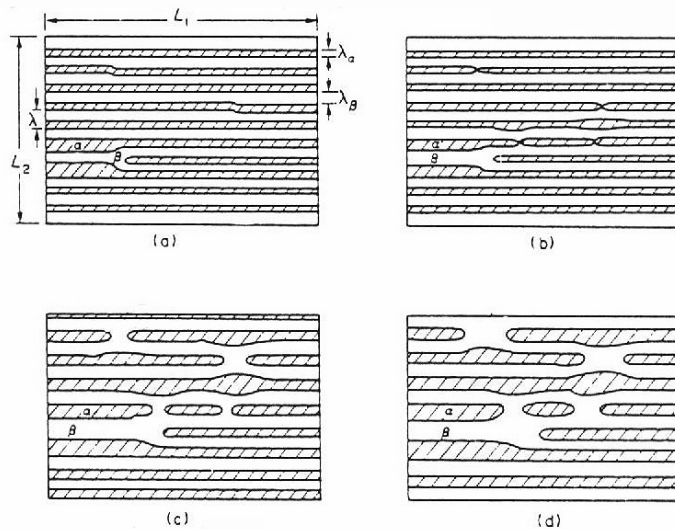


Figure 3.14 The microstructural evolution due to termination migration mechanism [71].

Courtney [69] constructed a diagram that illustrates the ratio of the internal surface energy release of an instability process (S) and the initial value of such energy in a material (S_0) as a function of process time (t') normalized to τ' , as shown in figure 3.16. According to figure 3.16, the plate with no internal boundaries coarsens by termination migration until t'/τ' approximately 23 followed by cylinderization process up to $t'/\tau' \sim 64$. An interesting phenomena occurs as a plate with internal boundaries splits fast. Even though the coarsening diagram (figure 3.15) indicates the domination of termination migration for the corresponding aspect ratio-dihedral angle combination, boundary splitting is concurrent with termination migration. While the volume transport rate of boundary splitting is less



than that of termination migration, the amount of transport needed for splitting is small so that it occurs fast.

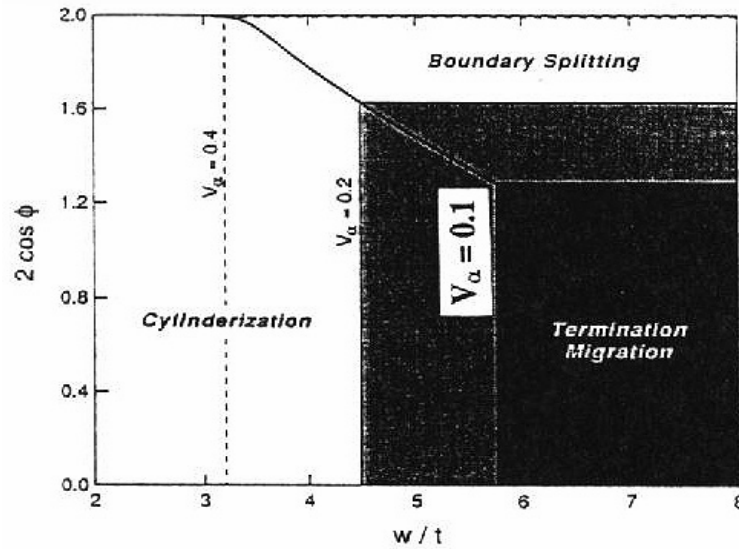


Figure 3.15 The coarsening diagram for volume diffusion controlled coarsening of plate-like structures [69].

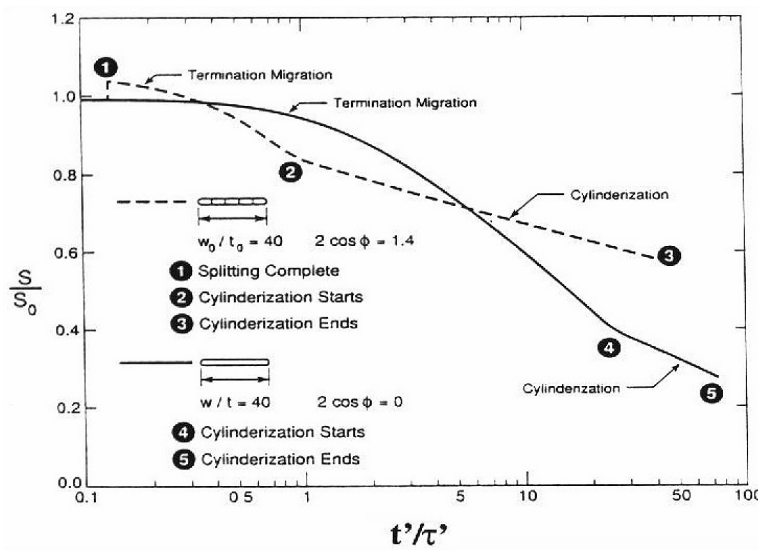


Figure 3.16 The internal surface energy change as a function of coarsening time of plate-like structures [69].

3.6 Cahn-Hilliard Approach for Simulation of Phase Evolution

3.6.1 Introduction

Alloys are not necessarily in homogeneous state of ideal solution. There are systems, in which by cooling for instance, experience phase separation. It produces spatially segregated regions or phases that differ by composition, structure or other characteristic behavior. The process of segregation is dynamic and strives to a final state by fixed boundary conditions such as temperature, pressure, and mass balance. Such final state is considered as thermodynamic equilibrium.



The phase segregation or evolution results in a microstructure with new characteristics. This microstructure again appoints to the mechanical and physical properties, such as elastic and plastic deformability or thermal and electrical conductivity. The intermediate and final states of this process can only be ascertained experimentally. However a conventionality of the boundary conditions mostly limits the possibility of sample preparation and actual measuring procedure. Based on this situation, it is sensible to utilize simple models in describing the phase segregation or evolution and to perform numerical simulations with the aid of such models.

The simulation can assist in clarifying which conceivable mechanism in a given circumstance contributes. Further with sufficient agreements to experiment, simulation can be implemented to predict the dynamic of the microstructure development. An applied continuous model based on diffusion process was developed by *John W. Cahn* and *John E. Hilliard* in 1959 [72-75]. This model implements an inhomogeneous, partial differential equation in concentration field $c(r,t)$ called Cahn-Hilliard equation (CHE). Originally, CHE was used in a linearized form to analytically describe spinodal decomposition [76]. CHE then provides a basis to calculate the diffusion field between precipitates. The Cahn-Hilliard model has the following advantages [77] :

- it does not make a restricting assumption regarding the geometry of diffusion and phase boundaries, and
- it describes the complete evolution, i.e. spinodal decomposition and coarsening (Ostwald ripening).

3.6.2 Thermodynamical Basis of Cahn-Hilliard Model

3.6.2.1 Terms of Free Energy

The model extends the total free energy (F) of Fick's first law by taking into account the energy of the concentration-gradient. The free energy of a phase transformation consists of the chemical free energy, the interfacial free energy, and the elastic free energy. Such condition can be expressed accordingly as :

$$\mathbf{F} = \int [\mathbf{f}_{\text{total}}] d\mathbf{V} = \int [\mathbf{f}_{\text{chemical}}(\mathbf{c}) + \mathbf{f}_{\text{interfacial}}(\mathbf{c}) + \mathbf{f}_{\text{elastic}}(\mathbf{c})] d\mathbf{V} \quad \text{Equation 3-74}$$

where :

F = the free energy of phase transformations

f_{total} = the free energy density



$f_{\text{chemical}}(c)$ = the chemical free energy as a function of concentration
 $f_{\text{interfacial}}(c)$ = the interfacial free energy as a function of concentration
 $f_{\text{elastic}}(c)$ = the elastic free energy as a function of concentration
 c = the concentration
 V = the entire volume of the system

This study deals with the copper-niobium system, which has apparently an incoherent interface due to different crystal structures of fcc (copper) and bcc (niobium). It means that it is unnecessary to include the anisotropic elastic free energy term ($f_{\text{elastic}}(c)$) in the free energy of phase transformations (equation 3-74).

The first derivative of total free energy (equation 3-74) without elastic part defines the effective chemical potential and can be expressed as the Euler-Lagrange equation :

$$\frac{\delta F}{\delta c} = \mu = \frac{\partial f_{\text{chemical}}(c)}{\partial c} - \gamma \Delta c \quad \text{Equation 3-75}$$

where :

F = the free energy of phase transformations (without elastic part)
 c = the concentration
 μ = the effective chemical potential
 $f_{\text{chemical}}(c)$ = the chemical free energy as a function of concentration
 γ = the gradient energy coefficient

Notice that the second term on the left side of equation 3-75 is the first derivative of the interfacial energy ($f_{\text{interfacial}}(c)$). Combining equation 3-75 with the mass conservation law of $\partial c / \partial t = -\nabla \cdot j$, where j is the diffusion flux density according to the Fick's first law, results in Cahn-Hilliard equation (CHE) of :

$$\frac{\partial c}{\partial t} = M \cdot \Delta \left[\frac{\delta F}{\delta c} \right] = M \cdot \Delta \left[\frac{\partial f_{\text{chemical}}(c)}{\partial c} - \gamma \Delta c \right] \quad \text{Equation 3-76}$$

where :

M = the mobility of interphase

3.6.2.2 Chemical Free Energy (f_{chemical})

The chemical free energy (Helmholtz free energy) in equation 3-74 is identical with the Gibbs free energy of mixing G_m under the assumption of constant pressure and volume [76,78]. The expression of G_m follows the approach of Redlich-Kister [79] :



$$\mathbf{G}_m = \mathbf{G}_{ideal} + \mathbf{G}_{excess} \quad \text{Equation 3-77}$$

where :

\mathbf{G}_m = the Gibbs free energy of mixing

\mathbf{G}_{ideal} = the free energy of ideal solution

\mathbf{G}_{excess} = the excess Gibbs energy

Equation 3-77 shows that the free energy of mixing consists mainly of the free energy of ideal solution and the interaction energy of neighboring atoms (excess term). Specific to the copper-niobium system, equation 3-77 can then be elaborated into :

$$\begin{aligned} \mathbf{G}_m &= \mathbf{x}_{Nb} \mathbf{G}_{Nb}^0 + \mathbf{x}_{Cu} \mathbf{G}_{Cu}^0 \\ &\quad \downarrow \\ &\quad \text{heat of mixing} \\ &+ \mathbf{RT} \cdot (\mathbf{x}_{Nb} \ln \mathbf{x}_{Nb} + \mathbf{x}_{Cu} \cdot \ln \mathbf{x}_{Cu}) \\ &\quad \downarrow \\ &\quad \text{entropy of mixing} \\ &\quad + \mathbf{x}_{Nb} \cdot \mathbf{x}_{Cu} \cdot \mathbf{L}_{CuNb}^0 \\ &\quad \downarrow \\ &\quad \text{interaction energy} \end{aligned} \quad \text{Equation 3-78}$$

where :

$\mathbf{x}_{Nb,Cu}$ = the mole fraction of niobium or copper respectively

$\mathbf{G}_{Nb,Cu}^0$ = the free energy density of niobium or copper respectively

\mathbf{L}_{CuNb}^0 = the interaction coefficients between copper and niobium

\mathbf{R} = the gas constant

\mathbf{T} = the absolute temperature

Based on equation 3-78, the Helmholtz free energy or the chemical free energy term ($\mathbf{f}_{chemical}(c)$) in equation 3-74 can be extended as :

$$\begin{aligned} \mathbf{f}_{chemical}(c) \cdot \mathbf{V}_{molar} &= \mathbf{c} \mu_{Nb}^0 + (1-c) \mu_{Cu}^0 \\ &+ \mathbf{RT} \cdot [\mathbf{c} \cdot \ln c + (1-c) \cdot \ln(1-c)] + \mathbf{c} \cdot (1-c) \cdot \mathbf{L}_{CuNb}^0 \end{aligned} \quad \text{Equation 3-79}$$

where :

\mathbf{V}_{molar} = the molar volume of niobium

\mathbf{c} = the mole fraction of niobium



The chemical potentials (μ) and the interaction coefficient (L) in equations 3-78 and 3-79 are optimized to fit the experimental data describing the critical line of the copper-niobium phase diagram at $T_c = 1080^\circ\text{C}$.

3.6.2.3 Interfacial Free Energy ($f_{\text{interfacial}}$)

The interfacial free energy represents the composition gradient of the system. Moreover, the Cahn-Hilliard approach visualizes such composition gradient across the interface as a diffusive path between matrix (i.e. copper) and precipitate or inclusion (i.e. niobium). Since the free energy can be formulated as a continuous function within the framework of phenomenological thermodynamics, the interfacial energy can be expanded in a Taylor series with respect to c . Thus the term of interfacial energy in equations 3-75 and 3-76 can be written as :

$$\mathbf{f}_{\text{interfacial}} = \gamma \Delta c = \frac{\gamma}{2} |\nabla c|^2 \quad \text{Equation 3-80}$$



References

1. *American Iron and Steel Institute* : "Wire and Rods, Alloy Steel : Steel Products Manual", (1975).
2. *Teupel, Fr.K.* : "Formgebung der Metalle", VEB Deutscher Verlag f. Grundstoffindustrie-Leipzig **2** (1980).
3. *Dieter, G.E.* : "Mechanical Metallurgy", McGraw-Hill **3** (1986).
4. *Wistreich, J.G.* : Proc. Inst. Mech. Eng.-London **169** (1955) 654.
5. *Linicus, W.; and Sachs, G.* : Mitt. Dtsch. Materialprüfungsanst. **16** (1932) 38.
6. *Wright, R.N.* : Wire Tech. **6** (1978) 131.
7. *Hosford, W.F.Jr.*: Trans. TMS AIME **230** (1964) 12.
8. *Gibson, R.F.* : "Principles of Composite Materials Mechanic", McGraw-Hill (1994).
9. *Adams, R.D.* : in : T.J. Reinhart et al. (eds.) : "Engineered Materials Handbook : Composites", ASM International-Ohio **1** (1987) 206.
10. *Garmong, G.; and Thompson, R.B.* : Metall. Trans. **4** (1973) 863.
11. *Piehler, H.R.* : Trans. TMS AIME **233** (1965) 12.
12. *Kelly, A.; and Tyson, W.R.* : J. Mech. Phys. Sol. **13** (1965) 329.
13. *Ahmad, I.; and Barranco, J.M.* : Metall. Trans. **1** (1970) 989.
14. *Kelly, A.; and Davies, G.J.* : Metall. Rev. **10(37)** (1967) 1.
15. *Tomota, Y.; Kuroki, K.; Mori, T.; and Tamura, I.* : Mat. Sci. Eng. **24** (1976) 85.
16. *Clarebrough, L.M.*: Australian J. Sci. Res. **A5** (1953) 114.
17. *Ankem, S.; and Margolin, H.* : Metall. Trans. **13(A)** (1982) 603.
18. *Petrovic, J.J.; and Vasudevan, A.K.* : Mat. Sci. Eng. **34** (1978) 39.
19. *Funkenbusch, P.D.; Lee, J.K.; and Courtney, T.H.* : Metall. Trans. **18A** (1987) 1249.
20. *Gladman, T.; McIvor, I.D.; and Pickering, F.B.* : J. Iron Steel Inst. **210** (1972) 916.
21. *Goel, N.C.; Sangal, S.; and Tangri, K.* : Metall. Trans. **16A** (1985) 2013.



22. Su, Y.L.; and Gurland, J. : Mat. Sci. Eng. **95** (1987) 151.
23. Wilson, D.W.; and Konnan, Y.A. : Acta metall. **12** (1964) 617.
24. Lee, H.C.; and Gurland, J. : Mat. Sci. Eng. **33** (1978) 125.
25. Ankem, S.; and Margolin, H. : Metall. Trans. **17A** (1986) 2209.
26. Tamura, I.; Tomota, Y.; and Ozawa, H. : "Proceedings of the 3rd International Conference on Strength of Metals and Alloys", Institute of Metals and Iron and Steel Institute-London **1** (1973) 611.
27. Fischmeister, H. ; and Karlsson, B. : Z. Metallkd. **68** (1977) 311.
28. Cho, K.; and Gurland, J. : Metall. Trans. **19A** (1988) 2027.
29. Embury, J.D.; and Duncan, J.L. : J. Metals **34** (1982) 24.
30. Ankem, S.; and Margolin, H. : Metall. Trans. **13A** (1982) 603.
31. Karlsson, B.; and Linden, G. : Mat. Sci. Eng. **17** (1975) 209.
32. Dvorak, G.J.; and Bahei-El-Din, Y.A. : J. Appl. Mech. **49** (1982) 327.
33. Kelly, A. : "Strong Solids", Oxford Univ. Press-London (1979) 172.
34. Brown, L.M.; and Stobbs, W.M. : Phil. Mag. **23** (1971) 1185.
35. Brown, L.M.; and Stobbs, W.M. : Phil. Mag. **23** (1971) 1201.
36. Brown, L.M.; and Stobbs, W.M. : Phil. Mag. **34** (1976) 351.
37. Hall, E.O. : Proc. Phys. Soc. London **643** (1951) 747.
38. Petch, N.J. : J. Iron Steel Inst. London **173** (1953) 25.
39. Li, J.C. : Trans. Amer. Inst. Min. Eng. **227** (1963) 239.
40. Li, J.C.; and Chou, Y. : Metall. Trans. **1** (1970) 1145.
41. Embury, J.D.; and Fisher, R.M. : Acta metall. **14** (1966) 147.
42. Gielisse, P.J.; and Bai, N.Z. : "Deformation-Processed High-Strength High-Conductivity Microcomposite Conductors", National High Magnetic Field Laboratory-Florida State University **1** (1992).
43. Spitzig, W.A. : Acta metall. Mater. **39(6)** (1991) 1085.



44. Ashby, M.F. : "Strengthening Methods in Crystals", Wiley-New York (1971) 137.
45. Sevillano, J.G. : in : P. Haasen, V. Gerold, G. Kostorz (eds.) : "Strength of Metals and Alloys", Proc. ICSMA 5 Pergamon Press-Oxford (1980) 819.
46. Trybus, C.L.; and Spitzig, W.A. : Acta metall. **37(7)** (1989) 1971.
47. Tegart, W.J.M. : "Elements of Mechanical Metallurgy", Macmillan-New York (1966) 169.
48. Brown, L.M.; and Ham, R.K. : in : A. Kelly, R.B. Nicholson (eds.) : "Strengthening Methods in Crystals", Applied Science-London (1971).
49. Funkenbusch, P.D.; and Courtney, T.H. : Acta metall. **33(5)** (1985) 913.
50. Ashby, M.T. : Phil. Mag. **21** (1970) 399.
51. Koehler, J.S. : Phys. Rev. **2(2)** (1970) 547.
52. Jastrzebski, Z.D. : "The Nature and Properties of Engineering Materials", Wiley-New York **2** (1976) 228.
53. Gottstein, G. : "Physikalische Grundlagen der Materialkunde", Springer-Verlag (1998).
54. Clarebrough, L.M.; Hargreaves, M.E.; and Loretto, M.H. : in : L. Himmel (ed.) : "Recovery and Recrystallization of Metals", Interscience Publishers (1963) 63.
55. Tanner, L.E.; and Servi, I.S. : "Metals Handbook", ASM-Ohio **8** (1973).
56. Smith, W.F. : "Structure and Properties of Engineering Alloys", McGraw-Hill (1981).
57. Avrami, M. : J. Chem. Phys. **7** (1939) 1103.
58. Kolmogorov, A.N. : 1st Akad. Nauk SSR, Ser. Fiz. **3** (1937) 355.
59. Johnson, W.A. : Trans. TMS AIME **135** (1939) 416.
60. Gottstein, G.; and Shvindlerman, L.S. : "Grain Boundary Migration in Metals : Thermodynamics, Kinetics, Applications", CRC Press (1999).
61. Mehl, R.F. : "Metals Handbook", ASM-Ohio (1948) 259-268.
62. McLean, M. : Metal Sci. **12** (1978) 113.
63. Ho, E.; and Weatherly, G.C. : Acta metall. **23** (1975) 1451.
64. Cline, H. : Acta metall. **19** (1971) 481.



65. *Graham, L.D.; and Kraft, R.W.* : Metall. Trans. **236** (1966) 94.
66. *Livingston, J.D.; and Cahn, J.W.* : Acta metall. **22** (1974) 495.
67. *Rayleigh, L.* : Proc. London Math. Soc. **10** (1878) 4.
68. *Nichols, F.A.* : J. Mater. Sci. **11** (1976) 1077.
69. *Courtney, T.H.* : in : N. Haasen (ed.) : "Metal Matrix Composites - Processing, Microstructure, and Properties", 12th Risø International Symposium on Materials Science, (1991) 17.
70. *Courtney, T.H.; and Malzahn Kampe, J.C.* : Acta metall. **37** (1989) 1747.
71. *Lin, L.Y.; Courtney, T.H.; and Ralls, K.M.* : Acta metall. **25** (1976) 99.
72. *Cahn, J.W.; and Hilliard, J.E.* : J. Chem. Phys. **28** (1958) 258.
73. *Cahn, J.W.* : Acta metall. **9** (1961) 795.
74. *Cahn, J.W.* : J. Chem. Phys. **42** (1965) 93.
75. *Cahn, J.W.; and Hilliard, J.E.* : Acta metall. **19** (1971) 151.
76. *Löchte, L.; and Gottstein, G.* : Comput. Mat. Sci. **7** (1996) 115-117.
77. *Gitt, A.F.* : Diplomarbeit, Mathematisch-Naturwissenschaftlichen Fakultät, RWTH Aachen-Germany (1997).
78. *Löchte, L.; Gitt, A.; Gottstein, G.; and Hurtado, I.* : Acta mater. **48** (2000) 2969.
79. *Meurer, B.* : Private Communication : Thermodynamic Data Base Chemsage, Lehrstuhl für Theoretische Hüttenkunde und Metallurgie der Kernbrennstoffe, RWTH Aachen-Germany.

CHAPTER FOUR

EXPERIMENTS AND

CAHN-HILLIARD SIMULATION

In order to review all the laboratory procedures conducted in this research work, five main stages (not necessarily in a consecutive order) of sample treatments are presented, i.e. drawing, annealing, macrotexture measurement, microstructural examinations and analyses, and mechanical tests. The implementation of Cahn-Hilliard equation (equation 3-76) to simulate the phase evolution in copper-niobium system is reviewed at the end of this chapter.

4.1 Drawing Process

4.1.1 Cu-18%Nb Cast Block

The cast block of Cu-18%Nb was received from the National High Magnetic Field Laboratory (NHMFL)-the Florida State University. Such block was cut from a large Cu-18%Nb production ingot with no significant subsequent process, such as equal channel angular extrusion (ECAE), until it was delivered to the author. The as-received Cu-18%Nb had an initial form of a cylinder with dimension of 26.00 mm x 278.00 mm, as schematically shown in figure 4.1.

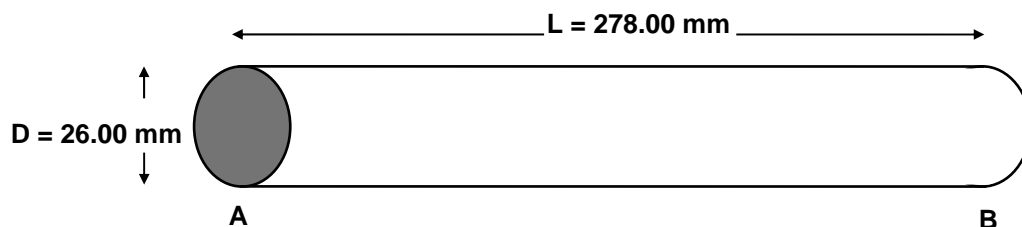


Figure 4.1 The schematic representation of the as-cast Cu-18%Nb sample.

The thickness of this cylinder was first reduced through desurfacing process until it became 18.00 mm, which was the initial diameter (D_0) for the wire drawing process. This cylinder was subsequently round-hammered into diameters of : 16.30 mm, 14.80 mm,



13.00 mm, and 9.50 mm. At the diameter of 9.50 mm, the cylinder was then cut into two pieces. The purpose of cutting was to provide an appropriate initial length for the subsequent wire drawing; i.e. such 278.00 mm long cylinder could yield a very long thin wire during or at the end of drawing process, which might be difficult to manage. Naturally, the wire could be cut at any time during drawing process. However, cutting the cast Cu-18%Nb into two pieces prior to the drawing process was more comfortable and made no significant difference or side effect. For the purpose of gripping during drawing, one end (A or B in figure 4.1) of each 9.50 mm thick cylinder was again round-hammered into 8.50 mm thick. The subsequent drawing process was conducted according to the pass sequence shown in table 4.1. The reduction ratio (η) or deformation and the reduction of area (ε) in table 4.1 were defined based on equation 2-1 to 2-3 with $D_0 = 18$ mm.

| | | | | | | | | |
|---------------------------|--------|-------|-------|-------|-------|--------|-------|-------|
| D₁ (mm) | 9.20 | 8.75 | 8.20 | 7.70 | 7.40 | 7.15 | 7.00 | 6.90 |
| ε (%) | 73.88 | 76.37 | 79.25 | 81.70 | 83.10 | 84.22 | 84.88 | 85.30 |
| η | 1.34 | 1.44 | 1.57 | 1.70 | 1.78 | 1.85 | 1.89 | 1.92 |
| D₁ (mm) | 6.35* | 6.20 | 6.00 | 5.80 | 5.70 | 5.55 | 5.40 | 5.20 |
| ε (%) | 87.55* | 88.14 | 88.89 | 89.62 | 89.97 | 90.49 | 91.00 | 91.65 |
| η | 2.08* | 2.13 | 2.20 | 2.27 | 2.30 | 2.35 | 2.41 | 2.48 |
| D₁ (mm) | 5.00 | 4.80 | 4.50 | 4.30 | 4.10 | 4.00* | 3.88 | 3.70 |
| ε (%) | 92.28 | 92.89 | 93.75 | 94.29 | 94.81 | 95.06* | 95.35 | 95.77 |
| η | 2.56 | 2.64 | 2.77 | 2.86 | 2.96 | 3.01* | 3.07 | 3.16 |
| D₁ (mm) | 3.50 | 3.20 | 2.98 | 2.92 | 2.70 | 2.50* | 2.40 | 2.30 |
| ε (%) | 96.22 | 96.84 | 97.26 | 97.37 | 97.75 | 98.07* | 98.22 | 98.37 |
| η | 3.28 | 3.45 | 3.60 | 3.64 | 3.79 | 3.95* | 4.03 | 4.11 |
| D₁ (mm) | 2.20 | 2.10 | 2.05 | 2.00 | 1.90 | 1.80 | 1.70 | 1.60 |
| ε (%) | 98.51 | 98.64 | 98.70 | 98.77 | 98.89 | 99.00 | 99.11 | 99.21 |
| η | 4.20 | 4.30 | 4.35 | 4.40 | 4.50 | 4.61 | 4.72 | 4.84 |
| D₁ (mm) | 1.50* | ... | ... | ... | ... | ... | ... | ... |
| ε (%) | 99.31* | ... | ... | ... | ... | ... | ... | ... |
| η | 4.97* | ... | ... | ... | ... | ... | ... | ... |

Table 4.1 The pass sequence of Cu-18%Nb wire drawing. Asterisks (*) indicate the observed or examined wire samples.

4.1.2 Copper Wire

In order to provide a reference for the microstructures and the mechanical properties (microhardness and tensile properties) of drawn-annealed Cu-18%Nb, a copper wire was utilized and tested. Unlike Cu-18%Nb wire, this copper wire was not produced from a cast block. Instead, it was simply an already finish product and taken from available wire sample stocks. The only known parameter was its diameter (D_{C0}) of 3.00 mm.



This copper wire was then annealed in a vacuum at temperature around 426°C, until its reduced microhardness was constant and the wire was completely recrystallized (i.e. around two hours). With such low microhardness of VHN 49.60 and recrystallized microstructure, the annealed copper wire could be comparable to a cast sample. This "cast" copper wire then experienced redrawing process, with deformations (η) close to those of Cu-18%Nb wire samples. Microstructural examinations and mechanical tests were subsequently conducted. The redrawing process of the annealed copper wire followed the pass sequence of :

| | | | | |
|----------------------------|------|------|-------|-------|
| D_{Cl} (mm) | 2.90 | 2.70 | 2.50 | 2.30 |
| η | 0.07 | 0.21 | 0.36 | 0.53 |
| D_{Cl} (mm) | 2.20 | 2.05 | 2.02 | 1.80 |
| η | 0.62 | 0.76 | 0.79 | 1.02 |
| D_{Cl} (mm) | 1.60 | 1.40 | 1.20 | 1.10* |
| η | 1.26 | 1.52 | 1.83 | 2.01* |
| D_{Cl} (mm) | 0.95 | 0.75 | 0.68* | 0.62 |
| η | 2.30 | 2.77 | 2.97* | 3.15 |
| D_{Cl} (mm) | 0.59 | 0.52 | 0.47 | 0.40* |
| η | 3.25 | 3.51 | 3.71 | 4.03* |
| D_{Cl} (mm) | 0.34 | 0.29 | 0.27 | 0.25* |
| η | 4.35 | 4.67 | 4.82 | 4.97* |

Table 4.2 The pass sequence of the redrawing of annealed copper wire. Asterisks (*) indicate the observed or examined wire samples.

4.2 Annealing

The annealing of Cu-18%Nb wire samples (section 4.1.1) was performed in two types of furnace : the salt bath furnace and the vacuum finger furnace, whereas that of copper samples (section 4.1.2) only in the vacuum finger furnace. The salt bath furnace was intended mainly for short-time annealing, while the finger furnace was used for long-time annealing.

To minimize the amount of corroding salt making contact with the sample, the wire specimen was well wrapped in a high-grade steel foil (22%Cr-14%Ni-60%Fe-2%Mn) during heat treatment in the salt bath furnace. The foil used for wrapping was stable up to 1100°C.

A schematic representation of the finger vacuum furnace is shown in figure 4.2. Unlike annealing in salt bath furnace, annealing in finger furnace did not require the steel foil. The main requirement for annealing in this furnace was a clean, stain- or fat-free sample surface. In addition, the recipient area (figure 4-2) in which the sample is placed should be kept moisture-free especially during change of the samples.

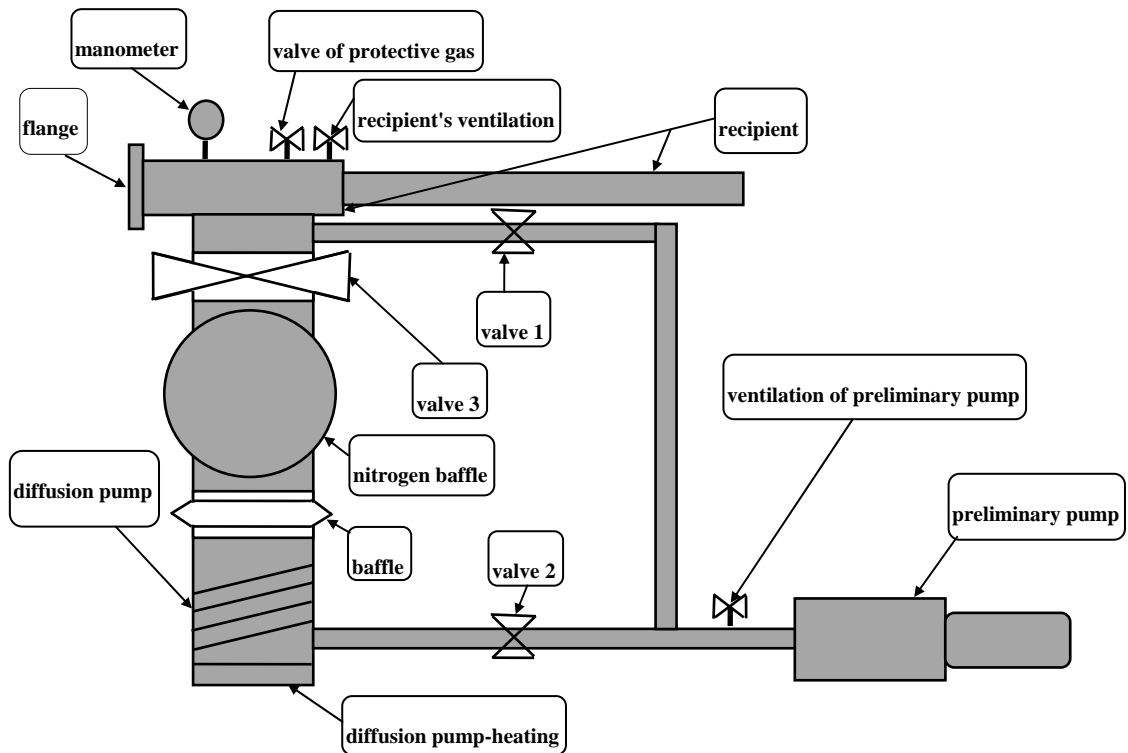


Figure 4.2 The schematic representation of the vacuum finger furnace.

The annealing of Cu-18%Nb samples was conducted at $T = 600^{\circ}\text{C}$, 800°C and 1000°C for $t = 60$ sec, 15 min, 30 min, 60 min, 12 hr, and 24 hr. For the finger furnace, a vacuum condition was attained by keeping the air pressure inside the recipient to be as low as around 2×10^{-3} Pa. The annealed Cu-18%Nb samples were wires that had experienced deformations (η) of : 2.08, 3.01, 3.95, and 4.97. As previously mentioned in section 4.1.2, the soft copper wire was redrawn. Such redrawn copper wire was then annealed at $T = 426^{\circ}\text{C}$ to 433°C for $t = 30$ min, 60 min, 90 min, and 120 min.

4.3 Macrotexture Measurement

4.3.1 Introduction

The determination of a material texture can be performed with the aid of x-rays in the Siemens-Lücke x-ray texture goniometer (figure 4.3). The fundamental of texture measurement is the diffraction of x-rays on lattice planes of a crystal according to Bragg's law :

$$\lambda = 2d\sin\theta \quad \text{Equation 4-1}$$

By a given wave length (λ) and a constant diffraction angle (θ), the lattice planes with spacing d will give some contributions to the reflected x-ray intensity.

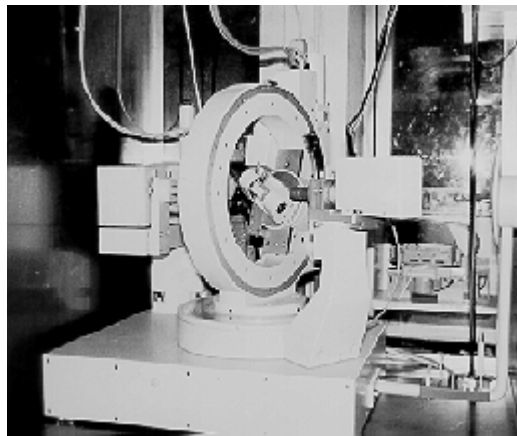


Figure 4.3 The Siemens-Lücke x-ray texture goniometer.

If a sample is exposed to these x-rays and systematically rotated with angle α and β (figure 4.4), one can attain the distribution of the corresponding lattice planes. The reflected intensity is detected by a counter tube with respect to angle α and β , and described in a stereographic projection called pole figure. From several pole figures, the orientation distribution function can be calculated. Such distribution function allows a scientifically accurate texture analysis, i.e. a quantitative statement of the distribution of individual grain orientations.

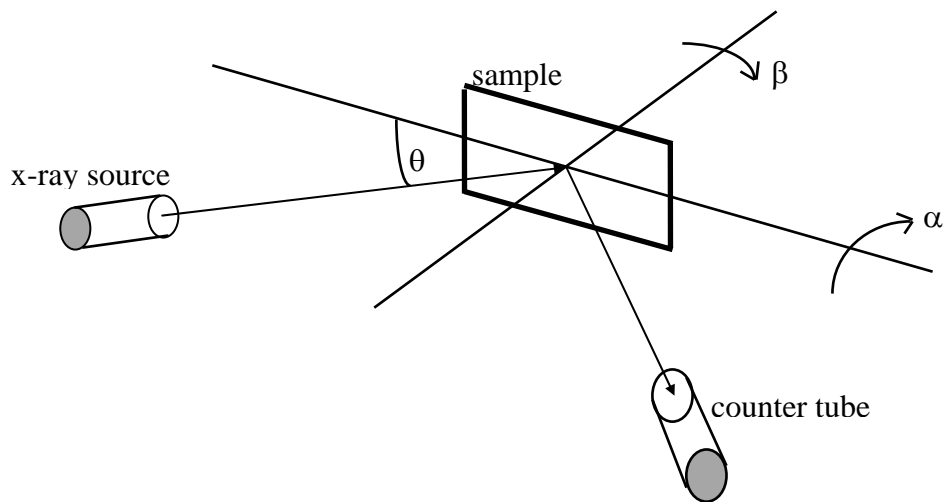


Figure 4.4 The x-ray diffraction and the corresponding angles θ , α , and β of a texture sample.

4.3.2 Main Measurement

In order to produce x-ray, a copper tube ($\text{Cu}_{K\alpha 1}$) with $\lambda = 1.54 \text{ \AA}$ was utilized. Reflections of other wave lengths from the source x-ray had to be filtered to avoid false results using 1 mm-aperture. The sample was oscillated on a sliding carriage/frame (as it was exposed to x-ray), in order to increase the reflection statistic. The Bragg angle (θ) had been set up to 20° , as the sample was measured and rotated about normal axis with the angle (β) of 5° . An incomplete pole figure was measured in the reflection range between $\alpha = 0^\circ$ and $\alpha = 85^\circ$ [1]. The intensity of reflection was given as a function of α and β . The lines of the same intensity were used to describe pole density. After the reduction of irregular background scattering, the pole figure was normalized and put into symmetry.

4.3.3 Peak Spectrums and Background Corrections

The concept of reflection maximums or peak spectrums indicates several maximum intensities that reflected by an irregularly oriented crystal structure (e.g. in compressed crystal powder) as a function of Bragg angle (θ). These spectrums become reference pole figures in configuring the texture orientations of a deformed crystal. These net planes together with their corresponding Bragg angles must be registered into the goniometer controlling program prior to the main texture measurement.

Copper powder and aluminum powder had been utilized to measure these maximum intensities of copper and niobium respectively. Instead of niobium powder (which was difficult to obtain), aluminum powder was implemented since it yielded



somewhat close characteristics of reflection maximums to those of niobium powder regardless of the difference in lattice structures (i.e. niobium is bcc and aluminum is fcc). The peak spectrums of compressed copper powder and niobium powder (which is actually aluminum powder) are shown in figure 4.5. The net plane-Bragg angle combinations of copper and niobium powders from figure 4.5 are listed in table 4.3.

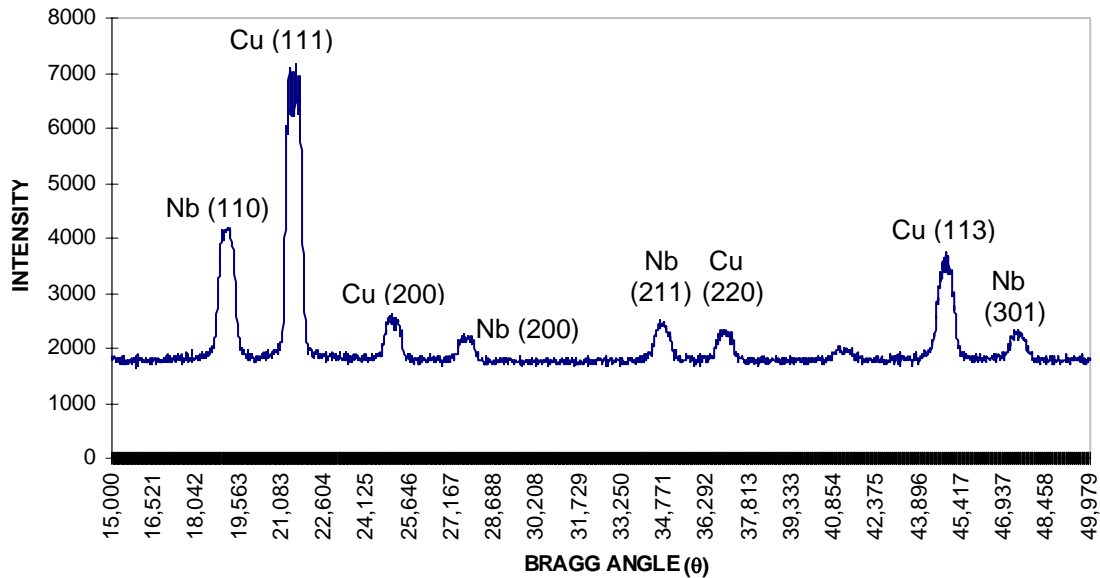


Figure 4.5 The peak spectrums of compact copper and niobium powders.

For correction of the irregular part reflections (background correction), a measurement at surrounding regions of the maximum intensities was performed as the texture of deformed sample was measured. It was very important to appropriately choose the range of this irregular background, so that an overlapping between two correction ranges of the adjacent maximums could be avoided. The range of background correction for copper and niobium is shown in table 4.4. The minus (-) sign indicates a correction range that lies on the left side of the corresponding maximum intensity and vice versa.

From the corrected data of pole figure measurements, a three dimensional orientation distribution function can be obtained. If $\Delta V(g)$ is the volume of all the crystallites with the orientations in the range from g to $g + \Delta g$, and V the volume of the whole sample, then the orientation distribution function is defined as [2] :

$$\frac{\Delta V(g)}{V} = f(g)dg \quad \text{Equation 4-2}$$



| Copper | | Niobium | |
|-----------|--------------------------|-----------|--------------------------|
| Net Plane | Bragg Angle (θ) | Net Plane | Bragg Angle (θ) |
| (111) | 21.58° | (110) | 19.13° |
| (200) | 25.02° | (200) | 27.60° |
| (220) | 36.81° | (211) | 34.60° |
| (113) | 44.81° | (301) | 47.42° |

Table 4.3 The net plane-Bragg angle combinations of copper and niobium powders.

| Copper | | | Niobium | | |
|-----------|--------------------------|-------------|-----------|--------------------------|-------------|
| Net Plane | Bragg Angle (θ) | Corr. Range | Net Plane | Bragg Angle (θ) | Corr. Range |
| (111) | 21.58° | +1.70° | (110) | 19.13° | -2.50° |
| (200) | 25.02° | -1.70° | (200) | 27.60° | +2.50° |
| (220) | 36.81° | +2.50° | (211) | 34.60° | -2.50° |
| (113) | 44.81° | -2.00° | (301) | 47.42° | +2.50° |

Table 4.4 The range of background corrections for copper and niobium.

The function $f(g)$ in equation 4-2 is the orientation distribution function (ODF) that characterizes the texture of the material. Here, the ODF was calculated using an iterative series expansion method after Dahms [3,4]. In the ODF, an orientation is described as a function of Euler angle (ρ_1, Φ, ρ_2) through the rotation of the sample coordinate system in the crystal coordinate system. For an orthorhombic sample coordinate system (rolling direction, normal direction, and transverse direction) and a cubic crystal coordinate system, the description of orientation is manifested in the reduced Euler space with $0 \leq \rho_1 \leq 90^\circ$, $0 \leq \Phi \leq 90^\circ$, and $0 \leq \rho_2 \leq 90^\circ$.

When an axial coordinate system is considered (drawn or compression direction with radial symmetry), such orientation description is now over-specified since normal direction and transverse direction are not distinguishable. In this case, the inverse pole figures in rolling direction (RD) are implemented. The use of such inverse pole figures allows a clear understanding of an axial sample symmetry in the standard triangular pole description. Again, the coefficients of expansion series from ODF after Dahms [3,4] were utilized to calculate the pole density in the standard inverse pole figures.

4.3.4 Sample Preparation

For the purpose of texture measurement in the Siemens-Lücke goniometer, the specimen has to fulfill an appropriate geometry, i.e. 14.00 mm wide x 24.00 mm long (see figure 4.6). The thickness of specimen is relatively undefined, as long as it does not surpass the surface of specimen holder (see figure 4.7). It means, when the sample is correctly mounted on the holder, the value of H must be zero. Such condition can be attained as long as $T \leq D$.

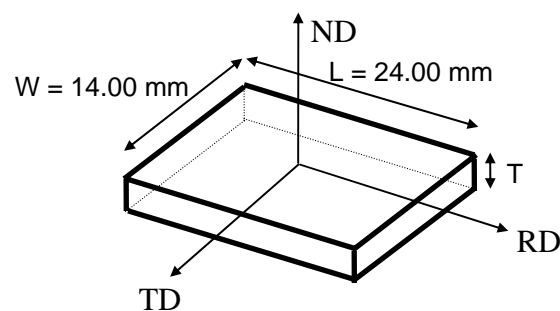


Figure 4.6 The schematic representation of the geometry of a texture sample with an example of orthorhombic sample coordinate system (RD, ND, and TD). The thickness (T) of sample is undefined.

It was impossible to provide a sample with the defined geometry from a single copper-niobium wire, since the largest thickness of the observed wires was 6.35 mm (see table 4.1). This geometry could be fulfilled, however, by cast copper-niobium sample. To solve such geometry problem of the wire, several copper-niobium wires (with the same deformation and/or annealing condition) were each cut into maximum 24.00 mm long and tightly arranged next to one another until their combined width was less or equal to 14.00 mm. Prior to the mounting on sample holder, these arranged wires were strongly embedded in a stiff polymer medium. Its broad surface was then ground halfway through the wire thickness and polished (see figure 4.8).

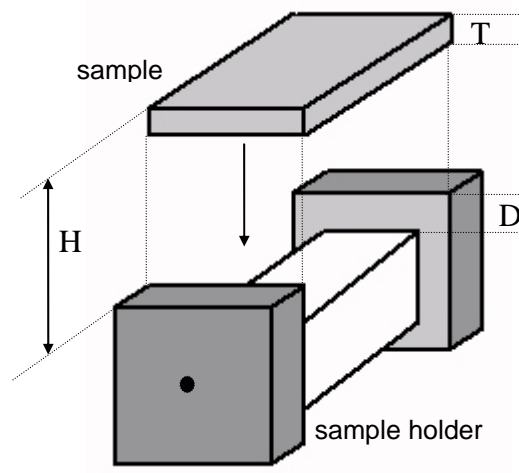


Figure 4.7 The mounting of a texture sample on sample holder.

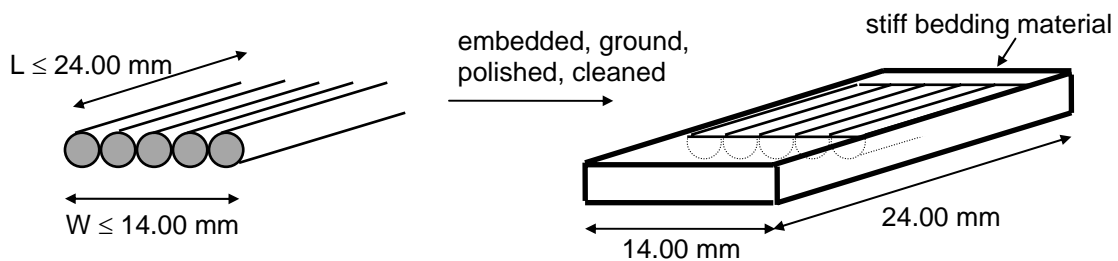


Figure 4.8 The schematic preparation of the texture sample from copper-niobium wires.

It was required that the surface of texture sample was smooth, scratch- and stain-free, likewise shiny. The copper-niobium samples were wetly ground using SiC grinding papers. The samples were then mechanically polished using diamond suspensions of 6 microns, 3 microns, and 1 micron. Finally they were rinsed with alcohol using ultrasonic cleaning and air dried.

4.4 Microstructural Examinations and Analyses

4.4.1 Light Microscope

It was necessary to firstly embed the sample in a stiff material or polymer to ensure flat surface and good sample stability. The embedded sample was ground, polished, and cleaned according to that described in section 4.3.4. Cu-18%Nb and copper samples were etched using a solution of 100 ml H₂O, 30 ml HCl, and 5 g FeCl₃ to observe the deformed and annealed structures in copper matrix. In the order of 5 to 10 seconds of etching,

deformed structures and grains in copper samples could be observable. For Cu-18%Nb samples, the optimal etching time was found to be 30 seconds. The deformed and/or recrystallized copper matrix was obvious when the interfilament spacings were sufficiently large. A ready-to-operate camera was placed on top of this microscope and connected to the binocular photo tube for taking sample pictures. The examination also made use of Quantimet 600 image analysis program for taking and analyzing sample pictures up to 1000x magnification.

4.4.2 Scanning Electron Microscope (SEM)

The Cu-18%Nb SEM samples were *lightly* etched using HNO₃ solution. HNO₃ etched away copper and allowed niobium filaments to protrude. A schematic representation of the mounting of SEM sample on the holder is shown in figure 4.9. There should be a good electrical contact between the samples and the holder. Thus, a two-side conducting tape was utilized to firmly put the sample on the holder. The microstructural observations were conducted using the JEOL JSM-6100 scanning microscope.

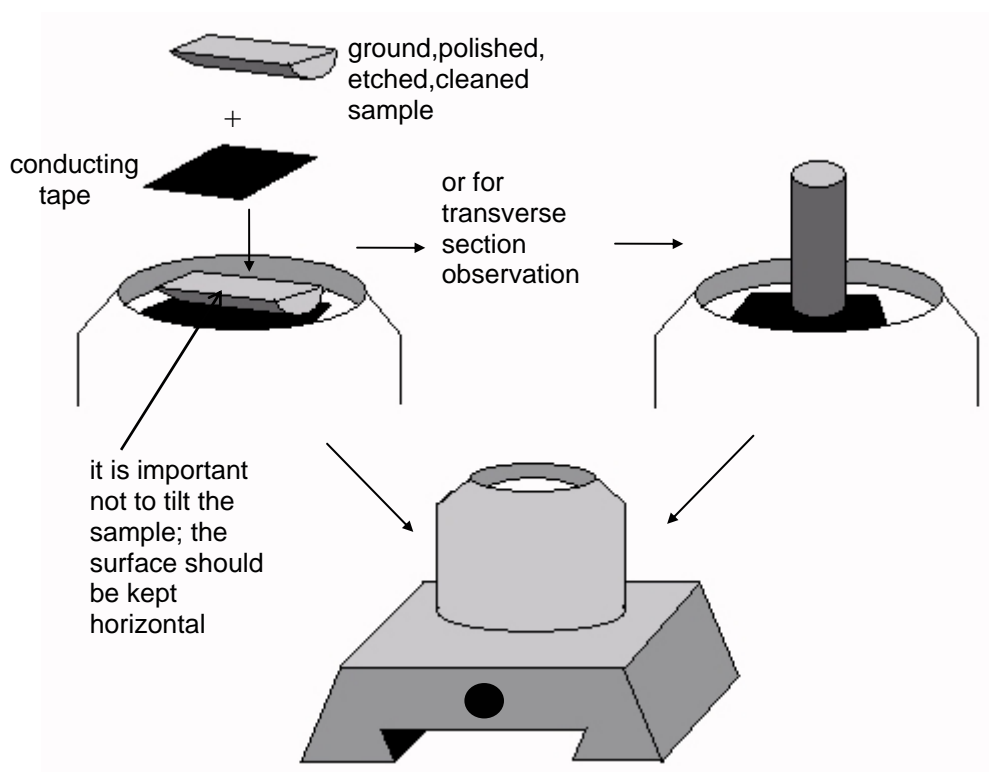


Figure 4.9 The schematic representation of the sample mounting on the SEM sample holder.



4.4.3 Transmission Electron Microscope (TEM)

4.4.3.1 Sample Preparation

The Cu-18%Nb TEM samples were prepared through the *ultramicrotomy process*. The process was conducted at the Diatome Company, Switzerland. The reason for implementing this process was firstly due to the encountered hazardous nature of thinning solution of : 38.5% alcohol C_2H_5OH , 38.5% hydrofluoric acid HF, and 23% nitric acid HNO_3 [5]. This solution was previously used, as a cyclic combination for Tenupol electrolytic thinning, to aid etching away niobium filaments until a hole was attained in a Cu-20%Nb TEM *cold rolled* sample. Such nature of the solution together with the insufficiently fulfilled TEM sample geometry of Cu-18%Nb wires (i.e. some deformed wires were too thin) raised great difficulty in preparing TEM samples through the thinning process.

The ultramicrotomy is a sectioning technique that advances a specimen past a cutting diamond knife to produce a thin section of the material [6]. This technique presents some advantages. The first of them is the possibility to obtain relatively thin sections of uniform thickness [7]. Further, the sectioning process does not affect the chemistry of the sample, i.e. there is no redeposition or preferential etching like in conventional ion beam milling. Thus, ultramicrotomy is suitable for the sample preparation from materials with phases of very distinguished chemistry [8]. In addition, sample preparation by ultramicrotomy can be fast since the optimal cutting parameters have been established for a specific material. The ultramicrotomy sectioning procedure is schematically presented in figure 4.10.

After cutting, the ultra-thin section is picked up using a special loop as the section is floated on a droplet of water (the loop diameter should be greater as the section size). The loop picks up the section through the water surface tension. The loop (together with the section sample) is then brought close to a special grid. Again, the grid will hold to the loop by surface tension. After removal of water with a filter paper, the grid (and the sample) is carefully separated from the loop and ready for TEM analysis. This picking up sequence is illustrated in figure 4.11.

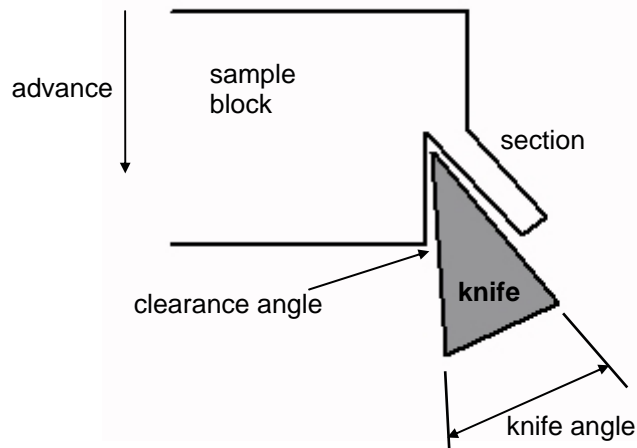


Figure 4.10 The schematic diagram of the ultramicrotomy sectioning process. As the moving samples comes in contact with the edge of diamond knife, the section is cut [7].

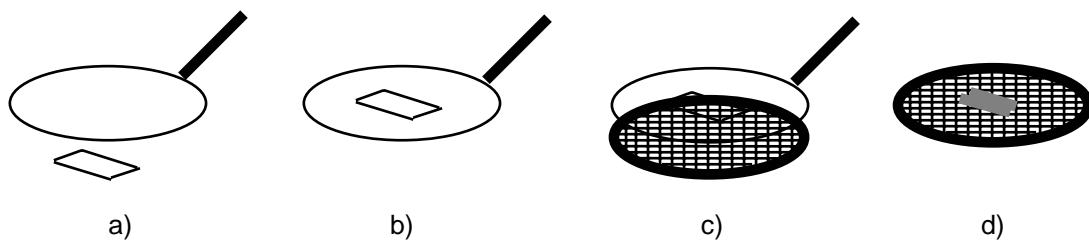


Figure 4.11 a) and b) The on-water floated section is picked up by a loop. c) The loop, with the section in it, is brought close to a special grid. They will stick to each other due to the water surface tension. d) After the removal of water, the grid together with the sample is separated from the loop.

The principles of ultramicrotomy process mentioned in the previous paragraphs were also implemented for Cu-18%Nb wire samples. However, some necessary fore steps took place due to the geometry of wire samples. The complete procedure for Cu-18%Nb samples can be summarized as follow :

- tapering the sample,
- cutting the sample surface with a diamond knife,
- trimming the sample sides with a razor blade,
- cutting with a 35° diamond knife : clearance angle was 8° , section thickness was nominal 40-50 nm, and cutting speed was between 0.40 to 1.00 mm/sec,
- mounting the section on a carbon-layered nickel grid.

It is very important to note that the observed Cu-18%Nb TEM substructures after the ultramicrotomy process come from *the transverse section*.



4.4.3.2 TEM Observations

The Cu-18%Nb samples were examined using the JEM 2000 FX II electron microscope. This TEM features 0.27 nm point resolution and ~10.00 nm lateral resolution. To detect copper and niobium phases, the EDS analyses were performed using the integrated XEDS Noran TN5500. The SADP was utilized to clarify some important phenomena in the TEM substructures, such as : twinning, orientations of copper grains, orientations of niobium filaments.

4.4.4 Measurements of Filament Thickness and Spacing

For the drawn-annealed samples, the measurements of filament thickness and interfilament spacing were performed only on the longitudinal section. Figure 4.12 illustrates the method of measurement with *sampling lines* and the corresponding parameters. In this figure, a filament thickness (D) was measured from one intersection (x) to another within a filament (shaded area), while an interfilament spacing (S) was determined as the distance between two intersections outside a filament. The collected measurement data were then analyzed and fitted for their distribution and average values using the following statistical formulas [9][10]:

$$D_0 = \frac{1}{n} \sum_{i=1}^r m_i n_i \quad \text{Equation 4-3}$$

where :

- D_0 = the average particle thickness
- r = the number of intervals (classes)
- n = the total number of data
- m_i = the median value of i^{th} interval
- n_i = the frequency of m_i

$$\sigma = \sqrt{\left[\frac{1}{n} \sum_{i=1}^r (m_i - D_0)^2 n_i \right]} \quad \text{Equation 4-4}$$

where :

- σ = the standard deviation

$$W(D) = \frac{1}{\sqrt{2\pi\sigma}} \exp\left[-\frac{1}{2}\left(\frac{D-D_0}{\sigma}\right)^2\right] \quad \text{Equation 4-5}$$

where :

$W(D)$ = the probability of the Gauss (Normal) Distribution

D = the particle thickness

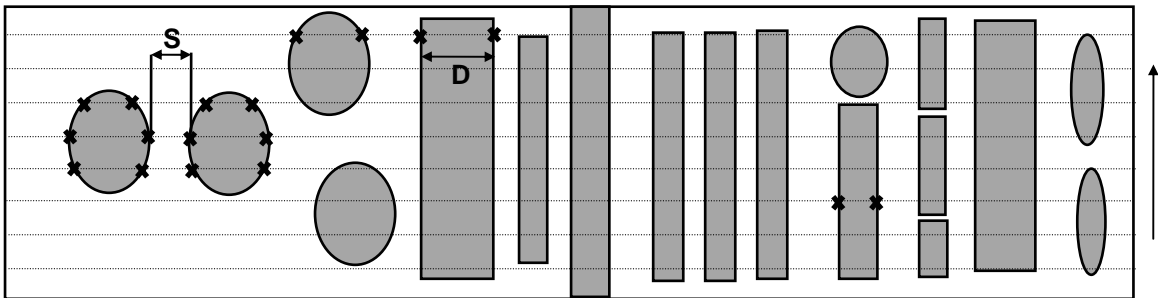


Figure 4.12 The schematic representation of the measurement method to determine average filament thickness and interfilament spacing. The shaded regions illustrate niobium-filaments. The horizontal dashed lines represent sampling lines with constant vertical distance. The vertical arrow indicates the drawing direction. S means interfilament spacing, whereas D is filament thickness.

4.5 Mechanical Tests

4.5.1 Microhardness Test

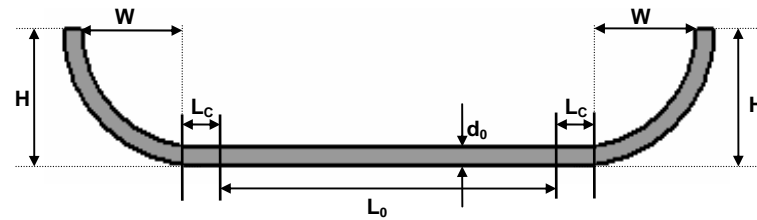
The test was performed on embedded and polished samples. The test was conducted using the DURIMET microhardness tester. The applied load was 200 g and the loading time was approximately 10 seconds.

4.5.2 Tensile Test

4.5.2.1 Sample Preparation

The first important aspect in preparing the tensile test specimen was a suitable sample geometry. Such geometry had to have an appropriate gage length (L_0) and sample ends that could be firmly fitted to the sample holder. Further, the total length of sample could not be too large (especially for the annealed specimens) to ensure a possible homogeneous temperature distribution along the sample length during annealing in the vacuum finger furnace. The implemented sample geometry along with its dimension is illustrated in figure 4.13. Prior to the test, surface of the sample must be clean and scratch-free to minimize the risk of notches. Thus, the sample was uniformly and carefully ground

with SiC papers and rinsed in alcohol using ultrasonic cleaner. The thickness of the sample after grinding was considered as the initial sample diameter, d_0 .



L_0 = the gage length = 25.00 - 30.00 mm
 L_C = the clearance length = 0.50 - 1.00 mm
 d_0 = the initial diameter
 W = 1.50 - 2.00 mm
 H = 3.00 mm

Figure 4.13 The schematic representation of the sample geometry for tensile test.

4.5.2.2 Test Method

The tensile test was conducted on Zwick 1484 test machine. The utilized *load transducer cell* had the maximum capacity (F) of 10.00 kN. The load range (ΔF) for copper samples was pre-adjusted to 0.20 kN, whereas for Cu-18%Nb samples 1.00 kN. The sample elongation was detected by means of an *inductive strain transducer*. The elongation range (ΔL) for drawn copper samples was pre-adjusted to 0.50 mm, while for the annealed samples 2.00 mm. ΔL for drawn and annealed Cu-18%Nb samples was preset to 0.50 mm. Another test parameter was strain rate. The strain rate for copper wire was 2×10^{-3} /sec, whereas that for drawn and annealed Cu-18%Nb ($T = 800^\circ\text{C}$) was 1×10^{-4} /sec. The strain rate for Cu-18%Nb samples annealed at $T = 1000^\circ\text{C}$ was 2×10^{-4} /sec. During the test, data from the load transducer cell and the inductive strain transducer were detected by a computer. These data were then analyzed using POGOWORK 6.7 program. The important elastic-plastic tensile parameters (i.e. : Young's modulus, yield strength, ultimate strength, etc.) could be then determined using this program.

4.6 Cahn-Hilliard Simulation

4.6.1 $\mu = \mu(T)$ and $L = L(T)$ for Copper-Niobium System

The experimentally fitted chemical potential (μ) and the interaction coefficient (L) were implemented to the chemical free energy equation (equation 3-79), that constitutes the Cahn-Hilliard equation (equation 3-76). Unlike in the ideal solution, the chemical



potentials for copper-niobium system do not proceed from a single function. Instead, they come from two separate functions since copper and niobium have two different structures and negligible solid solubility. These two functions have been denoted as *fcc_Cu_A₁* for fcc copper and *bcc-Nb_A₂* for bcc niobium. The interaction coefficient $L = L(T)$ of the system expands only up to L^0 . The utilized functions $\mu = \mu(T)$ and $L = L(T)$ are valid up to $T = 1358$ K.

- *fcc_Cu_A₁* :

The curve of *fcc_Cu_A₁* is a combined function of the *stable* $\mu_{\text{Cu}}^0(T)$, the *unstable* $\mu_{\text{Nb}}^0(T)$, and the interaction coefficient $L_{\text{CuNb}}^0(T)$ between copper and niobium atoms, which are all dependent upon temperature (T). The term $\mu_{\text{Nb}}^0(T)$ indicates an increase in the free energy corresponding to the conversion of the stable bcc arrangement of niobium atoms into an unstable fcc arrangement. According to the thermodynamic data bank by Lee [13], these three functions constituting *fcc_Cu_A₁* are :

$$\begin{aligned} \mu_{\text{Cu}}^0(T) = & -7770.46 + 130.49T - 24.11T \ln(T) \\ & - 2.66 \times 10^{-3} T^2 + 1.29 \times 10^{-7} T^3 + 52478.00 T^{-1} \end{aligned} \quad \text{Equation 4-6}$$

(J / mol)

$$\begin{aligned} \mu_{\text{Nb}}^0(T) = & 13500 + 1.7T + \{-8519.35 + \\ & 142.05T - 26.47T \ln(T) + 2.03 \times 10^{-4} T^2 \\ & - 3.50 \times 10^{-7} T^3 + 93399.00 T^{-1}\} \end{aligned} \quad \text{Equation 4-7}$$

(J / mol)

$$L_{\text{CuNb}}^0 = 45699.84 - 5.23T \quad \text{(J / mol)} \quad \text{Equation 4-8}$$

- *bcc_Nb_A₂* :

The curve of *bcc_Nb_A₂* is a combined function of the *unstable* $\mu_{\text{Cu}}^0(T)$, the *stable* $\mu_{\text{Nb}}^0(T)$, and the interaction coefficient $L_{\text{CuNb}}^0(T)$ between copper and niobium atoms, which are all dependent upon temperature (T). The term $\mu_{\text{Cu}}^0(T)$ indicates an increase in the free energy corresponding to the conversion of the stable fcc arrangement of copper



atoms into an unstable bcc arrangement. According to the thermodynamic data bank by Lee [13], these three functions constituting bcc_Nb_A₂ are :

$$\begin{aligned} \mu_{\text{Cu}}^0(\text{T}) = & 4017 - 1.26\text{T} + \{-7770.46 + \\ & 130.49\text{T} - 24.11\text{T}\ln(\text{T}) - 2.66 \times 10^{-3}\text{T}^2 \\ & + 1.29 \times 10^{-7}\text{T}^3 + 52478.00\text{T}^{-1}\} \end{aligned} \quad \text{Equation 4-9}$$

(J/mol)

$$\begin{aligned} \mu_{\text{Nb}}^0(\text{T}) = & -8519.35 + 142.05\text{T} - 26.47\text{T}\ln(\text{T}) \\ & + 2.03 \times 10^{-4}\text{T}^2 - 3.50 \times 10^{-7}\text{T}^3 + 93399.00\text{T}^{-1} \end{aligned} \quad \text{Equation 4-10}$$

(J/mol)

$$L_{\text{CuNb}}^0 = 49480.18 - 5.23\text{T} \quad (\text{J/mol}) \quad \text{Equation 4-11}$$

From equations 4-6 to 4-11, one can notice that :

- the term in curled bracket in the equation 4-7 is actually the stable $\mu_{\text{Nb}}^0(\text{T})$ from the equation 4-10;
- the term in curled bracket in the equation 4-9 is actually the stable $\mu_{\text{Cu}}^0(\text{T})$ from the equation 4-6, and
- the term $L_{\text{CuNb}}^0(\text{T})$ of fcc_Cu_A₁ (equation 4-8) is not necessarily the same as $L_{\text{CuNb}}^0(\text{T})$ of bcc_Nb_A₂ (equation 4-11).

4.6.2 Other Necessary Physical Parameters

4.6.2.1 Mobility

The mobility (M) in the C-H equation (equation 3-76) is independent of concentration but varies with temperature. The expression for mobility follows the Nernst-Einstein equation :

$$M(\text{T}) = \frac{D_0 e^{-\frac{Q_0}{RT}}}{RT} V_{\text{molar}} \quad \text{Equation 4-12}$$



where :

$D_0 = 5.13 \times 10^{-4} \text{ m}^2/\text{sec}$ for copper-niobium interdiffusion [14];

$Q_0 = 1.77 \times 10^5 \text{ J/mol}$ for copper-niobium interdiffusion [14];

$R = 8.31 \text{ J/molK}$

T = the absolute temperature

V_{molar} = the molar volume of niobium = $1.08 \times 10^{-5} \text{ m}^3/\text{mol}$

4.6.2.2 Gradient Energy Coefficient

A relation between the gradient energy coefficient (γ) and the interface energy (σ) has been suggested by Cahn and Hilliard [15], according to :

$$\sigma = 2 \cdot \left(\frac{R \cdot T_c \cdot \gamma}{V_{\text{molar}}} \right)^{1/2} \left(\frac{T_c - T}{T_c} \right)^{3/2} \quad \text{Equation 4-13}$$

where :

T_c = the critical temperature = 1080°C

γ = the gradient energy coefficient

R = the gas constant

V_{molar} = the molar volume of niobium

However, the resulted γ from equation 4-13 is only of an approximate value. Despite the nature of its proximity, equation 4-13 has been frequently used. The value of interface energy (σ) is known only in the order of magnitude. It has been suggested that σ of the copper-niobium system can be approximated as 1 J/m^2 . According to Gitt [12], σ can be practically taken as 0.05 J/m^2 for a two dimensional simulation.

4.6.3 Numerical Method for Solution to Cahn-Hilliard Equation

A simple explicit difference scheme in two dimensions on a x-y square grid with the edge length h [11,12] has been used to work out the highly non-linear Cahn-Hilliard differential equation. Periodic boundary conditions was implemented to avoid influence of the system boundaries. The discretized form of the CHE along y-axis (equation 3-76) follows :

$$\frac{c_i^{n+1} - c_i^n}{k} = M \cdot \Delta \left(\frac{\partial f(c_i^n)}{\partial c_i^n} - \gamma \cdot \Delta c_i^n \right) \quad \text{Equation 4-14}$$



where :

i = the spatial coordinate

n = the time discretization

k = the time step, in which $\Delta c_{\max}/c_i$ should be less than or equal to 10^{-4} .

The usual spatial discretization of Δ along y-axis :

$$\Delta y(c_i^n) = \frac{y(c_{i-1}^n) + y(c_{i+1}^n) - 2y(c_i^n)}{h^2}$$

Equation 4-15

The similar condition then holds for x-axis.



References

1. Schulz, L.G. : J. Appl. Phys. **20** (1949) 1030.
2. Bunge, H.J.; and Esling, C. (eds.) : "Quantitative Texture Analysis", DGM Informationsgesellschaft m.b.H. (1986).
3. Dahms, M.; and Bunge, H.J. : J. Appl. Crys. **22** (1989) 439.
4. Dahms, M. : Textures and Microstructures **19** (1992) 169.
5. Hangen, U.D. : Diplomarbeit, Mathematisch-Naturwissenschaftlichen Fakultät, RWTH Aachen-Germany (1994).
6. Phillips, R. : Brit. J. App. Phys. **12** (1961) 554.
7. Barreto, M.P.; Veillette, R.; and L'esperance, G. : Micros. Res. Tech. **31** (1995) 293.
8. Malis, T.F.; and Steele, D. : Mat. Res. Soc. Symp. Proc. **199** (1990) 3.
9. Gottstein, G. : "Physikalische Grundlagen der Materialkunde", Springer-Verlag (1998).
10. Sieber, H.; and Huber, L. : "Mathematische Formeln, Erweiterte Ausgabe E", Ernst Klett-Stuttgart (1980) 27-31.
11. Löchte, L.; and Gottstein, G. : Comput. Mat. Sci. **7** (1996) 115.
12. Gitt, A.F. : Diplomarbeit, Mathematisch-Naturwissenschaftlichen Fakultät, RWTH Aachen-Germany (1997).
13. Lee, B.J. : Private Communication : Thermodynamic Data Base Chemsage, Lehrstuhl für Theoretische Hüttenkunde und Metallurgie der Kernbrennstoffe, RWTH Aachen-Germany.
14. Borukhin, L.M.; and Shpichinetskii, E.S. : Zavod. Lab. **37** (1971) 1196 [Ind. Lab. (USSR) 37 (1972) 1530].
15. Cahn, J.W.; and Hilliard, J.E. : Acta metall. **28** (1958) 258.



CHAPTER FIVE

RESULTS

Keeping the results together and ordering them according to the outline of Chapter Four will be the objective of this chapter. Long or in-series results are presented in Appendix A to Appendix D.

5.1 Results of Macrotexture Measurement

5.1.1 As-Cast Cu-18%Nb

Figures A1 and A2 of the Appendix A show respectively the rolling direction (RD) inverse pole figures of copper and niobium of the as-cast Cu-18%Nb sample. The low-energy orientation of copper matrix indicates a somewhat high tendency in the $\langle 110 \rangle$ direction and some between $\langle 100 \rangle$ and $\langle 111 \rangle$ directions. In fact, the maximum intensity of 2.39 is located in the $\langle 110 \rangle$ direction. On the contrary, niobium dendrites show their preferred low-energy configurations mostly toward the $\langle 100 \rangle$ direction. The maximum intensity of niobium texture is located near the $\langle 100 \rangle$ direction.

5.1.2 As-Drawn Cu-18%Nb

The RD inverse pole figures of the drawn Cu-18%Nb samples are shown in figures A3 to A10 of the Appendix A. Departing from the orientation in as-cast texture, copper phase in the sample with $\eta = 2.08$ tries to orient into the $\langle 111 \rangle$ direction (figure A3). However, the extent of deformation does not yet allow such fully preferred texture orientation, as indicated by some deviations or scatters in the intensity distribution. As deformation increases, the maximum intensity of copper in the sample with $\eta = 3.01$ decreases and the number of intensity lines have been reduced (figure A5). Further deformation allows the intensity and the number of intensity lines of copper phase in the sample with $\eta = 3.95$ to reincrease (figure A7). Nevertheless, a small deviation in orientation around the $\langle 110 \rangle$ direction occurs. At $\eta = 4.97$, the maximum intensity increases to reach the value of 4.97 (figure A9). The number of intensity lines toward the $\langle 111 \rangle$ direction also increases. Yet, the number of deviation lines appears to be slightly



rising. Notice that the copper maximum intensities of the drawn samples ($\eta = 2.08, 3.01, 3.95$ and 4.97) are all located in the $\langle 111 \rangle$ direction.

The niobium phase in the sample with $\eta = 2.08$ tries to orient itself in the $\langle 110 \rangle$ direction (figure A4). Some deviations of low intensity lines occur, as the deformation is not yet adequate to fully align the niobium dendrites and thus to stamp their texture. As the deformation increases, the niobium maximum intensity in the sample with $\eta = 3.01$ slightly increases (figure A6). Although still present, the deviation lines have changed their orientation. Further deformation to $\eta = 3.95$ leads to a tremendous increase in the maximum intensity and the number of intensity lines toward the $\langle 110 \rangle$ orientation (figure A8). Some low intensity deviations now take place toward the $\langle 100 \rangle$ direction. At the highest deformation observed ($\eta = 4.97$), the intensity attains the value of 7.96 (figure A10). The highly preferred $\langle 110 \rangle$ orientation is maintained. The number of deviation lines have slightly increased. The niobium maximum intensities of the observed drawn samples are located in the $\langle 110 \rangle$ direction.

5.1.3 Drawn-Annealed Cu-18%Nb

The RD inverse pole figures of drawn-annealed samples are listed in figure A11 to figure A54. Despite the presence of low intensity deviation lines, these pole figures generally feature a "consistency" in maintaining a frequent copper orientation in $\langle 111 \rangle$ and $\langle 100 \rangle$ directions. Niobium orientation has also been kept toward the $\langle 110 \rangle$ direction.

5.1.4 Texture Maximum Intensities of Cu-18%Nb

Table 5.1 lists the maximum intensities of the Cu-18%Nb texture samples. In the drawn samples, the intensity of copper firstly decreases from $\eta = 2.08$ to $\eta = 3.01$ and steadily increases afterwards. The intensity of niobium, however, slowly increases from $\eta = 2.08$ to $\eta = 3.01$ and then rapidly rises. In the drawn-annealed samples, the maximum intensities of copper and niobium generally increase with deformation. Some exceptions occur in samples deformed at $\eta = 3.95$ and $\eta = 4.97$ and annealed at $T = 800^\circ\text{C}$. The maximum copper intensity decreases from $\eta = 3.95$ to $\eta = 4.97$, for both $t = 30$ min and 60 min. The niobium maximum intensity increases slightly from $\eta = 3.95$ to $\eta = 4.97$ for $t = 30$ min, and vice versa for $t = 60$ min.



In the drawn-annealed samples, it is also interesting to note the position of copper maximum intensity with respect to deformation. For a given annealing parameter (time and temperature), the copper maximum intensities at $\eta = 2.08$ mostly lie in the $\langle 111 \rangle$ direction (figures A11, A23, A31, A39, and A47). An exception occurs in the sample deformed at $\eta = 2.08$ and annealed at $T = 600^\circ\text{C}$ for 24 hr (figure A17), whose copper maximum intensity occurs in the $\langle 100 \rangle$ direction. At $\eta = 3.01$ and $\eta = 3.95$, the copper maximum intensities are all located in the $\langle 100 \rangle$ direction (figures A13, A15, A19, A21, A25, A27, A33, A35, A41, A43, A49, and A51). At $\eta = 4.97$, the copper maximum intensities go back in the $\langle 111 \rangle$ direction (figures A29, A37, A45, and A53). The niobium maximum intensities of the whole drawn-annealed samples are maintained in the $\langle 110 \rangle$ direction (figures A12, A14, A16, A18, A20, A22, A24, A26, A28, A30, A32, A34, A36, A38, A40, A42, A44, A46, A48, A50, A52, and A54). These characteristics of the maximum intensity position with respect to deformation within drawn-annealed samples are summarized in table 5.2.

| Deformation η | | Maximum Intensity | | | | | | |
|-----------------------|----|-------------------|-------|-------|--------|--------|--------|--------|
| | | As Drawn | 600°C | | 800°C | | 1000°C | |
| | | | 12 hr | 24 hr | 30 min | 60 min | 30 min | 60 min |
| 2.08 | Cu | 3.15 | 1.66 | 1.54 | 2.01 | 1.65 | 1.48 | 1.56 |
| | Nb | 3.45 | 3.95 | 2.81 | 4.10 | 2.81 | 1.98 | 1.68 |
| 3.01 | Cu | 2.14 | 1.98 | 1.85 | 2.69 | 2.03 | 1.86 | 1.84 |
| | Nb | 3.62 | 4.45 | 3.73 | 4.87 | 3.93 | 3.67 | 4.42 |
| 3.95 | Cu | 3.95 | 2.46 | 3.23 | 4.28 | 3.81 | 2.45 | 2.61 |
| | Nb | 7.75 | 7.74 | 8.45 | 9.86 | 11.00 | 7.64 | 8.65 |
| 4.97 | Cu | 4.97 | ... | ... | 3.38 | 3.60 | 5.21 | 4.78 |
| | Nb | 7.96 | ... | ... | 9.94 | 8.53 | 11.80 | 10.70 |

Table 5.1 The macrotecture maximum intensities of the drawn and drawn-annealed Cu-18%Nb samples.



| Deformation η | | Position of Maximum Intensity | | | | | |
|-----------------------|---------|-------------------------------|--------|--------|--------|--------|--------|
| | | 600°C | | 800°C | | 1000°C | |
| | | 12 hr | 24 hr | 30 min | 60 min | 30 min | 60 min |
| 2.08 | copper | <111> | <100>* | <111> | <111> | <111> | <111> |
| | niobium | <110> | <110> | <110> | <110> | <110> | <110> |
| 3.01 | copper | <100> | <100> | <100> | <100> | <100> | <100> |
| | niobium | <110> | <110> | <110> | <110> | <110> | <110> |
| 3.95 | copper | <100> | <100> | <100> | <100> | <100> | <100> |
| | niobium | <110> | <110> | <110> | <110> | <110> | <110> |
| 4.97 | copper | ... | ... | <111> | <111> | <111> | <111> |
| | niobium | ... | ... | <110> | <110> | <110> | <110> |

Table 5.2 The position of maximum intensities with respect to deformation. Asterisk (*) indicates an exception.

5.2 Results of Microstructural Examinations and Analyses

5.2.1 Light Microscope

The results of light microscope are shown in figures B1 to B9 of the Appendix B. The following phenomena are observed :

- The elongated copper grains parallel to drawing axis occur in the drawn sample with $\eta = 3.01$ (figure B1), verifying a deformed structure. Such structure is comparable to that of a provided copper wire, shown in figure 5.1.
- Within the regions of wide interfilament spacing, the recrystallized grains can form and grow relatively free (figures B2, B3, B4, B6a and B6b, B7a and B7b, B8 and B9). The neighboring grains may coalesce with one another to develop a bigger grain. Since the degree of freedom in growth is large, the shape and size of the copper grains appear to be indefinite.
- Within regions of small/narrow interfilament spacing, equiaxed grains are observed (figure B5a). Some deformed grains still coexist with recrystallized grains (figure B5b).
- A very wide and long copper matrix has been observed side by side with tightly arranged niobium filaments in the drawn-annealed sample with $\eta = 4.97$, $T = 800^\circ\text{C}$, and $t = 30$ min (figures B6a,b) and the one with $\eta = 4.97$, $T = 800^\circ\text{C}$, and $t = 60$ min (figures B7a,b). In each sample, it occurs along the longitudinal edge. This extreme situation has been the result of extremely uneven plastic flow during drawing. This wide copper phase is distinguishable from those in figures B2, B3, B4, B8, and B9, in such a

way, that it takes place in a great length (i.e. longer than the length of one light-microscope sample). In fact, the adjoining wires in the texture sample with $\eta = 4.97$, $T = 800^\circ\text{C}$, $t = 30$ min and the one with $\eta = 4.97$, $T = 800^\circ\text{C}$, $t = 60$ min mostly contain such region. For the sake of reliable quantitative measurement data (the average filament thickness and interfilament spacing), the Cu-18%Nb samples for statistical analysis (see section 4.4.4) with $\eta = 4.97$, $T = 800^\circ\text{C}$, $t = 30$ min and the one with $\eta = 4.97$, $T = 800^\circ\text{C}$, $t = 60$ min were selected not to possess this stupendous irregularity.

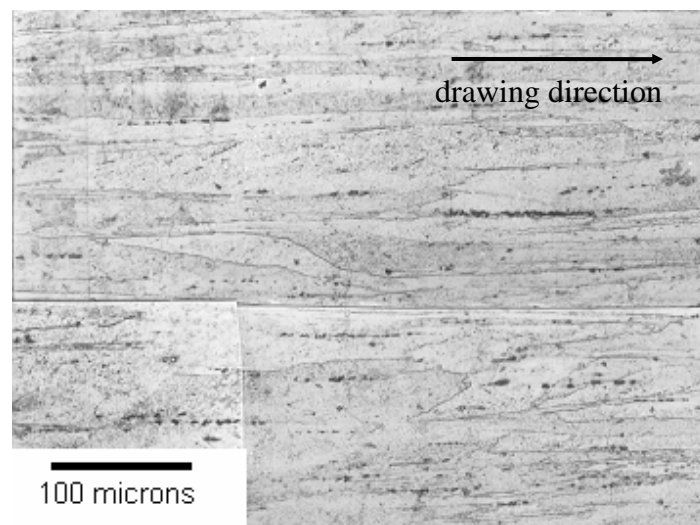


Figure 5.1 The elongated grains in drawn copper wire.

- At the highest deformation observed ($\eta = 4.97$), the recrystallized grains in annealed samples ($T = 800^\circ\text{C}$) still coexist with deformed grains (figures B6a and B7a). Many traces of material flow (see Chapter 3 : figure 3.1b) are here obvious, as shown by figures B6b and B7b. Such traces completely vanish with increasing annealing temperature and time, as shown by the drawn-annealed Cu-18%Nb sample with $\eta = 4.97$, $T = 1000^\circ\text{C}$, $t = 12$ hr (figure B8) and the one with $\eta = 4.97$, $T = 1000^\circ\text{C}$, $t = 24$ hr (figure B9). Here the grain size of the latter sample has grown approximately double from that of the former sample. In these two samples, some annealing twinings have also been observed (figures B8 and B9).



5.2.2 Scanning Electron Microscope

Figure B10 to figure B36 of the Appendix B show the results of SEM observation. To assist understanding the obtained results, a good review of the thermal instabilities of inclusion in figure 3.11 and figure 3.12 of Chapter Three is necessary. By solely looking at these SEM results, the following tendencies concerning the instabilities of niobium filaments are observed :

- Albeit the presence of non-homogeneous deformation in the filaments, the filament thickness and the interfilament spacing of drawn samples generally decrease with increasing deformation (figures B10, B17, B24, and B31).
- The filament thickening due to the interplate diffusion occurs more strongly in the wires annealed in the salt bath furnace than that in the vacuum furnace (figures B11, B18, and B25).
- For samples with $\eta = 2.08$, 3.01, and 3.95 and annealed at $T = 800^\circ\text{C}$ in the vacuum furnace, the thermal instabilities of niobium filament have been characterized exclusively by : filament thickening and sphere dropping (figures B12, B13, B19, B20, B26, and B27). This situation is also valid for the sample with $\eta = 2.08$, $T = 1000^\circ\text{C}$, $t = 15$ min (figure B14), the one with $\eta = 2.08$, $T = 1000^\circ\text{C}$, $t = 30$ min (figure B15), and the one with $\eta = 2.08$, $T = 1000^\circ\text{C}$, $t = 60$ min (figure B16).
- For samples with $\eta = 4.97$ and annealed at $T = 800^\circ\text{C}$ in the vacuum furnace, additional instability mechanisms appear, i.e. the formation of bamboo structures in thin filaments and some extent of edge spheroidizations in large filaments (figures B32 and B33a-b). The occurrence of filament thickening is somewhat difficult to judge.
- For samples with $\eta = 3.01$ and annealed at $T = 1000^\circ\text{C}$ in the vacuum furnace, the niobium instability has been mainly characterized by : ridge nucleation/sphere dropping, filament thickening, filament recrystallization (development of grain boundaries), bamboo structure, and edge spheroidization (figures B21a-b, B22a-b, and B23a-b).
- For samples with $\eta = 3.95$ and 4.97 and annealed at $T = 1000^\circ\text{C}$, the niobium shape evolution has been mainly characterized by : filament thickening, filament recrystallization (development of grain boundaries), bamboo structure, and edge spheroidization (figures B28a-b, B29a-b, B30a-b, B34a-b, B35a-b, and B36a-b).



5.2.3 Transmission Electron Microscope

The results of Cu-18%Nb TEM observations are shown in figure C1 to figure C48 of the Appendix C. These results come from the *transverse section* of sample wires. It is necessary to possibly distinguish between the observed phenomena as results of sample treatments (i.e. drawing and annealing) and TEM sample preparation (i.e. the ultramicrotomy process). The effects of these two processes may interfere with one another in the TEM results.

5.2.3.1 Drawn Samples

The overviews of niobium filaments in copper matrix of the drawn Cu-18%Nb samples with $\eta = 2.08$ and $\eta = 3.95$ are shown in figure C1 and figure C30 respectively. It is clear that the niobium filaments in the drawn sample with $\eta = 2.08$ are still round and elongated, whereas those in the drawn sample with $\eta = 3.95$ have flattened and slightly curled. The interfilament spacing in the latter sample appears to be smaller than that in the former sample. The structure of niobium in the drawn sample with $\eta = 2.08$ is very fine (figure C2), and its SADP reveals nanocrystalline pattern (figure C3). Twinnings have been observed in a small dynamically recrystallized copper grain (figure C4). The copper deformed microstructure has been characterized by dislocations (figure C7) and twinings (figures C5 and C7). The corresponding SADP of these twinings are shown in figure C6 and figure C8.

In the drawn sample with $\eta = 3.95$, almost no twinings are observed in copper matrix. Dislocations still predominate in copper matrix (figure C31), whereas niobium filaments feature nanocrystalline structure (figures C31 and C32). Copper matrix features elongated grains, as shown by figure C33.

5.2.3.2 Drawn-Annealed Samples

$T = 800^\circ\text{C}$, $t = 60 \text{ sec}$

In the drawn-annealed sample with $\eta = 2.08$, $T = 800^\circ\text{C}$, $t = 60 \text{ sec}$ (salt bath furnace), the equiaxed grains can be readily observed in the copper matrix (figure C9). Solely from the appearance in figure C10, some dislocations in niobium filament have tried to rearrange themselves, so that some areas have more dense dislocations than the others. In fact, there have been some regions in the filament that are free of dislocations. It



may indicate that the filament has experienced some extent of recovery-recrystallization. Nevertheless, niobium filaments in the drawn-annealed sample with $\eta = 2.08$, $T = 800^\circ\text{C}$, $t = 60$ sec still commonly feature fine, nanocrystalline structure (figures C11, C12 and C13).

In the drawn-annealed sample with $\eta = 3.95$, $T = 800^\circ\text{C}$, $t = 60$ sec (salt bath furnace), the niobium filaments keep featuring very fine microstructure (figure C34). Cell structures have been observed in the copper matrix (figure C35). Dislocation forests still coherently exist with these cell structures (figure C36), which indicate some extent of strain hardening in the copper matrix. Further, deformation twinings are also observed in copper matrix (figure C37).

$T = 800^\circ\text{C}$, $t = 30$ min

In the drawn-annealed sample with $\eta = 2.08$, $T = 800^\circ\text{C}$, $t = 30$ min, the niobium filaments have apparently rounder and wider shape (figure C14) than those in the drawn sample with $\eta = 2.08$ (figure C1). This situation verifies that the annealing has declared its effect on the phase instability of the filaments. Nevertheless, the substructure of niobium filament is yet mainly characterized by dislocations and fine microstructure (figure C15). However, some dislocations in the filaments have tried to form cell structure (figure C16). Cell structures and recrystallized grains are now observed in the copper matrix (figure C17 to figure C21). Annealing twinings occur within recrystallized copper grains, as shown in figure C17 and figure C20. Apparently, deformation twinings also take place outside the recrystallization nucleus or grains (figure C21). Figure C22 shows the SADP of these deformation twinings.

The recrystallized copper grains in the drawn-annealed sample with $\eta = 3.95$, $T = 800^\circ\text{C}$, $t = 30$ min are shown in figure C38 to figure C41. Figure C39 shows some adjacent recrystallized grains. The deformation twinings still take place in the copper matrix (figure C42).

$T = 800^\circ\text{C}$, $t = 60$ min

The recovery-recrystallization of copper matrix predominates in the drawn-annealed sample with $\eta = 2.08$, $T = 800^\circ\text{C}$, $t = 60$ min (figures C23 and C24). SADP of



such structure indicates polycrystalline nature (figure C25). Deformation twinings are still present in the copper matrix (figure C26).

Recrystallized copper grains along with cell structures in the drawn-annealed sample with $\eta = 3.95$, $T = 800^\circ\text{C}$, $t = 60$ min are shown in figure C43 to figure C47. Annealing twinings within the recrystallized grains are also observed (figure C43 and figure C46). Again, the deformation twinings in the copper matrix are still present (figure C48).

$T = 1000^\circ\text{C}$, $t = 30$ min

Small and large recrystallized copper grains of the drawn-annealed sample with $\eta = 2.08$, $T = 1000^\circ\text{C}$, $t = 30$ min are shown in figure C27 and figure C28 respectively. The large grain in figure C28 may come from the coalescence of neighboring growing grains, as its SADP shows a polycrystalline nature. Deformation twinings in copper matrix are shown in figure C29.

Concomitant to these observed phenomena in the TEM samples, one should also consider the possible influence of the cutting procedure in ultramicrotomy process. The diamond cutting may introduce some extent of deformation on the sample section. The most obvious effect is the presence of dislocations in the most observed samples, i.e. these dislocations hardly vanish in the drawn-annealed samples. Such dislocations may interfere with already existing dislocations and/or cell structures, causing difficulty in discerning them from one another. The next possible effect of the cutting procedure is apparently the introduction of deformation twinings (figures C21, C26, C29, C37, C42, and C48). It is believed, however, that the deformation twinings in the drawn sample with $\eta = 2.08$ (figures C4 and C5) have been the results of drawing process instead of cutting process.

The dynamically recrystallization twinings of copper grain (figure C4) have their own feature in contrast to the deformation twinning. Unlike these deformation twinings, annealing twinings mostly occur within the recrystallized grains (figures C17, C20, C43, and C46).



5.2.4 Statistical Analyses (Measurement of Filament Thickness and Spacing)

The results of statistical analyses are summarized in tables 5.3a,b. The statistic of the as-cast Cu-18%Nb sample features the highest average filament thickness (D_0) and the broadest data range, indicated by the greatest standard deviation (σ) in table 5.3a. As expected, the D_0 and the interfilament spacing (S) of drawn and drawn-annealed samples decrease as the deformation (η) increases.

Variations occur as the change in D_0 and S of wire samples is related to the annealing time (t), as indicated in table 5.3b. D_0 of the drawn-annealed samples with $\eta = 2.08$ and $\eta = 3.01$ increases with annealing time ($t = 30$ min to $t = 60$ min). D_0 of the sample with $\eta = 3.95$ firstly decreases at $t = 30$ min and then increases again at $t = 60$ min. D_0 of sample with $\eta = 4.97$ decreases with increasing annealing time. Only the interfilament spacing of the samples with $\eta = 2.08$ increases with annealing time. The interfilament spacing of the other samples with $\eta = 3.01$, 3.95 and 4.97 firstly decreases at $t = 30$ min and reincreases at $t = 60$ min.

The normal distributions or $W(D)$ of the Cu-18%Nb samples *fitted to* the Gauss equation (equation 4-5) are presented in figures 5.2 to 5.6. Figure 5.2 clearly shows that the peaks of distribution curves in as-cast and as-drawn samples shift and increase from right to left as η increases. Here the as-cast sample has the broadest data range but the lowest peak probability, whereas the drawn sample with $\eta = 4.97$ has the smallest data range but the highest peak probability. Due to very high standard deviation and extremely low peak probability, the $W(D)$ curve of cast sample appears to be linear in contrast to those of the drawn samples.

As the drawn sample with $\eta = 2.08$ is annealed at $T = 800^\circ\text{C}$ for $t = 30$ min, its filament thickness probability decreases readily but its distribution range broadens (figure 5.3). There is small difference in the distribution curves between the drawn-annealed sample with $\eta = 2.08$, $T = 800^\circ\text{C}$, $t = 30$ min and the one with $\eta = 2.08$, $T = 800^\circ\text{C}$, $t = 60$ min. The filament thickness probability of the latter sample is slightly lower and broader than that of the former sample.

Similar situation occurs for samples deformed at $\eta = 3.01$, as shown in figure 5.4. Here the filament thickness probability of the drawn-annealed sample with $\eta = 3.01$, $T = 800^\circ\text{C}$, $t = 30$ min decreases readily and its distribution range gets broader from that of the drawn sample with $\eta = 3.01$. The drawn-annealed sample with $\eta = 3.01$, $T = 800^\circ\text{C}$,



$t = 60$ min features the lowest probability and the broadest distribution. In contrast to figure 5.3, the difference in distributions in figure 5.4 between the samples with $\eta = 3.01$, $T = 800^\circ\text{C}$, $t = 30$ min and the one with $\eta = 3.01$, $T = 800^\circ\text{C}$, $t = 60$ min is more significant.

The fitted Gauss normal distributions of samples deformed at $\eta = 3.95$ are shown in figure 5.5. A distribution fluctuation takes place in these samples. As the drawn sample with $\eta = 3.95$ is annealed at $T = 800^\circ\text{C}$ for $t = 30$ min, the probability of filament thickness increases but its distribution range narrows. Further isothermal annealing for about $t = 60$ min results in a decrease in the probability but an increase in the distribution range. Nevertheless, the range of drawn-annealed sample with $\eta = 3.95$, $T = 800^\circ\text{C}$, $t = 60$ min does not exceed that of the drawn sample with $\eta = 3.95$.

| η | As-Cast/As-Drawn | | |
|--------|-------------------------|----------------------------|---------------------|
| | D_0 (μm) | σ (μm) | S (μm) |
| 0 | 5.57 | 47.21 | 8.66 |
| 2.08 | 2.54 | 2.39 | 3.93 |
| 3.01 | 1.95 | 2.08 | 2.82 |
| 3.95 | 1.68 | 3.02 | 1.99 |
| 4.97 | 1.03 | 1.36 | 0.64 |

Table 5.3a The results of statistical analyses of as-cast and as-drawn Cu-18%Nb samples.

| η | Annealed at $T = 800^\circ\text{C}$ | | | | | |
|--------|-------------------------------------|----------------------------|---------------------|-------------------------|----------------------------|---------------------|
| | 30 min | | | 60 min | | |
| | D_0 (μm) | σ (μm) | S (μm) | D_0 (μm) | σ (μm) | S (μm) |
| 2.08 | 3.11 | 5.20 | 4.56 | 3.54 | 5.25 | 5.23 |
| 3.01 | 2.13 | 2.39 | 1.45 | 2.45 | 2.87 | 1.93 |
| 3.95 | 1.35 | 1.54 | 0.66 | 2.14 | 2.66 | 1.63 |
| 4.97 | 0.77 | 0.37 | 0.46 | 0.65 | 0.21 | 0.49 |

Table 5.3b The results of statistical analyses of Cu-18%Nb samples annealed at $T = 800^\circ\text{C}$.

Figure 5.6 shows the fitted Gauss normal distributions of samples with $\eta = 4.97$. The drawn sample with $\eta = 4.97$ has the lowest probability but the broadest data range. As it is annealed at $T = 800^\circ\text{C}$ for $t = 30$ min, its probability increases with the narrowing

range. The drawn-annealed sample with $\eta = 4.97$, $T = 800^\circ\text{C}$, $t = 60$ min has the highest probability, but it mostly covers filament thickness less than about $1.5\ \mu\text{m}$.

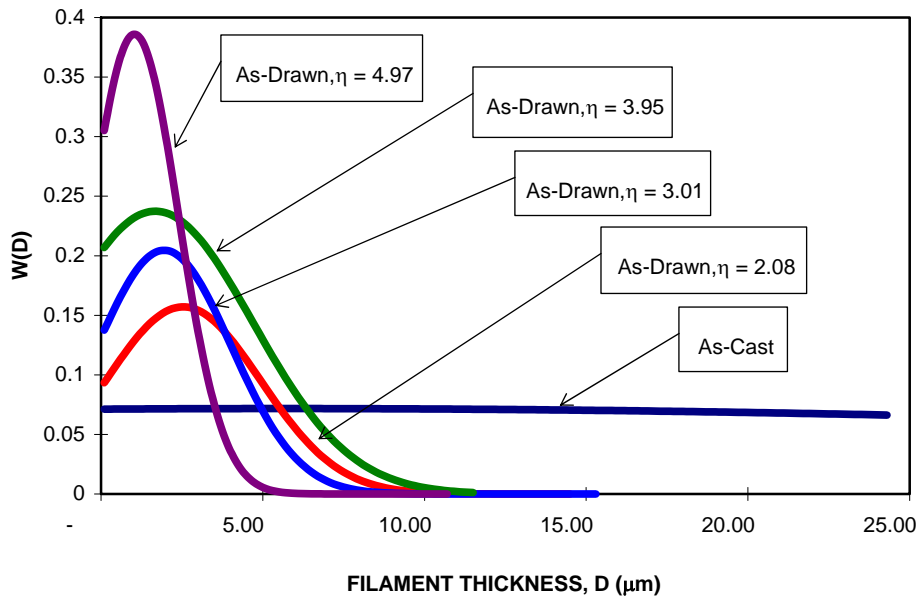


Figure 5.2 The *fitted* Gauss normal distributions of filament thickness in the as-cast and as-drawn Cu-18%Nb samples.

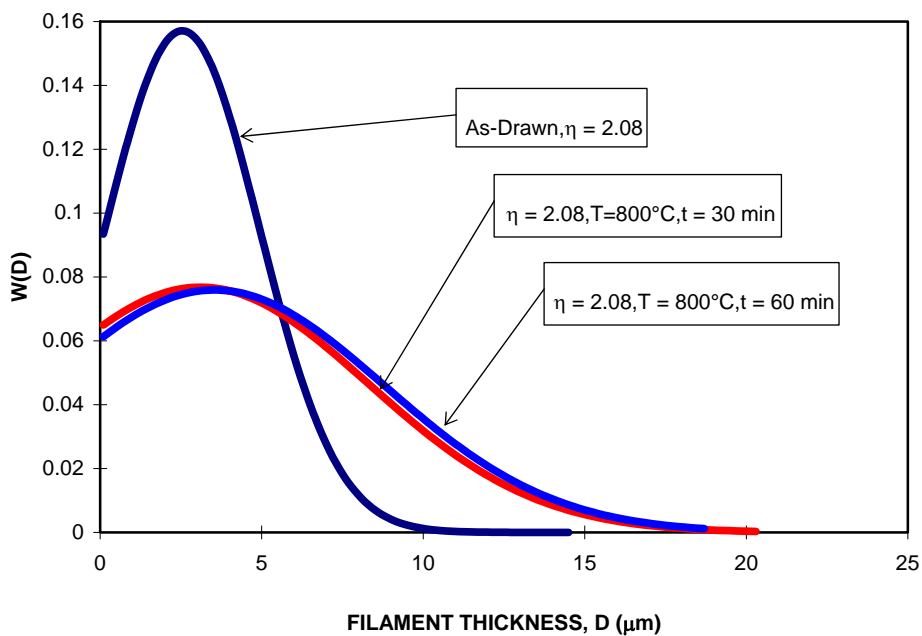


Figure 5.3 The *fitted* Gauss normal distributions of filament thickness in the drawn sample with $\eta = 2.08$; the drawn-annealed sample with $\eta = 2.08$, $T = 800^\circ\text{C}$, $t = 30$ min; and the drawn-annealed sample with $\eta = 2.08$, $T = 800^\circ\text{C}$, $t = 60$ min.

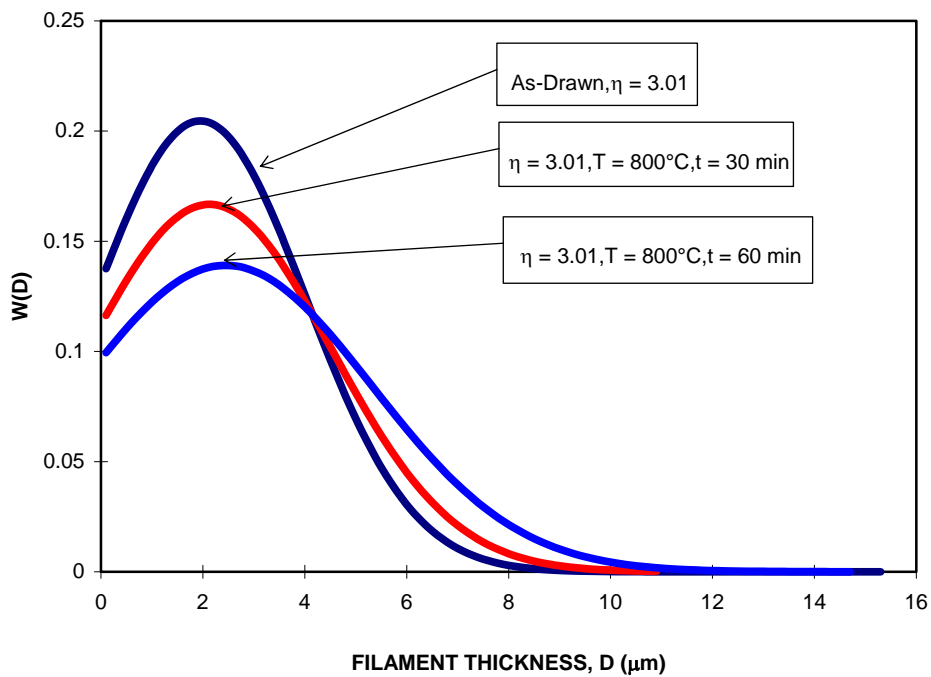


Figure 5.4 The fitted Gauss normal distributions of filament thickness in the drawn sample with $\eta = 3.01$; the drawn-annealed sample with $\eta = 3.01$, $T = 800^\circ\text{C}$, $t = 30$ min; and the drawn-annealed sample with $\eta = 3.01$, $T = 800^\circ\text{C}$, $t = 60$ min.

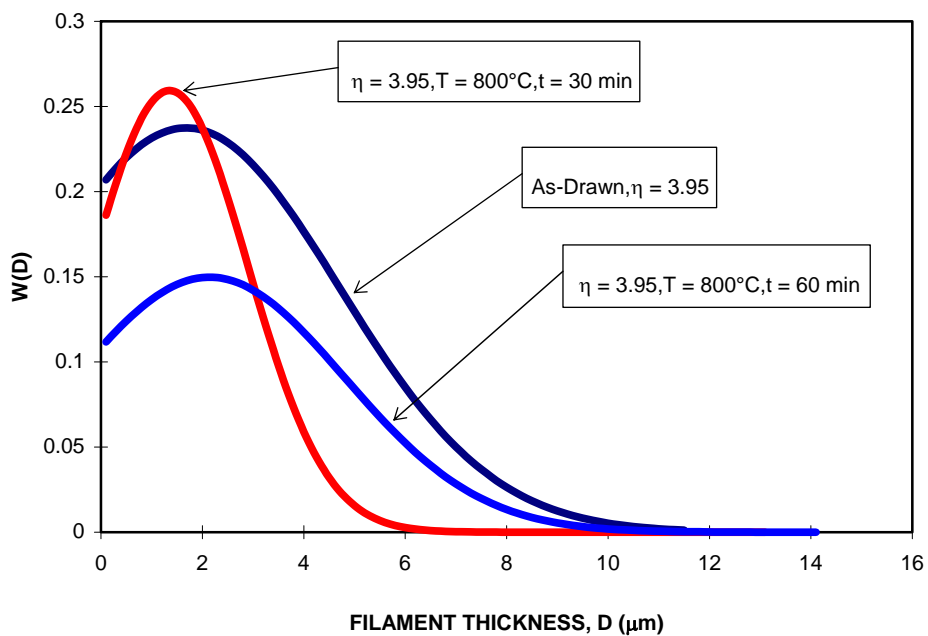


Figure 5.5 The fitted Gauss normal distributions of filament thickness in the drawn sample with $\eta = 3.95$; the drawn-annealed sample with $\eta = 3.95$, $T = 800^\circ\text{C}$, $t = 30$ min; and the drawn-annealed sample with $\eta = 3.95$, $T = 800^\circ\text{C}$, $t = 60$ min.

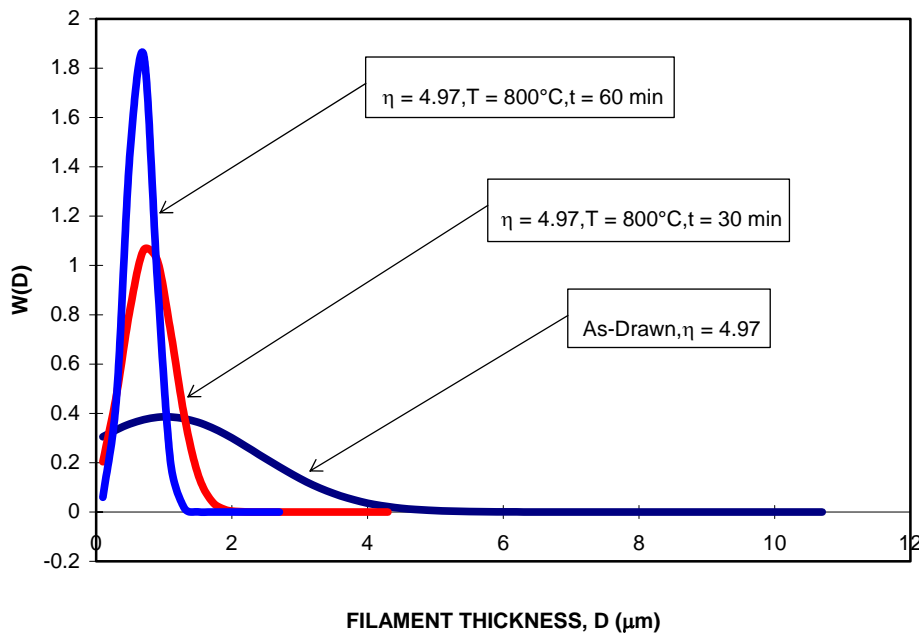


Figure 5.6 The fitted Gauss normal distributions of filament thickness in the drawn sample with $\eta = 4.97$; the drawn-annealed sample with $\eta = 4.97$, $T = 800^{\circ}\text{C}$, $t = 30$ min; and the drawn-annealed sample with $\eta = 4.97$, $T = 800^{\circ}\text{C}$, $t = 60$ min.

5.3 Results of Mechanical Tests

5.3.1 Microhardness Test

Table 5.4 and figure 5.7 show that the hardness values of the *redrawn copper* slowly decrease with increasing deformation. After annealing at 426°C for 60 min, the hardness values become much lower. Further isothermal annealing for about 2 hours yields slightly lower hardness values. A plateau has been observed as the hardness values are directly plotted as a function of annealing time at temperature 426°C (figure 5.8). It indicates that above $t = 60$ min (could be shorter) the copper has completely recrystallized.

| η | As Redrawn | 426°C | |
|--------|------------|-----------------------|-----------|
| | | 60 min | 120 min |
| 2.01 | 120.00 VHN | 54.00 VHN | 52.30 VHN |
| 2.97 | 118.00 VHN | 51.70 VHN | 51.40 VHN |
| 4.03 | 117.00 VHN | 50.50 VHN | 49.90 VHN |
| 4.97 | 117.00 VHN | 48.90 VHN | 47.60 VHN |

Table 5.4 The microhardness values of redrawn and redrawn-annealed copper samples.

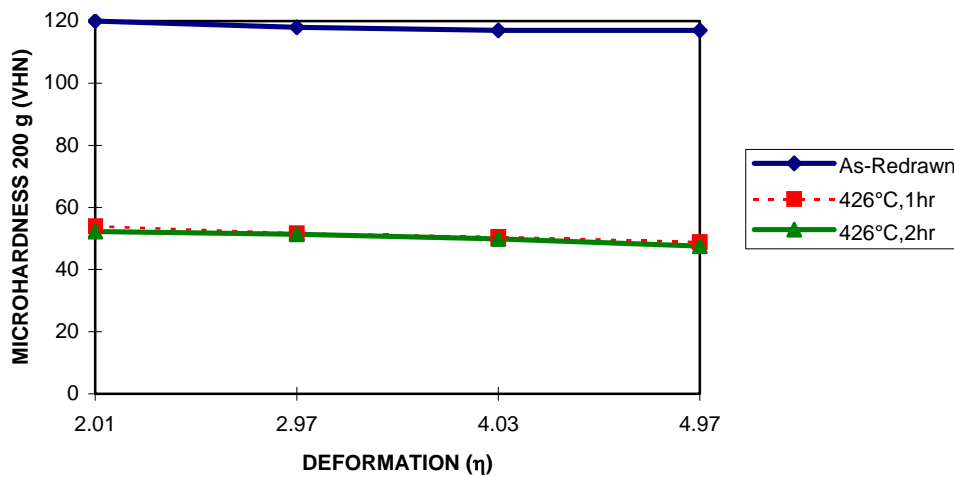


Figure 5.7 The microhardness of redrawn and redrawn-annealed copper samples as a function of deformation.

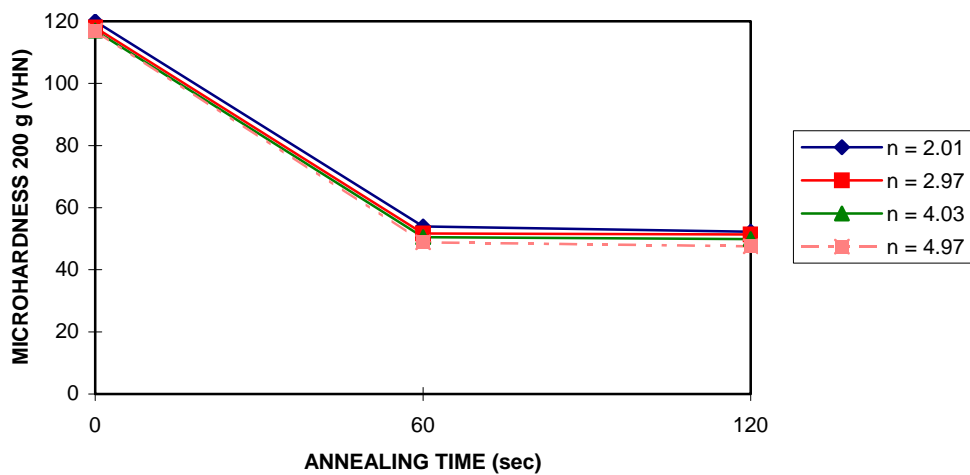


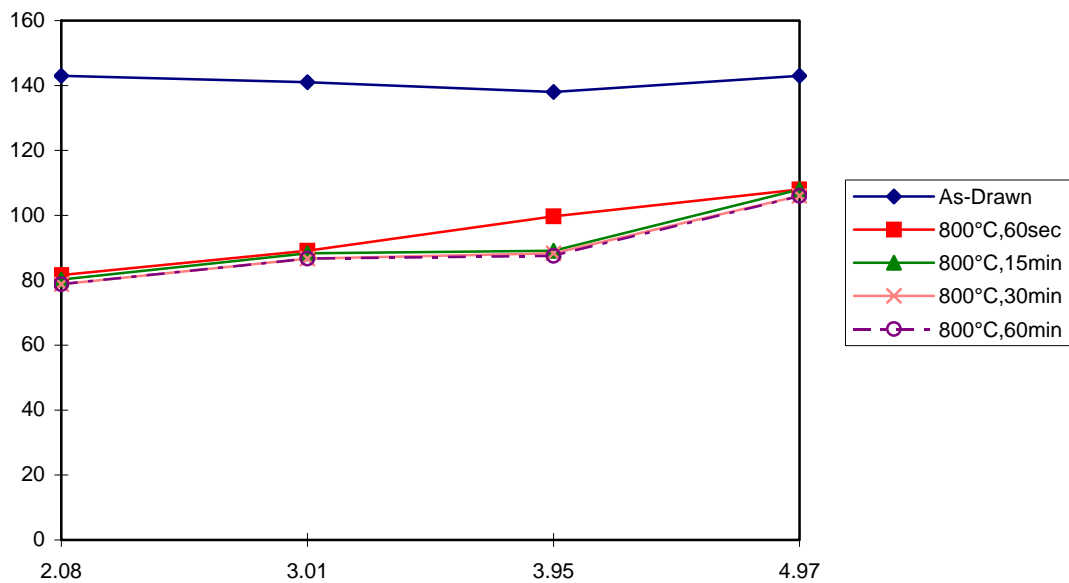
Figure 5.8 The microhardness of redrawn and redrawn-annealed copper samples as a function of annealing time ($T = 426^{\circ}\text{C}$).

The microhardness values of *Cu-18%Nb* samples are listed in table 5.5 and plotted accordingly in figures 5.9 to 5.12. In figure 5.9, the hardness values of drawn samples tend to be constant. After annealing, the hardness increases slowly with deformation (figures 5.9 and 5.11). This finding is in contrast to that of copper wires, whose hardness slowly decreases with increasing deformation (figure 5.7). A plateau in the hardness values for $t \geq 60$, $T = 800^{\circ}\text{C}$ (figure 5.10) or for $t \geq 15$ min, $T = 1000^{\circ}\text{C}$ (figure 5.12) accentuates the recrystallization of copper matrix.



| η | MICROHARDNESS VALUES (VHN) | | | | | | | | | |
|--------|----------------------------|--------|--------|--------|--------|--------|--------|--------|-------|-------|
| | As | 800°C | | | | 1000°C | | | | |
| | Drawn | 60 sec | 15 min | 30 min | 60 min | 15 min | 30 min | 60 min | 12 hr | 24 hr |
| 2.08 | 143.00 | 81.60 | 80.20 | 78.80 | 78.80 | 77.70 | 75.70 | 73.60 | ... | ... |
| 3.01 | 141.00 | 89.10 | 88.30 | 86.70 | 86.70 | 94.30 | 90.60 | 81.20 | 72.50 | 64.00 |
| 3.95 | 138.00 | 99.70 | 89.10 | 88.30 | 87.50 | 94.50 | 94.00 | 91.10 | 88.30 | 83.10 |
| 4.97 | 143.00 | 108.00 | 108.00 | 106.00 | 106.00 | 94.90 | 94.80 | 94.90 | 94.90 | 90.00 |

Table 5.5 The microhardness values of drawn and drawn-annealed Cu-18%Nb samples.

Figure 5.9 The microhardness of drawn and drawn-annealed Cu-18%Nb samples ($T = 800^\circ\text{C}$) as a function of deformation.

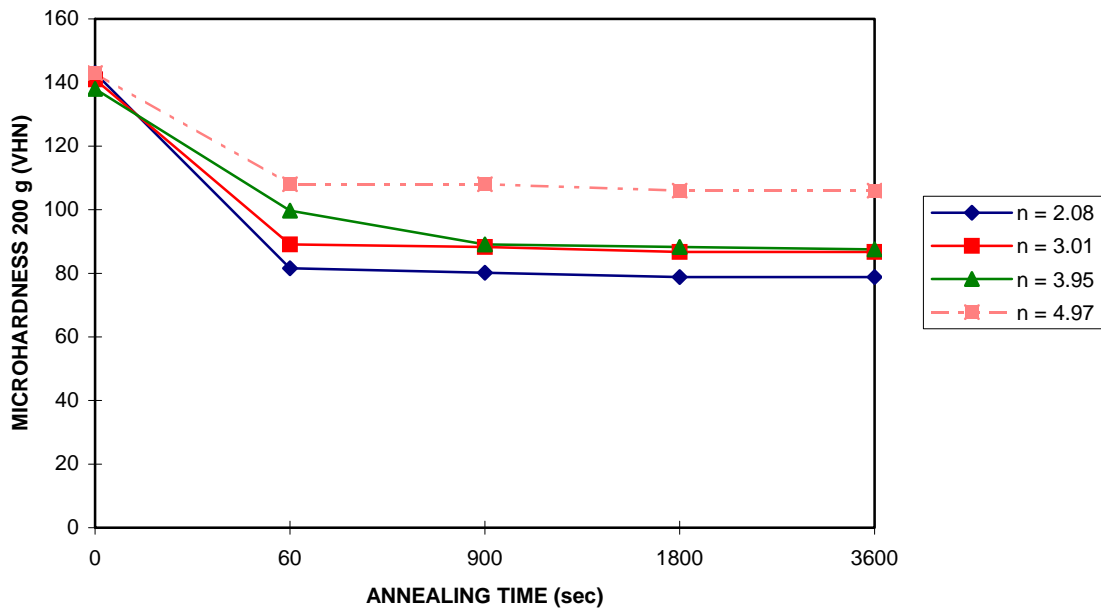


Figure 5.10 The microhardness of drawn and drawn-annealed Cu-18%Nb samples ($T = 800^{\circ}\text{C}$) as a function of annealing time.

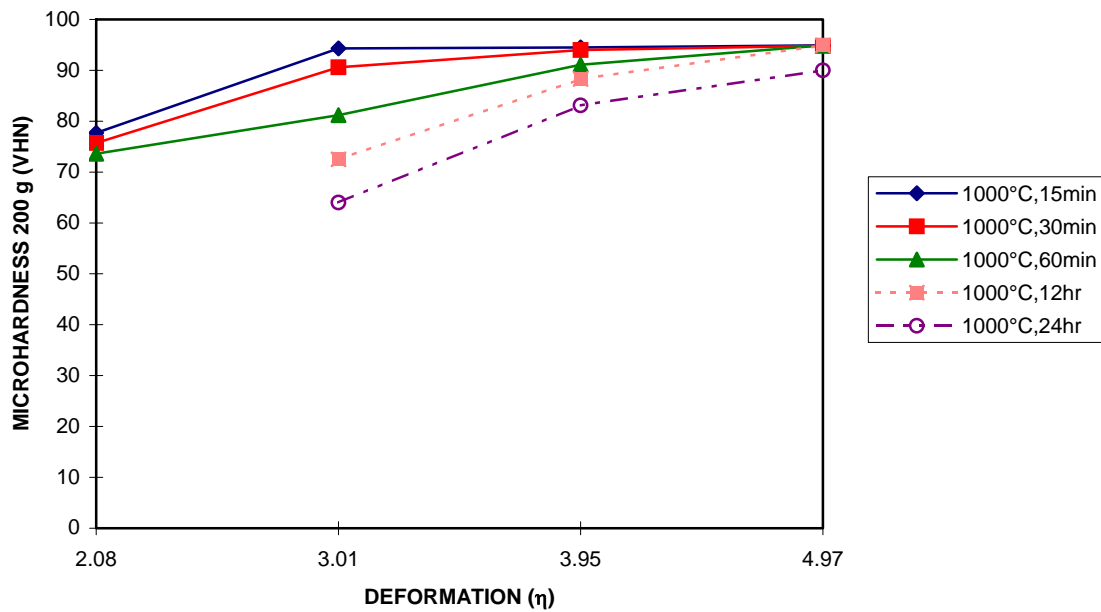


Figure 5.11 The microhardness of drawn-annealed Cu-18%Nb samples ($T = 1000^{\circ}\text{C}$) as a function of deformation.

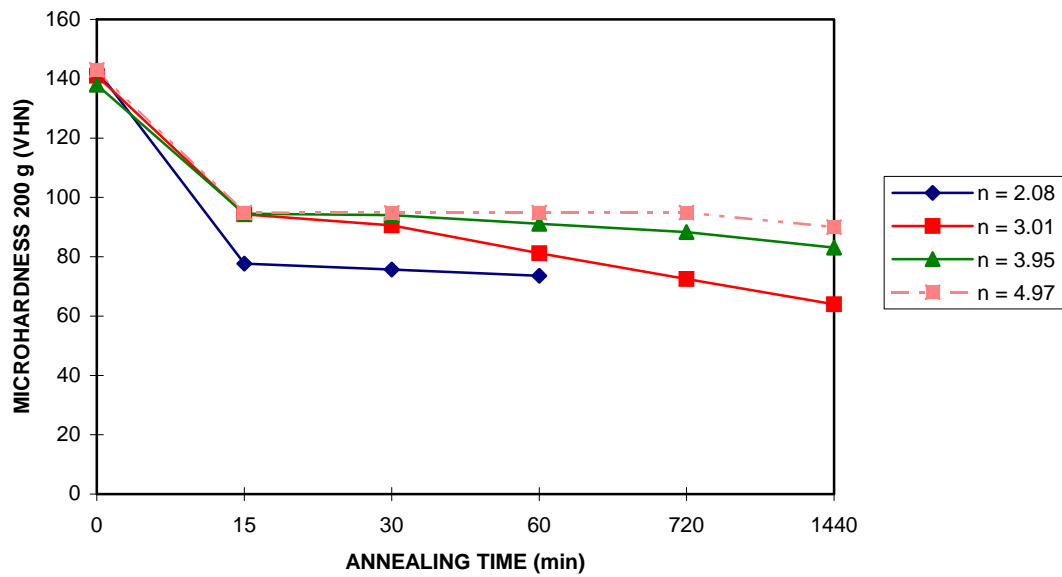


Figure 5.12 The microhardness of drawn and drawn-annealed Cu-18%Nb samples ($T = 1000^{\circ}\text{C}$) as a function of annealing time.

5.3.2 Tensile Test

The *engineering* tensile yield strength ($\sigma_{0.2}$) and ultimate tensile strength (σ_{UTS}) of *copper samples* are given in table 5.6 and figures 5.13 to 5.16. The redrawn copper sample with $\eta = 2.97$ exhibits little plastic deformation, yielding no value of $\sigma_{0.2}$ (table 5.6). The values of $\sigma_{0.2}$ and σ_{UTS} of redrawn and redrawn-annealed copper samples decrease from $\eta = 2.97$ to $\eta = 4.97$ (table 5.6, figure 5.13, and figure 5.14). As a function of annealing time, the values of $\sigma_{0.2}$ and σ_{UTS} of redrawn and redrawn-annealed copper samples decrease steadily from $t = 0$ min to $t = 60$ min (could be shorter) and build plateau afterwards, as shown in table 5.6, figure 5.15, and figure 5.16.

The results of tensile test of *Cu-18%Nb samples* are shown in table 5.7 and figure 5.17 to figure 5.20. Unlike those in copper wires, the engineering values of $\sigma_{0.2}$ and σ_{UTS} of drawn and drawn-annealed Cu-18%Nb samples *mostly* increase slowly with deformation (table 5.7, figure 5.17, and figure 5.18). A slight anomaly has been exhibited by the drawn-annealed sample with $\eta = 4.97$, $T = 800^{\circ}\text{C}$, $t = 30$ min, whose ultimate tensile strength is lower than that of the drawn-annealed sample with $\eta = 3.95$, $T = 800^{\circ}\text{C}$, $t = 30$ min (table 5.7 and figure 5.18). The yield strength and ultimate strength of Cu-18%Nb samples decrease with increasing annealing time, in accordance to the recrystallization of copper matrix (figure 5.19 and figure 5.20).



| Tensile Properties | $\eta = 2.97$ ($\phi = 0.68$ mm) | | | $\eta = 4.03$ ($\phi = 0.40$ mm) | | | $\eta = 4.97$ ($\phi = 0.25$ mm) | | |
|----------------------|-----------------------------------|--------|---------|-----------------------------------|--------|---------|-----------------------------------|--------|---------|
| | As Drawn | 433°C | | As Drawn | 433°C | | As Drawn | 433°C | |
| | | 60 min | 120 min | | 60 min | 120 min | | 60 min | 120 min |
| | | | | | | | | | |
| $\sigma_{0.2}$ (MPa) | N/A | 108.70 | 88.13 | 429.80 | 79.35 | 71.54 | 354.70 | 76.75 | 62.24 |
| σ_{UTS} (MPa) | 438.50 | 229.70 | 224.10 | 435.10 | 224.30 | 229.70 | 363.10 | 215.70 | 210.90 |

Table 5.6 The tensile yield strengths ($\sigma_{0.2}$) and ultimate tensile strengths (σ_{UTS}) of redrawn and redrawn-annealed copper specimens. N/A means no observed yield stress, since the sample features little plastic deformation.

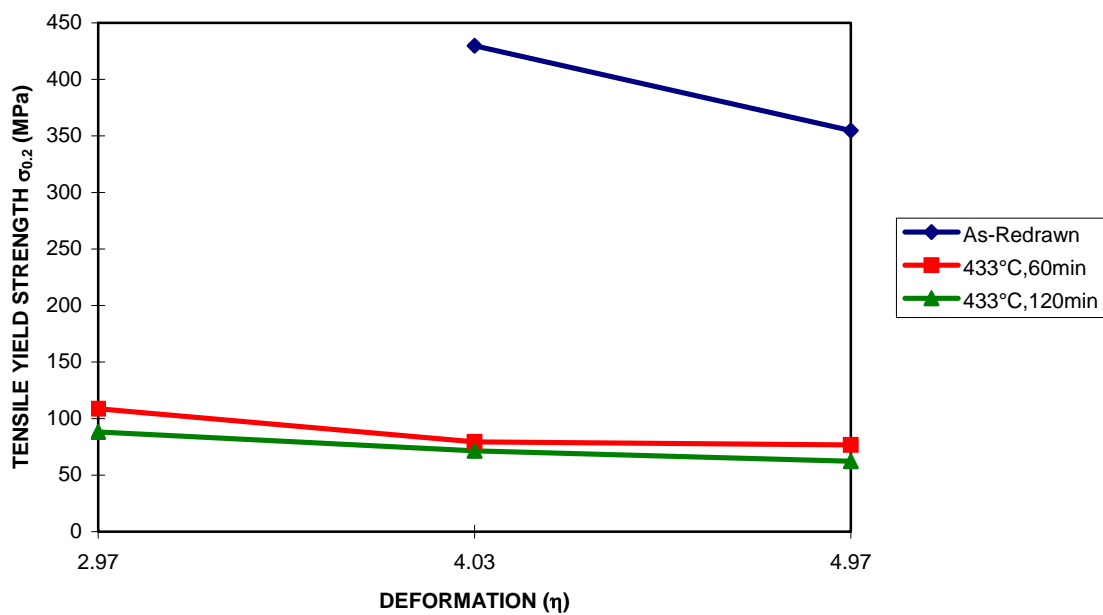


Figure 5.13 The tensile yield strengths of redrawn and redrawn-annealed copper samples ($T = 433^\circ\text{C}$) as a function of deformation.

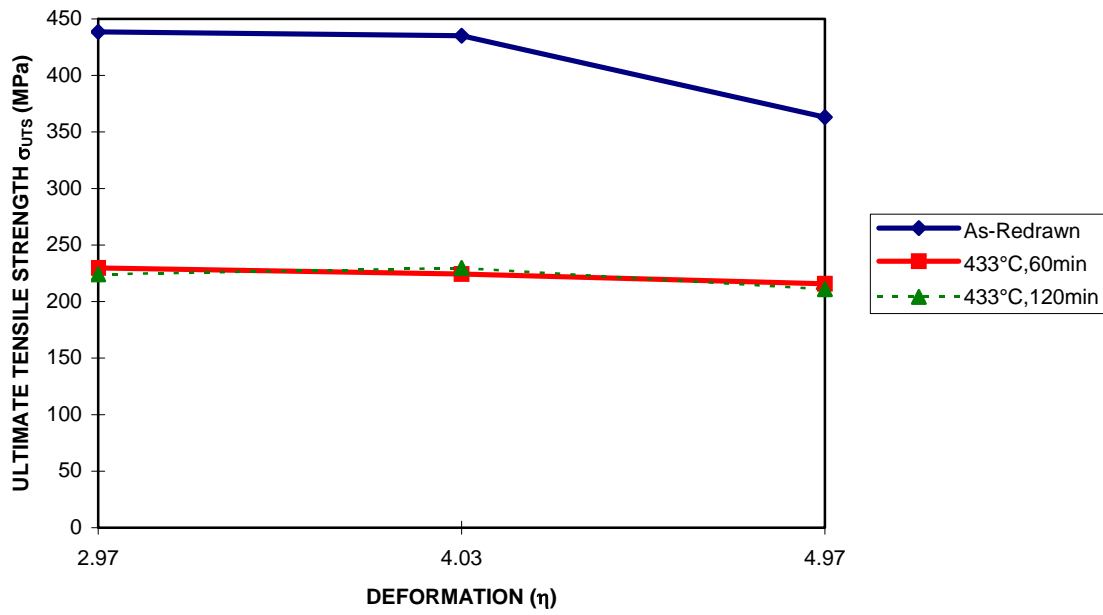


Figure 5.14 The ultimate tensile strengths of redrawn and redrawn-annealed copper samples ($T = 433^{\circ}\text{C}$) as a function of deformation.

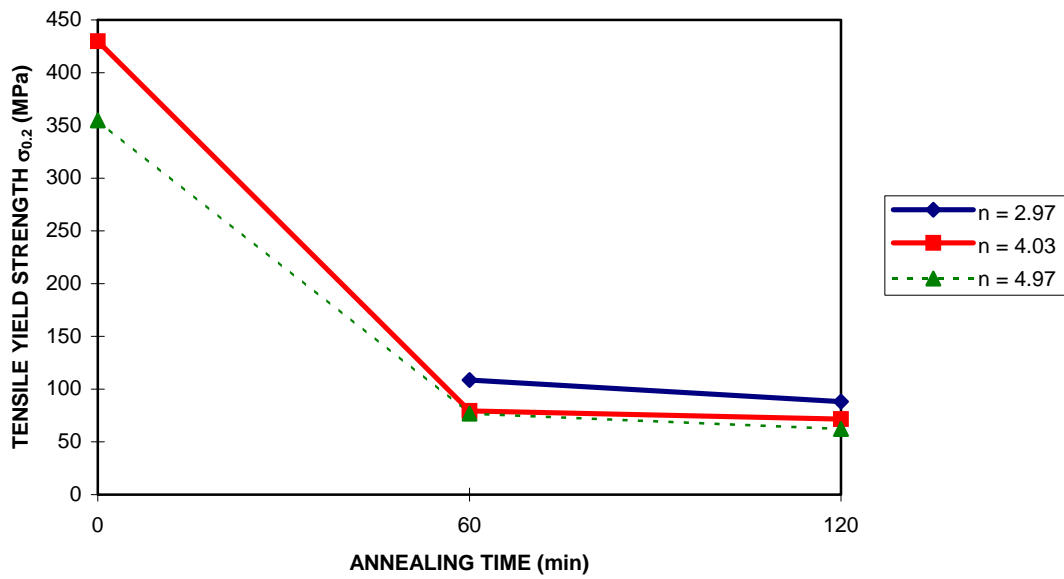


Figure 5.15 The tensile yield strengths of redrawn and redrawn-annealed copper samples ($T = 433^{\circ}\text{C}$) as a function of annealing time.

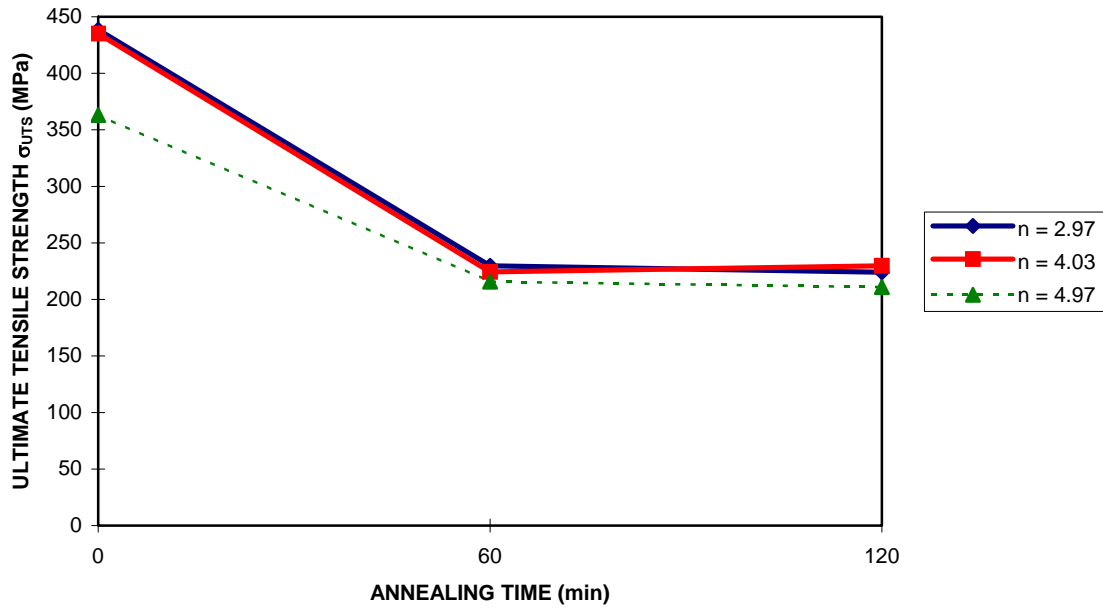


Figure 5.16 The ultimate tensile strengths of redrawn and redrawn-annealed copper samples (T = 433°C) as a function of annealing time.

| Tensile Properties | $\eta = 3.95$ | | | | | $\eta = 4.97$ | | | | |
|----------------------|---------------|--------|--------|--------|--------|---------------|--------|--------|--------|--------|
| | As | 800°C | | 1000°C | | As | 800°C | | 1000°C | |
| | Drawn | 30 min | 60 min | 30 min | 60 min | Drawn | 30 min | 60 min | 30 min | 60 min |
| $\sigma_{0.2}$ (MPa) | 531.11 | 290.51 | 245.85 | 225.99 | 212.43 | 556.40 | 302.98 | 296.90 | 255.17 | 246.52 |
| σ_{UTS} (MPa) | 573.10 | 392.00 | 336.70 | 313.70 | 304.10 | 608.90 | 360.90 | 374.20 | 339.30 | 334.10 |

Table 5.7 The tensile yield strength ($\sigma_{0.2}$) and ultimate tensile strength (σ_{UTS}) of drawn and drawn-annealed Cu-18%Nb samples.

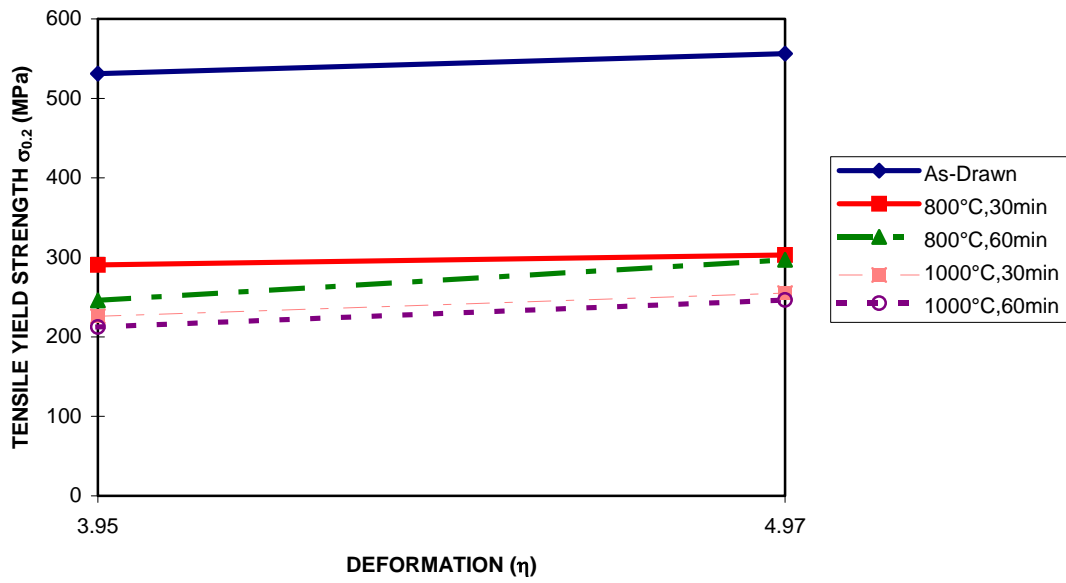


Figure 5.17 The tensile yield strength ($\sigma_{0.2}$) of Cu-18%Nb specimens as a function of deformation.

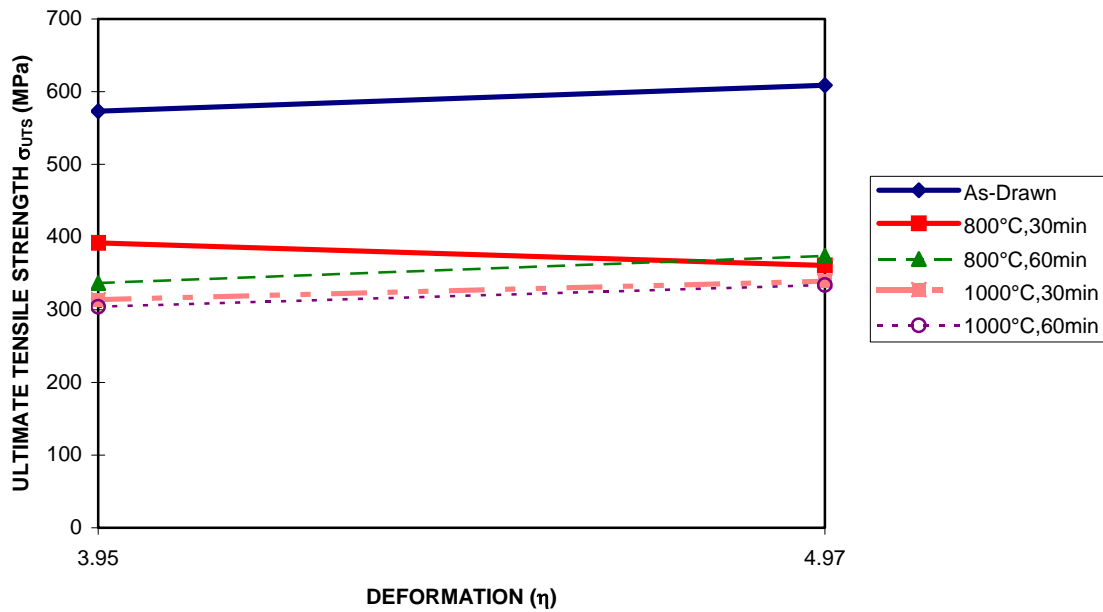


Figure 5.18 The ultimate tensile strength (σ_{UTS}) of Cu-18%Nb samples as a function of deformation.

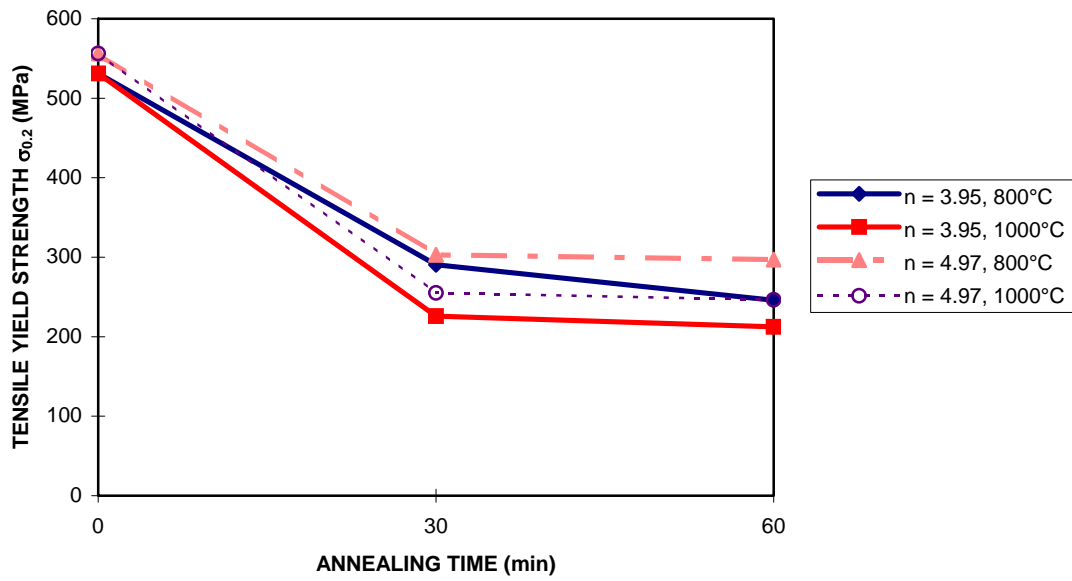


Figure 5.19 The tensile yield strength ($\sigma_{0.2}$) of Cu-18%Nb samples as a function of annealing time.

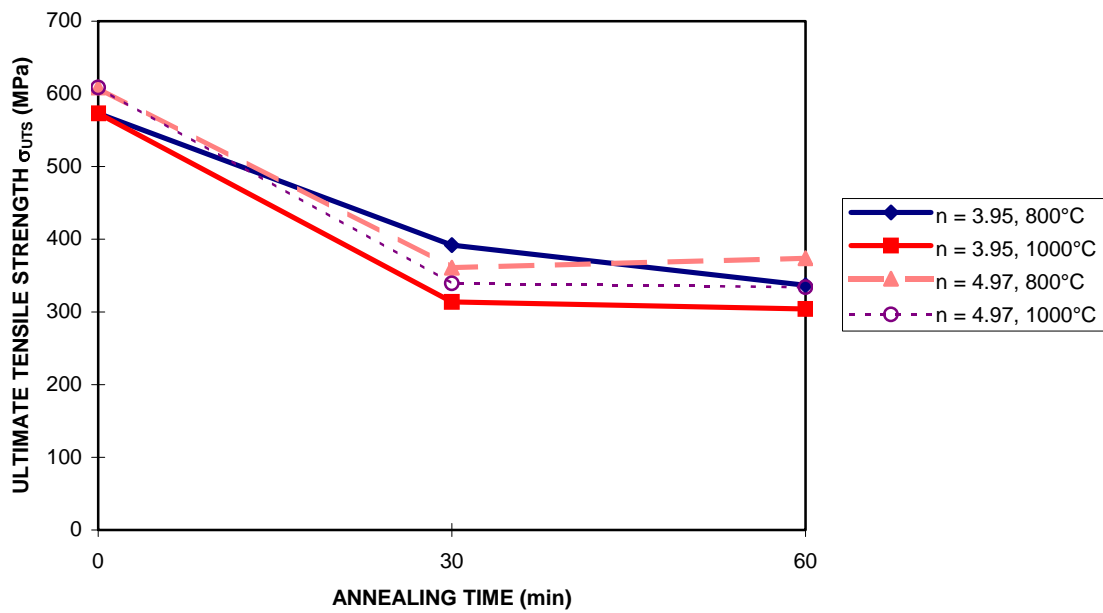


Figure 5.20 The ultimate tensile strength (σ_{UTS}) of Cu-18%Nb samples as a function of annealing time.

5.4 Results of Cahn-Hilliard Simulation

5.4.1 Molar Free Enthalpy Curves of Copper-Niobium System

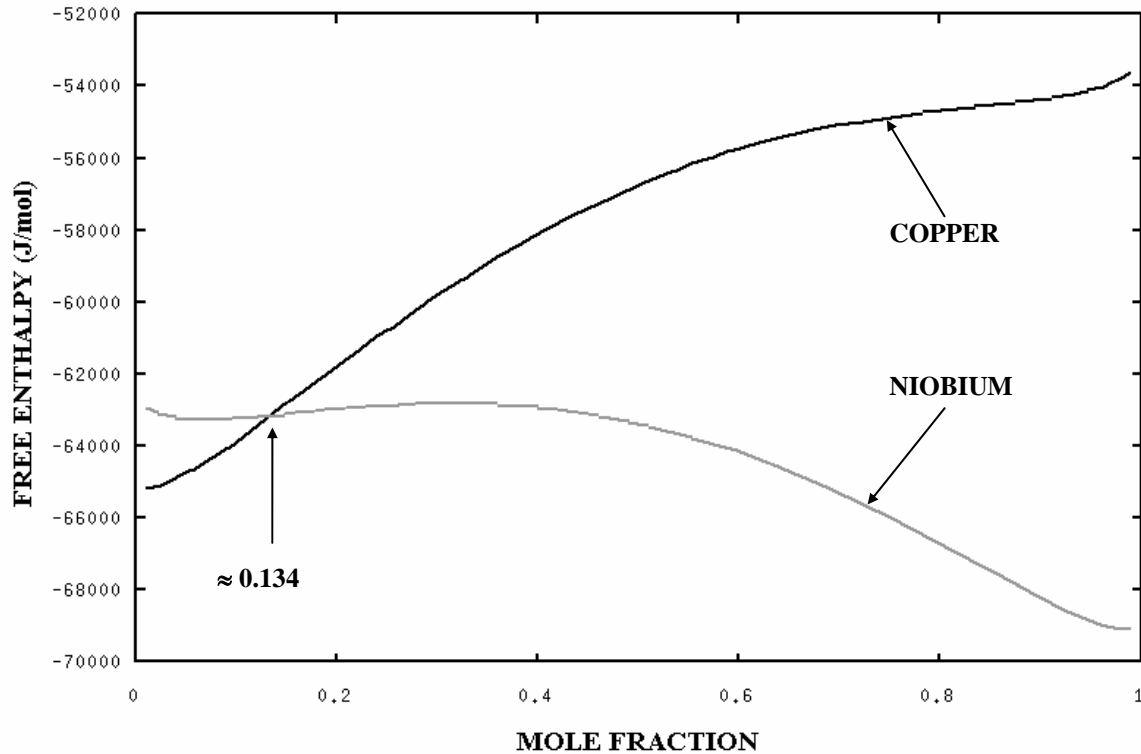


Figure 5.21 The molar free enthalpy curves of copper-niobium system at $T = 1000^{\circ}\text{C}$.

The molar free enthalpy curves of copper-niobium system based on equations 4-6 to 4-11 at $T = 1000^{\circ}\text{C}$ are shown in figure 5.21. There are two distinct curves corresponding to the two phases of copper and niobium having different crystal structure in their pure states at a given temperature. Both curves intersect at $x \approx 0.134$ indicating that, at this mole fraction and $T = 1000^{\circ}\text{C}$, copper and niobium have the same molar free energy. The equilibrium concentrations of copper and niobium based on the common tangent between the two curves are widely apart, i.e. the lowest free energy of copper is on the far left side ($x \approx 0.01$), whereas that of niobium on the far right side ($x \approx 0.99$). Based on these two distinct energy curves, the Cahn-Hilliard simulation program has been modified to include a "switch" that can define when the copper (or the niobium) free energy or chemical potential must be calculated. The simplest step is firstly to use the intersection point of $x \approx 0.134$ as a reference. When $x < 0.134$, the free energy of copper will prevail and vice versa (see figure 5.21). As the temperature changes, however, this intersection point shifts and its value changes (e.g. at $T = 800^{\circ}\text{C}$, $x \approx 0.149$). It means, the



switch part in the main program must be accordingly modified every time the applied temperature changes. The next possible step is to simply use the middle concentration of $x = 0.5$. Thus when $x < 0.5$, the free energy of copper will prevail and vice versa. This reference appears to be more independent from the temperature, practical, and reasonable with respect to the free energy curves, and hence is utilized throughout the simulation.

5.4.2 Simulation of Niobium Precipitation in Copper

The implemented unit of edge length or the spatial grid size (Δx) in this precipitation simulation is 1.0×10^{-4} m. It means for a square grid of 128×128 used in this simulation, its actual dimension would be $1.28 \text{ cm} \times 1.28 \text{ cm}$. For the simulation at $T = 1000^\circ\text{C}$, the influence of two different types of parameters has been observed : (1) the initial concentrations (in mole fraction) of matrix (C_m^0) and precipitate (C_p^0) and (2) the gradient energy coefficient (γ). To avoid the derivation of negative concentration during the calculation process of the Cahn-Hilliard simulation, these initial concentrations are selected outside their very narrow solid solubility range on the far left and the far right sides of the phase diagram. A nucleus of niobium phase has been introduced throughout the precipitation simulation. Two sufficiently large values of γ are utilized, i.e. 100 J/m and 500 J/m . Assuming a linear interpolation, the values of D_0 and Q_0 at $T = 1000^\circ\text{C}$ are those for the copper-niobium interdiffusion at $800^\circ\text{C} < T < 907^\circ\text{C}$ (see section 4.6.2.1). Hence $D_0 = 5.13 \times 10^{-4} \text{ m}^2/\text{sec}$ and $Q_0 = 1.77 \times 10^5 \text{ J/mol}$. Throughout the whole simulation, small perturbations (generated by a random number generator and simulating thermal fluctuations) are induced throughout the grid. The concentration of this perturbation (Δc) is 3.00×10^{-5} (in mole fraction), which is approximately only 3% of the solid solubility of niobium in copper and about 0.26% of the solid solubility of copper in niobium at $T = 1080^\circ\text{C}$. Such small amount of perturbation appears to be practical without yielding a derivation of negative concentration during the numerical calculation of the Cahn-Hilliard simulation.

Figures D1 to D4 of the Appendix D show the results of precipitation simulation for four different combinations of initial concentrations and gradient energy coefficient :

1. $C_m^0 = 0.4$; $C_p^0 = 0.6$; $\gamma = 100 \text{ J/m}$
2. $C_m^0 = 0.4$; $C_p^0 = 0.9$; $\gamma = 100 \text{ J/m}$



3. $C_m^0 = 0.4$; $C_p^0 = 0.6$; $\gamma = 500$ J/m

4. $C_m^0 = 0.4$; $C_p^0 = 0.9$; $\gamma = 500$ J/m

The following phenomena are observed :

- The initial stage of precipitation takes place at about $t = 3000$ sec for $\gamma = 100$ J/m, both for $C_m^0 = 0.4$; $C_p^0 = 0.6$ (figure D1c) and $C_m^0 = 0.4$; $C_p^0 = 0.9$ (figure D2c).
- The initial stage of precipitation takes place at about $t = 9000$ sec for $\gamma = 500$ J/m, both for $C_m^0 = 0.4$; $C_p^0 = 0.6$ (figure D3c) and $C_m^0 = 0.4$; $C_p^0 = 0.9$ (figure D4c).
- The distribution and morphology of precipitates for $\gamma = 100$ J/m appear to be irregular (figures D1e and D2e), whereas those for $\gamma = 500$ J/m are apparently regular and symmetrical (figures D3e and D4e). Moreover, the thickness of precipitate and the interparticle distance for $\gamma = 100$ J/m are generally smaller than those for $\gamma = 500$ J/m.
- The precipitate volume fraction for $\gamma = 500$ J/m is lower than that for $\gamma = 100$ J/m, especially for a given combination of initial matrix and precipitate (nucleus) concentration. Moreover, the resulted precipitate volume fraction increases with increasing initial precipitate concentration. These results have been calculated using the image analysis for $t = 3.00 \times 10^4$ sec (figures D1e, D2e, D3e, and D4e) and listed in table 5.8.
- The morphology of initial nucleus has changed from rectangular to a ridged form.

| Initial Matrix Concentration | Initial Precipitate Concentration | Gradient Energy Coefficient (J/m) | Precipitate Volume Fraction at $t = 3.00 \times 10^4$ sec |
|------------------------------|-----------------------------------|-----------------------------------|---|
| 0.40 | 0.60 | 100 | 30.85% |
| 0.40 | 0.90 | 100 | 32.45% |
| 0.40 | 0.60 | 500 | 28.35% |
| 0.40 | 0.90 | 500 | 29.02% |

Table 5.8 The precipitate volume fraction at $t = 3.00 \times 10^4$ sec as a function of gradient energy coefficient and initial concentrations.

- The concentration profiles parallel to y-axis are shown in figures 5.22 to 5.25.

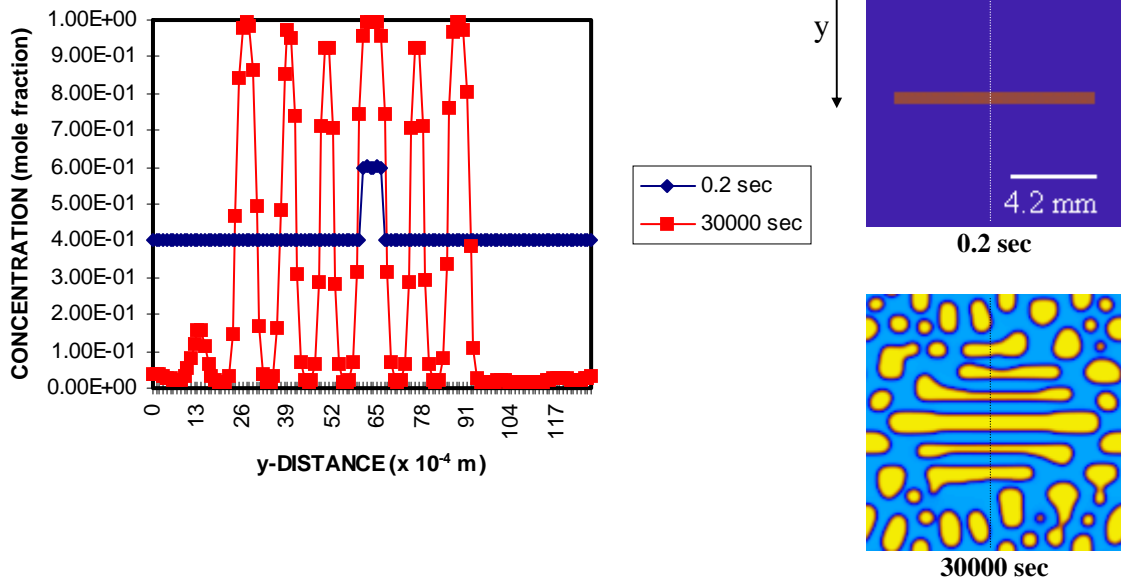


Figure 5.22 The concentration profile parallel to y-axis of the precipitation simulation with $C_m^0 = 0.40$, $C_p^0 = 0.60$, and $\gamma = 100$ J/m taken from figure D1 of Appendix D. Only two simulation states are chosen, i.e. at $t = 0.2$ sec and $t = 30000$ sec. At $t = 0.2$ sec, the concentration profile (left side) shows only one peak corresponding to the one precipitate or nucleus (top right side). At $t = 30000$ sec, the concentration profile features several peaks with various amplitudes. Their distribution with respect to $x = 64$ is non-symmetrical, corresponding to irregular distribution and morphology of precipitates (bottom right side).

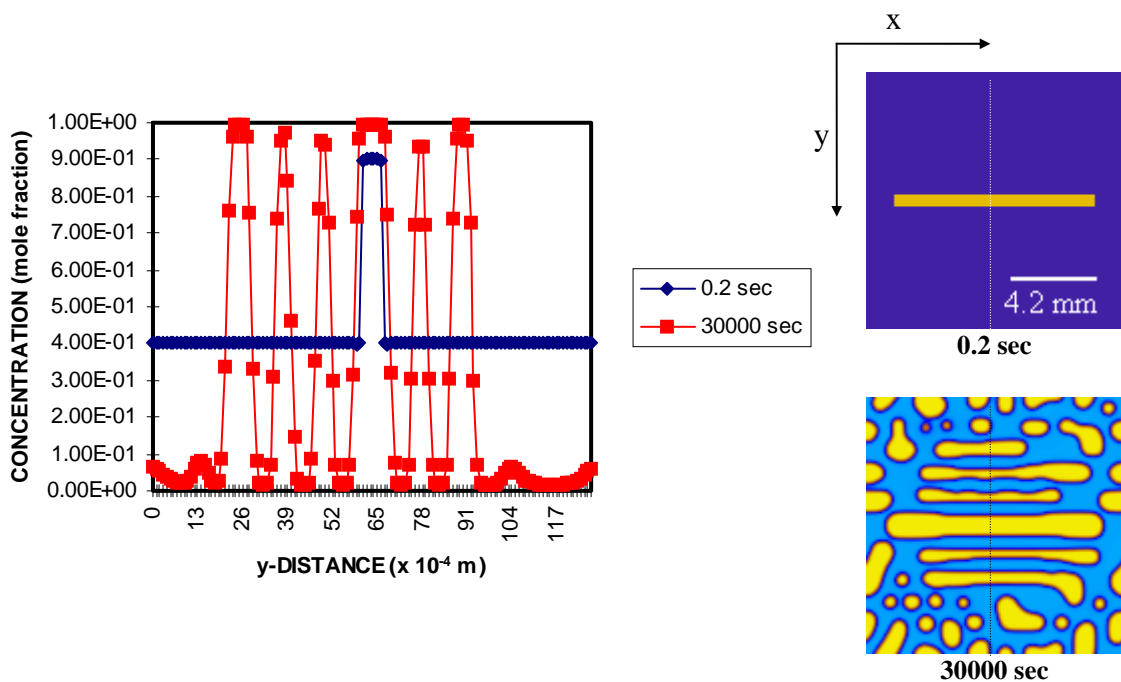


Figure 5.23 The concentration profile parallel to y-axis of the precipitation simulation with $C_m^0 = 0.40$, $C_p^0 = 0.90$, and $\gamma = 100$ J/m taken from figure D2 of Appendix D. Only two simulation states are chosen, i.e. at $t = 0.2$ sec and $t = 30000$ sec. At $t = 0.2$ sec, the concentration profile (left side) shows only one peak corresponding to the one precipitate or nucleus (top right side). At $t = 30000$ sec, the concentration profile features several peaks with various amplitudes. Their distribution with respect to $x = 64$ is non-symmetrical, corresponding to irregular distribution and morphology of precipitates (bottom right side).

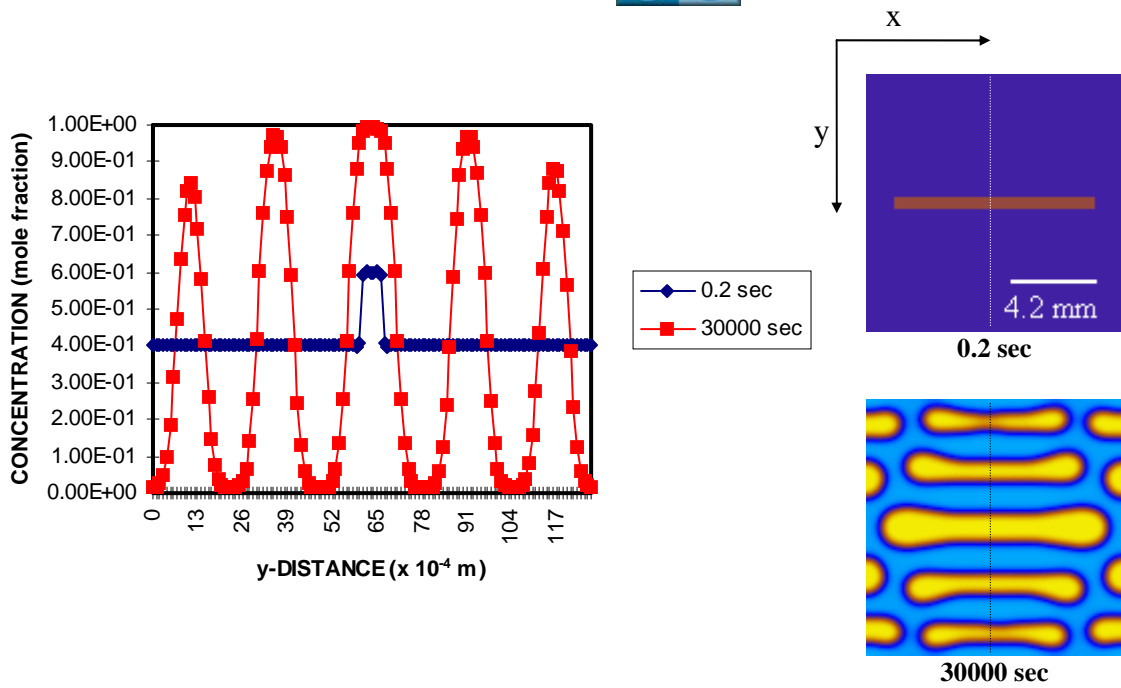


Figure 5.24 The concentration profile parallel to y-axis of the precipitation simulation with $C_m^0 = 0.40$, $C_p^0 = 0.60$, and $\gamma = 500$ J/m taken from figure D3 of Appendix D. Only two simulation states are chosen, i.e. at $t = 0.2$ sec and $t = 30000$ sec. At $t = 0.2$ sec, the concentration profile (left side) shows only one peak corresponding to the one precipitate or nucleus (top right side). At $t = 30000$ sec, the concentration profile features several peaks with slightly varied amplitudes. The distribution with respect to $x = 64$ is symmetrical, corresponding to regular distribution and morphology of precipitates (bottom right side).

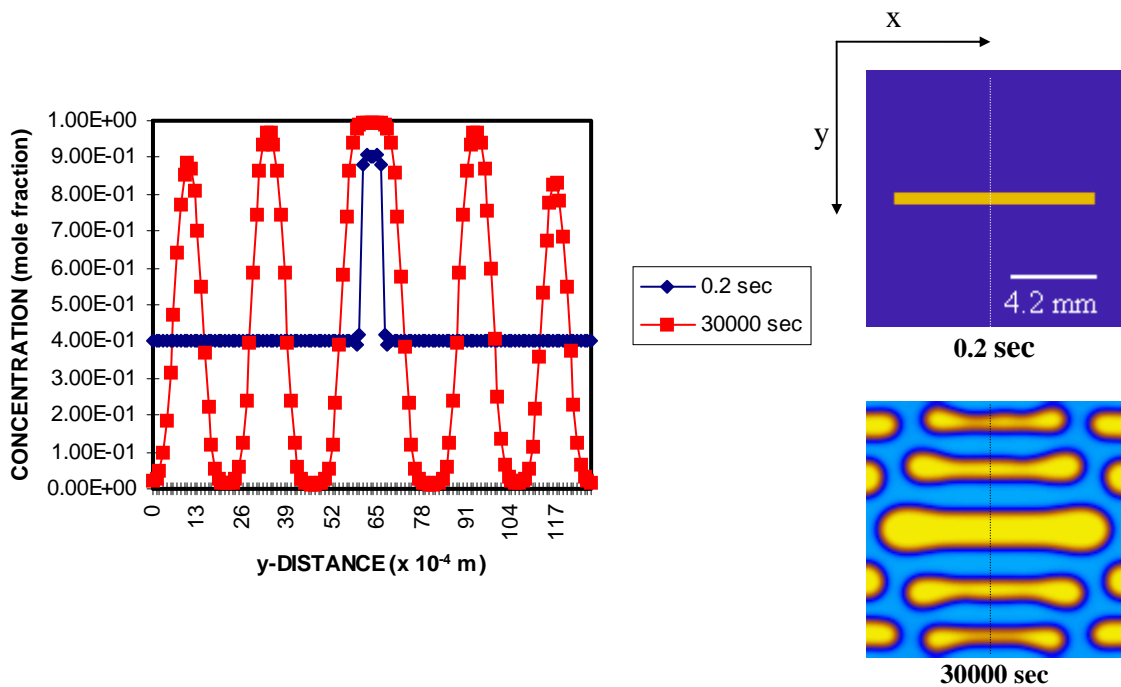


Figure 5.25 The concentration profile parallel to y-axis of the precipitation simulation with $C_m^0 = 0.40$, $C_p^0 = 0.90$, and $\gamma = 500$ J/m taken from figure D4 of Appendix D. Only two simulation states are chosen, i.e. at $t = 0.2$ sec and $t = 30000$ sec. At $t = 0.2$ sec, the concentration profile (left side) shows only one peak corresponding to the one precipitate or nucleus (top right side). At $t = 30000$ sec, the concentration profile features several peaks with slightly varied amplitudes. The distribution with respect to $x = 64$ is symmetrical, corresponding to regular distribution and morphology of precipitates (bottom right side).



5.4.3 Simulation of Niobium Thermal Instability in Copper

Again, the implemented spatial grid size (Δx) is 1.00×10^{-4} m. Lowering Δx can yield the derivation of a negative concentration. On the other hand, increasing Δx can bring the kinetic and the diffusion processes of the instability into much slower state, since the actual mesh area becomes relatively large. By this value of Δx , the kinetic of thermal instability can be carried out more reasonably and close to the experimental results. The simplest parameter to directly observe the effect of such kinetic is the time. In this case, one can compare the provoked thermal instability for a given time of the simulation with that of experiments. Moreover, this value of Δx also works quite well with the low grid dimension. $\Delta x = 1.00 \times 10^{-4}$ m can also give a precipitate dimension, which is comparable to that in reality.

Another parameter that can uphold the kinetic of simulated thermal instability is the mobility (see equation 4-12). By increasing mobility (multiplying it with a numerical factor), one can bring the process of thermal instability several steps faster. Unfortunately, the allowable maximum mobility without inducing a negative concentration is only 10 times higher. Nevertheless, such maximum value has brought a good and reasonable simulation results in this study. The D_0 and Q_0 for the mobility are still 5.13×10^{-4} m²/sec and 1.77×10^5 J/mol respectively (see section 4.6.2.1). The value of Δc for the thermal perturbations is still 3.00×10^{-5} . Lowering Δc gives a negligible influence of thermal fluctuations. Conversely, increasing Δc even only up to 5.00×10^{-5} results in a derivation of negative concentration.

The basic difference between the simulation of niobium precipitation in copper and the simulation of niobium thermal instability in copper is *the initial matrix and precipitate concentrations*. For the thermal instability simulation, both values of C_m^0 and C_p^0 should be around the equilibrium. However, the problem of negative concentration again rises when C_m^0 and C_p^0 are too close to the equilibrium concentrations. It happens since these concentrations of copper and niobium become very close to the narrow solid solubility range on the far left side and far right side of the phase diagram. A good and reasonable compromise without yielding a negative concentration has been found when the value of C_m^0 is 0.03 and C_p^0 is 0.90.



The next step is to determine the value of gradient energy coefficient (γ) as the diffusion path provider. The value of γ can not be too large or too small. However, it has nothing to do with the induced negative concentration. Instead, it is more or less about how strong the diffusion process will be. The low γ (e.g. after calculation using equation 4-13) gives a negligible effect of diffusion. As a result, the expected thermal instability does not occur even after sufficiently long simulation time. Conversely, the very large value of γ can provoke a strong interdiffusion process between copper and niobium. At the end, instead of thermal instability, one finds that the niobium has diffused away into the copper phase leaving no trace of precipitation at all. Moreover, the value of γ also depends on the grid size. Even though $\gamma = 100$ J/m and 500 J/m have worked well with the grid size of 128×128 during the precipitation simulation, they become too strong for the smaller grid dimension. As previously mentioned, the low grid dimension is a perfect match to the spatial grid size of $\Delta x = 1.00 \times 10^{-4}$ m. Combining all necessary parameters to give the reasonable results, one finds that the optimum value of γ for the thermal instability simulation is 70 J/m.

Figures D5 to D19 of the Appendix D show the results of thermal instability of a single niobium precipitate in copper phase as a function of aspect ratio (L/W). The simulation of thermal instability of niobium in copper phase works very well with the low grid (and precipitate) dimensions. Figures D5 to D13, for instance, have originated from the 32×32 grid size. Figures D14 to D17 were from 16×128 grid size, whereas figures D18 and D19 from 16×256 grid size. By such all grid sizes, however, the resulted simulation graphics of niobium phase evolution were relatively small to present or show. Therefore, all the figures of thermal instability simulation have been enlarged two-times. It is simply a matter of picture editing, and not the utilization of higher original grid size. The scale bar, nevertheless, denotes the actual size of the system with respect to the spatial grid size (Δx) of 1.00×10^{-4} m. In these results, the following phenomena are then observed :

- The thermal instability process throughout the simulation has been the ridge nucleation, the sphere dropping, and the Ostwald ripening.
- The single sphere has been produced up to the aspect ratio of 13.00 (figure D11).
- The average size of single sphere for a given time increases slowly with increasing aspect ratio (i.e. increasing length of precipitate). This situation has been quantitatively proven for $t = 6000$ sec. The results are listed in table 5.9 and plotted in figure 5.26.

| L/W | Average Single Sphere Size at $t = 6000 \text{ sec (} \times 10^{-4} \text{ m)}$ | Figure |
|-------|---|--------|
| 6.00 | 5.50 | D5h |
| 8.00 | 5.50 | D6h |
| 9.00 | 7.50 | D7h |
| 10.00 | 7.50 | D8h |
| 11.00 | 8.00 | D9h |
| 12.00 | 8.00 | D10h |
| 13.00 | 9.00 | D11h |

Table 5.9 The average single sphere size at $t = 6000 \text{ sec}$ as a function of aspect ratio.

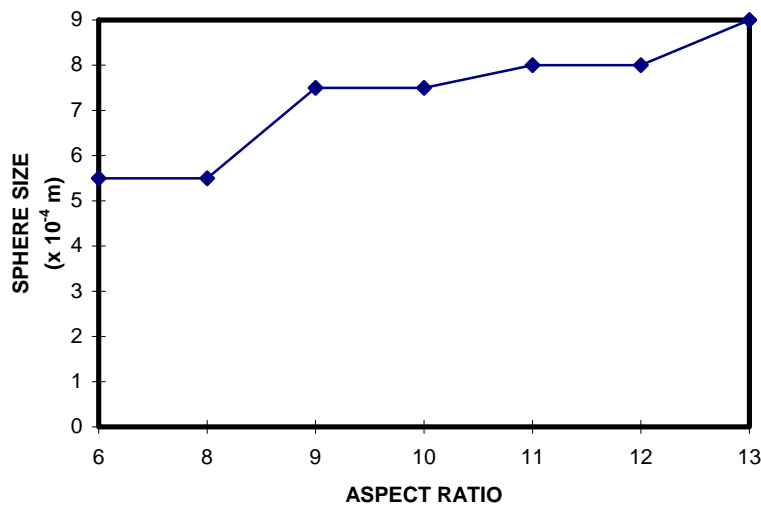


Figure 5.26 Average single sphere size at $t = 6000 \text{ sec}$ as a function of aspect ratio.

- The number of spheres increases with increasing aspect ratio. Moreover, its formation time (i.e. the time in which a sphere or a string of complete spheres firstly develops) gradually shifts to a later stage with increasing aspect ratio. The number of resulted spheres as a function of aspect ratio is listed in table 5.10 and plotted in figure 5.27.
- The annihilation of small sphere (in contrary to the growing large sphere) during the Ostwald ripening mechanism is shown by examples in figure D14 ($L/W = 20.00$) and figure D16 ($L/W = 40.00$). The small middle sphere in figure D14g ($t = 3000 \text{ sec}$) vanishes in figure D14h ($t = 6000 \text{ sec}$). The small middle sphere in figure D16i ($t = 9000 \text{ sec}$) vanishes in figure D16j ($t = 10000 \text{ sec}$). Unfortunately, such situation does not occur at $L/W = 60.00$ (figure D18) and $L/W = 80.00$ (figure D19), when one expects that it will repeat either every 20.00 value or every multiplication factor of two of the aspect ratio.



| L/W | Number of Spheres | L/W | Number of Spheres | L/W | Number of Spheres | L/W | Number of Spheres |
|------|-------------------|-------|-------------------|-------|-------------------|-------|-------------------|
| 6.00 | 1 | 10.00 | 1 | 14.00 | 2 | 40.00 | 5 |
| 7.00 | 1 | 11.00 | 1 | 15.00 | 2 | 50.00 | 6 |
| 8.00 | 1 | 12.00 | 1 | 20.00 | 2 | 70.00 | 7 |
| 9.00 | 1 | 13.00 | 1 | 30.00 | 3 | 80.00 | 9 |

Table 5.10 The number of resulted spheres as a function of aspect ratio.

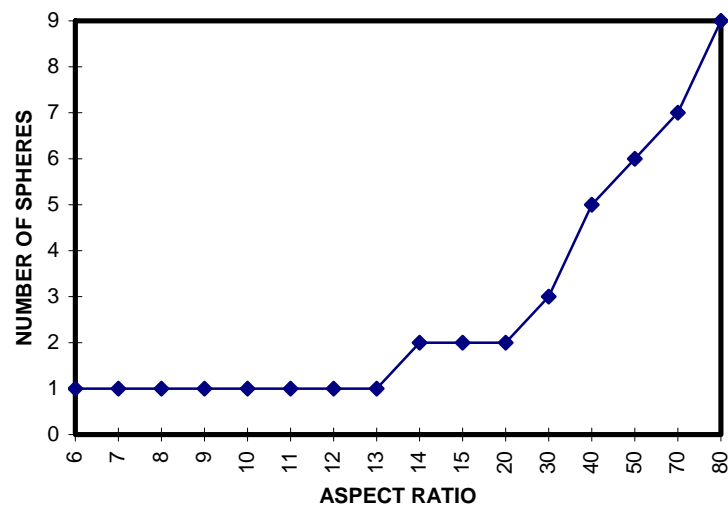


Figure 5.27 The number of resulted spheres as a function of aspect ratio.



CHAPTER SIX

DISCUSSION

Argumentation and discussion regarding the obtained results in Chapter Five and Appendices are elaborated in this chapter. The outline of Chapter Six generally follows that of Chapter Five. Nevertheless, some mutual interactions among results are conceivable.

6.1 Macrotecture

The inverse pole figure of copper matrix in the cast sample (figure A1) shows the orientations towards $\langle 110 \rangle$ direction and some between $\langle 100 \rangle$ and $\langle 111 \rangle$ directions. This finding is in contrast to the texture of copper phase in the as-cast Cu-20%Nb after Raabe et al. [1], shown in figure 2.15a of Chapter Two. Considering no applied directional solidification during the production process, this result accentuates the nature of random orientation distribution of copper matrix in the cast sample. Since the copper and niobium have closely similar values of density (table 2.1), the effect of gravitational force on solidification and thus orientation distribution along longitudinal and transverse directions during production becomes relatively insignificant.

The inverse pole figure of niobium dendrites in the cast sample (figure A2) shows the weak orientations towards $\langle 100 \rangle$ direction. These orientations represent the Goss-texture of $\{hkl\}\langle 100 \rangle$ and are more or less comparable to those of as-cast Cu-20%Nb [2] in figure 2.16a. The cellular microstructure, which is the predecessor of the dendritic structure, is only stable for a certain range of temperature gradients. At adequately low temperature gradients, the cells can develop secondary or even tertiary arms. Simultaneous to such morphological evolution, the direction of dendritic arms can alter away from the direction of heat flow into the crystallographically preferred directions such as $\langle 100 \rangle$ for cubic metals. Such certain crystallographic directions in cubic and hcp metals were experimentally observed by Chalmers [3].

The copper phase in the drawn Cu-18%Nb samples (figures A3, A5, A7 and A9 of the Appendix A) features a $\langle 111 \rangle$ orientation and a weaker $\langle 100 \rangle$ orientation. Nevertheless, these distributions are not yet stable, since some deviations or scatters still



occur. Such dual texture by deformation with axial symmetry has been well-known for pure copper [4]. The difference to the pure copper is that copper phase in copper-niobium system shows the stable formation of strong $\langle 111 \rangle$ and weak $\langle 100 \rangle$ orientations not until high deformation ($\epsilon > 99.5\%$) [5].

The maximum intensity of copper phase firstly decreases at $\eta = 3.01$ and reincreases for $\eta \geq 3.95$ (table 5.1). It indicates that at $\eta = 3.01$ some extent of copper orientations have become randomly distributed. Considering the nature of drawing process, the dynamic recrystallization of the copper matrix may become the responsible mechanism for such phenomenon by increasing the randomly distributed parts or the texture backgrounds. The activation of such recrystallization process comes from the situation, that the samples experience strong heating with decreasing thickness or volume after each drawing pass. The combination of plastic deformation and friction between dies and samples can generate wire temperatures of several hundreds degree centigrade. Dynamic recrystallization is the predominant softening mechanism in the hot working of all fcc metals other than aluminum [6]. The presence of weak copper orientation in $\langle 100 \rangle$ direction in the drawn sample with $\eta = 2.08$ (figure A3), $\eta = 3.01$ (figure A5), $\eta = 3.95$ (figure A7), and $\eta = 4.97$ (figure A9) can be the result of the dynamic recrystallization in the copper matrix.

The gradually decreasing microhardness values of drawn copper samples (figure 5.8) indicate that some extent of dynamic recrystallization process may have taken place already within the corresponding range of deformation. The light microscope observation of the drawn copper sample with $\eta = 4.03$ and the one with $\eta = 4.97$ accentuates the presence of dynamic recrystallization in copper (figures 6.1a,b). In contrast to the structure of provided copper wire (figure 5.1), many small recrystallized but visible copper grains are more extensively shown in figures 6.1a,b at the expense of elongated grains. These dynamically recrystallized grains are naturally more obvious under transmission electron microscope. When these highly dense grains occur in a sufficiently narrow copper matrix (small interfilament spacing) within the Cu-18%Nb sample, they can lead to the difficulty in attaining a good quality microstructure impression after etching under the light microscope.

Presumably, the provided copper wire (figure 5.1) had experienced the process of dynamic recovery followed by the static recovery during drawing. As a result, no dynamic

recrystallized grains have been observed. Such process (dynamic recovery - static recovery) was proposed by McQuenn and Jonas [69] for hot worked material. The other possible processes are dynamic recovery - static recrystallization and dynamic recrystallization - static recrystallization.

As deformation increases, a material experiences cold or strain hardening. With increasing deformation, the dislocations have the possibility (due to high shear stress) to leave their slip plane and to cross-slip [7,8]. In the region of high dislocation density, the dislocations can annihilate or arrange themselves into energetically favorable cell structures according to the Orowan mechanism, known as the dynamic recovery. These cell walls have higher dislocation density than the area surrounded by the walls. With increasing deformation, these cell structures should compete with the existing dynamically recrystallized grains. Pelton et al. [9] have reported that, at the highest deformation observed, the copper phase consisted of cells and recrystallized grains. The dynamic recrystallization may further take place, but not the dominant microstructure process. Despite the presence of these grains, the cells become more elongated and texturized with increasing deformation. In the as-drawn Cu-18%Nb samples, the gradual increase in the copper maximum intensity for $\eta \geq 3.95$ occurs as the copper orientations within these cells try to predominate into $\langle 111 \rangle$ direction, while those into $\langle 100 \rangle$ direction (due to the dynamic recrystallization) stay stable.

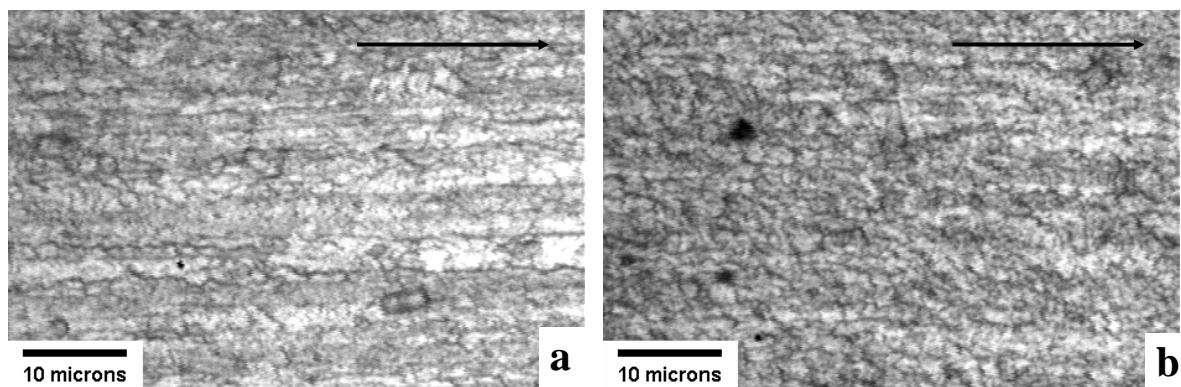


Figure 6.1 The dynamically recrystallized grains in the drawn copper samples with : a) $\eta = 4.03$ and b) $\eta = 4.97$. Arrow indicates the drawing direction.

Niobium phase generally develops the $\langle 100 \rangle$ orientation with increasing deformation (figures A4, A6, A8 and A10). Table 5.1 shows that there is a gradual increase (almost stable) in the niobium intensity from $\eta = 2.08$ to $\eta = 3.01$. Similar phenomenon



also occurs in Cu-20%Nb wire, as observed and discussed by Heringhaus [5] and Raabe et al. [2]. In Cu-20%Nb wire, the niobium intensity decreases from $\eta = 2.60$ to $\eta = 3.60$ and reincreases afterwards. Such situation happens due to a slow or a moderate rotation of niobium crystals from the weak $\langle 100 \rangle$ orientation in as-cast sample towards the stable $\langle 110 \rangle$ orientation during low deformations. Other than the highly dense $\langle 110 \rangle$ direction, the drawn Cu-18%Nb sample with $\eta = 2.08$ also features some other niobium texture components oriented approximately in $\langle 122 \rangle$, $\langle 133 \rangle$, $\langle 123 \rangle$, $\langle 013 \rangle$, and $\langle 012 \rangle$ directions (figure A4). The drawn Cu-18%Nb sample with $\eta = 3.01$ shows the deviated niobium texture components in approximately $\langle 122 \rangle$, $\langle 133 \rangle$, $\langle 112 \rangle$, $\langle 013 \rangle$, and $\langle 012 \rangle$ directions other than the $\langle 110 \rangle$ direction (figure A6). Besides the $\langle 110 \rangle$ direction, the drawn sample with $\eta = 3.95$ (figure A8) and the sample with $\eta = 4.97$ (figure A10) also feature some deviations towards $\langle 013 \rangle$ and $\langle 012 \rangle$ orientations. It then appears that the highly textured $\langle 110 \rangle$ orientation will not be developed completely until sufficiently high deformation.

In Cu-20%Nb wire, this leisure rotation of niobium dendrites has also been underlined by the fact that niobium deforms slower than the wire itself [5]. For instance, when deformation of niobium (η_{Nb}) equals 2, the wire has deformed into $\eta_{\text{wire}} \approx 4$. Further, as η_{Nb} is equal to 5, η_{wire} has reached the value of 8.5. The effect of such rotation in niobium phase within low deformations can also be observed in the microhardness result of Cu-18%Nb (figure 5.9). In figure 5.9, it is obvious that the microhardness values of Cu-18%Nb gradually decrease for $2.08 \leq \eta \leq 3.95$ and reincrease afterwards.

Table 5.1 shows that the copper and niobium intensities of drawn-annealed samples generally increase with deformation. It indicates that, albeit the existence of recrystallized grains or even spheroidized filaments, the strain hardening of materials still has higher effect on the annealed texture. Figure A11 to figure A54 verify that copper is still preferably oriented in the $\langle 111 \rangle$ and $\langle 100 \rangle$ directions, whereas niobium in the $\langle 110 \rangle$ direction. Such situation can be traced back to the behavior of recrystallization nucleation and grain growth in a deformed material after heat treatment.

Primary recrystallization occurs by two principal mechanisms, of which an isolated nucleus expands within a deformed grain or an original high-angle grain boundary migrates into a more highly deformed region of the metal [10]. Assuming that the critical radius ($r_c \approx 2000 \text{ \AA}$ in a strongly deformed material [11]) has been surpassed,



recrystallization nuclei can grow within narrow copper regions (small interfilament spacing). It is highly possible that the so-called *orientation dependency of nuclei* occurs within these narrow regions, and these nuclei are themselves specially oriented with respect to the local deformed matrix.

First considerations of the orientation-dependency of nucleation departs from the situation that the regions of recrystallization nucleation already exist within the deformed structure, where the differences between rolled and recrystallization texture components are interpreted from the local lattice bending with the preferred $\langle 112 \rangle$ rotations [12-16]. Further, the origin of recrystallization nuclei also considers that the nucleation can develop in regions with a high orientation gradient during deformation, e.g. : kink band [17-19]. The critical requirement for nucleation can also be easily fulfilled in regions with a strong non-homogeneous deformation, such as shear band and twinning [20-22]. Nucleation also favors hard particle and precipitation to develop [23]. They introduce obstruction for dislocation motion and thus strongly hinder the flow of surrounding matrix, so that high orientation gradient and dislocation density can build.

As the nuclei begin to grow, the boundaries between the new strain-free grains and the original deformed grains experience a free energy change (due to the difference in dislocation strain energy between the two grains) that drives the atoms across the boundary. Such free energy difference (expressed as $\Delta G/V_{\text{molar}}$) can be thought of as a force pulling the grain boundary towards the grain with the higher free energy [39]. Due to the nature of stamped macrotexture, many deformed copper grains in this small interfilament spacing can also feature low-angle grain boundaries. If it is the case, the grain growth can have a problem with the kinetic instability. Kinetic instability requires that the grain boundary of nucleus must be mobile, which is possibly achieved only by a high-angle grain boundary. The combination of the dynamically recovered structure, the low-angle grain boundary, and the highly preferable $\langle 111 \rangle$ orientation of deformed matrix may provoke *the growth selection of recrystallized grains*.

The presence of growth selection has been frequently observed in cast ingots of many metals and alloys, of which the solidification direction moves toward the center of ingot. In heat treated material, the meaning of growth selection is different. After nucleation, not all grains will grow at the same rate. Those grains having special orientation with respect to the matrix will have boundaries with a higher mobility. These



faster grain boundaries can overgrow the boundaries of randomly oriented grains. In an annealed single crystal metal (i.e. : fcc aluminum), the highest growth rate occurs in the $40^\circ\langle 111 \rangle$ -orientation relationship [24]. In fcc metals with low stacking fault energy (i.e. silver), the $30^\circ\langle 111 \rangle$ -orientation relationship has been favored, despite the development of recrystallization twinning [25]. The growth selection can also be observed in polycrystals, such as in 85% cold rolled Cu-2%Ge [26]. The $40^\circ\langle 111 \rangle$ -orientation, which is well-known for recrystallization of deformed fcc metals, is valid not only for the ideal position or orientation but also for its scatters. These growth selections, likewise, become the reason for the apparently consistent $\langle 111 \rangle$ orientation of recrystallized copper in Cu-18%Nb. In this case, the newly developed recrystallization orientations systematically depend on the deformed texture.

The deviations observed in the copper orientation distribution may result partly from the oriented nucleation in pre-existing deformation twinings (figures C4 and C5) and its subsequent growth, the orientation of resulted annealing twinings (figures B7d, B9, B10, C17, C20, C43, and C46), or the grain growth of pre-existing deformation subgrains (due to the dynamic recovery). In the last case, the crystal orientations of cells may or may not be maintained in the induced recrystallized grains depending on how free the grain boundary moves. The grain boundary movement can be hindered or altered in course by some impurity particles.

The positions of maximum intensity of copper phase in drawn-annealed samples feature a distinct pattern (see table 5.2). At $\eta = 2.08$, the maximum intensity is located in the $\langle 111 \rangle$ direction. At $\eta = 3.01$ and $\eta = 3.95$, it changes its position into the $\langle 100 \rangle$ direction. Finally at $\eta = 4.97$, it goes back to the $\langle 111 \rangle$ direction. Such behavior can be argued from the nature of cube orientation and growth selections. Cube texture $\{001\}\langle 100 \rangle$ has been a common type of recrystallization texture of fcc metals and their alloys other than Ms-recrystallization texture of $\{236\}\langle 385 \bar{} \rangle$. Examples of cube texture in the drawn-annealed Cu-18%Nb samples have been shown in the Appendix A by figures A15, A21, A25, A27, A29, A35, A37, A43, A45, A51, and A53. Despite various discussions regarding its origin [15,20,27-32], a texture measurement after Hirsch [26] clearly shows that the quantity of cube texture of $\{100\}\langle 001 \rangle$ prevails during the primary recrystallization of cold-rolled copper ($\varepsilon = 95\%$ or $\eta \approx 3.00$) after sufficient annealing time. This situation is depicted in figure 6.2. Here, it is also shown that the role of copper-

texture $\{112\}\langle 111 \rangle$ decreases steadily with increasing annealing time. This result can ascertain the $\langle 100 \rangle$ -position behavior of copper maximum intensity of Cu-18%Nb at $\eta = 3.01$ and $\eta = 3.95$. At $\eta = 4.97$, the driving force for growth selections based on the deformed texture and the specially oriented nucleation is stronger than that of cube texture formation. Thus the copper maximum intensity goes back to the highly stable $\langle 111 \rangle$ orientation.

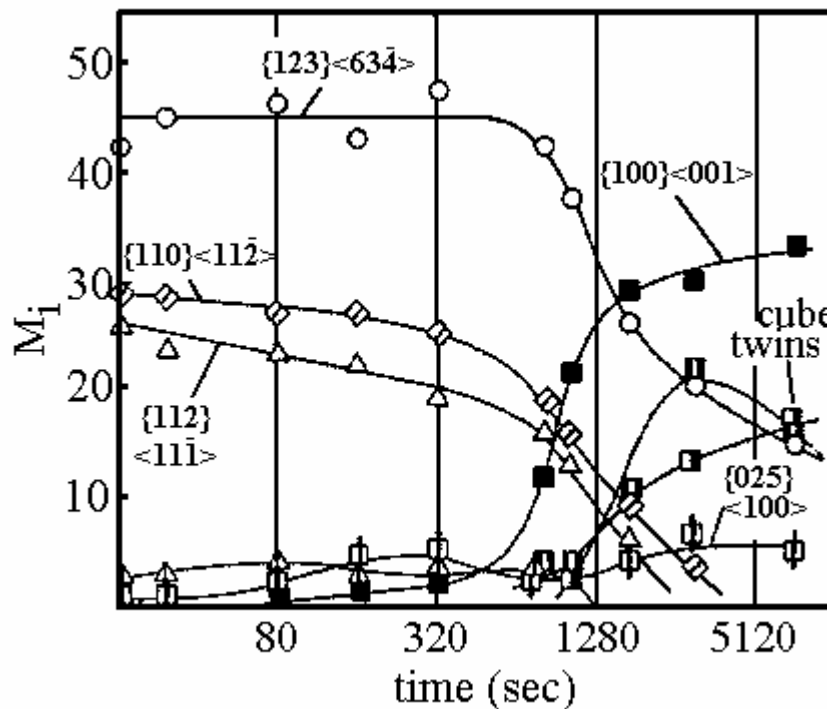


Figure 6.2 The quantity of texture components as a function of annealing time during primary recrystallization of pure copper after 95% rolling deformation [26].

Recovery (either dynamically or thermally activated) can be generated through rearrangement of screw, edge or mixed dislocations (i.e. by the development of network of many low-angle grain boundaries). Further, recovery can also originate from climb and cross-slip mechanisms. The last two processes show strong dependency on the stacking fault energy (SFE), of which climb and cross-slip are encouraged with increasing SFE. Therefore the materials with high SFE (mostly bcc metals) show the strong tendency of recovery, whereas those with low SFE (silver, copper, and fcc alloys) hardly exhibit such preference [33]. TEM pictures of the drawn Cu-18%Nb samples with $\eta = 2.08$ and $\eta = 3.95$ (figures C2 and C31 respectively) unfortunately show no trace of dynamic recovery in the niobium filaments. Instead they exhibit mostly very fine niobium



substructures, which are verified by their SADP (figures C3 and C32). Nevertheless, after annealing in the salt bath furnace, the recovery-recrystallization process in niobium filament has been encouraged, as indicated by some cell structures and grains (dislocation-free area) in figure C10.

It is then as well suspected that the thermally activated recovery-recrystallization of niobium phase in Cu-18%Nb has also a strong orientation dependency on the deformed structure. Raabe [1] showed that, in cold-rolled/annealed pure niobium and Cu-20%Nb, the recrystallized niobium phase exhibited a weak γ -texture that presumably originated from the oriented nucleation in regions of neighboring $\{111\}\langle uvw \rangle$ grains. In this case, $\{111\}\langle uvw \rangle$ could indicate $\{111\}\langle 112 \rangle$ and/or $\{111\}\langle 110 \rangle$ orientation. This situation is especially true for thin sheets, i.e. after massive rolling deformation. It is considered that the grains, originating from the middle layer and having a strong $\{111\}\langle uvw \rangle$ orientation, expand until the sheet surface. The analogy of this thin sheet may then explain the strong $\langle 110 \rangle$ -recrystallization texture of niobium filaments in Cu-18%Nb wires. Such strong texture is maintained even after extensive spheroidizations, owing that the spheroidization process is based upon a surface diffusion and not a volume diffusion.

6.2 Microstructural Examinations and Analyses

6.2.1 Light Microscope

It has been ascertained by figure 5.1 and figure B1 that the grains of deformed copper have the elongated morphology. Moreover, figure C33 shows as well the elongated copper morphology in the transverse section. The wide and long copper matrix due to extremely non-homogeneous plastic flow in the drawn-annealed Cu-18%Nb sample with $\eta = 4.97$, $T = 800^\circ\text{C}$, $t = 30$ min (figures B6a,b) and the one with $\eta = 4.97$, $T = 800^\circ\text{C}$, $t = 60$ min (figures B7a,b) allows the recrystallized grains to grow relatively free and to coalesce with neighboring grains until they reach the interphase. It is believed that the recrystallization in this region is responsible for the decrease in the copper maximum intensity of these two samples (see table 5.1). In this case, the freely growing grains can increase randomly distributed parts or backgrounds in the macrottexture measurement. In addition, these grains may overcome the growth selections originating from the oriented nucleations.

It is rather difficult, however, to judge the same reason for the decrease in niobium maximum intensity of the Cu-18%Nb sample with $\eta = 4.97$, $T = 800^\circ\text{C}$, $t = 60$ min (see table 5.1). Nevertheless since such deviation does not occur in sample with $\eta = 4.97$, $T = 800^\circ\text{C}$, $t = 30$ min, the situation becomes slightly easier and more significant. The interplate diffusion or the volume diffusion of tightly arranged niobium filaments (due to the non-homogeneous plastic flow) is presumably responsible for the decrease in the niobium maximum intensity of the sample with $\eta = 4.97$, $T = 800^\circ\text{C}$, $t = 60$ min. Figure 6.3 shows a portion of the niobium interplate diffusion in this sample. With respect to the annealing time, the interplate diffusion in the sample with $\eta = 4.97$, $T = 800^\circ\text{C}$, $t = 60$ min is more extensive than that in the sample with $\eta = 4.97$, $T = 800^\circ\text{C}$, $t = 30$ min. As previously mentioned in section 4.3.4, the texture sample consists of tightly arranged Cu-18%Nb wires with the same deformation and/or annealing condition (see figure 4.8). The portion of interplate diffusion will then increase with the number of adjoining wires having similar irregularity within the texture sample. The interplate diffusion increases the randomly distributed parts of niobium texture and hence reduces its maximum intensity.

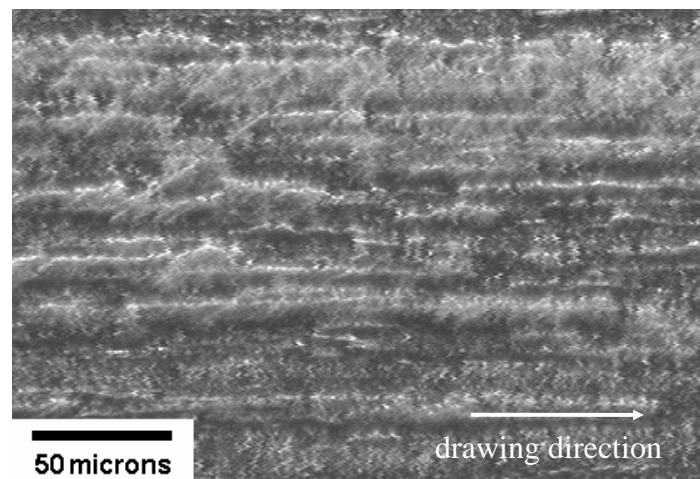


Figure 6.3 The interplate diffusion of tightly arranged niobium filaments (brighter areas) in the drawn-annealed Cu-18%Nb sample with $\eta = 4.97$, $T = 800^\circ\text{C}$, $t = 60$ min.

The presence of equiaxed grains in the relatively narrow interfilament spacing (figure B5a) firstly indicates that there is a large number of nucleation sites (either oriented or not) within this region. Moreover, the distribution of these nucleation sites is so arranged that the resulting grains can grow approximately equally in all directions. Here, the deformed parent grains are so strongly elongated that the nucleation sites at grain

boundaries appear to be closely arranged, as schematically shown in figure 6.4 (left side). Nevertheless, such condition can not be entirely guaranteed throughout the highly deformed copper spacing. Some big grains with indefinite shapes (figure B5b) can still grow at the expense of deformed matrix due to rarely arranged nucleation sites, as shown in figure 6.4 (right side).

As the annealing time and temperature increase, the recrystallized copper grains can further grow and/or coalesce with one another (figures B2, B3, B4, B8, and B9). Likewise, the traces of material flow (as shown in figures B6b and B7b) and the deformed grains vanish with the growing grains. In this case, the grain growth has taken over the recrystallization stage and entirely the deformed structure. The grain size has become proportional to the annealing time, as indicated by samples with $\eta = 4.97$, $T = 1000^\circ\text{C}$, $t = 12$ hr (figure B8) and with $\eta = 4.97$, $T = 1000^\circ\text{C}$, $t = 24$ hr (figure B9). The grain size of copper matrix in the latter sample is approximately double-in-size to that in the former sample. Within some large grains, the presence of annealing twinings can be observable under the resolution of light microscope (figures B8 and B9).

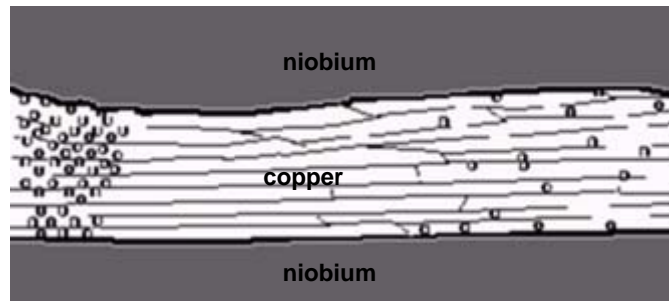


Figure 6.4 The nucleation sites in copper matrix that can result in equiaxed grains (left side) and big grains (right side).

6.2.2 Scanning Electron Microscope

A good review of the thermal instabilities of inclusion in figures 3.11 and 3.12 of Chapter Three is necessary to discuss the results of SEM. The decrease in filament thickness and interfilament spacing with increasing deformation in drawn samples is apparently observable in figures B10, B17, B24, and B31. This finding is verified by the results of quantitative analysis in table 5.3a. The average filament thickness (D) of the drawn samples has decreased from $2.54 \mu\text{m}$ ($\eta = 2.08$), to $1.95 \mu\text{m}$ ($\eta = 3.01$), to $1.68 \mu\text{m}$



($\eta = 3.95$) and finally to $1.03 \mu\text{m}$ ($\eta = 4.97$). Correspondingly, the average interfilament spacing (S) has decreased from $3.93 \mu\text{m}$, to $2.82 \mu\text{m}$, to $1.99 \mu\text{m}$, and to $0.64 \mu\text{m}$.

The interplate diffusion occurs within the samples that are annealed in the salt bath furnace (figures B11, B18, and B25). This interplate diffusion along with the intraplate diffusion (i.e. the diffusion within a filament; can be surface or volume diffusion) can provoke the thickening of filaments, as the closely adjacent filaments coalesce and fuse with one another during coarsening. The interplate diffusion can be considered likewise as the volume diffusion. By the volume diffusion, the plate instability or coarsening should take into account the concept of termination migration (see section 3.5.2.4 for review). By termination migration, the dominant mechanism is the one yielding the greatest rate of volume transport dV/dt [34]. The driving force for the volume diffusion is the internal surface energy release (S) of the induced instability process. As the sample (wrapped in a high-grade steel foil) is plunged into a heated salt, it experiences a much higher heating rate than that in the vacuum finger furnace. This sudden and fast heating induces the rapid release of a large amount of internal energy of the corresponding provoked instability process. The higher heating rate means the faster internal energy release, whose quantity can closely reach the initial value of such energy in a deformed material (S_0). In other words, the ratio of S/S_0 can be close to one. Figure 3.16 in Chapter Three shows that the termination migration process will be firstly declared as S/S_0 is approximately one, whether or not the sample has built-in internal boundaries. By annealing in the vacuum finger furnace (i.e. much lower heating rate), the amount of corresponding internal energy release is way lower than that of initial internal energy. Therefore, the cylinderization process may firstly initiate the filament instability process.

The shape instabilities of samples with $\eta = 2.08$, 3.01 , and 3.95 annealed at $T = 800^\circ\text{C}$ in the vacuum furnace (figures B12, B13, B19, B20, B26, and B27) and likewise the samples with $\eta = 2.08$, $T = 1000^\circ\text{C}$, $t = 15 \text{ min}$ (figure B14), with $\eta = 2.08$, $T = 1000^\circ\text{C}$, $t = 30 \text{ min}$ (figure B15), and with $\eta = 2.08$, $T = 1000^\circ\text{C}$, $t = 60 \text{ min}$ (figure B16) have been filament thickening and sphere dropping. Such instabilities are analogous to those of a cylindrical precipitate proposed a century ago by Rayleigh [35]. Rayleigh instability can dominate in infinite fibers, whereas the drop attachment or sphere dropping at the end of fibers should be the faster process (see section 3.5.2.2 for review). By the Rayleigh instability :



- when the aspect ratio of cylinder is less than 7.2, the precipitate will turn out to be a single sphere;
- when the aspect ratio is greater than 7.2, a drop detachment or sphere dropping at the end of the cylinder will be preferred; and
- as the length of cylinder appears to be infinite, a string of spheres will be produced.

In our case, the shape relaxation of the above SEM samples apparently follows the second and the third type of process. Nevertheless, the plate-like morphology of the niobium filaments after higher deformation can have its own influence on the instability process.

Tables 5.3a and 5.3b show that, at $\eta = 2.08$, the average filament thickness has increased from 2.54 μm (deformed) to 3.11 μm (annealed at $T = 800^\circ\text{C}$; $t = 30\text{min}$), and finally to 3.54 μm (annealed at $T = 800^\circ\text{C}$; $t = 60\text{ min}$). Correspondingly, the average interfilament spacing has increased from 3.93 μm to 4.56 μm and finally to 5.23 μm . Figures B10, B12, and B13 indicate that the drop nucleations and the resulting spheres have dominated the microstructure at the expense of long filaments. Such domination can influence the statistical filament size distribution in this sample. The drop or ridge nucleation at the end of filament has radius (r_R) bigger than the filament thickness (D) itself, as shown in figure 6.5. As the instability proceeds, the ridge continuously grows and finally separates itself from the filament, resulting in a dropped sphere. The radius of resulting sphere (r_S) should be bigger than that of the ridge. Based upon the calculation after Courtney and Malzahn Kampe [36], the relationship between r_S and r_R follows :

$$r_S > 1.225 r_R \qquad \text{Equation 6-1}$$

Depending upon whether or not the equilibrium concentrations between filament and matrix have been reached and also the size of r_S (considered as relatively small or large), the sphere may continuously grow according to *the Ostwald ripening mechanism*. From this point, it is understood that the increasing average filament thickness with annealing time at $\eta = 2.08$ (tables 5.3a and 5.3b) in a roundabout way represents the increase in size from initial filament thickness (D) to ridge radius (r_R) and finally to sphere radius (r_S). The experimental time scale, however, does not necessarily correspond to the instability process. Thus, it does not certainly mean that the ridge nucleation occurs at $t = 30\text{ min}$ and

the sphere formation takes place at $t = 60$ min. It is more appropriate to consider that there is a certain time range for each type of instability to prevail.

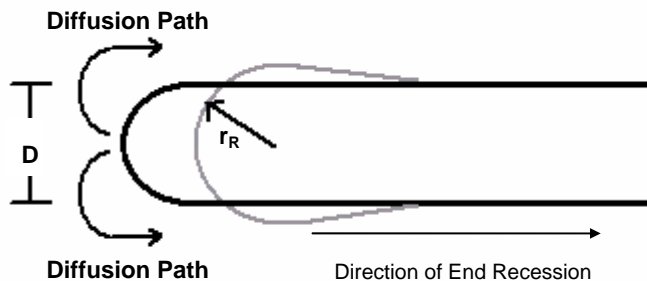


Figure 6.5 The drop or ridge nucleation at the end of filament.

It is surprising that, at $\eta = 2.08$, the average interfilament spacing also increases with the average filament thickness (tables 5.3a and 5.3b). One may expect that the interfilament spacing decreases with increasing filament thickness. Such situation can be explained from the combined aspects of measurement method and nature of ridge nucleation and dropped sphere. Figure 4.12 shows the schematic representation of the measurement method to determine the average filament thickness and interfilament spacing in drawn and drawn-annealed samples. The applied sampling lines are constantly spaced. It is clear that the obtained data are simply those measured parallel to the transverse direction, regardless of whether or not the inclusion morphology is filament, ridge or sphere. Moreover, figure B12 very well represents the situation, in which the ridge nucleations and thus the dropped spheres are randomly distributed. Further, not all the dropped spheres grow with increasing annealing time. According to Gleiter [37], an array of inclusions, but different sizes, interact since the concentration of solute atoms in the vicinity of small (large) particles is higher (lower) than the average supersaturation. Hence, the solute proceeds from the smaller to the larger particles. Therefore, the smaller particles shrink, whereas the large particles can continuously grow. Figure 6.6 clarifies and summarizes the origin of large interfilament spacings together with the increasing average filament/particle thickness. Figure 6.6a schematically depicts the niobium filaments after drawing. The round shape at the end of one filament indicates the effect of non-homogeneous plastic flow during drawing. Figure 6.6b shows the process of ridge nucleation and some extent of sphere formation. In figure 6.6c, the sphere formation has prevailed over the ridge nucleation. The horizontal lines in figure 6.6c indicate the



measured interfilament spacings with respect to constantly-spaced sampling lines. Naturally, depending on how close the implemented sampling lines are, the number of sampling lines and measured interfilament spacings can increase. Nevertheless, the indicated interfilament spacings in figure 6.6c (formerly not present) are definitely larger than those in figures 6.6a and 6.6b for given sampling lines. With increasing annealing time and temperature, the number of such interfilament spacings increases and may affect the whole statistical interfilament spacing distribution in the measured locations. Such large interfilament spacings have been likewise exhibited by the structure of drawn-annealed Cu-14.3vol%Fe composite and cold rolled-annealed hypoeutectic Ni-W alloy observed by Malzahn Kampe et al. [38], as shown in figures 6.7 and 6.8 respectively.

At $\eta = 3.01$, the observed instability process is similar to that at $\eta = 2.08$ (i.e. : filament thickening and sphere dropping). Tables 5.3a and 5.3b show that, at $\eta = 3.01$, the average filament thickness has increased from 1.95 μm (deformed) to 2.13 μm (annealed at $T = 800^\circ\text{C}$; $t = 30\text{min}$), and finally to 2.45 μm (annealed at $T = 800^\circ\text{C}$; $t = 60\text{ min}$). Nevertheless, the microstructure of the sample with $\eta = 3.01$, $T = 800^\circ\text{C}$, $t = 30\text{ min}$ (figure B19) hardly shows the ridge nucleations or even sphere droppings. Instead, the long and closely spaced filaments prevail. Therefore the filament thickening process in the sample with $\eta = 3.01$, $T = 800^\circ\text{C}$, $t = 30\text{ min}$ has a distinct feature in contrast to the sample with $\eta = 2.08$, $T = 800^\circ\text{C}$, $t = 30\text{ min}$. Moreover, table 5.3b also shows that the average interfilament spacing of samples with $\eta = 3.01$ firstly decreases at $T = 800^\circ\text{C}$ and $t = 30\text{ min}$ and reincreases afterwards. All of these aspects suggest that, despite the ridge nucleation and sphere dropping, the copper-niobium longitudinal planar interface has grown during the annealing.

The concept of growth behind planar interface highly contemplates the nature of interface itself. The copper-niobium interface has been considered as an incoherent one, since the atomic configuration in the two adjoining phases is very different. Thus, there is no or very little possibility of good matching across the interface. Incoherent interfaces have many features in common with high-angle grain boundaries [39]. It indicates that the incoherent interfaces are highly mobile. One example of which approximately planar incoherent interfaces may be found is after grain boundary nucleation. The growth rate (v) of the incoherent planar interface can be expressed as :

$$v = \frac{D(C_0 - C_e)^2}{2(C_\beta - C_e)(C_\beta - C_0)x} \quad \text{Equation 6-2}$$

where :

- D = the interdiffusion coefficient
- C₀ = the initial matrix concentration
- C_e = the equilibrium matrix concentration
- C_β = the initial precipitate or filament concentration
- x = the distance along the growth direction

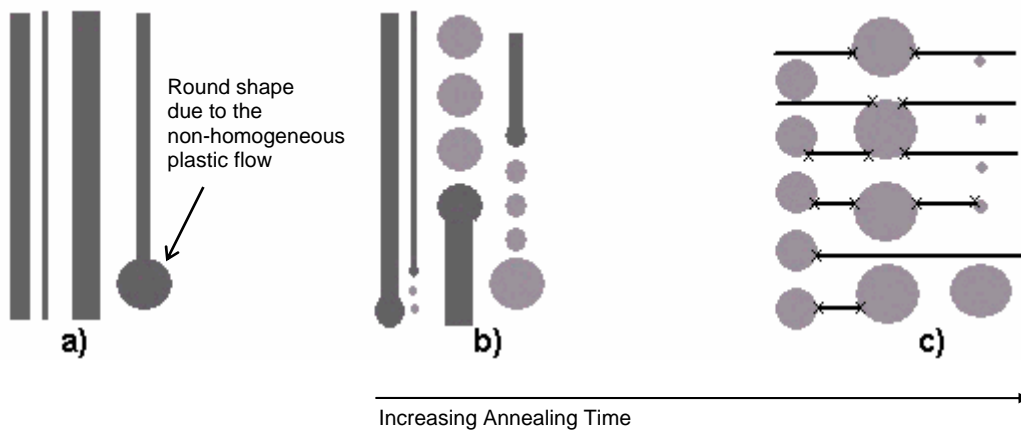


Figure 6.6 a) The niobium filaments and interfilament spacings after drawing, b) the ridge nucleation and sphere formation as the annealing proceeds, and c) the large and small spheres after longer period of annealing. The horizontal lines in figure 6.6c indicate the larger interfilament spacings that are not previously present in figures 6.6a and 6.6b for given sampling lines.

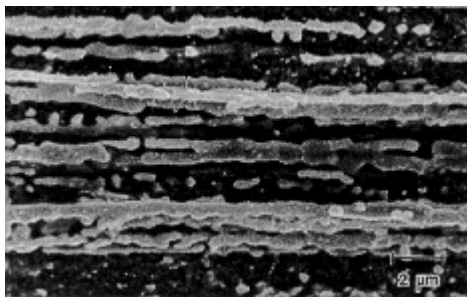


Figure 6.7 The large interfilament spacings in the Cu-14.3vol%Fe *in-situ* composite wire after annealing at the T = 1073 K for 2 hr [38].

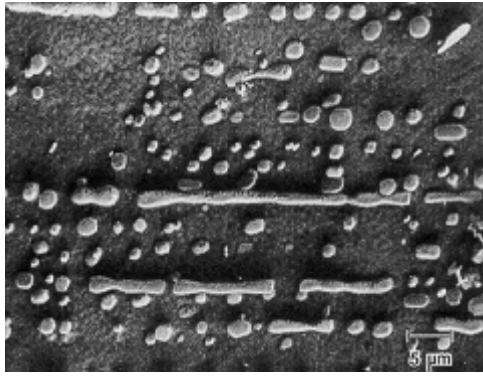


Figure 6.8 The large interfilament spacings in the "hypoeutectic" Ni-W alloy after annealing at the $T = 1673$ K for 5 hr [38].

Figure B20 shows that the ridge nucleation and the sphere dropping have already begun in the sample with $\eta = 3.01$, $T = 800^\circ\text{C}$, $t = 60$ min. Simultaneously, the average interfilament spacing of this sample has increased from that of the sample with $\eta = 3.01$, $T = 800^\circ\text{C}$, $T = 30$ min as verified in table 5.3b. It indicates that the ridge nucleation and the sphere dropping have actually predominated over the process of growing planar interface.

Although the observed instability process of samples with $\eta = 3.95$ and annealed at $T = 800^\circ\text{C}$ in the vacuum furnace has been likewise filament thickening and sphere dropping (figures B26 and B27), the statistical analyses feature a slight contradiction. Tables 5.3a and 5.3b show that, at $\eta = 3.95$, the average filament thickness decreases from $1.68 \mu\text{m}$ (deformed) to $1.35 \mu\text{m}$ (annealed at $T = 800^\circ\text{C}$; $t = 30$ min), but reincreases to $2.14 \mu\text{m}$ (annealed at $T = 800^\circ\text{C}$; $t = 60$ min). The behavior of average interfilament spacing is also similar to that of samples with $\eta = 3.01$. These phenomena can be then related to the cross-sectional morphology of niobium filaments. At $\eta = 3.95$, the niobium filaments exhibit flat and curled shapes in the transverse section. This situation has also been verified by the TEM sample (figure C30). Despite the presence of curling, the aspect ratio of filaments in the transverse section (i.e. width to thickness) has been considerably large. In other words, the transverse morphology of filaments can be treated as the flat or the plate-like morphology. If it is the case, the subsequent thermal instability process here will be different in contrast to that of the smaller transverse aspect ratio (i.e. lower deformation).

As previously mentioned in section 3.5.2.3, there are several modes of shape instability of plate-like structure. By the presence of internal boundaries, the process of boundary splitting can take place over the plate with a large aspect ratio (figure 3.12c). The reduced average filament thickness and interfilament spacing of the sample with $\eta = 3.95$, $T = 800^\circ\text{C}$, $t = 30$ min (see also table 5.4b) occurs as the niobium filament is divided into

some thinner filaments according to the number of internal longitudinal boundaries. When such system is annealed at high temperature, a groove can develop along the line of intersection with the settlement of static equilibrium among surface tensions. The ridges are then formed at two sides of the filament. The morphology of ridges allows a diffusion of plate material away from the groove, yielding the flattening of the ridges themselves. Simultaneously, such flattening process capsizes the static equilibrium by enlarging the dihedral angle. As the vertical components of the interfacial tensions can no longer balance the boundary tension, the triple points (upper and lower ones) are pulled toward each other yielding the splitting of filament. Such instability process is summarized in figure 6.9.

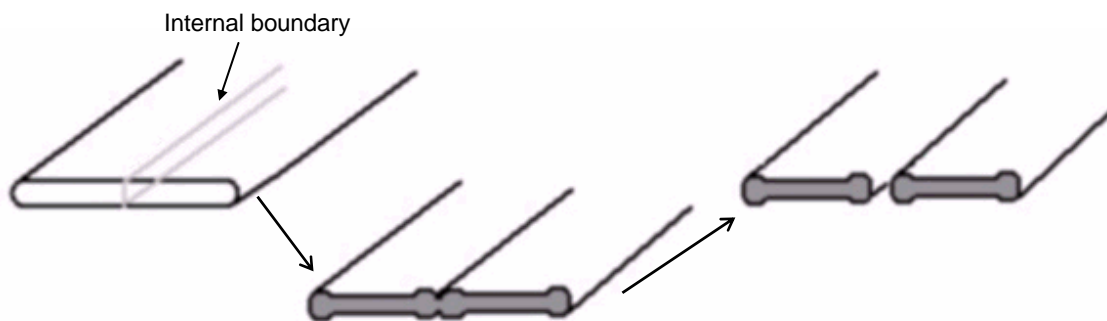


Figure 6.9 The splitting of one filament into two parts due to the presence of internal longitudinal boundary. The number of resulting parts is then proportional to the number of internal boundaries. The splitting process is provoked by the groove development and the groove deepening.

As the transverse aspect ratio of the resulting parts is sufficiently low (about less than 7.2), their shape may transform into cylinder with increasing annealing time. Simultaneously or shortly after, the ridge nucleation and the sphere dropping occur along the longitudinal section. This situation is verified by the sample with $\eta = 3.95$, $T = 800^\circ\text{C}$, $t = 60$ min in figure B27. Similar to samples with $\eta = 2.08$, $T = 800^\circ\text{C}$, $t = 60$ min and with $\eta = 3.01$, $T = 800^\circ\text{C}$, $t = 60$ min, the ridge formations and sphere droppings provoke an increase in the average filament thickness and interfilament spacing in the sample with $\eta = 3.95$, $T = 800^\circ\text{C}$, $t = 60$ min (statistically verified in table 5.3b).

For the samples with $\eta = 4.97$ annealed at $T = 800^\circ\text{C}$, some additional instability mechanisms have been observed, i.e. the formation of bamboo structure in thin filaments and some extent of edge spheroidizations in large filaments (figures B32 and B33a-b). Moreover, the statistical analyses indicate the decreasing average filament thickness with the increasing annealing time (tables 5.3a and 5.3b). This situation may firstly indicate that



the boundary splitting process has become a chain reaction. Such continuous splitting prevails as long as the resulted parts have sufficiently large transverse aspect ratio and/or internal longitudinal boundaries. This instability process also explains the reduced average interfilament spacing in the sample with $\eta = 4.97$, $T = 800^\circ\text{C}$, $t = 30$ min, as quantitatively proven in table 5.3b. Nevertheless, some extent of bamboo structure and subsequent spheroidization have taken place already (figure B32). The boundary splitting process further continues, as the number of bamboo structure formation and edge spheroidization tries to increase and distribute.

The reduced average filament thickness in the sample with $\eta = 4.97$, $T = 800^\circ\text{C}$, $t = 60$ min (statistically verified in table 5.3b) has been the result of boundary splitting process, which may or may not yet cease. Moreover, the increase in average interfilament spacing of this sample (again in table 5.3b) occurs as the bamboo structure along with the edge spheroidization provoke the formation of some large interfilament spacings. These large interfilament spacings have affected the interfilament spacing statistical distributions of the measured regions. Figure 3.12b [36] in Chapter Three schematically represents the process of edge spheroidization.

The observed thermal instabilities in samples with $\eta = 2.08$, $T = 1000^\circ\text{C}$, $t = 15$ min (figure B14), with $\eta = 2.08$, $T = 1000^\circ\text{C}$, $t = 30$ min (figure B15), and with $\eta = 2.08$, $T = 1000^\circ\text{C}$, $t = 60$ min (figure B16) have been filament thickening and sphere dropping. No statistical analysis has been conducted to support these SEM results. Nevertheless, such observation appears to be true by considering that, at $\eta = 2.08$, the transverse morphology of niobium filaments in the drawn sample features a roundly elongated shape (see figure C1). By comparing with that of the drawn sample with $\eta = 3.95$ (figure C30), it is rather inappropriate to suppose the formation of edge spheroidization or even the boundary splitting in these samples with $\eta = 2.08$. The cylinderization (with respect to the transverse section) and the ridge formation along with the sphere dropping (in the longitudinal section) emerge as the highly possible instability mechanisms. The ridge formation and the sphere dropping can presumably increase the statistical distribution of filament thickness within the sample.

For samples with $\eta = 3.01$, $T = 1000^\circ\text{C}$, $t = 15$ min (figures B21a-b), with $\eta = 3.01$, $T = 1000^\circ\text{C}$, $t = 30$ min (figures B22a-b), and with $\eta = 3.01$, $T = 1000^\circ\text{C}$, $t = 60$ min (figures B23a-b), the instability mechanisms appear to be : the ridge nucleation/sphere



dropping, the filament thickening, the filament recrystallization, the bamboo structure, and the edge spheroidization. Again, no statistical analysis has been conducted. Nevertheless, the only mechanism that should be statistically proven is the filament thickening. One may assume that the filament thickening occurs due to the growing planar interface combined with the ridge nucleation and sphere dropping. The ridge nucleations and sphere droppings (figure B21a) are produced by some finite filaments, whose longitudinal aspect ratio is greater than 7.2. The filament recrystallization, the bamboo structure, and the edge spheroidization have already been obvious from the appearance.

The samples with $\eta = 3.95$ and $\eta = 4.97$ and annealed at $T = 1000^\circ\text{C}$ do not feature the ridge nucleation and sphere dropping process. Instead, they show : the filament thickening, the filament recrystallization, the bamboo structure, and the edge spheroidization (figures B28a-b, B29a-b, B30a-b, B34a-b, B35a-b, and B36a-b). At $\eta = 3.95$, the sphere droppings are not obvious since they are hardly distinguished from sphere formations resulted from the spheroidizations of bamboo structures and edge spheroidizations. However, at $\eta = 4.97$, the absence of sphere dropping can be the result of infinitely long filaments that prefer the formation of bamboo structures. There is no better way than to verify the observed filament thickening in this sample with the statistical analysis.

| η | 800°C | | | 1000°C | | |
|--------|----------------------|--|--------|--|--------|--------|
| | 60 sec | 30 min | 60 min | 15 min | 30 min | 60 min |
| 2.08 | interplate diffusion | ridge nucleation, sphere dropping | | ridge nucleation, sphere dropping | | |
| 3.01 | interplate diffusion | planar interface growth, ridge nucleation, sphere dropping | | ridge nucleation, sphere dropping, planar interface growth, filament recrystallization, bamboo structure, edge spheroidization | | |
| 3.95 | interplate diffusion | boundary splitting, ridge nucleation, sphere dropping | | filament thickening (planar interface growth), filament recrystallization, bamboo structure, edge spheroidization | | |
| 4.97 | ... | boundary splitting, bamboo structure, edge spheroidization | | | | |

Table 6.1 The summary of filament thermal instabilities of drawn-annealed Cu-18%Nb samples.

Table 6.1 summarizes the observed filament thermal instabilities of Cu-18%Nb drawn-annealed samples. The thermal instability mechanisms within the column 800°C (30 min and 60 min) are in good agreement with the results of statistical analysis.



6.2.3 Transmission Electron Microscope

The results of TEM observations are shown in figure C1 to figure C48 of the Appendix C. In the drawn sample with $\eta = 2.08$, the transverse morphology of niobium filaments is roundly elongated (figure C1). Moreover, the spacing between filaments is apparently large. These situations mean that the extent of deformation and the corresponding plastic flow is still considerably low to produce a so-called flat and curled morphology and to densely pack the filaments. Unlike the drawn sample with $\eta = 2.08$, the sample with $\eta = 3.95$ features the expected thin and curly (but not yet extensive) niobium forms (figure C30). Moreover, the niobium filaments have been brought much closer to each other. The aspect of curled morphology [40] has been well known for the deformed bcc phase in fcc matrix and reviewed in more detail in Chapter Three. The $\langle 110 \rangle$ fiber texture allows only two of the four $\langle 111 \rangle$ bcc slip directions to endow plastic deformation along the longitudinal axis. Nevertheless, such activation of only two symmetrical slip systems leads to a local plane strain deformation which results in a bent shape of niobium phase, known as the curling. The substructure of niobium filaments in drawn samples is very fine (figures C2 and C31), and its SADPs reveal nanocrystalline patterns (figures C3 and C32). The structurally less ordered glassy areas, as investigated by Hangen [41] and discussed by Raabe et al. [2] in the cold rolled Cu-20%Nb, were not observed. The presence of twinings within small copper grain in the drawn sample with $\eta = 2.08$ (figure C4) upholds the argumentation of dynamic recrystallization of copper matrix that may have already been initiated within a low deformation. Dislocation forests (figures C7 and C31) represent the strain hardening development of the copper matrix. As deformation begins, one copper slip system is activated. The number of activated slip systems then increases with the deformation. Dislocations of one slip system becomes dislocation forests or obstructions for those of other slip system to cut through. As the shear stress of corresponding slip systems has been increased, the dislocations can either cross-slip (screw dislocations) or climb (edge dislocations) to overcome the obstruction. The deformation twinings in figures C5, C6, C7 and C8 of the drawn sample with $\eta = 2.08$ are obvious, since the electrons are differently transmitted according to the orientations of twinned and untwinned regions. Deformation twinning is generally not favorable in a material with many slip systems [6]. Nevertheless, the twinings in copper matrix occur either when the



slip systems are restrained or when the critical resolved shear stress has been increased so that the twinning stress is lower than the stress for slip.

Figure C10 shows a large niobium filament in the drawn-annealed Cu-18%Nb sample with $\eta = 2.08$, $T = 800^\circ\text{C}$, $t = 60$ sec, heat treated in the salt bath furnace. Here it is obvious that the niobium filament has experienced some extent of recovery and recrystallization due to annealing. Owing that such phenomena are hardly observed in other samples annealed in the vacuum finger furnace, their occurrence may also be driven by the high heating rate in the salt bath furnace. Despite the presence of recovery-recrystallization areas (figure C10), the niobium filament still mostly features very fine substructure (figures C11 and C12) along with its nanocrystalline pattern (figure C13). The copper equiaxed grains have been observed in the drawn-annealed sample with $\eta = 2.08$, $T = 800^\circ\text{C}$, $t = 60$ sec (figure C9). It is thought that the formation of equiaxed grains is related to the extremely rapid heating during annealing in the salt bath furnace. The recrystallized grains begin to grow fast almost the same rate in all directions with the existence of high temperature gradient. It is also highly suspected that the rapid growth of equiaxed grains may conquer the possible growth selections within the copper matrix. The corresponding possible consequences are the increase in random backgrounds of texture data and the reduced copper maximum intensity.

The nanocrystalline substructure of niobium filaments has also been featured by the drawn-annealed sample with $\eta = 3.95$, $T = 800^\circ\text{C}$, $t = 60$ sec, heat treated in the salt bath furnace (figure C34). Surprisingly, the copper equiaxed grains are hardly observed in this sample. Instead some cell structures occur as shown in figure C35. The presence of cell structures (figure C35) and dislocation tangles (figure C36) may presumably indicate the considerable on-going process of rearrangement and annihilation of dislocations, regardless of the highly applied heating rate. Such rearrangement and annihilation of dislocations must operate to a large extent at the same time with recrystallization, since the ratio of S_r (energy released during recovery) and S (total energy released) is small [42]. The increase in dislocation density from $\eta = 2.08$ to $\eta = 3.95$ may be responsible to the retardation of spontaneous release of the recovery energy. Nevertheless, such presumed rearrangement and annihilation of dislocation in the sample with $\eta = 3.95$, $T = 800^\circ\text{C}$, $t = 60$ sec does not stand as a lone factor to explain its unique microstructure. It is also



conceivable that the microstructure of this sample has been affected to some extent by the compression introduced during cutting process of the ultramicrotomy.

In the rest of drawn-annealed TEM samples, many well expected phenomena have been observed such as :

- rounder shape of niobium filaments in the sample with $\eta = 2.08$, $T = 800^\circ\text{C}$, $t = 30$ min (figure C14),
- annealing twinings in the samples with $\eta = 2.08$, $T = 800^\circ\text{C}$, $t = 30$ min (figures C17 and C20) and with $\eta = 3.95$, $T = 800^\circ\text{C}$, $t = 60$ min (figures C43 and C46),
- recrystallized copper grains in the sample with $\eta = 3.95$, $T = 800^\circ\text{C}$, $t = 30$ min (figures C38 to C41) and in the sample with $\eta = 3.95$, $T = 800^\circ\text{C}$, $t = 60$ min (figures C43 to C47),
- or even small and large recrystallized copper grains in the sample with $\eta = 2.08$, $T = 1000^\circ\text{C}$, $t = 30$ min (figures C27 and C28).

The annealing twinings are formed in association with the recrystallization and growth of new grains. The formation of annealing twinings is instigated as the emerging grains (during the formation of a new packing order in the new crystals) meet some packing sequence defects (such as stacking faults) in the original grains. The pre-existing stacking faults in the deformed grains become the likely requirement for the development of annealing twinings [48]. Since copper has a low stacking fault energy (high stacking fault probability), the annealing twinings are then easily observed. The number of annealing twinings can represent the extent of prior deformation, since the amount of stacking faults increase with deformation.

Aside from these results, some unexpected phenomena have also been observed in the drawn-annealed samples. These deviations include the hardly disappearing dislocations and the apparently deformation-resulted twinings. The difficulty in TEM examinations arises as these deviations interfere with pre-existing phenomena in the samples, causing difficulty in distinguishing them from one another. Similar to the drawn-annealed sample with $\eta = 3.95$, $T = 800^\circ\text{C}$, $t = 60$ sec, such deviations are believed to be the result of induced compression during cutting procedure in the ultramicrotomy process.

By the ultramicrotomy process, the compression is a phenomenon taking place in regions of which the section bends. Figure 6.10 shows the formation of a section with a 25° diamond knife at a clearance angle (β) of 8° from a descending sample block, based on



the works of J̄esior [43-45]. Figure 6.10 is a more detailed scheme of figure 4.10 in Chapter Four. The sectioning angle (γ) is the sum of the clearance angle and the knife angle. In figure 6.10, two other examples of knife angle (i.e. 15° and 45°) have also been shown. The amount of compression in the section can be related to the so-called bending factor (in the unit of degree per μm). After rough calculation with $\gamma = 33^\circ$, it has been derived that the bending factor in region I is about $330^\circ/\mu\text{m}$, whereas that in region II is $15^\circ/\mu\text{m}$. It means that the induced distortion in region I is approximately 20 times higher than that in region II. By higher knife angle (i.e. 45°), the amount of distortion becomes roughly 65 times. Using linear interpolation of these data, the amount of distortion experienced by our Cu-18%Nb samples with knife angle of 35° (see section 4.4.3.1) in region I is approximately 40 times greater than that in region II. Regardless of the exact value of resulting distortion, it is now well accepted that the compression does occur on the cut section of the ultramicrotomy process and its amount and effect can not be ignored.

As previously mentioned, the amount of dislocations in the annealed TEM samples hardly reduces. Such phenomenon can be the result of the introduction of *geometrically necessary dislocations* during the bending of section. The geometrically necessary dislocations are the opposite of *statistically stored dislocations* produced by the dislocation multiplication during glide process accompanying plastic flow. As the material bent, its upper part (convex side) experiences tensile deformation with increasing length ($L + \Delta L$). Conversely, the inner circumference (concave side) undergoes compressive deformation with decreasing length ($L - \Delta L$). These situations are depicted in figure 6.11. The presence of extremely distinct deformations (i.e. change in length) between upper and lower portions induces the occurrence of strain gradient within the material. Such strain gradient produces an uneven distribution of the number of atomic planes between the two surfaces. To accommodate this difference, some amount of edge dislocations of the like sign is introduced. The density of geometrically necessary dislocations needed (ρ_G) can be expressed as [46]:

$$\rho_G = 2 \frac{\Delta L}{Lbt} = \frac{\text{strain} - \text{gradient}}{b} \quad \text{Equation 6-3}$$

where :

b = the interatomic spacing = the Burgers vector magnitude

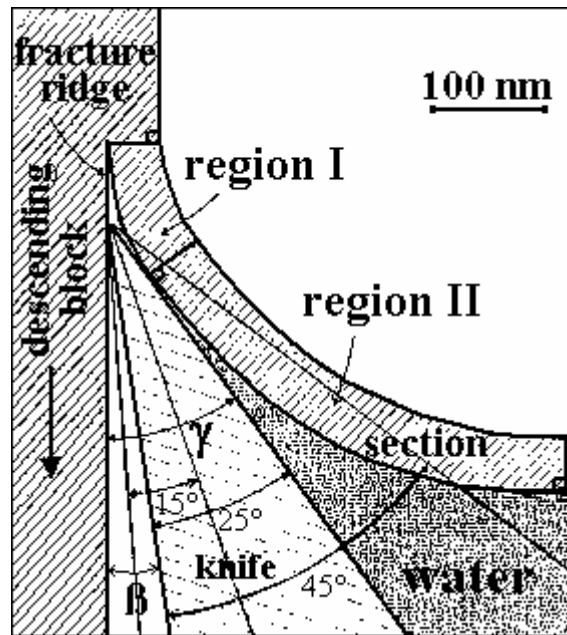


Figure 6.10 The formation of a section during ultramicrotomy process with the sectioning angle (γ) of 33° [43].

The observed deformation twinings in the TEM annealed samples are also produced by the induced deformation during the diamond cutting. The applied cutting speed of 0.40 to 1.00 mm/sec (see section 4.4.3.1) apparently does not provoke the development of deformation twinings. This argumentation is supported by Barreto et al. [47], whose ultramicrotomy results of galvaneal sheet coatings and pure aluminum give the best feature at the cutting speed from 0.1 to 1.00 mm/sec. Moreover, it is now generally known that the twinning initiation stress is much larger than the stress required to propagate a preexistent twinning [48]. It is then believed that, at some regions in the section, the critical resolved shear stress to lower the twinning initiation stress (below stress for slip) has been surpassed by the applied force of cutting. In these regions, the density of geometrically necessary dislocations has been combined with the density of statistically stored dislocations (either in the form of dislocation forests or cell structures). The combined dislocation density is so locally high that it hinders the activation of local slip systems. To accommodate this problem, the twinings are instead produced.

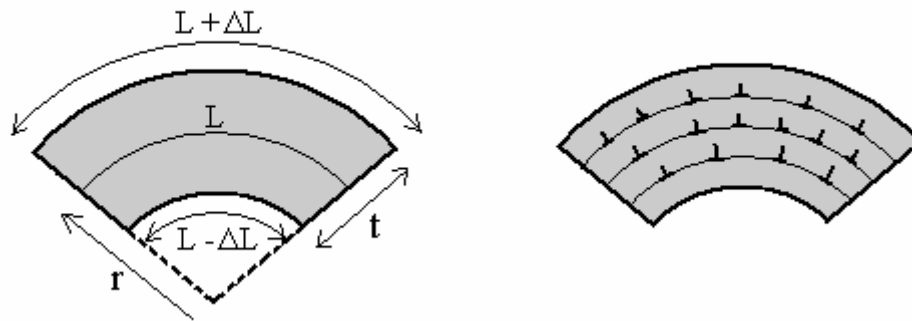


Figure 6.11 The formation of geometrically necessary dislocations in a bent material.

The compression or distortion during diamond cutting can be reduced by the use of low sectioning angle (γ) [43]. By reducing compression, a section with smoother surface can be produced. The low-angle knives prevent the "curling" of a hard material. In case of brittle material, the low-angle knives reduce the dispersion of the sectioned specimen on the surface of water. Reducing the sectioning angle does not only mean reducing the knife angle, but also means reducing the clearance angle (β) as long as it allows the compression relaxation of the sample block.

6.2.4 Statistical Analyses (Measurement of Filament Thickness and Spacing)

It has been shown in section 6.2.2 that statistical results in tables 5.3a and 5.3b significantly help in verifying the thermal instabilities of Cu-18%Nb samples under the scanning electron microscope. Moreover, the results of as-cast and drawn samples (table 5.3a) follow reasonably well the exponential equation (equation 2-7) after Spitzig and Krotz [49]. By using $\bar{t}_0 = D_0 = 5.57 \mu\text{m}$ and $\bar{\lambda}_0 = S = 8.66 \mu\text{m}$, the statistical results of this study and equation 2-7 are plotted in figure 6.12.

The fitted Gauss normal distribution of filament thickness in the cast sample (figure 5.2) appears flat or linear due to a very low probability and extremely broad data range (large standard deviation) in contrast to those of the other samples. Nevertheless, it actually still takes the parabolic form as verified in figure 6.13. This situation simply upholds the fact that, in contrast to those of drawn and drawn-annealed samples, the average niobium dendrite size in the cast sample is way larger and relatively more uniform throughout the sample.

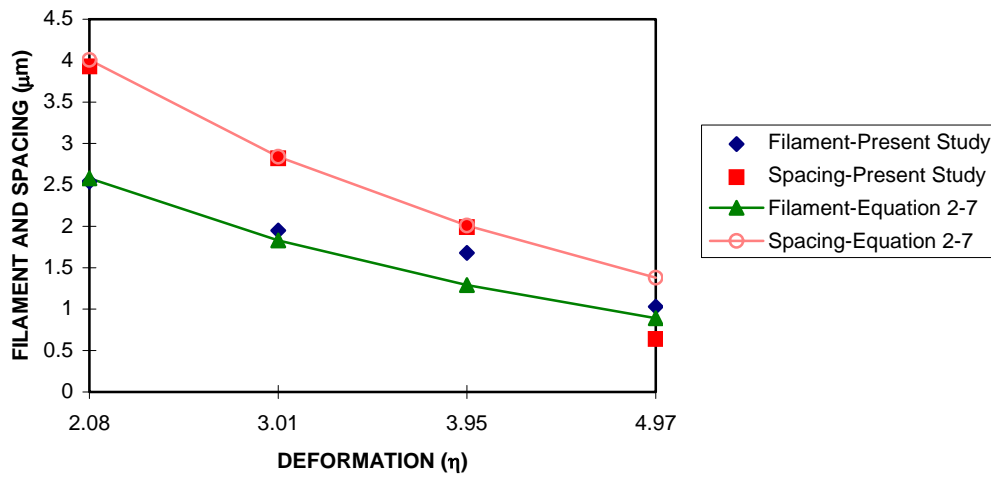


Figure 6.12 The comparison of the average filament thickness and interfilament spacing of present study with those calculated according to equation 2-7 after Spitzig and Krotz [49].

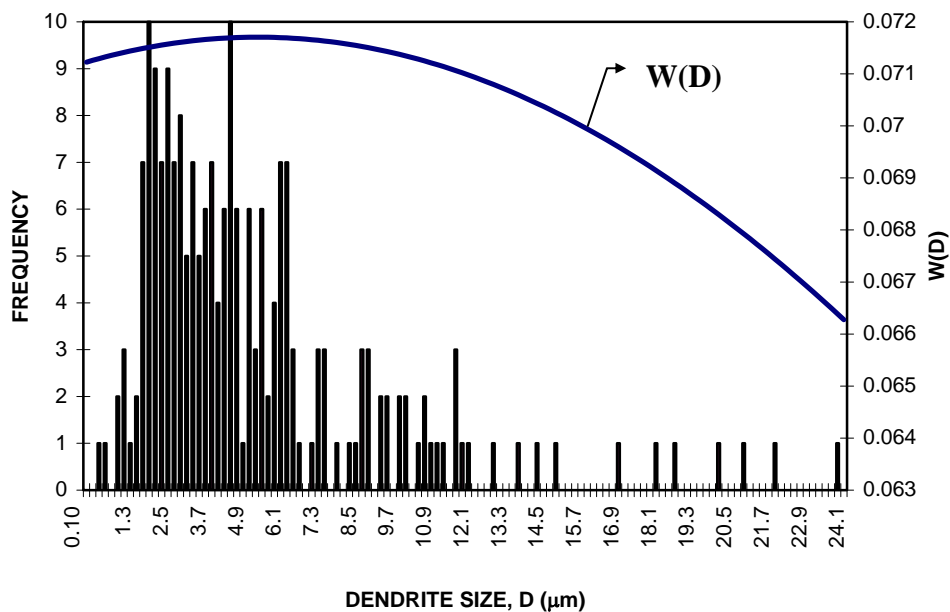


Figure 6.13 The fitted Gauss normal distribution, $W(D)$, and its original frequency data of dendrite size in the as-cast Cu-18%Nb sample.

The shift in the maximum probability of as-cast and as-drawn samples from right to left along with the corresponding reduce in distribution range (figure 5.2) represents the decrease in size from dendrites to filamentary morphology. It also suggests the narrowing filament thickness distribution across a drawn sample with increasing deformation for a given unit length parallel to the transverse direction.



Figure 5.3 and figure 5.4 show the similar statistical behavior of samples with $\eta = 2.08$ and $\eta = 3.01$ after heat treatment, respectively. Here, the filament thickness distributions widen and its probability lowers as the annealing time increases. The gradual change in the distribution from the drawn-annealed sample with $\eta = 2.08$, $T = 800^\circ\text{C}$, $t = 30$ min to the sample with $\eta = 2.08$, $T = 800^\circ\text{C}$, $t = 60$ min (figure 5.3) suggests that the corresponding ridge nucleations and sphere droppings (listed in table 6.1) do occur throughout the samples and the difference in size between ridge and the resulted sphere is relatively not large. Equation 6-1 shows that this difference accounts at least 18.4%. Using similar analogy, one can infer that the process of planar interface growth at $\eta = 3.01$ (listed in table 6.1) really takes place and forces the filament statistical distribution of the sample with $\eta = 3.01$, $T = 800^\circ\text{C}$, $t = 60$ min to broaden and lower from that of the sample with $\eta = 3.01$, $T = 800^\circ\text{C}$, $t = 30$ min (figure 5.4). In this case, the ridge nucleation and sphere dropping only play a smaller role. This situation may simultaneously uphold the fact that the growth of planar interface is a rapidly extensive process due to a highly mobile interface.

The shift in the statistical distribution from the drawn sample with $\eta = 3.95$ to the drawn-annealed sample with $\eta = 3.95$, $T = 800^\circ\text{C}$, $t = 30$ min (figure 5.5) corresponds to the boundary splitting process (table 6.1), of which the average filament thickness decreases. Conversely, the lowering and broadening data range of the sample with $\eta = 3.95$, $T = 800^\circ\text{C}$, $t = 60$ min in figure 5.5 represents the process of ridge nucleation and sphere dropping, of which the average filament thickness rises. Nevertheless, the results of this process can not surpass the filament thickness distribution of the drawn sample with $\eta = 3.95$, as verified by the standard deviations (tables 5.3a and 5.3b). In this case, the standard deviation of the drawn sample is still higher than that of the drawn-annealed sample with $\eta = 3.95$, $T = 800^\circ\text{C}$, $T = 60$ min. This situation suggests that, as the annealing time increases, the ridge nucleation and sphere dropping are sufficiently strong to counter-balance the boundary splitting process.

The ever narrowing statistical distributions of the drawn sample with $\eta = 4.97$ to the drawn-annealed sample with $\eta = 4.97$, $T = 800^\circ\text{C}$, $t = 60$ min (figure 5.6) indicate the strongly predominating boundary splitting process. Even though some bamboo structures and edge spheroidizations have initiated, either their rate or quantity can not overcome that of the boundary splitting process. It means that the transverse aspect ratio of niobium



filaments within the samples with $\eta = 4.97$, $T = 800^\circ\text{C}$, $t = 30$ min and with $\eta = 4.97$, $T = 800^\circ\text{C}$, $t = 60$ min is mostly still above 7.2 and the longitudinal internal boundaries are generally still present.

6.3 Mechanical Tests

6.3.1 Microhardness Test

The hardness values of redrawn copper slowly decrease with increasing deformation (table 5.4 and figure 5.7). This phenomenon occurs as the result of dynamic recrystallization of copper during the drawing process. The extent of dynamic recrystallization increases with increasing deformation. As elaborated previously in section 6.1, the activation of such recrystallization process comes from the situation, that the copper samples experience strong heating with decreasing thickness or volume after each drawing pass. Such heat generation has been the result of plastic deformation combined with friction between the dies and the copper samples. Figures 6.1a and 6.1b verify the presence of dynamically recrystallized grains in the redrawn copper samples with $\eta = 4.03$ and $\eta = 4.97$.

The gradually decreasing hardness with increasing deformation is also observed in the redrawn-annealed copper samples (table 5.4 and figure 5.7). Increasing annealing time apparently does not much affect this hardness behavior. Such situation is again well rooted to the process of dynamic recrystallization. According to Mehl [50] (see also section 3.4.3.4), the greater the degree of deformation, the lower the annealing temperature for recrystallization. Conversely, the smaller the degree of deformation (above the minimum), the higher the temperature needed to induce recrystallization. In other words, it also means that during drawing (assuming isothermal heating due to plastic deformation and friction) the amount of released stored-energy in dislocations due to dynamic recrystallization is the highest at $\eta = 4.97$. It happens since the appropriate temperature to reach the same amount of dynamic recrystallization like in lower deformations has been actually surpassed. By isothermally annealing these drawn coppers, such imbalance in the released stored-energy with respect to deformation is not better off. Instead, it is even multiplied until the process has reached the equilibrium. It should be now well understood that the redrawn-annealed copper sample with $\eta = 4.97$, $T = 426^\circ\text{C}$, $t = 120$ min (table 5.4) is the most dynamically and primarily recrystallized one.



The hardness of drawn Cu-18%Nb appears to be constant (table 5.5 and figure 5.9). As previously discussed in section 6.1, this situation has been the result of leisure rotation toward $\langle 110 \rangle$ direction of niobium dendrites within low deformations. The highly textured but stable $\langle 110 \rangle$ orientation of niobium will apparently be reached only at sufficiently high deformation ($\eta > 6$). The difference in elongation between Cu-20%Nb wire and its niobium filaments (i.e. niobium filaments deform slower) underline such gradual niobium rotation [5]. In Cu-18%Nb texture samples, this situation is also verified by a slow increase (close to stable) in the niobium maximum intensity for $2.08 < \eta < 3.01$.

| η | D_0/S | | |
|--------|----------|--------------|--------------|
| | As Drawn | 800°C, 30min | 800°C, 60min |
| 2.08 | 0.65 | 0.68 | 0.68 |
| 3.01 | 0.69 | 1.47 | 1.27 |
| 3.95 | 0.84 | 2.05 | 1.31 |
| 4.97 | 1.61 | 1.67 | 1.33 |

Table 6.2 The ratios of D_0/S from the statistical data in tables 5.3a and 5.3b.

All the hardness values of drawn-annealed Cu-18%Nb samples are below those of drawn samples (figures 5.9 and 5.11). By comparing to figure 5.7 of pure copper wire, it can be inferred that this decrease in hardness values has been much more provoked by the recrystallization in copper phase, rather than in niobium phase. This situation can also be thought from the aspect of copper and niobium portions on the sample surface. The simplest representing parameter to describe these portions is the ratio of D_0/S from tables 5.3a and 5.3b (summarized in table 6.2). All the D_0/S ratios are greater than 0.5. It means that the apparent portion of niobium on the sample surface is larger than that of copper. Assuming a relatively uniform filament-distribution (very little effect of the non-homogeneous plastic flow), this portion can also be valid for the area under a macro- or even microhardness indentation. Moreover, the D_0/S values of drawn-annealed samples are mostly greater than those of drawn samples for a given deformation, except for the sample with $\eta = 4.97$, $T = 800^\circ\text{C}$, $t = 60$ min (table 6.2). It is then clear that, even though the niobium portion in the drawn-annealed samples is generally larger than that in the drawn samples, the microhardness values exhibit an opposite behavior. In other words, the



recrystallization of copper phase has stronger influence to lower the hardness values as exhibited in figures 5.9 and 5.11.

The second aspect to look at in comprehending the microhardness behavior of drawn-annealed Cu-18%Nb samples is the influence of heat treatment on niobium phase. In the as-drawn state, the dislocations in niobium filaments highly probable take the form of cell structures since niobium has a high stacking fault energy (i.e. strong tendency for recovery). As previously mentioned, such cell structures are unfortunately hard to observe under transmission electron microscope. Again, this difficulty might arise from the interference induced by compression during the diamond cutting process. As the annealing time increases, these cell structures transform themselves into subgrain structures, whose grain diameter is comparable to that of cell structures. According to Sevillano et al. [51] and Kuhlmann-Wilsdorf [52], a subgrain structure is always harder than a cell structure of the same geometrical dimension. On the basis of geometrical considerations after Courtney [46], the boundaries of subgrain structures are expected to provide stronger obstacles or resistance to dislocation motion than the line defects (i.e. dislocations) of cell structures, since the intersection of a surface with a slip plane is a line rather than a point. In this case, the motion of a dislocation along its entire slip plane length is blocked by a boundary, yielding a greater resistance to slip than isolated point obstruction lying in the slip plane. Moreover, the value of factor k (intrinsic resistance to dislocation motion) for subgrains in the Hall-Petch type equation (equation 3-34) is somewhat higher than that for cell structures.

It can be then accordingly thought that the niobium filaments in the drawn-annealed samples are actually harder than those in the drawn samples. Nevertheless, such increase could be insignificant compared to the hardness decrease in copper phase due to heat treatment. Moreover, the niobium maximum intensities of drawn-annealed samples mostly increase with deformation (see again table 5.1). The deviation in the drawn-annealed sample with $\eta = 4.97$, $T = 800^\circ\text{C}$, $t = 60$ min had been previously discussed (see section 6.1). This situation means that the niobium subgrain structure at $\eta = 3.01$, for instance, is more textured toward the $\langle 110 \rangle$ direction and harder than that at $\eta = 2.08$. It is then well accepted that the subgrain structure at $\eta = 4.97$ is the hardest one. Since D_0/S of drawn-annealed samples is higher than 0.5 (table 6.2), i.e. more niobium portion, the increase in niobium hardness from $\eta = 2.08$ to $\eta = 4.97$ overwhelms the corresponding hardness



change in copper phase. It is highly suspected that the hardness change in copper phase within the drawn and drawn-annealed Cu-18%Nb samples generally also features an increasing tendency with deformation, as supported by the behavior of copper maximum intensities in table 5.1. If it is the case, then the increase in niobium hardness is even upheld instead of counter-balanced. This situation may explain the gradual increase in the Cu-18%Nb hardness after annealing (figures 5.9 and 5.11).

Figures 5.8, 5.10, and 5.12 show the decrease and the plateau in hardness values with increasing annealing time. This phenomenon simply suggests that the extent of primary recrystallization in both phases increases with time and finally reaches the supersaturated state, in which the recrystallization process ceases, the grain growth predominates, and the hardness change is no longer sensitive to the microstructure. Even though rather hard to see, the lowering sequence (top to bottom) of the copper hardness in figure 5.8 for a given annealing time is $\eta = 2.01$, $\eta = 2.97$, $\eta = 4.03$, and finally $\eta = 4.97$. It suggests that the extent of copper dynamic recrystallization is more accentuated with increasing deformation. The lowering sequences of Cu-18%Nb in figures 5.10 and 5.12, however, show the reversed situation. Since the volume fraction or the ratio D_0/S gets higher and the niobium $\langle 110 \rangle$ orientation is more pronounced with increasing deformation, figures 5.10 and 5.12 endorse the fact that the overall hardness of a Cu-18%Nb sample (at given annealing time) is influenced more by the hardness of niobium filaments rather than by that of copper phase.

6.3.2 Tensile Test

Table 5.6 and figure 5.13 show that at $\eta = 2.97$, the drawn copper wire exhibits little plastic deformation and, thus, no $\sigma_{0.2}$. The plastic deformation appears at the higher deformations (i.e. $\eta = 4.03$ and 4.97). The stress-strain curve of drawn copper samples is shown in figure 6.14. By looking at this figure, it is then clear that the portion of plastic deformation of the drawn copper sample with $\eta = 2.97$ is slightly below 0.2% and not sufficient to interpolate $\sigma_{0.2}$. This sample has actually a yield stress (or flow stress), which is approximately 400 MPa. The presence of dynamic recrystallization within each sample is proven by the existence of jagged characteristics in the plastic region. The amount of dynamic recrystallization increases with the sample prior deformation, as indicated by the higher amplitude of jagged part. The dynamic recrystallization is the predominant



softening mechanism of all fcc metals other than aluminum, especially during high temperature deformation.

The dynamic recrystallization in a deformed copper single crystal has been well documented [53-56]. It has been shown that the dynamic recrystallization of copper single crystals during tensile testing at high temperatures is initiated at a defined stress level, instead of at a critical value of shear strain. Moreover, it is improper to consider the dynamic recrystallization as the static recrystallization taking place during deformation. Instead, the dynamic recrystallization is strongly related to the concurrent development of the dislocation structure. Some certain amount of recovery is crucial for the initiation of dynamic recrystallization. In this case, the dynamic recovery contributes to the creation of nucleus in the form of well defined subgrains. The nucleation of dynamic recrystallization is provoked by the instabilities of the subgrain structure and, hence, its orientation follows that of the subgrain. At about $T = 1000^{\circ}\text{C}$, the dynamic recrystallization in the copper single crystal has been well understood as the growth of single nucleus, whose subsequent subgrain grows into macroscopic dimension (i.e. *in-situ* recrystallization). At some lower temperature ($T \approx 670^{\circ}\text{C}$), the growing subgrains propagate by the chain reaction of annealing twinings. These dislocation-free annealing twinings grow directly into the deformed matrix, through migration of incoherent segments of the twin boundary.

The dynamic recrystallization has been documented to also occur in deformed polycrystalline copper and copper alloys ($\eta > 3$) at ambient temperature, i.e. $\approx 0.2T_m$ [9,51,57-62]. Here, the dynamic recrystallization microstructurally takes the form of low-dislocation-density grains, which are subsequently followed and accompanied by the polygonization provoked by the climb process (as normally occurs at elevated temperatures). It has been proposed that the mechanism of dynamic recrystallization at ambient temperatures is initiated by a rapid nucleation with little or no incubation time. The boundary of nucleus can then move very rapidly due to excessively high vacancy concentrations during deformation. As the boundary (nucleus) is capable to grow into a grain, the probability of vacant sites of the grain interior can increase the boundary diffusivity into high values, and thus rising the grain boundary velocity. However, such high velocity can not be trivially passed across other grains due to the vacancy depletion at the boundary region. As a consequence, individual grains prevail instead of highly deformed material (see also figures 6.1a and 6.1b). The subsequent and accompanying

polygonization can also be well understood using the analogy of vacancy supersaturation that allows diffusional dislocation climb.

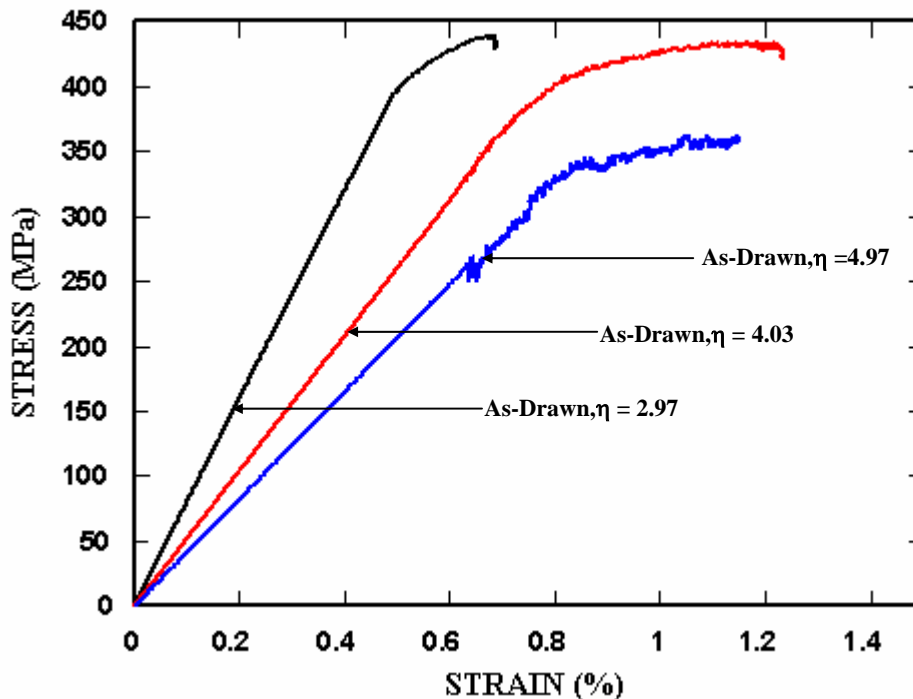


Figure 6.14 The stress-strain curve of redrawn copper samples.

Based upon this knowledge of dynamic recrystallization in copper single and polycrystal at high and ambient temperatures, the observed phenomena in figure 6.14 can now be described. The observed dynamic recrystallization in the drawn copper samples with $\eta = 4.03$ and $\eta = 4.97$ (figures 6.1a and 6.1b) has been induced by elevated temperatures due to the plastic flow and the friction between dies and samples during drawing. The mechanism of this process occurs according to the rapid nucleation and the diffusional dislocation climb provoked by the vacancy supersaturation. The cell structures due to dynamic recovery conversely occur with increasing drawing deformation, as the dislocations have the possibility (due to high shear stress) to cross-slip and annihilate or arrange themselves into energetically favorable structure according to the Orowan mechanism. This dynamic recovery has to compete with the preexistent on-going dynamic recrystallization. In other words, the copper structure now features two different but beneficial sites for further dynamic recrystallization to propagate, namely the preexistent dynamically recrystallized grains and the cell structures due to dynamic recovery. Again, the first one will induce further dynamic recrystallization by the rapid nucleation and the



diffusional dislocation climb provoked by the vacancy supersaturation, while the latter one will be crucial for the nucleation in form of well defined subgrains. According to Courtney [46], the dynamic recrystallization could take place not only at high temperatures but also at low strain rate. As the tensile test is initiated with $\dot{\epsilon} = 2 \times 10^{-3}/\text{sec}$ (see section 4.5.2.2) at low temperatures, the dynamic recrystallization is then provoked simultaneously from the both beneficial sites. The amount of dynamic recrystallization after yielding can be related to those of preexistent dynamically recrystallized grains and cell structures, which are the highest for the sample with $\eta = 4.97$ (figure 6.14). The higher the amount of dynamic recrystallization (before *and* during the tensile test), the higher the extent of softening in the material. This situation clarifies the decreasing flow stress (figure 6.14), yield stress ($\sigma_{0.2}$ in figure 5.13), and ultimate tensile strength (σ_{UTS} in figure 5.14) with increasing deformation. The premature failure of the sample with $\eta = 4.97$ in figure 6.14 has been apparently caused by the strain localization within the sample.

The behavior of $\sigma_{0.2}$ and σ_{UTS} in drawn-annealed copper samples generally follows that of drawn samples but with lower values (table 5.6, figure 5.13, and figure 5.14). This situation can be simply attributed to the lowering of dislocation density due to heat treatment. Figure 6.15 shows the stress-strain curve of the drawn copper sample with $\eta = 4.97$ and the drawn-annealed one with $\eta = 4.97$, $T = 433^\circ\text{C}$, $t = 120$ min. It is clear that the extent of dynamic recrystallization in the latter sample is more significant than that in the former sample during the tensile testing. The dynamic recrystallization in the sample with $\eta = 4.97$, $T = 433^\circ\text{C}$, $t = 120$ min is analogous to that in polycrystalline copper at ambient temperature, i.e. it is driven by the rapid nucleation and the diffusional dislocation climb. Nevertheless, the large grains (corresponding to prior grain growth during annealing, i.e. statically recrystallized grains) may accentuate the difference. It is assumed that the rapid nucleations preferentially occur at the grain boundaries. As the excessive amount of vacancies is created during deformation, the boundaries of growing nuclei can move rapidly. Despite its high velocity, this moving boundary still has sufficient time to reach vacancy-depletion region. This vacancy-depletion region can be either the boundary of large statically recrystallized grains or the boundary of the growing neighboring nuclei (as they coalesce). Either way, the process is now slightly longer due to a relatively large distances among these nuclei (corresponding to the large average diameter of statically recrystallized grain). This situation is represented by the higher amplitude of jagged part in



the S-S curve of the sample with $\eta = 4.97$, $T = 433^\circ\text{C}$, $t = 120$ min (figure 6.15). Generally, the pit and the peak of amplitude can respectively indicate the initiation and the termination of dynamically recrystallized grain(s).

Figures 5.15 and 5.16 show the decrease and the plateau of $\sigma_{0.2}$ and σ_{UTS} with increasing annealing time. The lowering sequence (top to bottom) of both values for a given annealing time is $\eta = 2.97$, $\eta = 4.03$, and $\eta = 4.97$. This result emphasizes the fact that the extent of dynamic recrystallization due to drawing process and tensile test is the highest at $\eta = 4.97$.

The tensile yield strength ($\sigma_{0.2}$) and the ultimate tensile strength (σ_{UTS}) of the drawn and drawn-annealed Cu-18%Nb gradually increases with the deformation, as shown in figures 5.17 and 5.18. A deviation, however, is shown by the sample with $\eta = 4.97$, $T = 800^\circ\text{C}$, $t = 30$ min in figure 5.18, whose ultimate strength is lower than that of the sample with $\eta = 3.95$, $T = 800^\circ\text{C}$, $t = 30$ min. This situation has been the consequence of a wide and long copper matrix (due to the non-homogeneous plastic flow) within the sample, similar to that observed in figures B6a and B6b. Such region, however, does not take place within the tensile test sample with $\eta = 4.97$, $T = 800^\circ\text{C}$, $t = 60$ min. As previously discussed, the primary recrystallization in this wide copper phase overcomes the growth selection in deformed matrix, yielding soft recrystallized grains. Moreover, the volume or interplate diffusion among the tightly arranged niobium filaments may at very low extent degrade their mechanical strength. As a result, the overall strength of the tensile test sample with $\eta = 4.97$, $T = 800^\circ\text{C}$, $t = 30$ min becomes lower than it should be. It is understood, however, that this phenomenon only occurs by a chance and not in general. Therefore, one can still expect the proper mechanical behavior of this sample at the absence of wide and long copper spacing.

The phenomenon of increasing $\sigma_{0.2}$ and σ_{UTS} with deformation in all samples can be related to the lowering of average interfilament spacing. Tables 5.3a and 5.3b show that for all samples, the average interfilament spacing decreases with increasing deformation. The appropriate theories to explain this situation are the barrier model [63-65] and the lamellar structures model [66]. These theories are reviewed in Chapter Three. As the average interfilament spacing becomes sufficiently small, the filaments become effective barriers for the matrix dislocations. According to Bevk et al. [67], the nature of barrier is induced by several reasons, such as the difference in slip systems in the two phases, the interactions



of the glide dislocations with the boundary dislocations, or even the change of elastic properties across the interface. As the spacing is reduced, the Frank-Read source will not be able to generate since the dislocation loops will be pinned down by the interphase boundaries. Similar to the results of hardness test, the decreasing values of $\sigma_{0.2}$ and σ_{UTS} in drawn-annealed samples (figures 5.17 and 5.18) are more influenced by the recrystallized copper rather than niobium for a given deformation. Figures 5.17 and 5.18 also show the expected lowering sequence (top to bottom) from the drawn condition, to $T = 800^{\circ}\text{C}$; $t = 30\text{min}$, to $T = 800^{\circ}\text{C}$; $t = 60\text{ min}$, to $T = 1000^{\circ}\text{C}$; $t = 30\text{ min}$, and finally to $T = 1000^{\circ}\text{C}$; $t = 60\text{ min}$. It agrees well with the fact that the longer (the higher) heat-treatment time (temperature), the softer than the material. Unlike the results of hardness test, the gradually increasing values $\sigma_{0.2}$ and σ_{UTS} in the drawn-annealed samples with deformation have been more influenced by the decreasing interfilament spacing rather than by the strength of niobium phase. At least within the observed deformation range ($2.08 < \eta < 4.97$), the strength of the niobium filaments is important, in such a way, that the interface capability as a dislocation barrier can be related to its strength. Its direct influence to the overall strength is more significant with increasing filament volume fraction (i.e. at very high deformation).

Figures 5.19 and 5.20 show how the supersaturation of recrystallization does not any longer affect the change in $\sigma_{0.2}$ and σ_{UTS} with increasing annealing time, for a given deformation and annealing temperature. Despite the by-chance deviation exhibited by the sample with $\eta = 3.95$, $T = 800^{\circ}\text{C}$, $t = 30\text{ min}$, the lowering sequence of $\sigma_{0.2}$ and σ_{UTS} (top to bottom) in figures 5.19 and 5.20 for a given annealing time should follow $\eta = 4.97$ (800°C), $\eta = 4.97$ (1000°C), $\eta = 3.95$ (800°C), and finally $\eta = 3.95$ (1000°C). This situation is quite surprising, especially when one thinks that the combined effect of dynamic recrystallization and static primary recrystallization should be the highest at $\eta = 4.97$. Unlike that for microhardness results (figures 5.10 and 5.12), the reasonable explanation for such phenomena in figures 5.19 and 5.20 does not originate from the niobium's property. Instead, it still depends on the size of interfilament spacing. Even though no statistical analysis had been conducted for samples annealed at $T = 1000^{\circ}\text{C}$, it is highly suspected that the average interfilament spacing at this temperature is higher than that at $T = 800^{\circ}\text{C}$. In other words, there are more large spacings in samples annealed at $T = 1000^{\circ}\text{C}$ than at $T = 800^{\circ}\text{C}$ for a given annealing time and deformation, and hence the

lower probability for dislocation pinnings and multiplications to occur and to provoke the material strengthening.

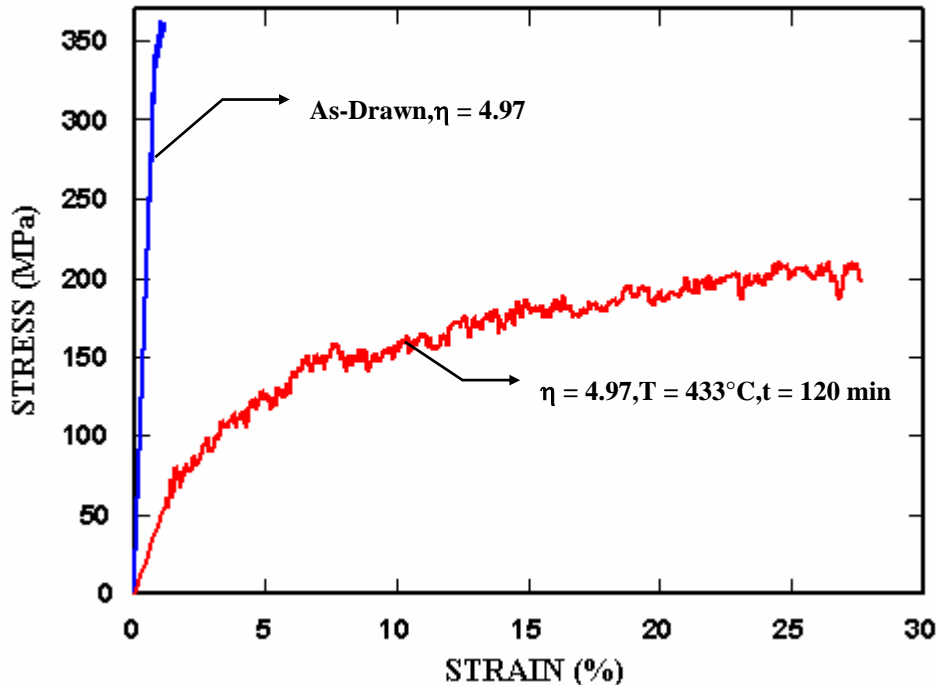


Figure 6.15 The stress strain curve of the drawn copper sample with $\eta = 4.97$ and the drawn-annealed one with $\eta = 4.97$, $T = 433^\circ\text{C}$, $t = 120 \text{ min}$.

It is interesting to observe how niobium particles (figure 6.16) can affect the failure of sample during the tensile testing. These particles, found at the fracture surface, can be the result of : the insufficient melting temperature during copper-niobium melting process (as also observed by Raabe et al. [2] at the fracture surface of the broken Cu-20%Nb wire during drawing), the non-homogeneous plastic deformation across the wire during drawing, the spheroidization, or a combination of the three. According to Decker [68], the initiation of microcracks can be greatly influenced by the presence of second-phase particles. Fine dispersions of particles result in increased toughness under proper circumstances. In this case, the slip distance is greatly reduced by a dispersion of fine impenetrable particle so that the number of dislocations that can be sustained in a pile-up is reduced. It is then assumed that, the large or spheroidized particles in figure 6.16 provoke the formation of relatively large dislocation pile-ups through strain localization or locally high plastic deformation, which leads to high stresses and easy initiation of microcracks.

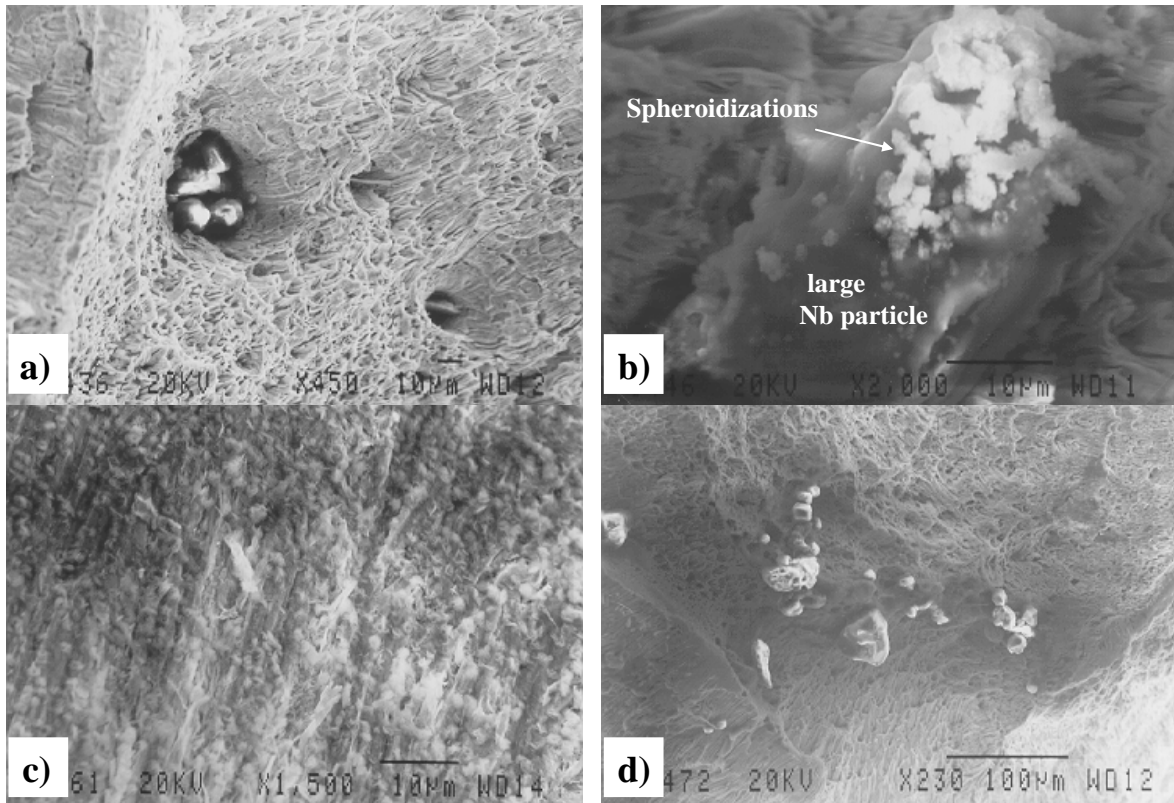


Figure 6.16 The large or spheroidized niobium particles *on the fracture surfaces* of the drawn-annealed Cu-18%Nb samples with : a) $\eta = 3.95$, $T = 800^\circ\text{C}$, $t = 30$ min, b) $\eta = 3.95$, $T = 800^\circ\text{C}$, $t = 60$ min, c) $\eta = 3.95$, $T = 1000^\circ\text{C}$, $t = 30$ min, and d) $\eta = 3.95$, $T = 1000^\circ\text{C}$, $t = 60$ min.

6.4 Cahn-Hilliard Simulation

6.4.1 Appropriate Parameters

It is necessary to firstly describe all the possible factors that can derive a negative concentration during the numerical calculation of the Cahn-Hilliard simulation in the copper-niobium system. If the negative concentration is produced, the simulation program automatically ceases. These factors include those such as :

- The initial concentrations (C_m^0 and C_p^0) in the range of extremely narrow mutual solid solubility or near equilibrium concentrations (far left side and far right side of the phase diagram). In this case, the negative concentration is yielded as the chemical potential is dominated by the entropy term (in form of natural logarithm) that exhibits a singularity as C_m and C_p approaches zero and unity respectively. By the thermal instability simulation, a good compromise has been found for $C_m^0 = 0.03$ and $C_p^0 = 0.90$.
- The spatial grid size (Δx) less than 1.00×10^{-4} m.
- The thermal perturbation (Δc) greater than 3.00×10^{-5} .



- The multiplication factor of mobility (M) greater than 10.

Moreover, the possible factors that can give unexpected results without deriving a negative concentration are those such as :

- The spatial grid size (Δx) greater than 1.00×10^{-4} m. Large Δx will principally give a large actual grid dimension. If it is the case, the kinetic and the diffusion processes become very slow and insignificant, since the actual mesh area has been too large.
- Too large or too small gradient energy coefficient (γ). When γ is too large, the diffusion process takes place very strongly and the niobium phase can diffuse away into copper phase leaving no trace of precipitation at all. Conversely, when γ is too small, the diffusion process does not have much access to propagate, since γ represents a diffusive concentration gradient across the interface. As a result, very little or very slow precipitation or thermal instability will be observed.
- The inappropriate combination between the grid size and γ , even for $\Delta x = 1.00 \times 10^{-4}$ m. Its effect is similar to that when γ is either too large or too small. In this case, the optimal 500 J/m and 100 J/m for 128 x 128 grid size become too strong for 32 x 32 grid size. This aspect is crucial when one considers the simulation of niobium thermal instability, which gives good and reasonable results using 32 x 32 grid size. A reasonable compromise of gradient energy coefficient has been found for the thermal instability simulation with $\gamma = 70$ J/m. This situation also implies that the derivation of γ using equation 4-13 is apparently not appropriate in this copper-niobium simulation. For $\sigma = 1.00$ J/m² (a rough approximation for copper-niobium system), the value of γ after equation 4-13 is about 5.00×10^{-8} J/m. Such value becomes too small either for precipitation or thermal instability simulation and has no significant effect.

6.4.2 Simulation of Niobium Precipitation in Copper

The copper-niobium precipitation simulation at $T = 1000^\circ\text{C}$ is shown in figures D1 to D4 of the Appendix D. As the value of γ increases (from 100 J/m to 500 J/m), the initial decomposition shifts into a later stage (from $t = 3000$ sec to $t = 9000$ sec). This situation can be argued firstly from the thermodynamic of nucleation. Nucleation in solids, as in liquids, is almost always heterogeneous [39]. The driving force for the heterogeneous nucleation is :



$$\Delta G_{\text{het}} = -V(\Delta G_v - \Delta G_s) + A\sigma - \Delta G_d \quad \text{Equation 6-4}$$

where :

ΔG_{het} = the total free energy change of heterogeneous nucleation

V = the volume of nucleus

ΔG_v = the volume free energy reduction

ΔG_s = the possible misfit strain energy increase

A = the area of interface

σ = the interfacial energy

ΔG_d = the possible defect energy reduction

It is clear from equation 6-4 that an increase in the interfacial energy (σ) can rise the total free energy change of nucleation (ΔG_{het}). For nucleation in solids, σ can vary widely from very low values for coherent interfaces to high values for incoherent interfaces. Further, the magnitude of interfacial energy also depends on the composition gradient across the interface [39,70,71], i.e. the gradient energy coefficient (γ). The differentiation of equation 6-4 yields the critical energy change necessary for nucleation to develop (ΔG_{het}^*). Moreover, the nucleation rate (N) has been proportional to ΔG_{het}^* according to the equation 6-5. Assuming a constant temperature, equation 6-5 shows that increasing ΔG_{het}^* will lower the nucleation rate and vice versa. In other words, higher gradient energy coefficient will result in slow nucleation growth. This situation generally can explain the shift of initial decomposition of niobium into a later stage with increasing γ .

$$N \propto \exp\left(\frac{-\Delta G_{\text{het}}^*}{kT}\right) \quad \text{Equation 6-5}$$

Physically, the gradient energy coefficient represents the composition gradient across the interface and thus provides how long the diffusive path will be. For the same kinetic rate (the same temperature, mobility and initial compositions), the initial stage of decomposition is earlier to attain with smaller γ (i.e. shorter diffusive barrier).

During the decomposition process, a resulted precipitate may act as a nucleus for the surrounding undeveloped matrix. In reality, the nucleation rate may fluctuate : initially it will be low, then gradually rise, and finally lower again as the nuclei begin to grow and reduce the supersaturation of the remaining matrix [39]. It is then suspected that such



fluctuation can also act more locally, i.e. differs from several precipitates to others. When the nucleation rate is relatively high, such fluctuation may have significant impact on the resulted morphology of nucleus. In this case, the difference between the highest nucleation rate (peak) and the lowest one (valley) is distinct. Presumably, the irregularity in morphology and distribution of precipitations in figures D1e and D2e (with $\gamma = 100$ J/m) has been resulted from such nucleation rate fluctuation. The concentration profiles in figures 5.22 and 5.23 uphold the aspect of irregular precipitation distribution with the $\gamma = 100$ J/m. Conversely, the effect of this fluctuation becomes relatively insignificant when the nucleation rate is already low (with high γ). The concentration profiles in figures 5.24 and 5.25 support the symmetrical distribution of precipitation with $\gamma = 500$ J/m.

With a relatively high nucleation rate and a short diffusive barrier, the formation of one precipitate and subsequent ones becomes faster. As a result, relatively thin precipitates occur together with the formation of low interparticle distances. When the aspect ratio of the resulted precipitate is high, the Rayleigh instability can take place and a string of spheres will be developed. Moreover, when the interparticle distances are low, the neighboring precipitates may easily coalesce with one another as they ripen or grow. This situation is depicted in figures D1d-e and D2d-e. For a given time and region, the total surface area of small and close precipitates is naturally larger than that of big and rarely distanced ones. This situation is described in table 5.8 in term of precipitate volume fraction. The higher precipitate volume fraction with increasing initial precipitate concentration (C_p^0) occurs as the initial nucleus with $C_p^0 = 0.90$ reaches the equilibrium concentration first and then experiences the Rayleigh instability and the Ostwald ripening (i.e. increase in the surface area). Figures D3e and D4e show how the resulted structures of niobium are the same in both figures, except the size of initial nucleus which is slightly bigger in figure D4e than in figure D3e.

6.4.3 Simulation of Niobium Thermal Instability in Copper

Figures D5 to D19 show the results of thermal instability of niobium in the copper phase at $T = 1000^\circ\text{C}$. As previously mentioned, the basic difference between the precipitation simulation and the thermal instability simulation is the initial matrix and precipitate compositions. A good compromise without yielding a negative concentration has been found for $C_m^0 = 0.03$ and $C_p^0 = 0.90$. Nevertheless the kinetic rate of thermal

instability appears to be low with 128 x 128 grid size, even using $\gamma = 100 \text{ J/m}$ and 500 J/m . In this case, no sphere dropping has been observed even up to $t = 9000 \text{ sec}$. This problem can then be overcome using a smaller grid size. However, the value of γ must also be reduced to avoid a strong interdiffusion process. The following combination of necessary parameters has been found to yield the simulation results comparable to those of experiments :

- $\Delta x = 1.00 \times 10^{-4} \text{ m}$
- $\Delta c = 3.00 \times 10^{-5}$
- $\gamma = 70 \text{ J/m}$
- Mobility (M) = 10 x the value after the Nernst-Einstein equation (ratio = 10 : 1)
- Grid size = 32 x 32 (should be in the form of $2^n \times 2^n$)
- Inclusion size = 2 x length (the length should be of an even number)

A slight increase in the width of precipitate/inclusion (W) from 2 to 4 results in a slow thermal instability, especially at large aspect ratio (L/W). As the L/W increases, the grid size should also be increased properly. Instead of using a square grid size, a rectangular grid size has been preferred to minimize the mesh area. Nevertheless, the height of grid can not be too small (slightly larger than W) to avoid side effect especially during the Ostwald ripening process, as shown in figure 6.17.

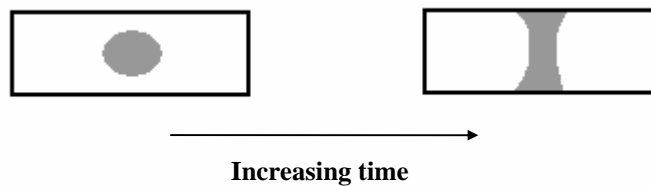


Figure 6.17 The side effect when the grid height is slightly larger than the precipitate width.

The thermal instability process observed during the simulation has been the ridge nucleation, sphere dropping and the Ostwald ripening. All of these processes are clear and also observed in Cu-18%Nb samples after annealing (see section 6.2.2 and Appendix B). The ridge nucleation and sphere dropping also represent the thermal instability of plate-like structure viewed in the transverse section, i.e. due to the edge spheroidization. No grooving, bamboo structure, and boundary splitting have been observed, since the present Cahn-Hilliard simulation does not account for the occurrence of internal boundary. Even



for a large aspect ratio, the dropping of spheres from both ends of inclusion is one at a time without accompanied by sinusoidal perturbations or grooving phenomena along the undeveloped inclusion length (flat area). Nevertheless, such results are in the good agreement with the observed ridge nucleation and sphere dropping processes in the drawn-annealed Cu-18%Nb samples, especially at $\eta = 2.08$ (see Appendix B). Moreover, the simulation results are also comparable to those of experiments in term of the annealing time. The formation of sphere(s) between $t = 3000$ sec and 6000 sec in figures D5 to D19 can represent or go side by side with the observed sphere droppings in the Cu-18%Nb samples after annealing at $t = 3600$ sec.

The development of a single sphere (cylinderization) has been observed with the aspect ratio (L/W) up to 13.00 (figure D11). This result is in contrast to that after Rayleigh [35] and McLean [72], who show that a single sphere is produced for $L/W < 7.20$. On the other hand, this simulation result is in a good agreement with the cylinderization process after the two-dimensional finite difference analysis by Lee and Courtney [73], who show that the cylinderization occurs up to $L/W = 14.00$. It seems that the formation of depression (for instance : figures D8f, D9f, D10f, and D11g) can not provoke the splitting process. Instead, the direction of mass flow reverses, and an equilibrium circular shape is reached.

Based on the average sphere size at $t = 6000$ sec (for instance), the average inclusion area has been calculated and plotted against the aspect ratio (figure 6.18). For $L/W > 13.00$, the inclusion area is obtained by the summation of those of resulting spheres. It is obvious from figure 6.18 that the inclusion area at $t = 6000$ sec is higher than that at $t = 0$ sec for $9.00 \leq L/W \leq 13.00$, and vice versa outside this aspect ratio range. It means that somehow the kinetic and diffusion processes for $9.00 \leq L/W \leq 13.00$ have been increased so that the resulting inclusion area for a given time is higher than the original inclusion area. Regardless of the aspect ratio, such process is possible only through the development of a single sphere instead of two.

The increase in average sphere size for $L/W \leq 13.00$ at $t = 6000$ sec (figure 5.26) is related to the increase in inclusion length. Such situation is schematically depicted in figure 6.19. In this case, the increasing sphere area correlates to the mass transport from both ends of inclusion to regions above and below the common area. The larger the length

(L) of inclusion, the higher the amount of transported mass and, thus, the larger the resulting sphere.

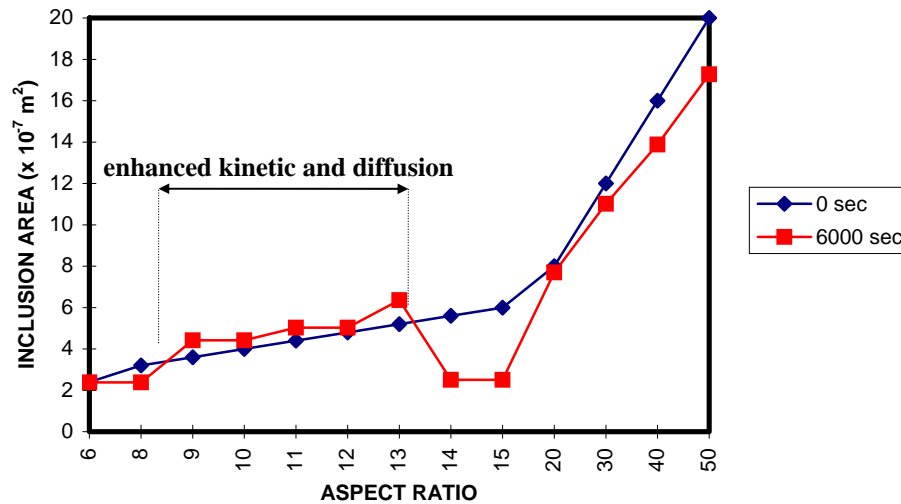


Figure 6.18 The inclusion area as a function of aspect ratio at t = 0 sec and 6000 sec.

Figure 5.27 shows the number of resulted spheres as a function of aspect ratio. It is shown that two plateaus are present, corresponding to $1.00 \leq L/W \leq 13.00$ (the number of resulted sphere is one) and $14.00 \leq L/W \leq 20.00$ (the number of resulted spheres is two). For $L/W \geq 30.00$, the number of spheres increases rapidly.

The diminishing small sphere and the growth of large sphere according to the Ostwald ripening mechanism are shown in figures D14 and D16. Again, as discussed by Gleiter [37], an array of inclusions with different sizes can interact since the concentration of solute atoms surrounding the small (large) particles is higher (lower) than the average supersaturation. The solutes then flow from the smaller to the larger particles. As a result, the smaller particles shrink and larger particles grow at the expense of small ones. When the particle is sufficiently small, it can then vanish by diffusing away into the matrix. This process also upholds the fact that some large interfilament spacings can be developed after annealing.

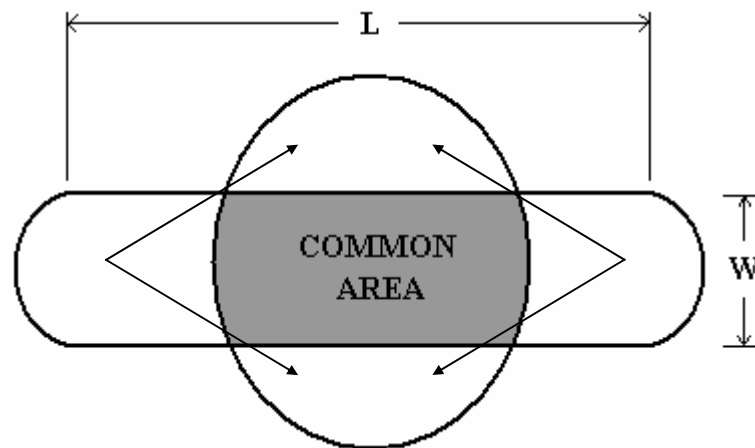


Figure 6.19 The schematic representation of a mass transport during the cylinderization.

From this stand point, it is well understood that the simulation of phase evolution based on the Cahn-Hilliard equation takes the simplest form of diffusion process. It means that, regardless of the shape of inclusion or precipitate (i.e. square, rectangular or ridge) and its size (low or high aspect ratio), the resulted thermal instabilities will always be sphere dropping and the Ostwald ripening. Such instabilities do not take into account the formation of grooving, boundary splitting, bamboo structure, or edge spheroidization (with respect to the longitudinal section, i.e. the formation of string of small spheres along the edge of inclusion). To be more reliable, much more closely representing the reality, and able to compete with the other methods of microstructure-evolution simulation, this Cahn-Hilliard simulation program has to be accordingly modified. The apparently first possible step is to improve the main program itself so that it can accommodate the presence of internal boundaries within the inclusion during the simulation initiation (i.e. especially true for the thermal instability simulation). By means of the C programming language, these boundaries can also be applied randomly in the inclusion. Such boundaries will be areas in the inclusion (with the thickness of several mesh points) that feature the same or higher mobility than the interphase. As the simulation runs, one can expect that the diffusion will take place along these boundaries as well as in the interphase. As the results, the grooving and the boundary splitting can take place. For the precipitation simulation, Löchte et al. [70] suggests the improvement of C-H model to include effects of non-equilibrium vacancy concentrations on precipitation kinetics that is connected to nucleation models. Moreover, the numerical algorithms for the solution of Cahn-Hilliard equation should also be improved to overcome the problem of singularity resulting in the derivation of negative



concentration. By solving such problem, the Cahn-Hilliard simulation program should be applicable to any alloy systems regardless of their mutual solid solubility behaviors. Finally by adjusting appropriate parameters (i.e. grid size and mobility) to attain good and reasonable simulation results (close to those of experiment) without inducing a negative concentration, the Cahn-Hilliard simulation program can simultaneously predict the gradient energy coefficient of an alloy system.



References

1. Raabe, D. : Dissertation, Fakultät für Bergbau, Hüttenwesen und Geowissenschaften, RWTH Aachen-Germany (1992).
2. Raabe, D.; Heringhaus, F.; Hangen, U.; and Gottstein, G. : Z. Metallkd. **86** (1995) 405.
3. Chalmers, B. : "Principles of Solidification", Wiley (1964) 116.
4. Wassermann, W.; and Greven, J. : "Texturen metallischer Werkstoffe", Springer-Verlag (1992).
5. Heringhaus, F. : Diplomarbeit, Institut für Metallkunde und Metallphysik, RWTH Aachen-Germany (1994).
6. Dieter, G.E. : "Mechanical Metallurgy", McGraw-Hill **3** (1986).
7. Cahn, R.W.; Haasen, P.; and Kramer, E.J. : in : H. Mughrabi (ed.) : "Material Science and Technology : Plastic Deformation and Fracture of Materials", VCH **6** (1991).
8. Hangen, U.D. : Diplomarbeit, Mathematisch-Naturwissenschaftlichen Fakultät, RWTH Aachen-Germany (1994).
9. Pelton, A.R.; Laabs, F.C., Spitzig, W.A.; and Cheng, C.C. : Ultramicroscopy **22** (1987) 251.
10. Smith, W.F. : "Principles of Materials Science and Engineering", McGraw-Hill **3** (1996).
11. Köhlhoff, G.D.; and Gottstein, G. : in : G. Gottstein (ed.) : "Rekristallisation metallischer Werkstoffe : Grundlagen, Analyse, Anwendung", Deutsche Gesellschaft für Metallkunde (1984) 39.
12. Dehlinger, U. : Metallw. **7** (1928) 1172.
13. Burgers, W.G.; and Louwse, P.C. : Z. Physik **61** (1931) 605.
14. Burgers, W.G. : in : G. Masing (ed.) : "Handbuch der Metallphysik", Akademische Verlagsgesellschaft Leipzig **III/2** (1941).
15. Burgers, W.G.; and Tiedeman, T.J. : Acta metall. **1** (1953) 234.
16. Dehlinger, U. : Z. Metallkd. **52** (1961) 44.
17. Hutchinson, W.B. : Metal Science **8** (1974) 185.
18. Hu, H. : in J. Grewen, G. Wassermann (eds.) : "Texturen in Forschung und Praxis", Springer-Verlag Berlin (1969) 200.
19. Dillamore, I.L.; and Katoh, H. : Metal Science **8** (1974) 73.



20. *Ridha, A.A.; and Hutchinson, W.B.* : Acta metall. **30** (1982) 1929.
21. *Huber, J.; and Hatherly, M.* : Metal Science **13** (1979) 665.
22. *Huber, J.; and Hatherly, M.* : Z. Metallkd. **71** (1980) 15.
23. *Humphreys, E.J.; and Juul Jensen, D.* : in : Hansen, N., D. Juul Jensen, T. Leffers, B. Ralph (eds.) : "Annealing Processes - Recovery, Recrystallization and Grain Growth", 7th Risø International Symposium (1986) 93.
24. *Liebmann, B.; Lücke, K.; and Masing, G.* : Z. Metallkd. **47** (1956) 57.
25. *Hirsch, J.R.* : Habilitation, Fakultät für Bergbau, Hüttenwesen und Geowissenschaften, RWTH Aachen-Germany (1988) 33.
26. *Hirsch, J.R.* : in : G. Gottstein (ed.) : "Rekristallisation metallischer Werkstoffe : Grundlagen, Analyse, Anwendung", Deutsche Gesellschaft für Metallkunde (1984) 173.
27. *Stadelmaier, H.; and Brown, B.F.* : Z. Metallkd. **47** (1956) 1.
28. *Burgers, W.G.; and Verbraak, C.A.* : Acta metall. **5** (1957) 765.
29. *Verbraak, C.A.* : Z. Metallkd. **51** (1960) 646.
30. *Verbraak, C.A.* : Acta metall. **8** (1960) 56.
31. *Rowland, P.R.* : J. Inst. Metals **83** (1954) 455.
32. *Beck, P.A.; and Hu, H.* : in : H. Margolin (ed.) : "Recrystallization, Grain Growth and Textures", ASM Metals Park-Ohio (1966) 393.
33. *Gottstein, G.* : "Physikalische Grundlagen der Materialkunde", Springer-Verlag (1998).
34. *Courtney, T.H.* : in : N. Haasen (ed.) : "Metal Matrix Composites - Processing, Microstructure, and Properties", 12th Risø International Symposium on Materials Science, (1991) 17.
35. *Rayleigh, L.* : Proc. London Math. Soc. **10** (1878) 4.
36. *Courtney, T.H.; and Malzahn Kampe, J.C.* : Acta metall. **37** (1989) 1747.
37. *Gleiter, H.* : in R.W. Cahn; and P. Haasen (eds.) : "Physical Metallurgy", 4th ed., North-Holland (1996) 844.
38. *Malzahn Kampe, J.C.; Courtney, T.H.; and Leng, Y.* : Acta metall. **37** (1989) 1735.
39. *Porter, D.A.; and Easterling, K.E.* : "Phase Transformations in Metals and Alloys", 2nd ed., Chapman&Hall (1992).
40. *Hosford, W.F.Jr.*: Trans. TMS AIME **230** (1964) 12.
41. *Hangen, U.D.* : Diplomarbeit, Mathematisch-Naturwissenschaftlichen Fakultät, RWTH Aachen-Germany (1994).



42. Clarebrough, L.M.; Hargreaves, M.E.; and Loretto, M.H. : in : L. Himmel (ed.) : "Recovery and Recrystallization of Metals", Interscience Publishers (1963) 63.
43. J̄esior, J-C. : Scann. Micros. Supp. **3** (1989) 147.
44. J̄esior, J-C. : J. Ultrastruct. Res. **90** (1985) 135.
45. J̄esior, J-C. : J. Utrastruct. Molec. Struct. Res. **95** (1986) 210.
46. Courtney, T.H. : "Mechanical Behavior of Materials", McGraw-Hill (1990).
47. Barreto, M.P.; Veillette, R.; and L'esperance, G. : Micros. Res. Tech. **31** (1995) 293.
48. Hertzberg, R.W. : "Deformation and Fracture Mechanics of Engineering Materials", John-Wiley&Sons **4** (1996) 111.
49. Spitzig, W.A.; and Krotz, P.D. : Scripta metall. **21** (1987) 1143.
50. Mehl, R.F. : "Metals Handbook", American Society for Metals-Ohio, (1948) 259-268.
51. Sevillano, J.G.; Van Houte, P.; and Aernoudt, E. : Prog. Mat. Sci. **25** (1981) 69.
52. Kuhlmann-Wilsdorf, D. : Trans. AIME **224** (1962) 1047.
53. Gottstein, G.; Zabardjadi, D.; and Mecking, H. : Metal Science **13** (1979) 223.
54. Gottstein, G.; and Kocks, U.F. : Acta metall. **31** (1983) 175.
55. Sample, V.M.; Fitzsimons, G.L.; and DeArdo, A.J. : Acta metall. **35** (1987) 367.
56. Wantzen, A.; Karduck, P.; and Gottstein, G. : in : P. Haasen, G. Gerold, and G. Kostorz (eds.) : "Strength of Metals and Alloys", Pergamon Press, NY (1979) 517.
57. Cairnes, J.H.; Clough, J.; Dewey, M.A.P.; and Nutting, J. : J. Inst. Met. **99** (1971) 93.
58. Flaquer, J.; and Sevillano, J.G. : J. Mat. Sci. **19** (1984) 423.
59. Sevillano, J.G.; and Aernoudt, E. : Mat. Sci. Eng. **86** (1987) 35.
60. Spitzig, W.A.; Pelton, A.R.; and Laabs, F.C. : Acta metall. **35** (1987) 2427.
61. Verhoeven, J.D.; Downing, H.L.; Chumbley, L.S.; and Gibson, E.D. : J. App. Phys. **65** (1989) 1293.
62. Kvam, E.P. : Scripta Metall. **23** (1989) 1341.
63. Li, J.C.; and Chou, Y.: Metall. Trans. **1** (1970) 1145.
64. Li, J.C. : Trans. Amer. Inst. Min. Eng. **227** (1963) 239.
65. Embury, J.D.; and Fisher, R.M. : Acta metall. **14** (1966) 147.
66. Koehler, J.S. : Phys. Rev. **2(2)** (1970) 547.
67. Bevk, J.; Harbison, J.P.; and Bell, J.L. : J. Appl. Phys. **49(12)** (1978) 6031.
68. Decker, R.F. : Metall. Trans. **4** (1973) 2508.
69. McQueen, H.J.; and Jonas, J.J. : Treat. Mat. Sci. Tech. **6** (1975) 394.



70. Löchte, L.; Gitt, A.; Gottstein, G.; and Hurtado, I. : Acta mater. **48** (2000) 2969.
71. Gitt, A.F. : Diplomarbeit, Mathematisch-Naturwissenschaftlichen Fakultät, RWTH Aachen-Germany (1997).
72. McLean, M. : Met. Sci. J. **12** (1978) 113.
73. Lee, K.; and Courtney, T.H. : Met. Trans. **20A** (1989) 1385.



CHAPTER SEVEN

SUMMARY

With respect to Chapters 5 and 6, some substantial points regarding the observed thermomechanical properties of Cu-18%Nb *in-situ* metal matrix composite (MMC) and the Cahn-Hilliard computer simulation of its phase evolution at high temperatures are presented in this chapter. Nevertheless, it is firstly necessary to generally mention the significance and the importance of copper-niobium metal matrix composites. The copper-niobium MMCs play an important role as highly potential candidate materials for the production of mechanically stressed electrical devices, since they have a good combination of high strength and good electrical conductivity. The Cu-20mass%Nb, for instance, is a very challenging material since it possesses a very high tensile strength that exceeds the expected value of rule of mixture (ROM). The composition of 18to20mass%Nb appears to have an optimum effect on the electrical and the mechanical properties of copper-niobium composites. Reducing the Nb content causes the lowering of strength, while increasing the Nb content leads to the degradation of ductility and electrical conductivity. The production of copper-niobium composites can be done through powder metallurgy (PM) method, quenching a liquid solution of two mutually insoluble components, or directionally solidifying eutectic phases. A sheet and a wire can then be manufactured from a compact or a cast block through the hot/cold rolling and the drawing process respectively, yielding the elongated niobium phase parallel to the deformation axis (similar to the duplex structure). According to the materials selection chart (MSC) for designing a pulse magnet, Cu-18to20%Nb falls into the category that is excellent for short to medium pulses of an intermediate to high field application.

The observed orientation of copper phase in the as-cast Cu-18%Nb has been random in nature. On the other hand, the niobium phase features the Goss texture of $\{hkl\}\langle 100 \rangle$ orientation, which is typical for the dendritic arms. As the cast Cu-18%Nb is drawn, the copper phase features the $\langle 111 \rangle$ and the weak $\langle 100 \rangle$ orientations, whereas the niobium phase exhibits the $\langle 110 \rangle$ orientation. For both phases, such orientations will not be stable and developed completely until high deformations.



The dynamic recrystallization in copper phase due to a heat generation during drawing process is characterized by a short decrease in the maximum intensity from $\eta = 2.08$ to $\eta = 3.01$, and the weak $\langle 100 \rangle$ orientation. A reincrease in the copper maximum intensity for $\eta > 3.01$ is influenced mostly by the orientations of copper cells (due to the dynamic recovery) trying to predominate into the $\langle 111 \rangle$ direction, whereas the orientations of grains (due to the dynamic recrystallization) stay stable in the $\langle 100 \rangle$ direction. In this case, the amount of cell structures (i.e. the extent of dynamic recovery) increases with deformation. The niobium phase exhibits a gradual increase in the maximum intensity towards $\langle 110 \rangle$ direction from $\eta = 2.08$ to $\eta = 3.01$ and a rapid one afterwards. Similar to that in Cu-20%Nb, such gradual increase is caused by a leisure rotation of niobium phase from the Goss texture $\{hkl\}\langle 100 \rangle$ to the $\langle 110 \rangle$ orientation.

The copper orientation in drawn/annealed Cu-18%Nb samples is still preferably toward the $\langle 111 \rangle$ and $\langle 100 \rangle$ directions, whereas that of niobium in the $\langle 110 \rangle$ direction. The copper and niobium maximum intensities of these samples generally increase with deformation. By copper matrix, this situation has been induced by the orientation dependency of recrystallization nuclei and the subsequent growth selection of recrystallized grains especially in the narrow interfilament spacings. Some deviations in the copper orientation distribution can be related to : the oriented nucleation in pre-existing deformation twinings and its subsequent growth, the orientation of resulted annealing twinings, or the grain growth of pre-existing deformation subgrains (due to the dynamic recovery). By niobium filaments, the maintained $\langle 110 \rangle$ direction and the increasing maximum intensity is initiated by the recovery process (due to the high stacking fault energy) followed by the orientation dependency of recrystallized grains.

Moreover, the positions of copper maximum intensities throughout the samples are significant with respect to deformation, i.e. : at $\eta = 2.08$ by $\langle 111 \rangle$ direction, at $\eta = 3.01$ and 3.95 by $\langle 100 \rangle$ direction, and finally at $\eta = 4.97$ again in $\langle 111 \rangle$ direction. These phenomena are related to the increasing (decreasing) amount of $\{100\}\langle 001 \rangle$ texture ($\{112\}\langle 11\bar{1} \rangle$ texture) with increasing annealing time for $\eta \geq 3.00$. At $\eta = 4.97$, the driving force for growth selections takes over the cube texture formation and, thus, the copper maximum intensity goes back to the highly stable $\langle 111 \rangle$ orientation.

The deformed copper grains (either in pure copper or Cu-18%Nb) have been elongated parallel to the drawing axis. A by-chance occurrence of a wide and long copper



phase in the Cu-18%Nb sample, due to the non-homogeneous plastic flow during the drawing process, can lead to the development of freely growing grains during annealing. Such grains can overcome the growth selection process and reduce the maximum intensity of copper. Moreover, such stupendous irregularity correspondingly results in the tightly arranged (densely packed) niobium filaments. During annealing, these filaments undergo a volume diffusion. As a result, the filaments easily fuse with one another causing the decrease in the niobium maximum intensity.

Some equiaxed grains are also observed within the narrow interfilament spacing. These grains are resulted from the densely arranged nuclei taking place at grain boundaries of extremely elongated copper grains. Nevertheless, such distribution of nuclei (i.e. the equiaxed grains) can not be guaranteed throughout the deformed matrix.

The thermal instabilities of niobium phase (observed under the scanning electron microscope) are summarized and listed in table 7.1.

| η | 800°C | | | 1000°C | | |
|--------|----------------------|--|--------|--|--------|--------|
| | 60 sec | 30 min | 60 min | 15 min | 30 min | 60 min |
| 2.08 | interplate diffusion | ridge nucleation, sphere dropping | | ridge nucleation, sphere dropping | | |
| 3.01 | interplate diffusion | planar interface growth, ridge nucleation, sphere dropping | | ridge nucleation, sphere dropping, planar interface growth, filament recrystallization, bamboo structure, edge spheroidization | | |
| 3.95 | interplate diffusion | boundary splitting, ridge nucleation, sphere dropping | | filament thickening (planar interface growth), filament recrystallization, bamboo structure, edge spheroidization | | |
| 4.97 | ... | boundary splitting, bamboo structure, edge spheroidization | | | | |

Table 7.1 The summary of filament thermal instabilities of Cu-18%Nb drawn/annealed samples.

The results, listed in the column $T = 800^\circ\text{C}$ ($t = 30$ min and 60 min), exhibit a good mutual correlation with the results of statistical analyses fitted to the Gauss normal distribution equation.

Under the transmission electron microscope, the deformation-related phenomena of dislocation forest, deformation twinning, and dynamically recrystallized grain along with dynamically recrystallized twinning have been observed in the transverse substructure of copper matrix within the drawn Cu-18%Nb samples. Furthermore, many well expected phenomena have been also observed within the drawn/annealed samples, such as : rounder shape of niobium filaments, copper cell structures, recrystallized copper grains, and copper



annealing twinings. The copper annealing twinings have been developed as the emerging grains encounter some packing sequence defects (such as stacking faults). The niobium phase mostly exhibits very fine or nanocrystalline substructures throughout the whole samples. Nevertheless, the application of high heating rate (such as in the salt bath furnace) may rapidly provoke the recovery-recrystallization of niobium filament, in contrast to the heat treatment in vacuum finger furnace.

Some unexpected results also take place within the drawn/annealed samples, which comprise the hardly disappearing dislocations and the apparently deformation twinings. These deviations arise the difficulty in TEM observations, since they interfere with preexisting phenomena in the samples. Such dislocations and deformation twinings have been induced by the compression during the ultramicrotomy (diamond cutting) process. In this case, the hardly disappearing dislocations are mostly the geometrically necessary dislocations introduced by the bending mechanism during the sample cutting. The deformation twinings, on the other hand, are resulted from the retardation of local slip systems due to the excessive combination of the statistically stored and geometrically necessary dislocations.

The gradually decreasing hardness of copper samples with increasing deformation accentuates the dynamic recrystallization. In this case, the extent of dynamic recrystallization increases with deformation. Conversely, the hardness of Cu-18%Nb samples appears to be constant throughout the observed deformation ($2.08 \leq \eta \leq 4.97$), due to the niobium's leisure rotation toward $\langle 110 \rangle$ direction. For a given deformation, the hardness of drawn/annealed samples is lower than that of drawn samples. This situation is much more provoked by the recrystallization of copper phase. The gradually increasing hardness of drawn/annealed samples with deformation is mostly caused by the increasing tendency of niobium orientation toward the $\langle 110 \rangle$ direction as well as the increasing portion (i.e. the volume fraction) of niobium filaments. As the annealing time increases, the hardness change is no longer sensitive to the microstructure. For a given annealing time, the hardness of Cu-18%Nb sample is influenced more by the hardness of niobium filaments rather than by that of copper phase. It means, the sample with $\eta = 4.97$ is the hardest one.

The amount of plastic deformation in copper wires (during the tensile testing) increases with increasing drawing deformation, whereas the σ_{UTS} and $\sigma_{0.2}$ gradually



decrease (the material gets softer). Such phenomena have been the results of dynamic recrystallization taking place during the drawing process and the tensile testing. The dynamic recrystallization is characterized by the presence of jagged phenomena in the S-S curve after yielding. During the drawing process, the dynamic recrystallization occurs according to the rapid nucleation and the diffusional dislocation climb provoked by the vacancy supersaturation. With the increasing drawing deformation, the dynamic recovery after the Orowan mechanism can also take place. Hence, the copper structure now features two different but beneficial sites for further dynamic recrystallization (i.e. during the tensile testing) to propagate, namely the preexistent dynamically recrystallized grains and the cell structures due to the dynamic recovery. At low temperature, the dynamic recrystallization can easily propagate during the tensile testing since the applied strain rate is low ($2 \times 10^{-3}/\text{sec}$).

The same process also happens to the drawn/annealed copper samples. However, the values of σ_{UTS} and $\sigma_{0.2}$ are lower due to the decrease in dislocation density during the heat treatment. The jagged phenomena in the S-S curve have now a higher amplitude compared to those in the drawn wires for the same drawing deformation. It occurs since the rapidly moving boundaries of the dynamically recrystallized nuclei must proceed through a larger distance before they reach the vacancy-depletion region (i.e. the boundary of large statically recrystallized grains or the boundary of growing neighboring nuclei). In this case, the larger distance simply corresponds to the average diameter of large statically recrystallized grains due to the heat treatment.

The values of σ_{UTS} and $\sigma_{0.2}$ of drawn and drawn/annealed Cu-18%Nb gradually increases with the deformation. This situation can be related to the lowering of average interfilament spacing. As the interfilament spacing becomes small, the filaments become effective barriers for the matrix dislocations. In this case, the Frank-Read source can not be able to generate since the dislocation loops will be pinned down by the interphase boundaries. The niobium's contribution to the overall strength is more significant with increasing filament volume fraction (i.e. at very high deformation). The lowering sequence of σ_{UTS} and $\sigma_{0.2}$ in drawn/annealed Cu-18%Nb samples (for a given annealing time) follows : $\eta = 4.97$ (800°C), $\eta = 4.97$ (1000°C), $\eta = 3.95$ (800°C) and $\eta = 3.95$ (1000°C), corresponding to the increasing average interfilament spacing.



Some niobium particles have been found at the fracture surfaces of some Cu-18%Nb samples. These particles originate from : the insufficient melting temperature, the non-homogeneous plastic deformation across the wire during drawing, the spheroidization, or a combination of the three. During the tensile testing, they can provoke the formation of relatively large dislocation pile-ups through locally high plastic deformation, leading to high stresses and easy initiation of microcracks.

For the Cahn-Hilliard (C-H) simulation at $T = 1273$ K utilizing the explicit numerical process, the following combined parameters have been found to yield good and reasonable results without deriving a negative concentration :

- the spatial grid size or the discretization length, $\Delta x = 1.00 \times 10^{-4}$ m
- the applied thermal perturbation concentration to induce concentration or phase evolution, $\Delta c = 3.00 \times 10^{-5}$ (in mole fraction)
- the grid size :
 - for the precipitation simulation :
 - 128 x 128 (i.e. equals 1.28 cm x 1.28 cm with respect to Δx)
 - for the thermal instability simulation :
 - ◆ 32 x 32 (i.e. equals 0.32 cm x 0.32 cm with respect to Δx)
 - ◆ 16×2^n ($n > 5$) for a larger inclusion's aspect ratio (L/W)
- the gradient energy coefficient (γ) :
 - $100 \text{ J/m} \leq \gamma \leq 500 \text{ J/m}$ for the precipitation simulation
 - 70 J/m for the thermal instability simulation
- the mobility (M) :
 - ratio = 1 : 1 for the precipitation simulation (i.e. simply the value of mobility after the Nernst-Einstein equation)
 - ratio = 10 : 1 for the thermal instability simulation (i.e. the value of mobility after the Nernst-Einstein equation times 10)
- the initial concentrations (C_p^0 and C_m^0) :
 - for the precipitation simulation :
 - ◆ $0.50 < C_p^0 < C_p^e$ (precipitation equilibrium concentration)
 - ◆ C_m^e (matrix equilibrium concentration) $< C_m^0 < 0.50$
 - for the thermal instability simulation :



$$\blacklozenge C_p^0 = 0.90$$

$$\blacklozenge C_m^0 = 0.03$$

■ the inclusion size :

- any reasonable nucleus dimension for the precipitation simulation
- $2 \times L$ (L of an even number, but not necessarily in the order of 2^n) for the thermal instability simulation

For the precipitation simulation, the initial decomposition shifts into a later stage (from $t = 3000$ sec to 9000 sec) as the γ increases (from 100 J/m to 500 J/m). It happens, since the higher γ will result in the higher total free energy change of nucleation, and consequently the slower nucleation growth. Moreover, increasing γ also means more access of diffusive path, since γ represents the composition gradient across the interface. At $\gamma = 100$ J/m, the precipitation morphology and distribution has been irregular as a result of the fluctuation of high nucleation rate. Conversely, the effect of such fluctuation in the low nucleation rate ($\gamma = 500$ J/m) is insignificant yielding more regular and symmetrical precipitation morphology and distribution. With a relatively high nucleation rate and a short diffusive path, the formation of one precipitate and subsequent ones becomes faster. This situation results in the thin precipitates and the low interparticle distances. Moreover, the higher C_p^0 will yield the higher precipitation volume fraction, since the nucleus reaches the equilibrium first and then experiences the Rayleigh instability and the Ostwald ripening mechanism (i.e. increase in the surface area).

The observed thermal instabilities during the C-H simulation have been the ridge nucleation, the sphere dropping, and the Ostwald ripening. These results are comparable to those of drawn/annealed Cu-18%Nb samples at $\eta = 2.08$ observed under SEM. No grooving, bamboo structure, and boundary splitting have been observed since the simulation does not account for the presence of internal boundary. The thermal instability simulation is in a good agreement with the experimental results in term of annealing time, especially for $3000 \text{ sec} \leq t \leq 6000 \text{ sec}$. The cylinderization (single sphere formation) process dominates up to the aspect ratio (L/W) of 13.00 . It is suspected that this situation has been provoked by the enhanced kinetic and diffusion processes for $9.00 \leq L/W \leq 13.00$. Furthermore, the increase in average sphere size during the cylinderization with

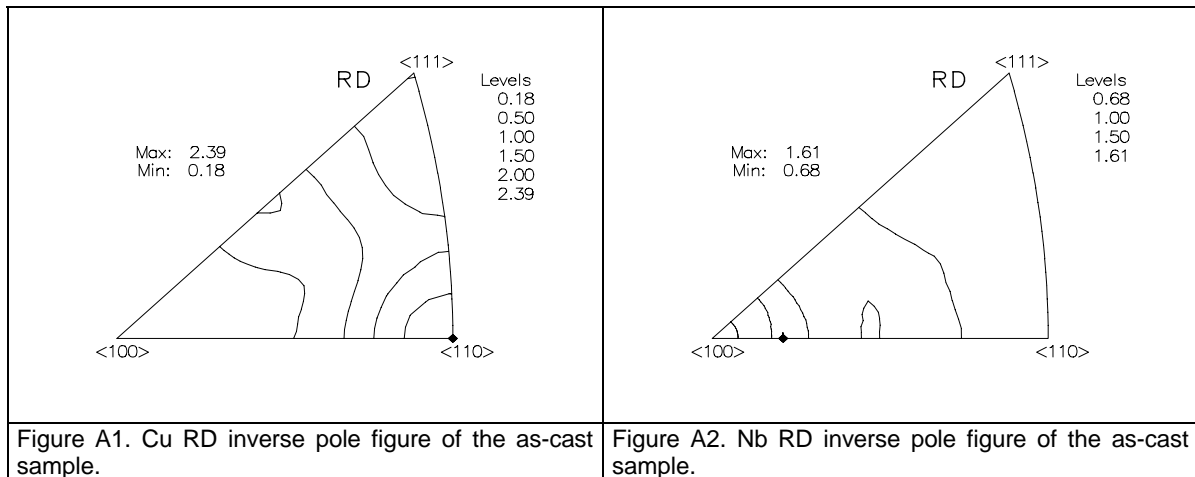


increasing aspect ratio is simply related to the increase in inclusion length. The number of resulted spheres also increases with the aspect ratio. Nevertheless, a rapid increase in the number of resulted spheres takes place not until $L/W \geq 30.00$. At $L/W = 20.00$ and 40.00 , the simulation also shows the process of diminishing small sphere and the growing of large sphere with respect to the Ostwald ripening mechanism.

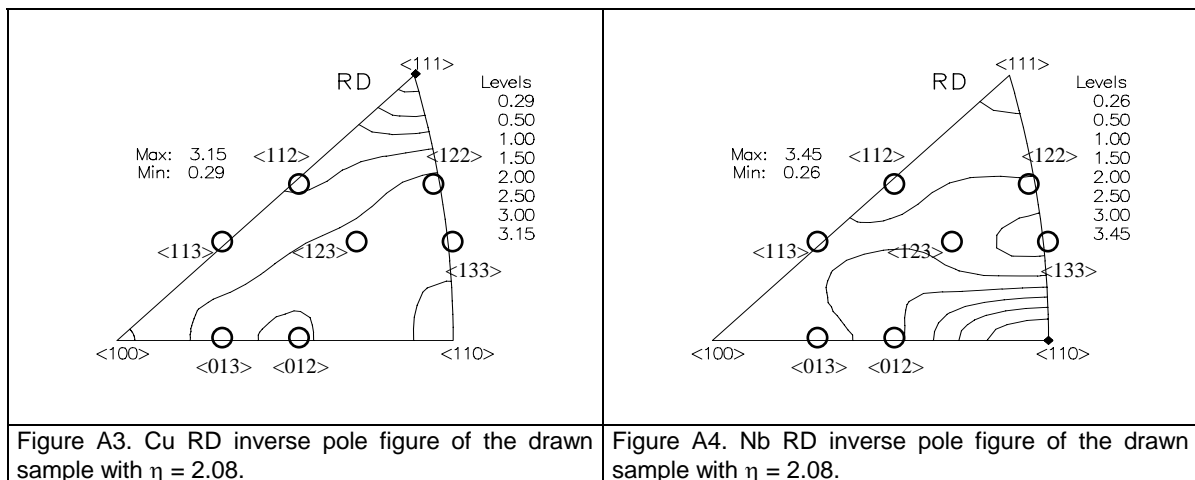
APPENDIX A

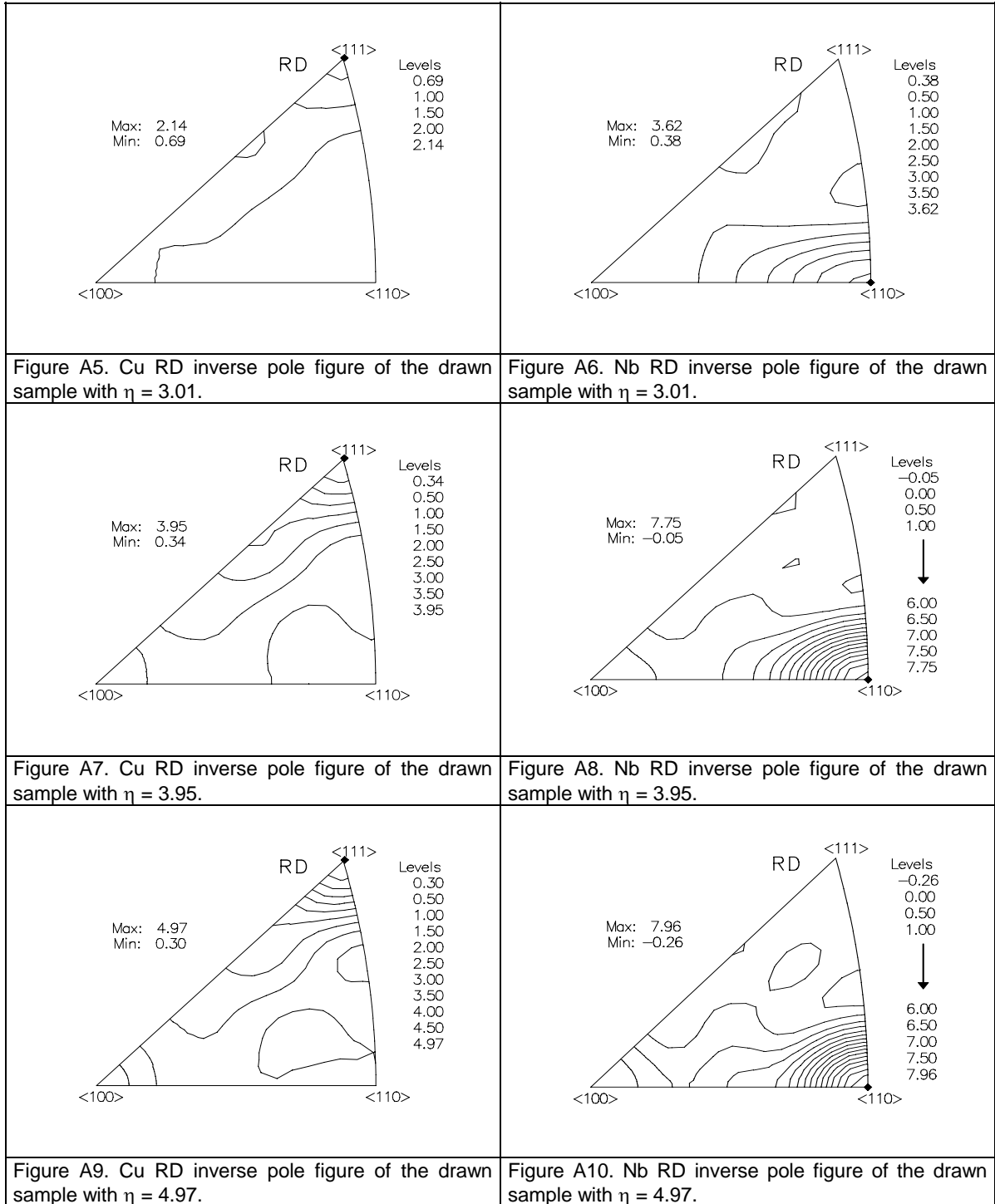
MACROTEXTURE RESULTS

1. As-Cast Cu-18%Nb



2. As-Drawn Cu-18%Nb





3. Drawn-Annealed Cu-18%Nb at T = 600°C

3.1 T = 600°C, t = 12 hr

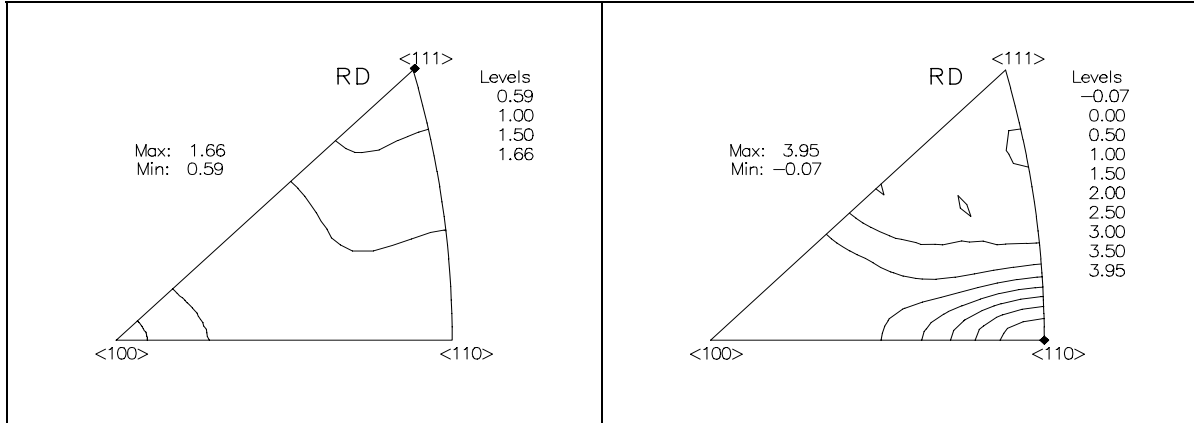


Figure A11. Cu RD inverse pole figure of the drawn-annealed sample with $\eta = 2.08$, T = 600°C, t = 12 hr.

Figure A12. Nb RD inverse pole figure of the drawn-annealed sample with $\eta = 2.08$, T = 600°C, t = 12 hr.

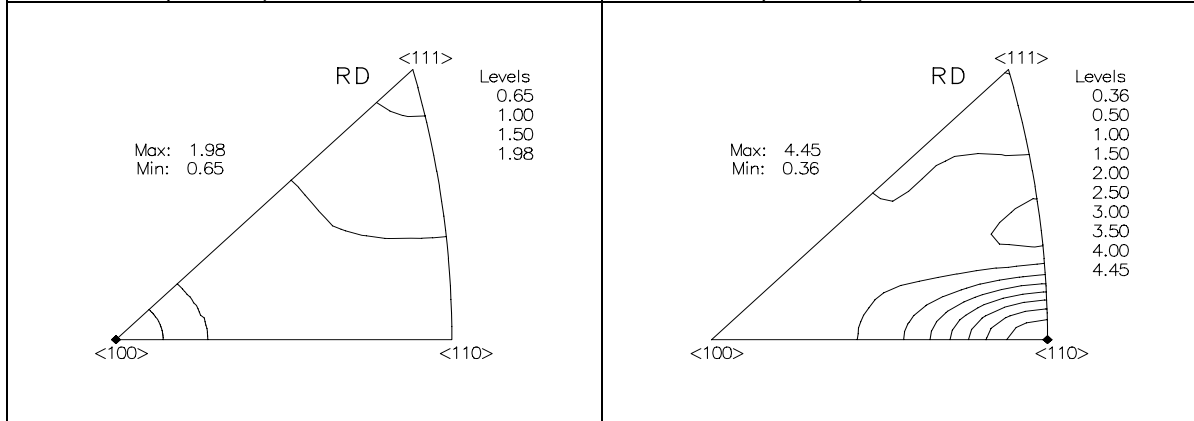


Figure A13. Nb RD inverse pole figure of the drawn-annealed sample with $\eta = 3.01$, T = 600°C, t = 12 hr.

Figure A14. Nb RD inverse pole figure of the drawn-annealed sample with $\eta = 3.01$, T = 600°C, t = 12 hr.

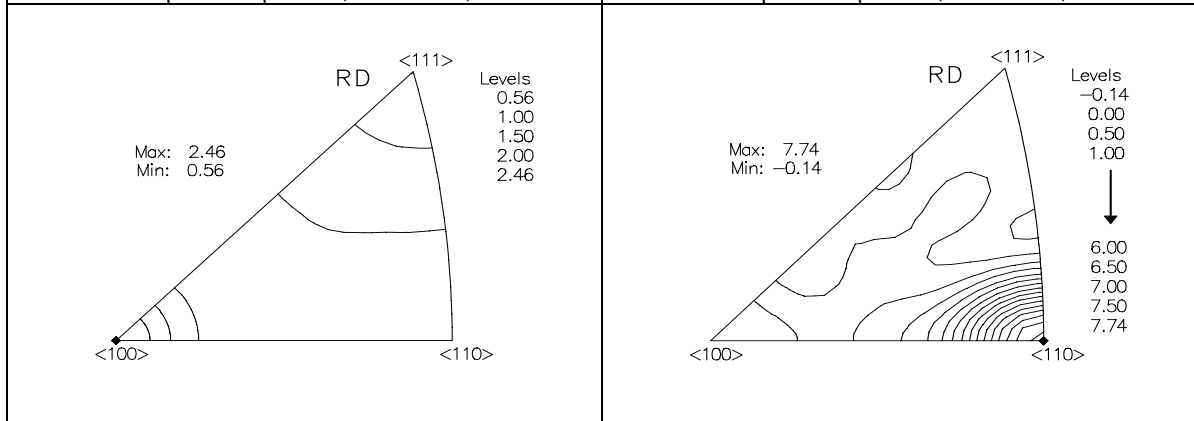
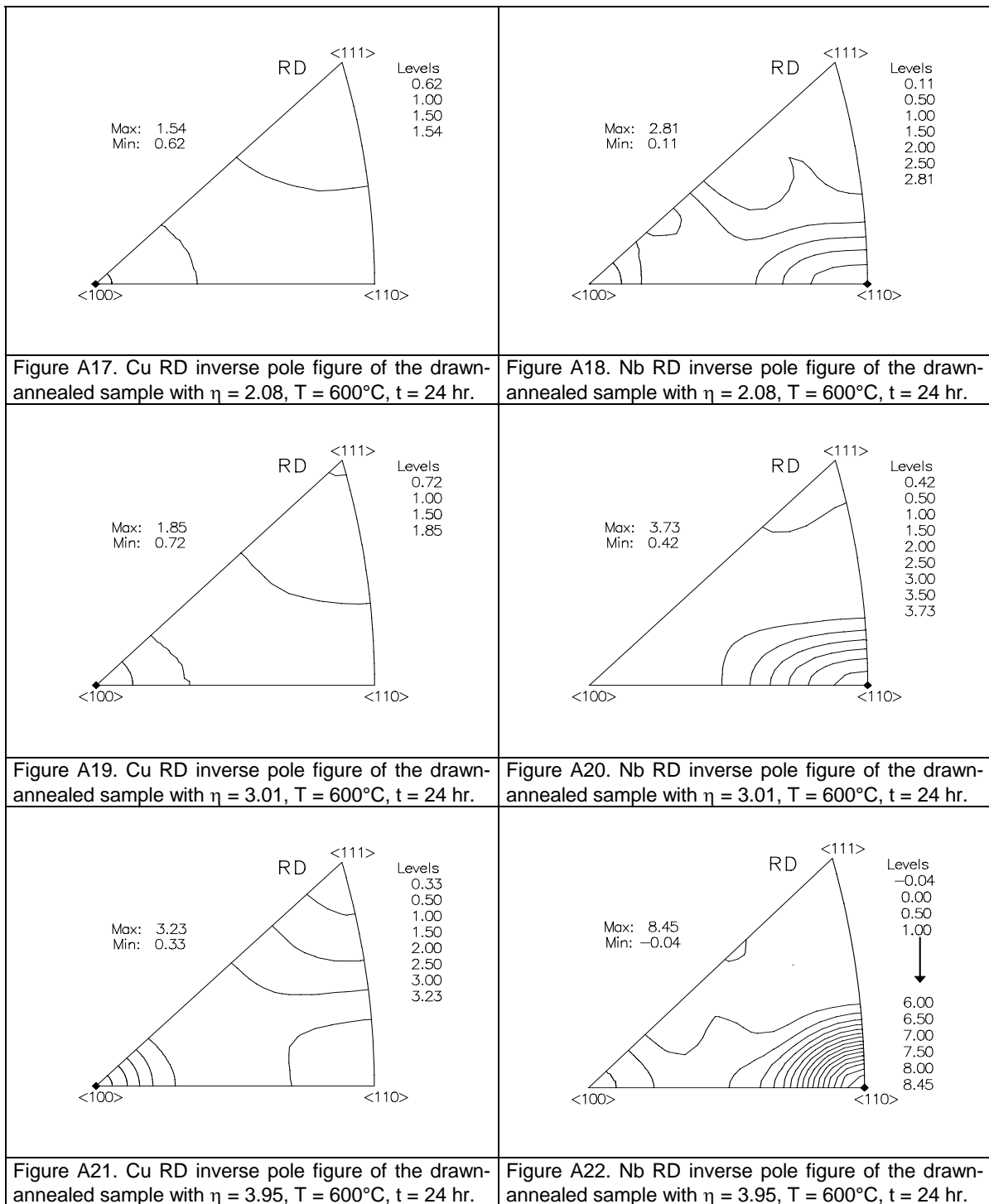


Figure A15. Cu RD inverse pole figure of the drawn-annealed sample with $\eta = 3.95$, T = 600°C, t = 12 hr.

Figure A16. Nb RD inverse pole figure of the drawn-annealed sample with $\eta = 3.95$, T = 600°C, t = 12 hr.



3.2 $T = 600^{\circ}\text{C}$, $t = 24 \text{ hr}$



4. Drawn-Annealed Cu-18%Nb at $T = 800^{\circ}\text{C}$

4.1 $T = 800^{\circ}\text{C}$, $t = 30 \text{ min}$

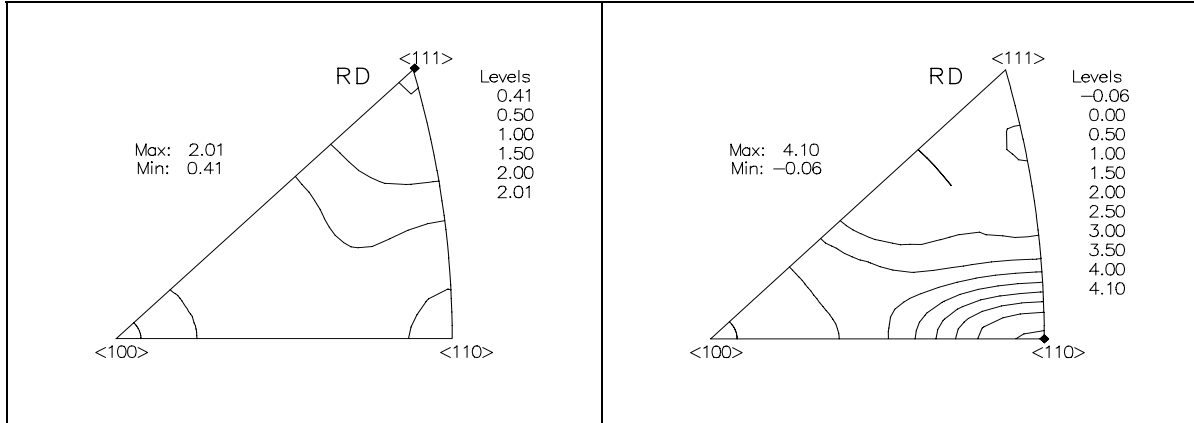


Figure A23. Cu RD inverse pole figure of the drawn-annealed sample with $\eta = 2.08$, $T = 800^{\circ}\text{C}$, $t = 30 \text{ min}$.

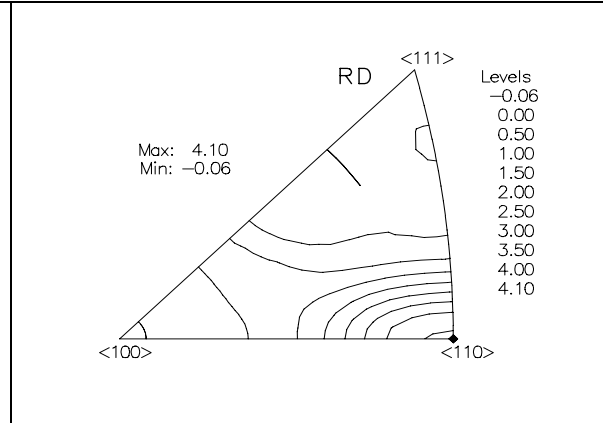


Figure A24. Nb RD inverse pole figure of the drawn-annealed sample with $\eta = 2.08$, $T = 800^{\circ}\text{C}$, $t = 30 \text{ min}$.

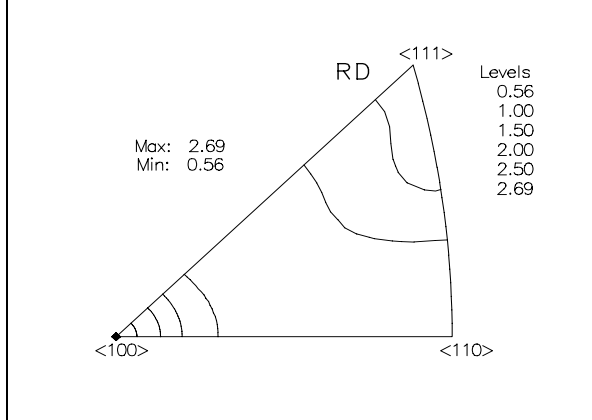


Figure A25. Cu RD inverse pole figure of the drawn-annealed sample with $\eta = 3.01$, $T = 800^{\circ}\text{C}$, $t = 30 \text{ min}$.

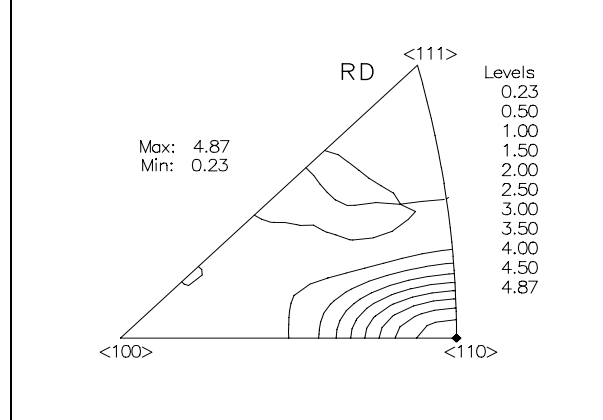


Figure A26. Nb RD inverse pole figure of the drawn-annealed sample with $\eta = 3.01$, $T = 800^{\circ}\text{C}$, $t = 30 \text{ min}$.

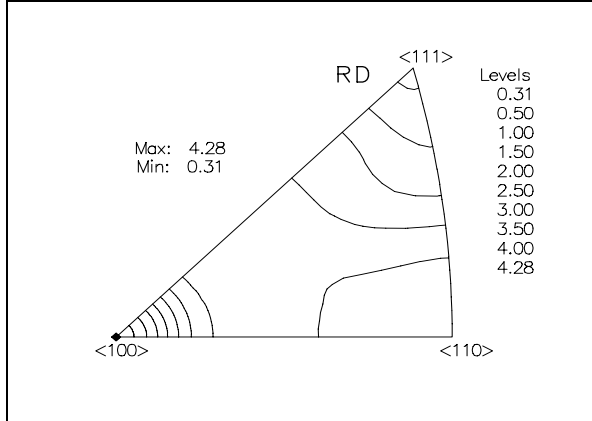


Figure A27. Cu RD inverse pole figure of the drawn-annealed sample with $\eta = 3.95$, $T = 800^{\circ}\text{C}$, $t = 30 \text{ min}$.

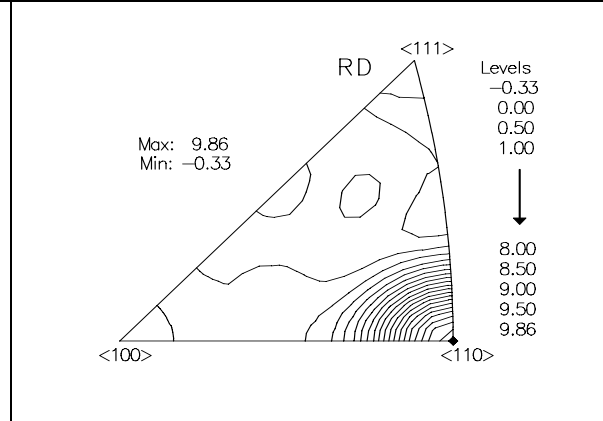


Figure A28. Nb RD inverse pole figure of the drawn-annealed sample with $\eta = 3.95$, $T = 800^{\circ}\text{C}$, $t = 30 \text{ min}$.

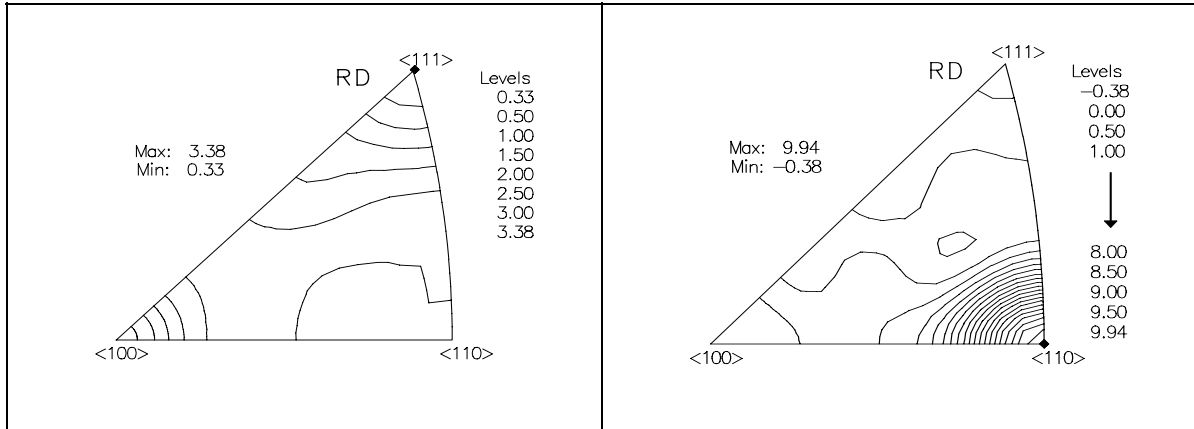


Figure A29. Cu RD inverse pole figure of the drawn-annealed sample with $\eta = 4.97$, $T = 800^\circ\text{C}$, $t = 30$ min.

Figure A30. Nb RD inverse pole figure of the drawn-annealed sample with $\eta = 4.97$, $T = 800^\circ\text{C}$, $t = 30$ min.

4.2 $T = 800^\circ\text{C}$, $t = 60$ min

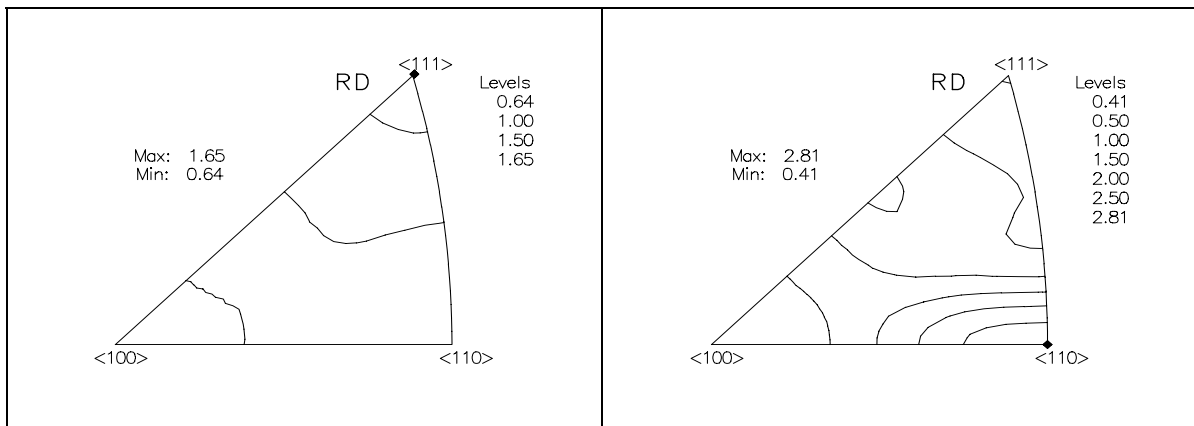


Figure A31. Cu RD inverse pole figure of the drawn-annealed sample with $\eta = 2.08$, $T = 800^\circ\text{C}$, $t = 60$ min.

Figure A32. Nb RD inverse pole figure of the drawn-annealed sample with $\eta = 2.08$, $T = 800^\circ\text{C}$, $t = 60$ min.

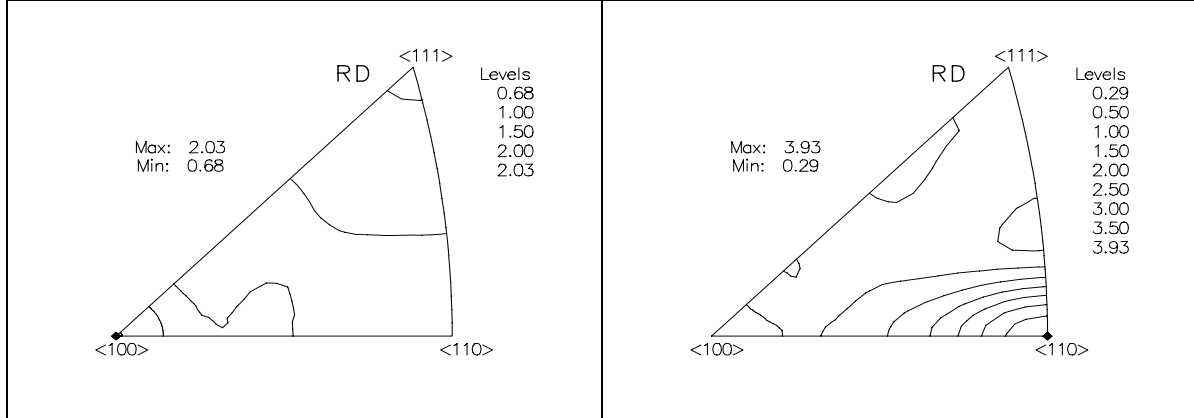


Figure A33. Cu RD inverse pole figure of the drawn-annealed sample with $\eta = 3.01$, $T = 800^\circ\text{C}$, $t = 60$ min.

Figure A34. Nb RD inverse pole figure of the drawn-annealed sample with $\eta = 3.01$, $T = 800^\circ\text{C}$, $t = 60$ min.

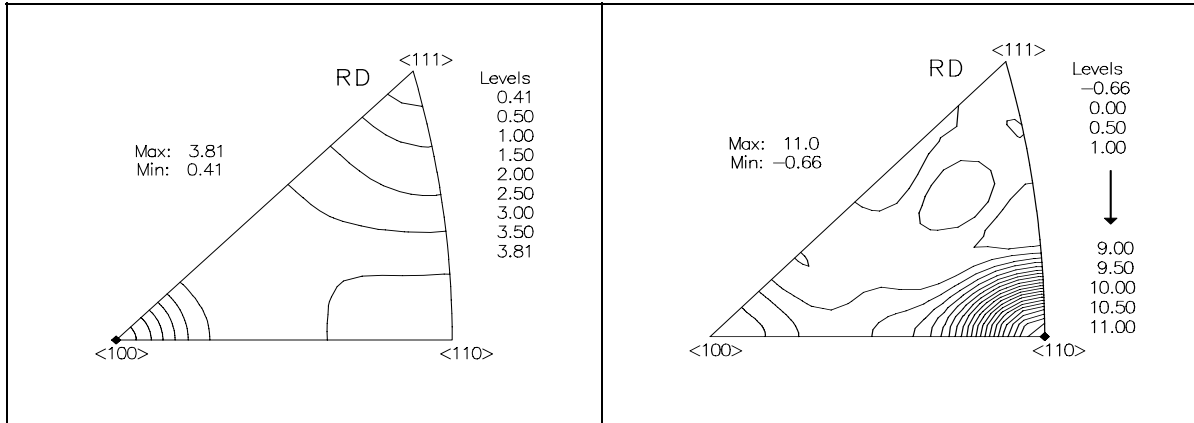


Figure A35. Cu RD inverse pole figure of the drawn-annealed sample with $\eta = 3.95$, $T = 800^\circ\text{C}$, $t = 60$ min.

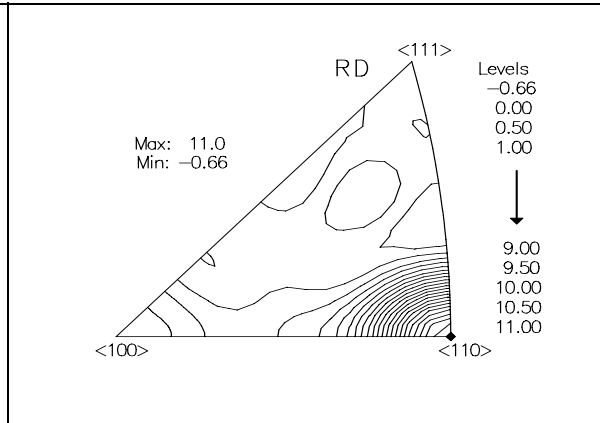


Figure A36. Nb RD inverse pole figure of the drawn-annealed sample with $\eta = 3.95$, $T = 800^\circ\text{C}$, $t = 60$ min.

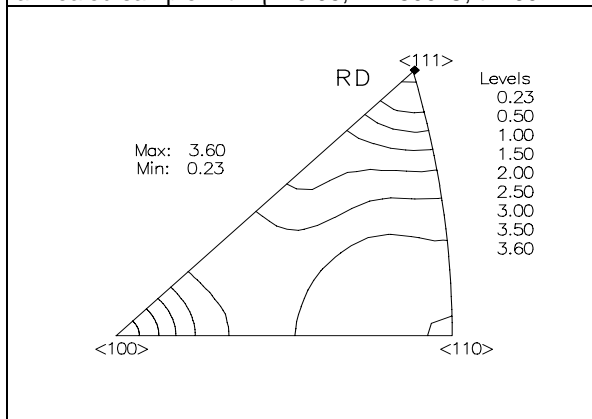


Figure A37. Cu RD inverse pole figure of the drawn-annealed sample with $\eta = 4.97$, $T = 800^\circ\text{C}$, $t = 60$ min.

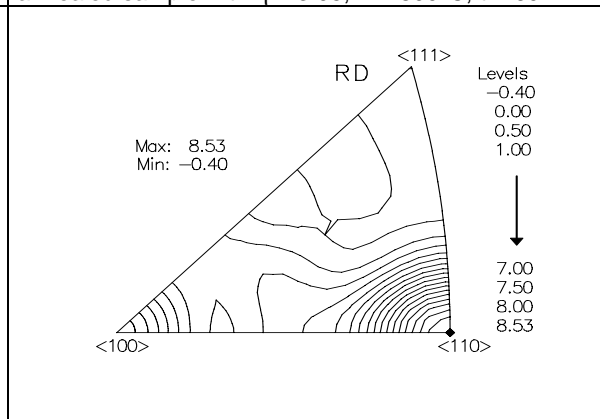


Figure A38. Nb RD inverse pole figure of the drawn-annealed sample with $\eta = 4.97$, $T = 800^\circ\text{C}$, $t = 60$ min.

5. Drawn-Annealed Cu-18%Nb at $T = 1000^\circ\text{C}$

4.1 $T = 1000^\circ\text{C}$, $t = 30$ min

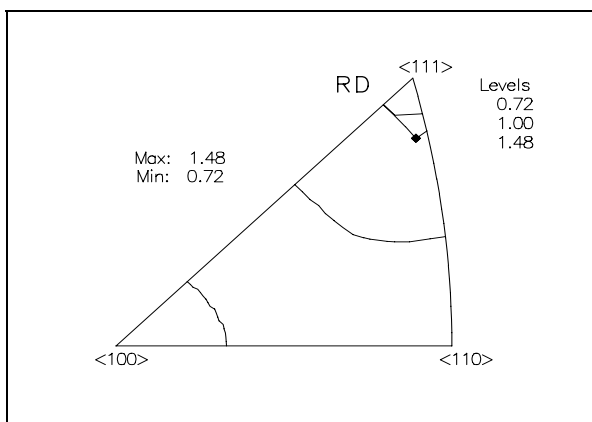


Figure A39. Cu RD inverse pole figure of the drawn-annealed sample with $\eta = 2.08$, $T = 1000^\circ\text{C}$, $t = 30$ min.

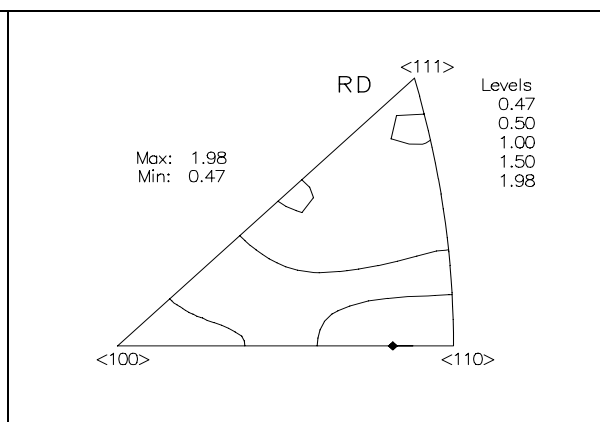


Figure A40. Nb RD inverse pole figure of the drawn-annealed sample with $\eta = 2.08$, $T = 1000^\circ\text{C}$, $t = 30$ min.

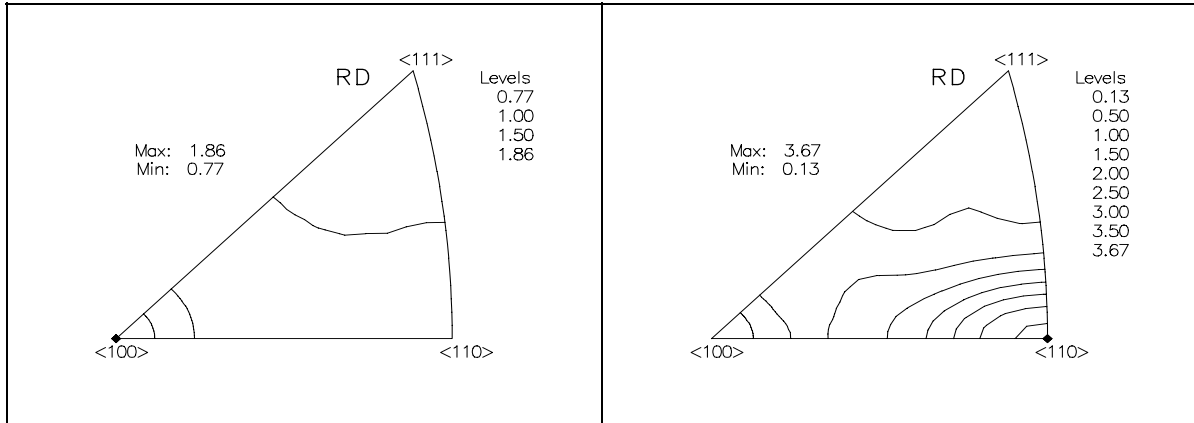


Figure A41. Cu RD inverse pole figure of the drawn-annealed sample with $\eta = 3.01$, $T = 1000^\circ\text{C}$, $t = 30$ min.

Figure A42. Nb RD inverse pole figure of the drawn-annealed sample with $\eta = 3.01$, $T = 1000^\circ\text{C}$, $t = 30$ min.

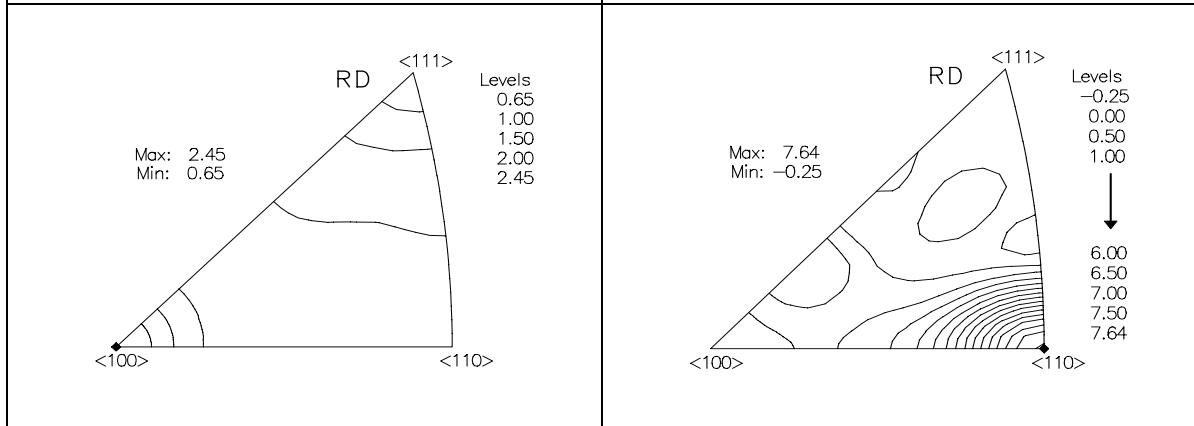


Figure A43. Cu RD inverse pole figure of the drawn-annealed sample with $\eta = 3.95$, $T = 1000^\circ\text{C}$, $t = 30$ min.

Figure A44. Nb RD inverse pole figure of the drawn-annealed sample with $\eta = 3.95$, $T = 1000^\circ\text{C}$, $t = 30$ min.

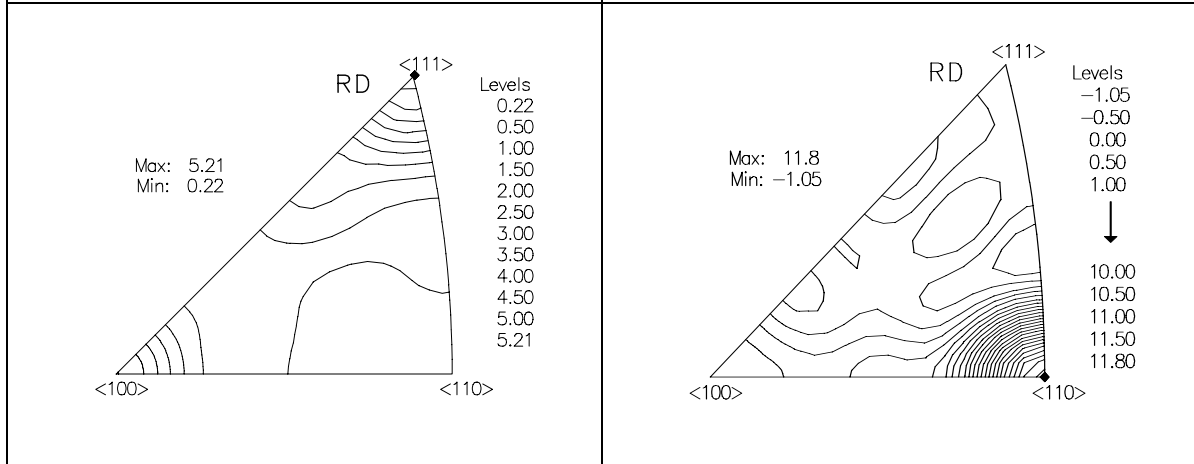


Figure A45. Cu RD inverse pole figure of the drawn-annealed sample with $\eta = 4.97$, $T = 1000^\circ\text{C}$, $t = 30$ min.

Figure A46. Nb RD inverse pole figure of the drawn-annealed sample with $\eta = 4.97$, $T = 1000^\circ\text{C}$, $t = 30$ min.

5.2 $T = 1000^{\circ}\text{C}$, $t = 60 \text{ min}$

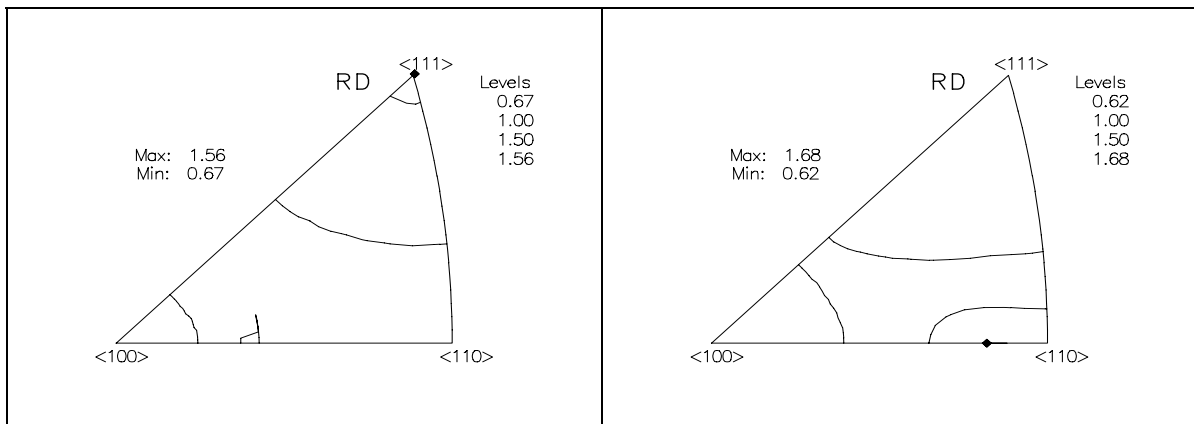


Figure A47. Cu RD inverse pole figure of the drawn-annealed sample with $\eta = 2.08$, $T = 1000^{\circ}\text{C}$, $t = 60 \text{ min}$.

Figure A48. Nb RD inverse pole figure of the drawn-annealed sample with $\eta = 2.08$, $T = 1000^{\circ}\text{C}$, $t = 60 \text{ min}$.

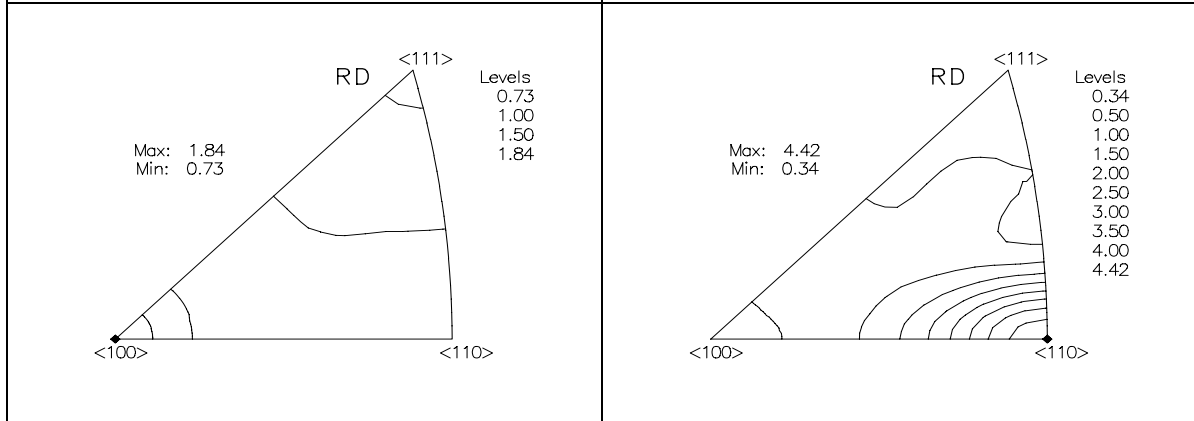


Figure A49. Cu RD inverse pole figure of the drawn-annealed sample with $\eta = 3.01$, $T = 1000^{\circ}\text{C}$, $t = 60 \text{ min}$.

Figure A50. Nb RD inverse pole figure of the drawn-annealed sample with $\eta = 3.01$, $T = 1000^{\circ}\text{C}$, $t = 60 \text{ min}$.

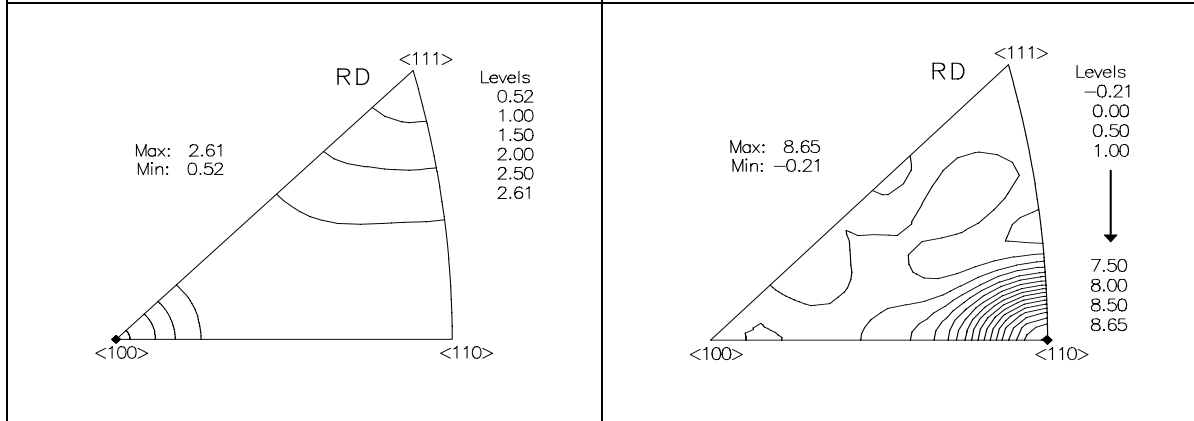
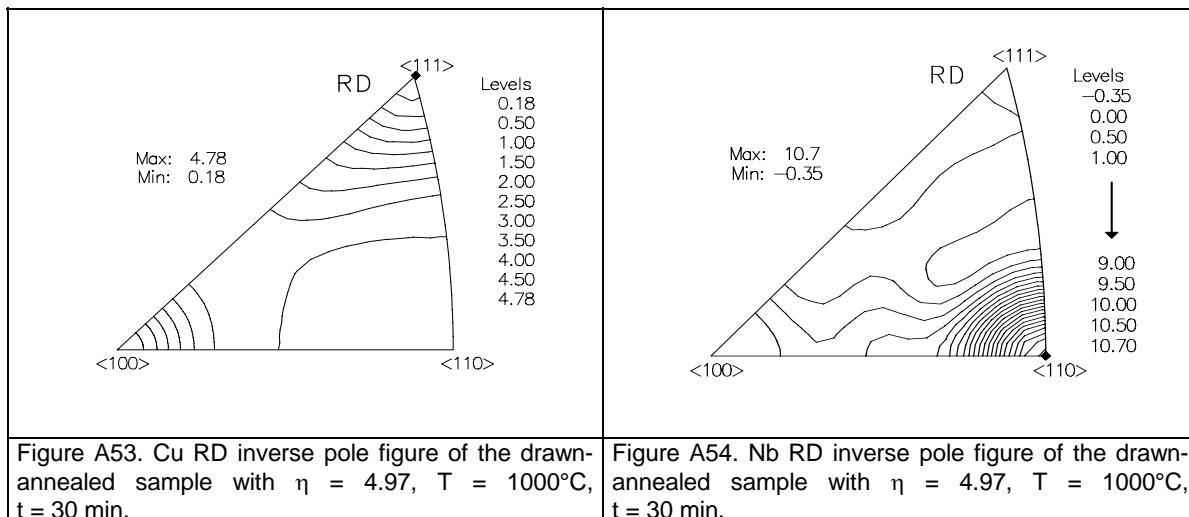


Figure A51. Cu RD inverse pole figure of the drawn-annealed sample with $\eta = 3.95$, $T = 1000^{\circ}\text{C}$, $t = 60 \text{ min}$.

Figure A52. Nb RD inverse pole figure of the drawn-annealed sample with $\eta = 3.95$, $T = 1000^{\circ}\text{C}$, $t = 60 \text{ min}$.



APPENDIX B

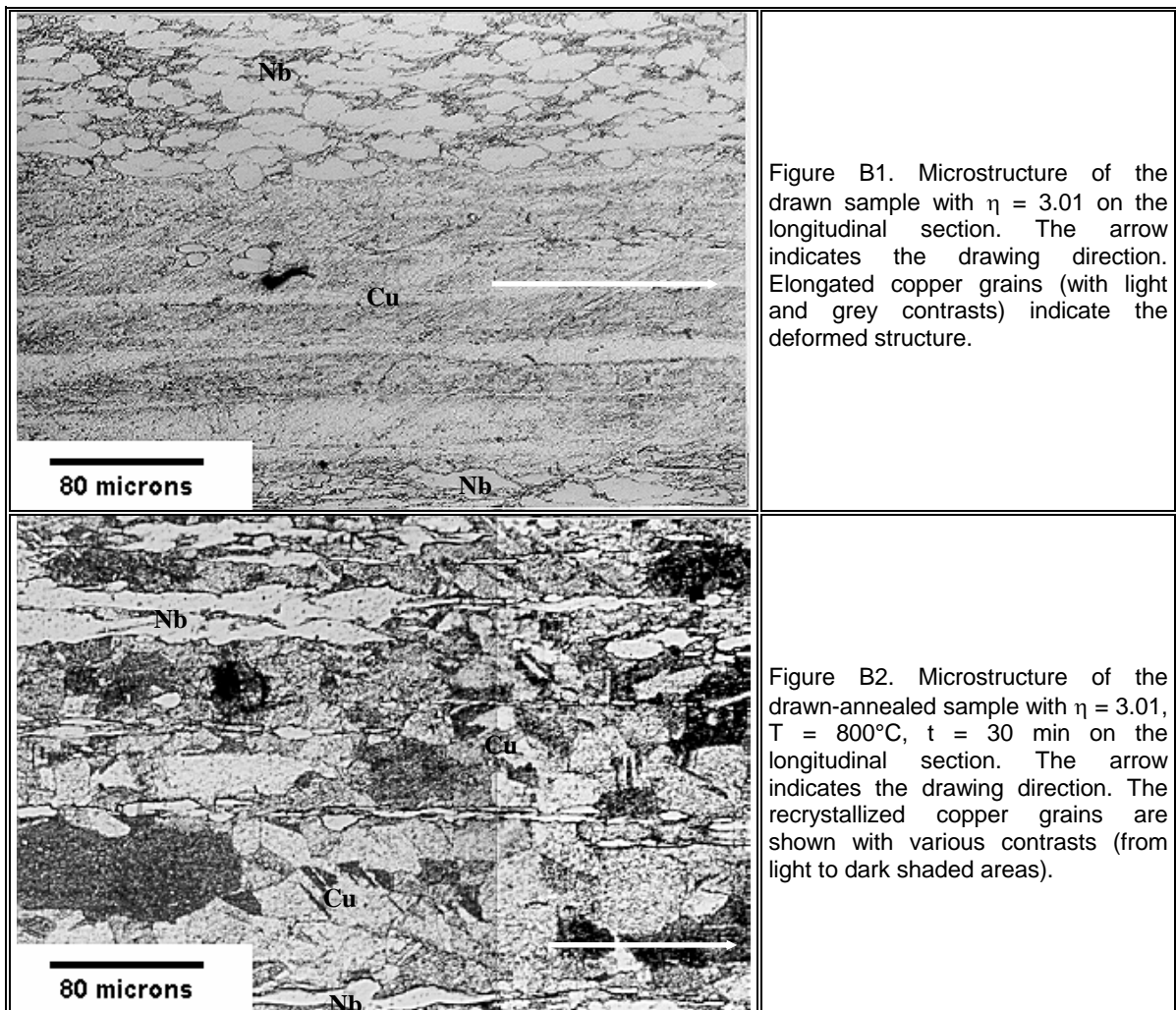
RESULTS OF

LIGHT AND SCANNING

ELECTRON MICROSCOPES

1. Light Microscope Results of Cu-18%Nb

1.1 $\eta = 3.01$



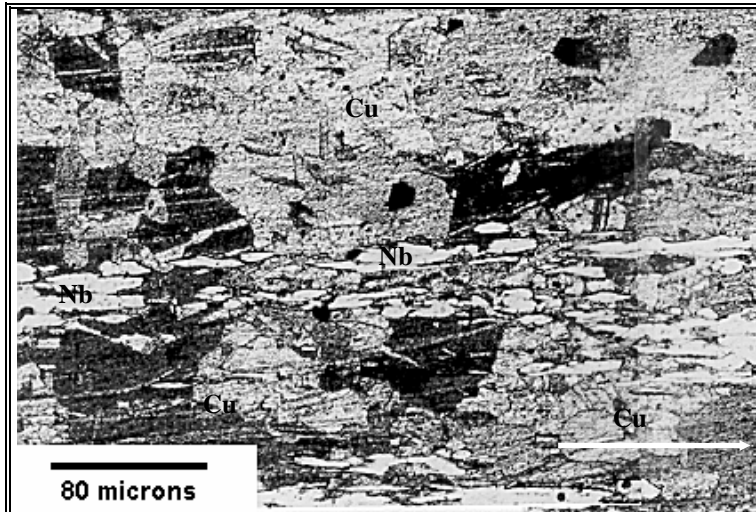


Figure B3. Microstructure of the drawn-annealed sample with $\eta = 3.01$, $T = 800^\circ\text{C}$, $t = 60$ min on the longitudinal section. The arrow indicates the drawing direction. The recrystallized copper grains are shown with various contrasts (from light to dark shaded areas).

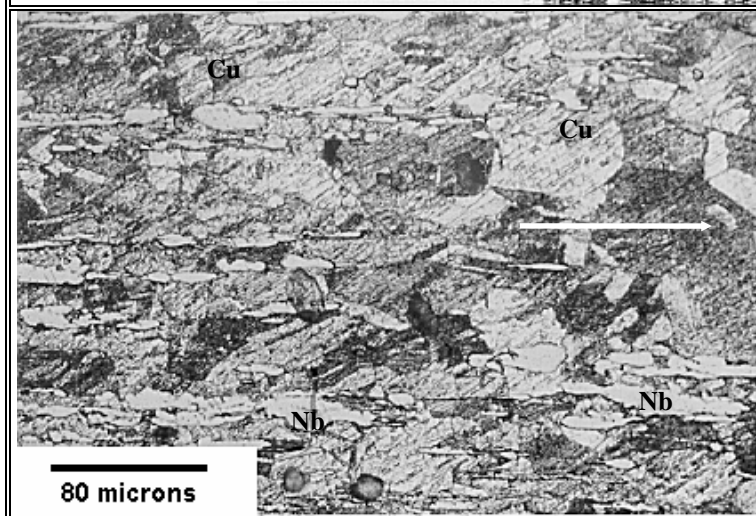


Figure B4. Microstructure of the drawn-annealed sample with $\eta = 3.01$, $T = 1000^\circ\text{C}$, $t = 12$ hr on the longitudinal section. The arrow indicates the drawing direction. The recrystallized copper grains are shown with various contrasts (from light to dark shaded areas).

1.2 $\eta = 3.95$

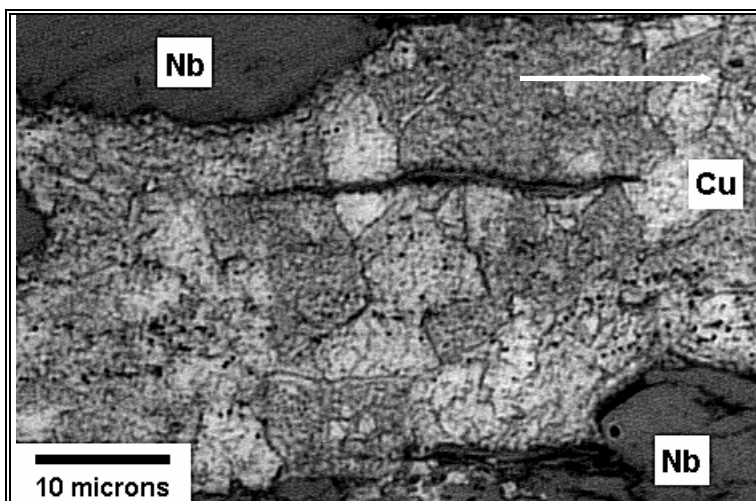


Figure B5a. Microstructure of the drawn-annealed sample with $\eta = 3.95$, $T = 800^\circ\text{C}$, $t = 30$ min on the longitudinal section. The arrow indicates the drawing direction. Some equiaxed grains occur in the copper phase.

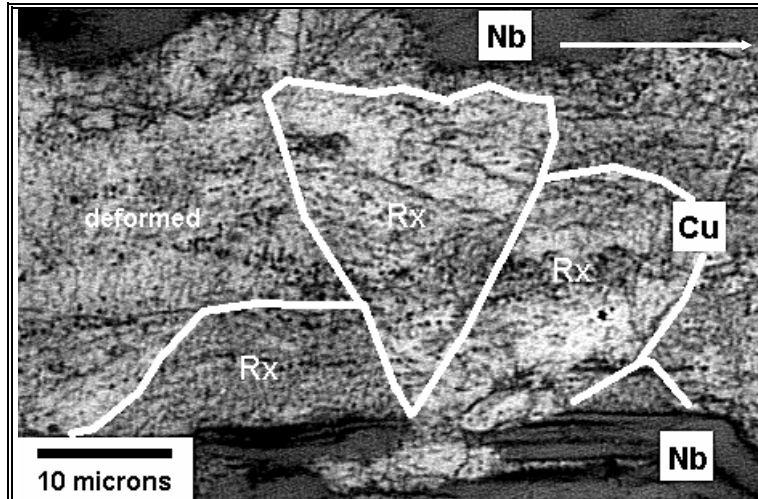


Figure B5b. Another microstructure of the drawn-annealed sample with $\eta = 3.95$, $T = 800^\circ\text{C}$, $t = 30$ min on the longitudinal section. The arrow indicates the drawing direction. The recrystallized copper grains coexist with the deformed structure.

$1.3 n = 4.97$

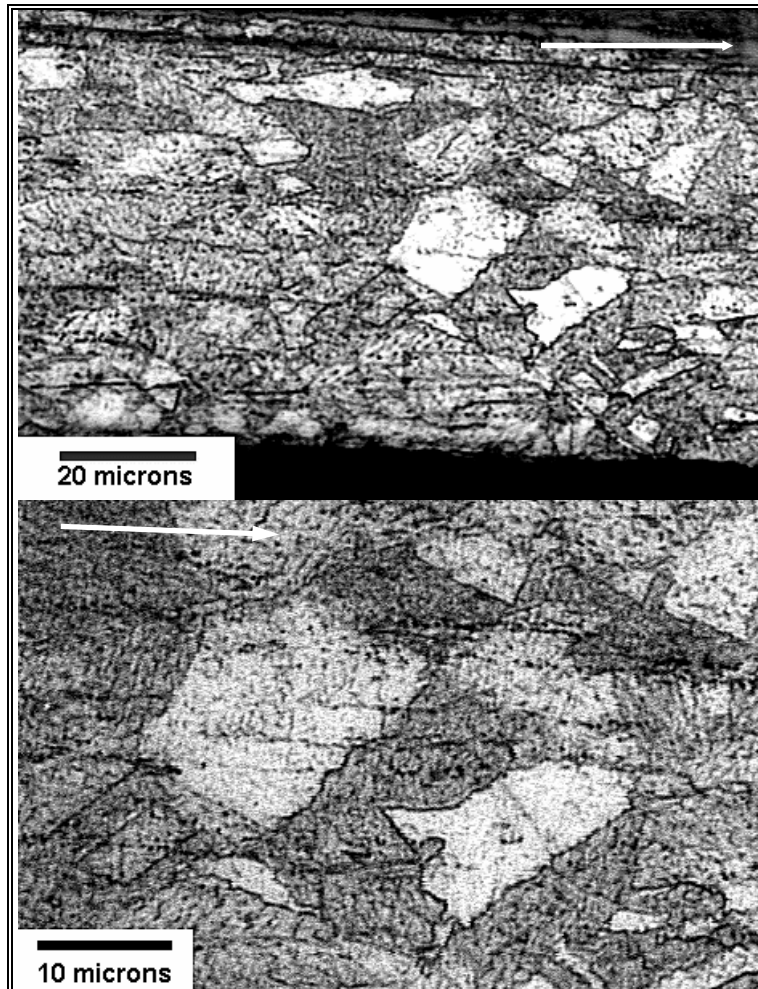
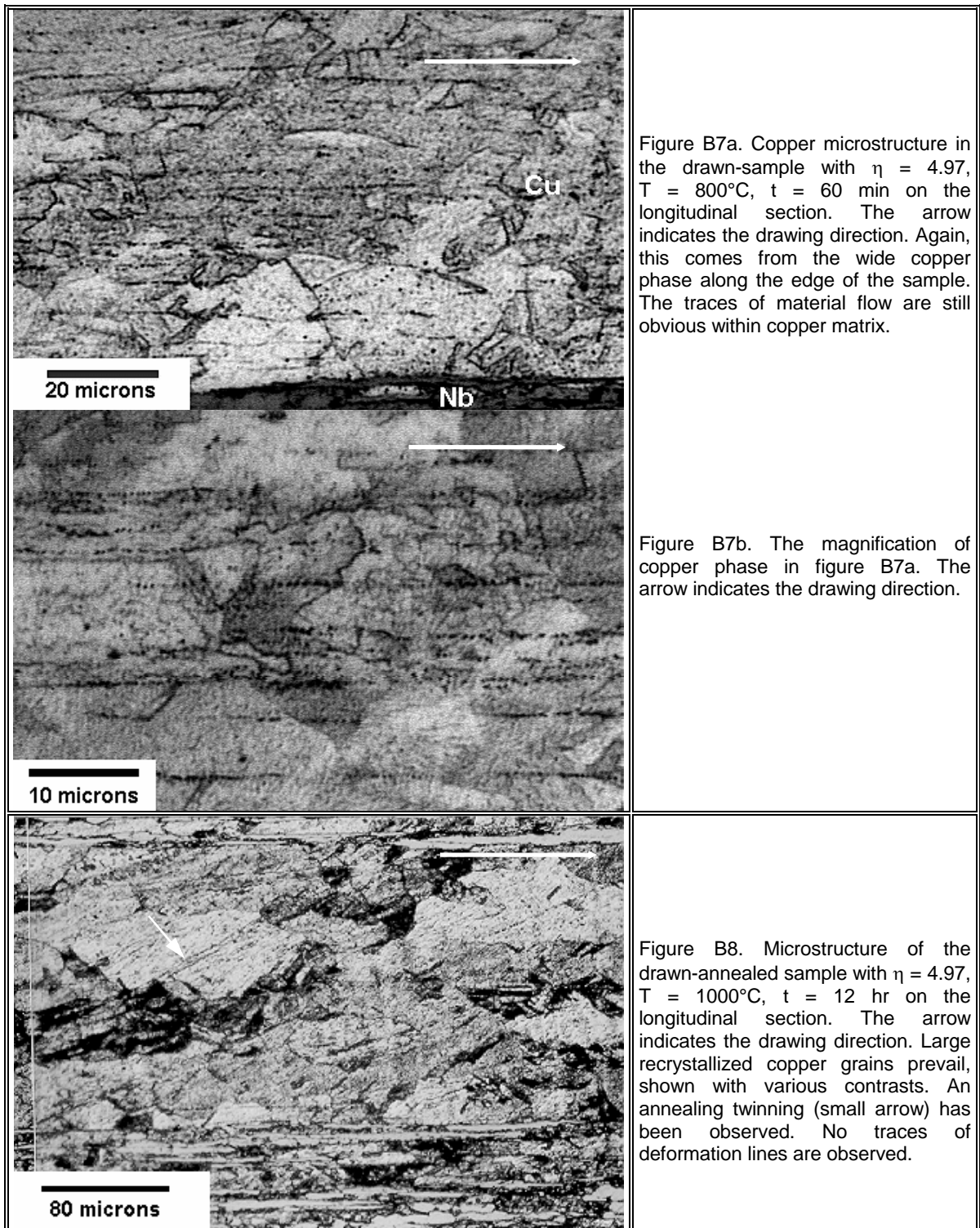
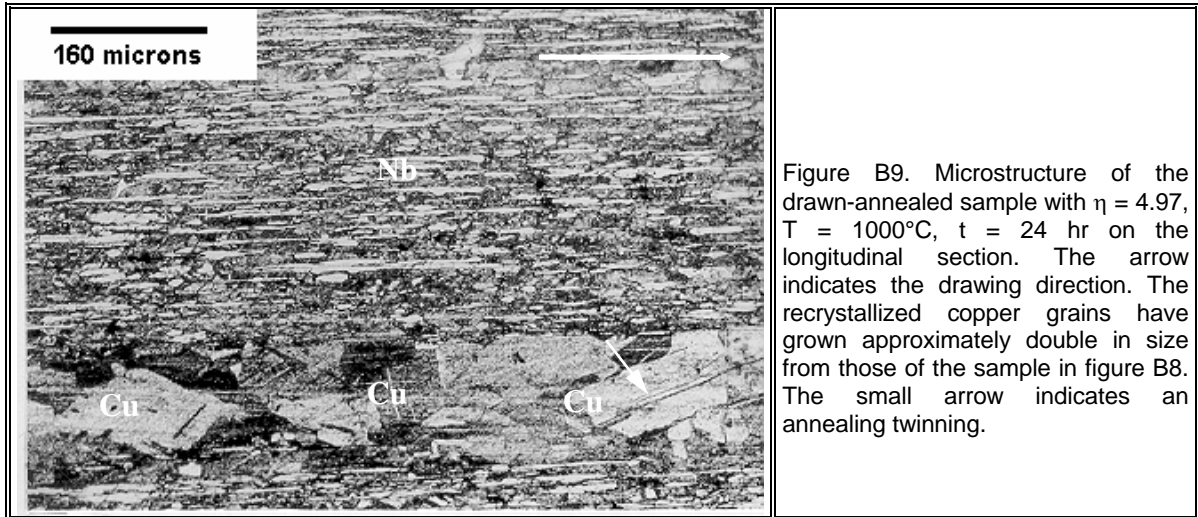


Figure B6a. A wide copper phase occurs along the edge of the drawn-annealed sample with $\eta = 4.97$, $T = 800^\circ\text{C}$, $t = 30$ min on the longitudinal section. The arrow indicates the drawing direction. Niobium filaments are thus much more densely arranged above this copper region (partially shown). Large recrystallized grains coexist with the deformed copper structure.

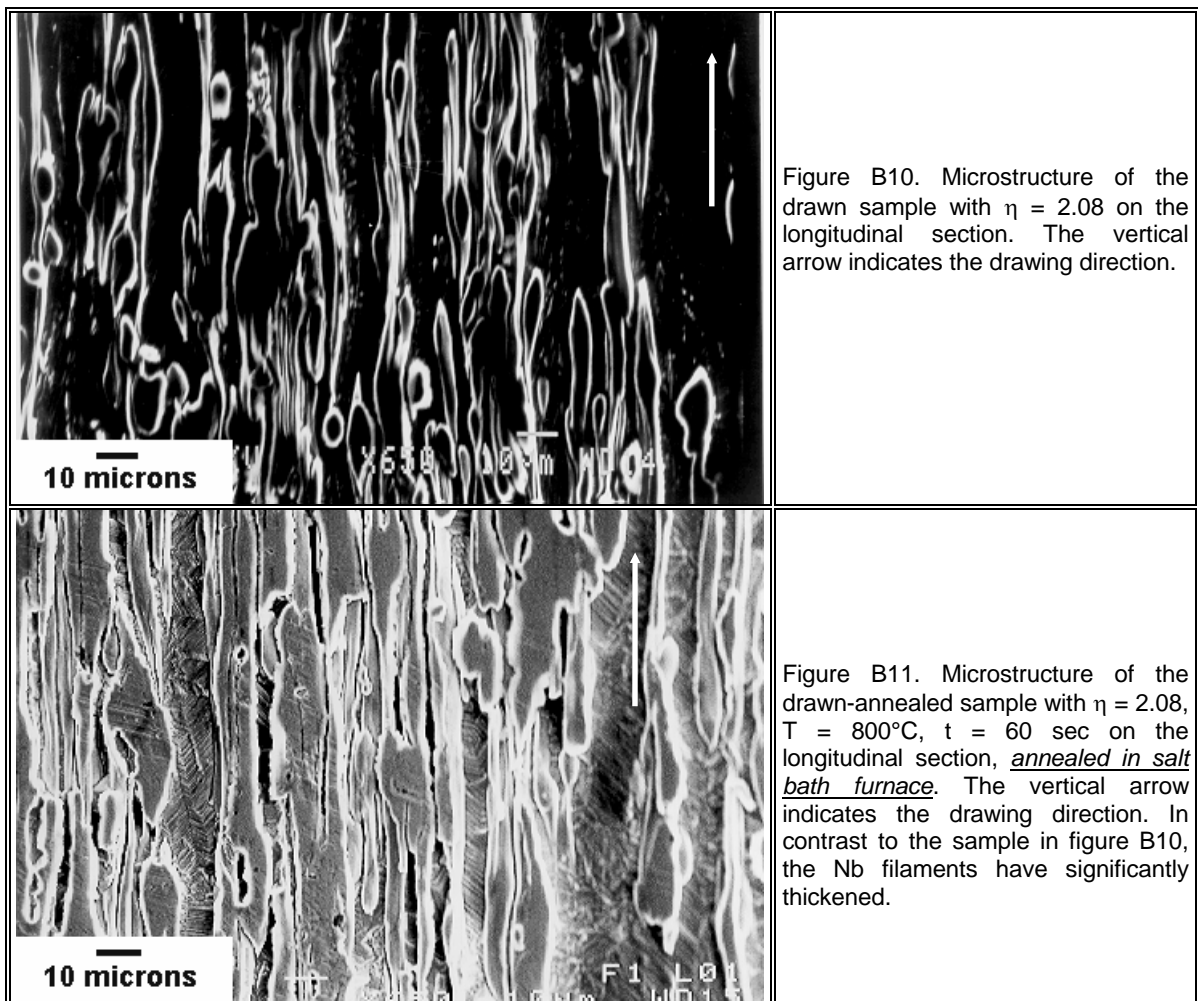
Figure B6b. The magnification of the copper phase in the drawn-annealed sample with $\eta = 4.97$, $T = 800^\circ\text{C}$, $t = 30$ min (figure B6a). Traces of material flow are obvious and parallel to the drawing direction (arrow).

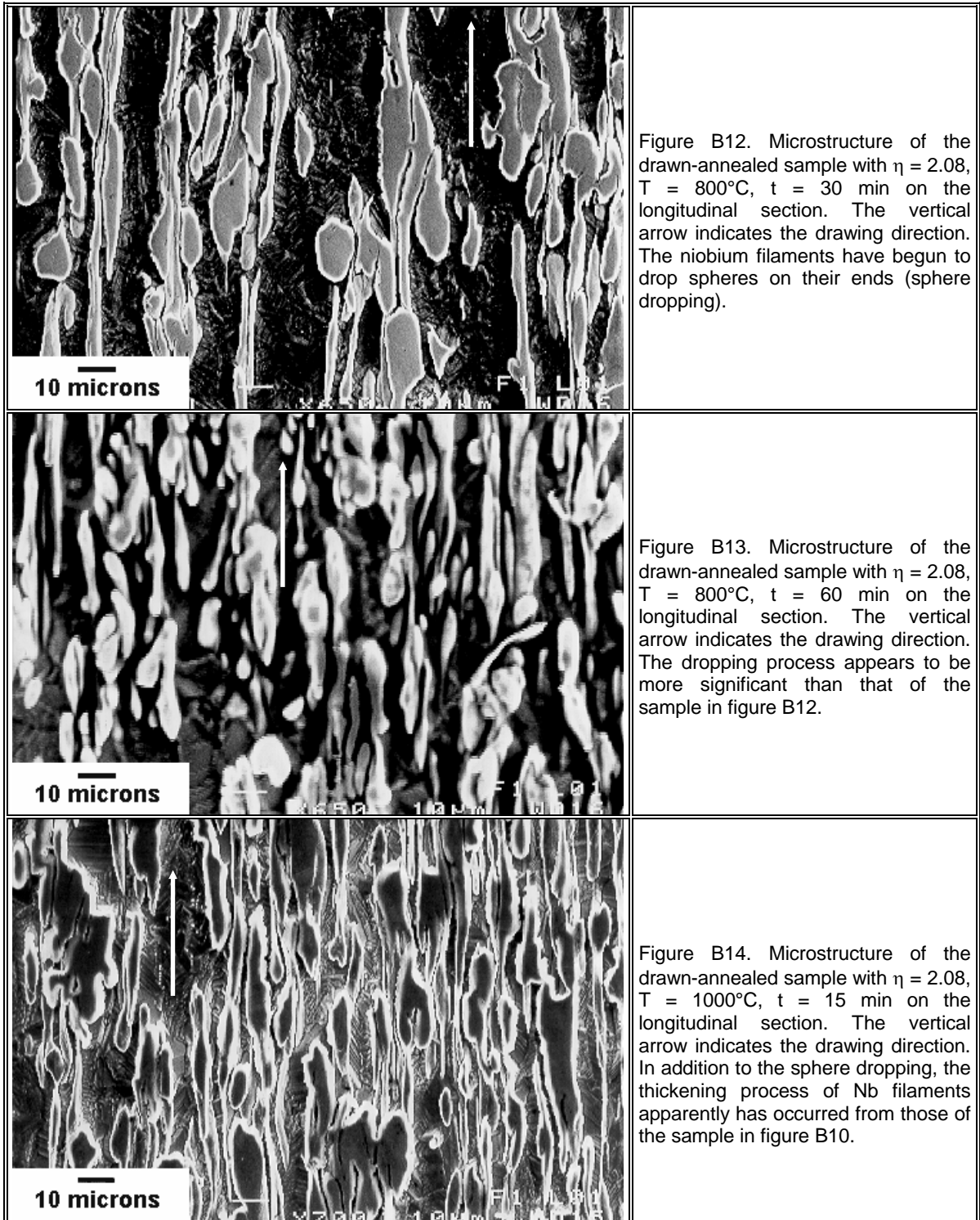




2. Scanning Electron Microscope Results of Cu-18%Nb

2.1 $\eta = 2.08$





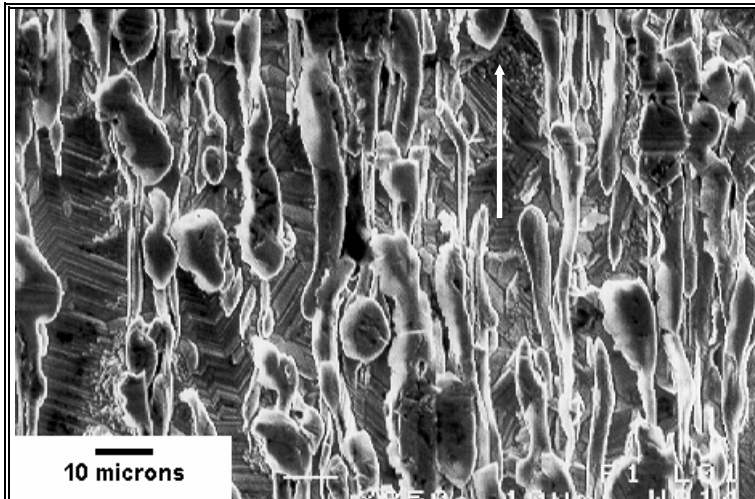


Figure B15. Microstructure of the drawn-annealed sample with $\eta = 2.08$, $T = 1000^{\circ}\text{C}$, $t = 30$ min on the longitudinal section. The vertical arrow indicates the drawing direction.

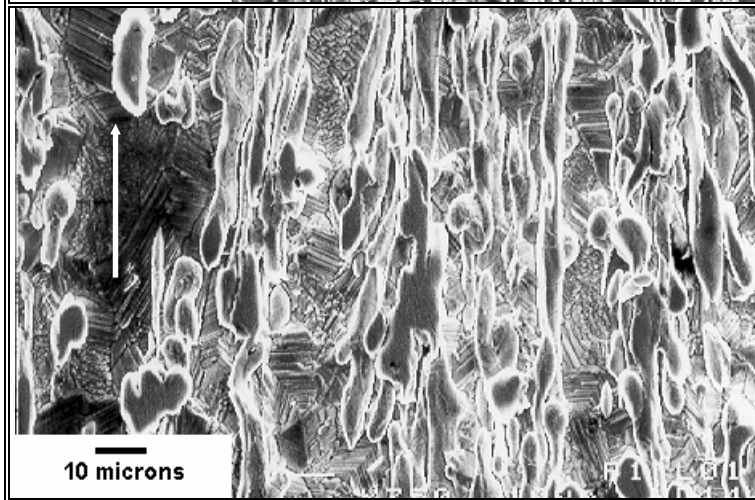


Figure B16. Microstructure of the drawn-annealed sample with $\eta = 2.08$, $T = 1000^{\circ}\text{C}$, $t = 60$ min on the longitudinal section. The vertical arrow indicates the drawing direction. Number of droplets has apparently increased from that of the sample in figure B15.

2.2 $\eta = 3.01$

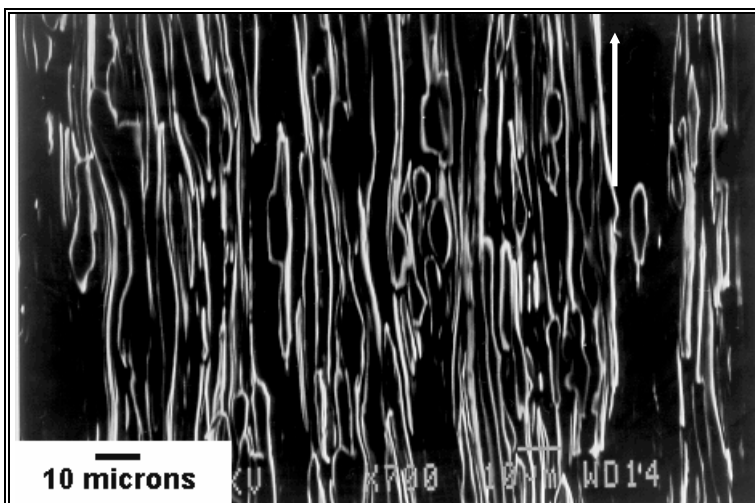
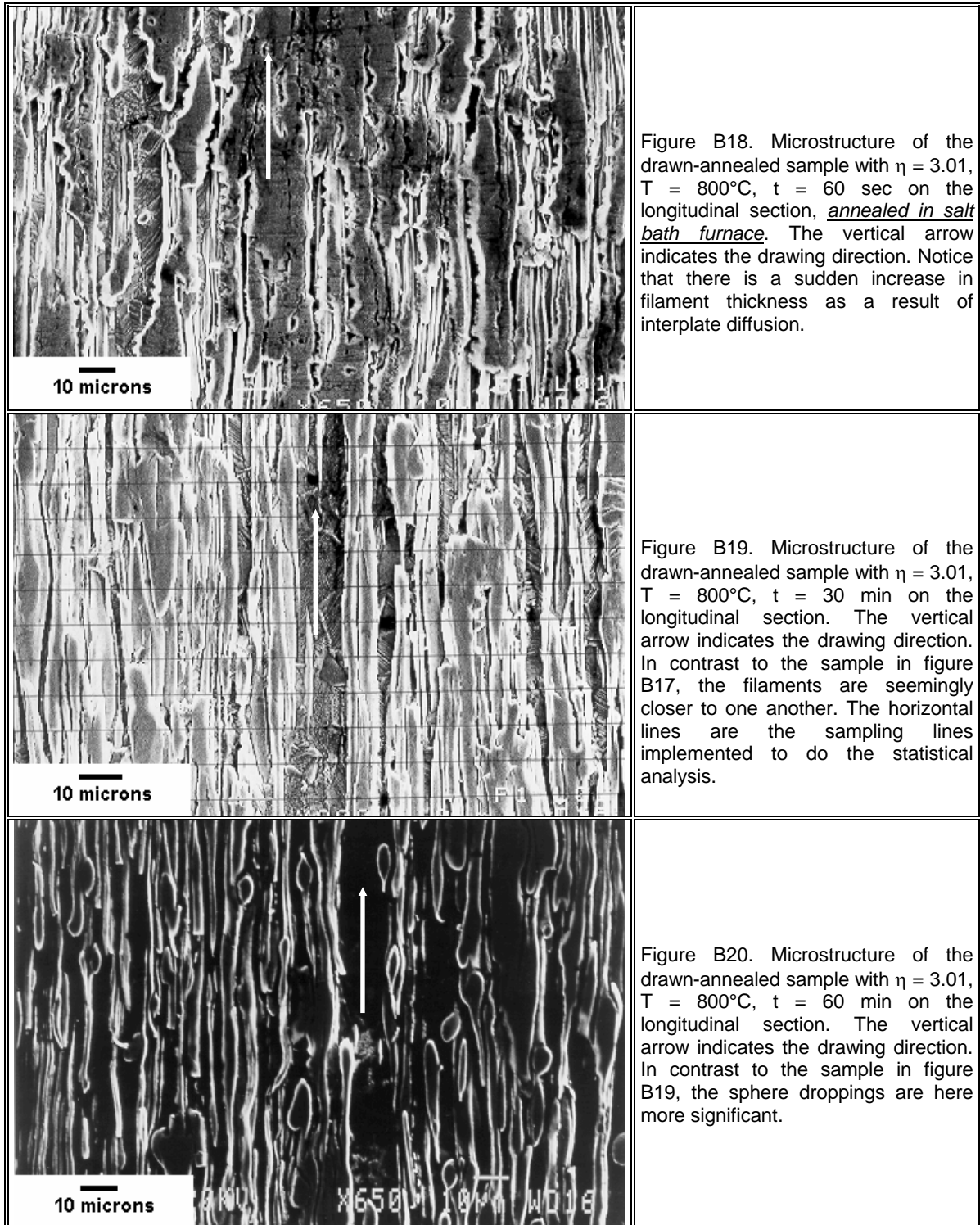
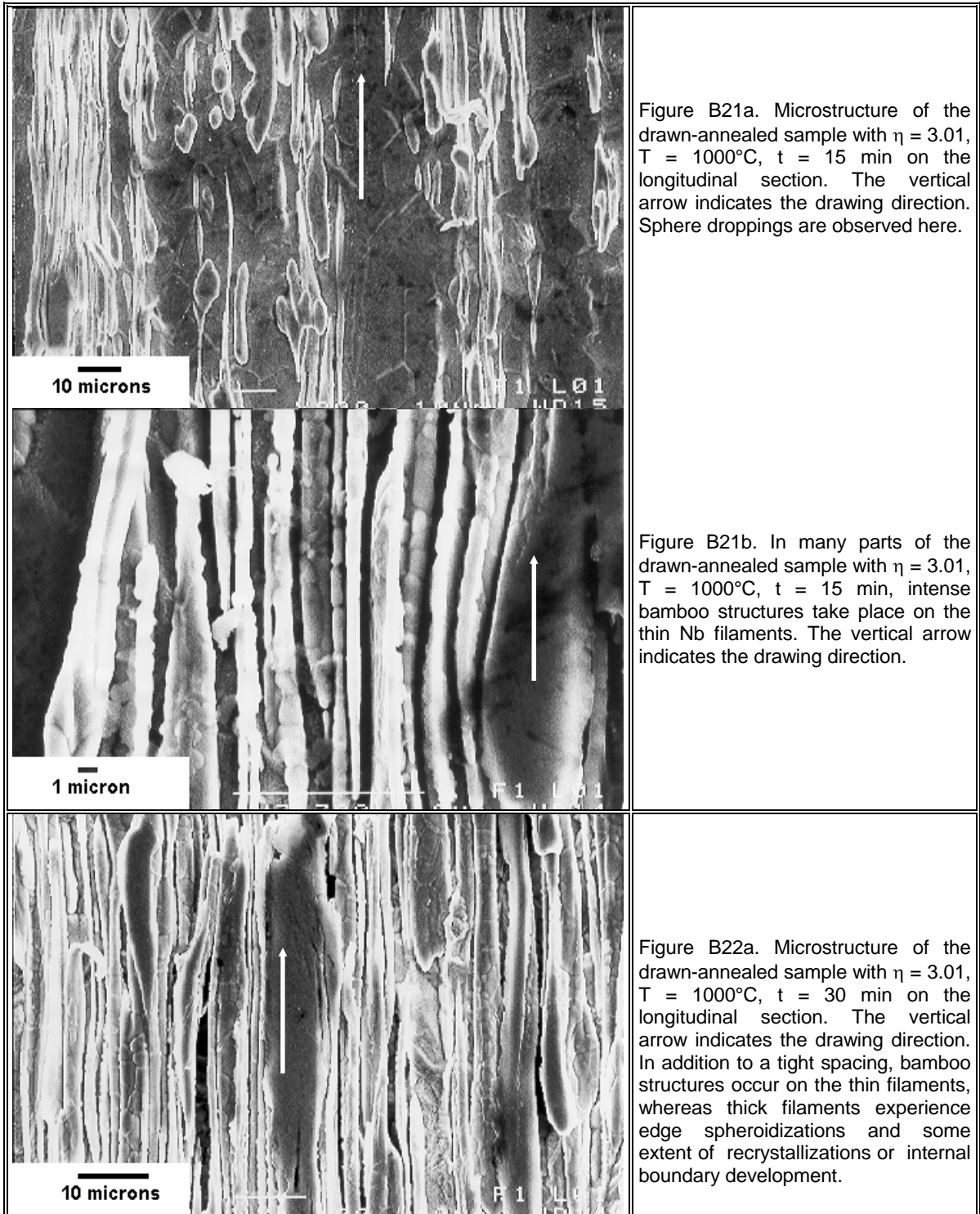
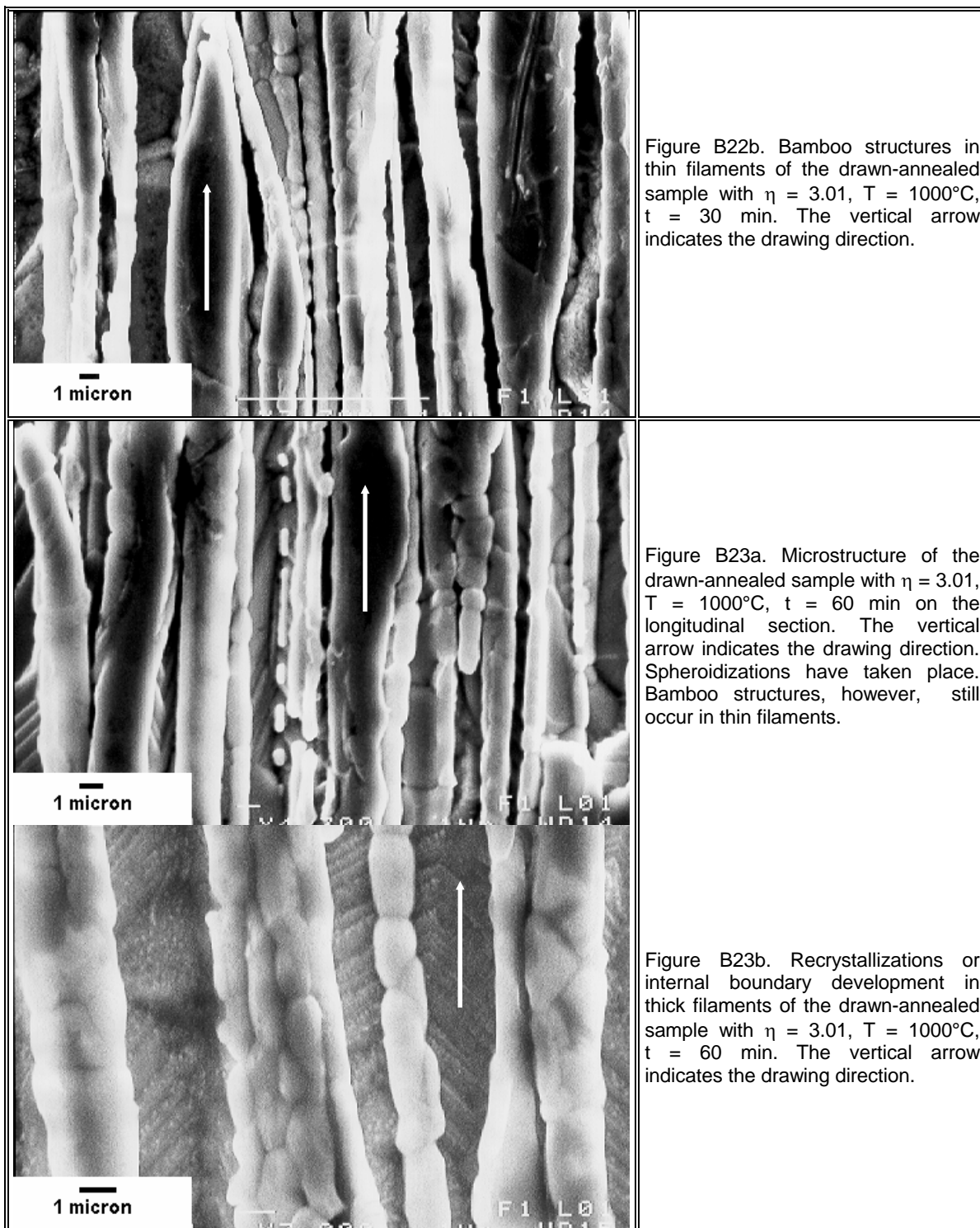


Figure B17. Microstructure of the drawn sample with $\eta = 3.01$ on the longitudinal section. The vertical arrow indicates the drawing direction. In contrast to the sample in figure B10, the filament thickness seems to be smaller now.



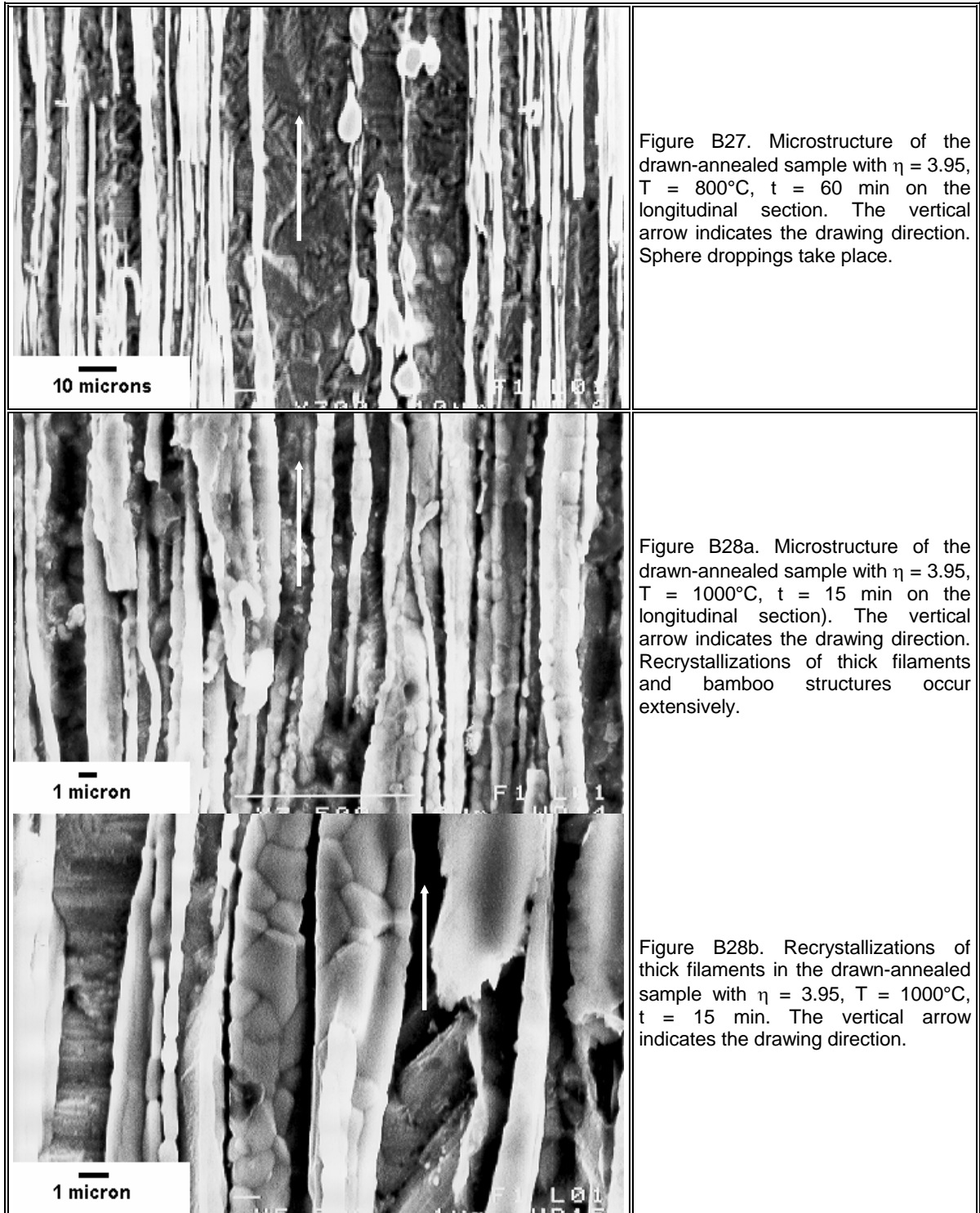


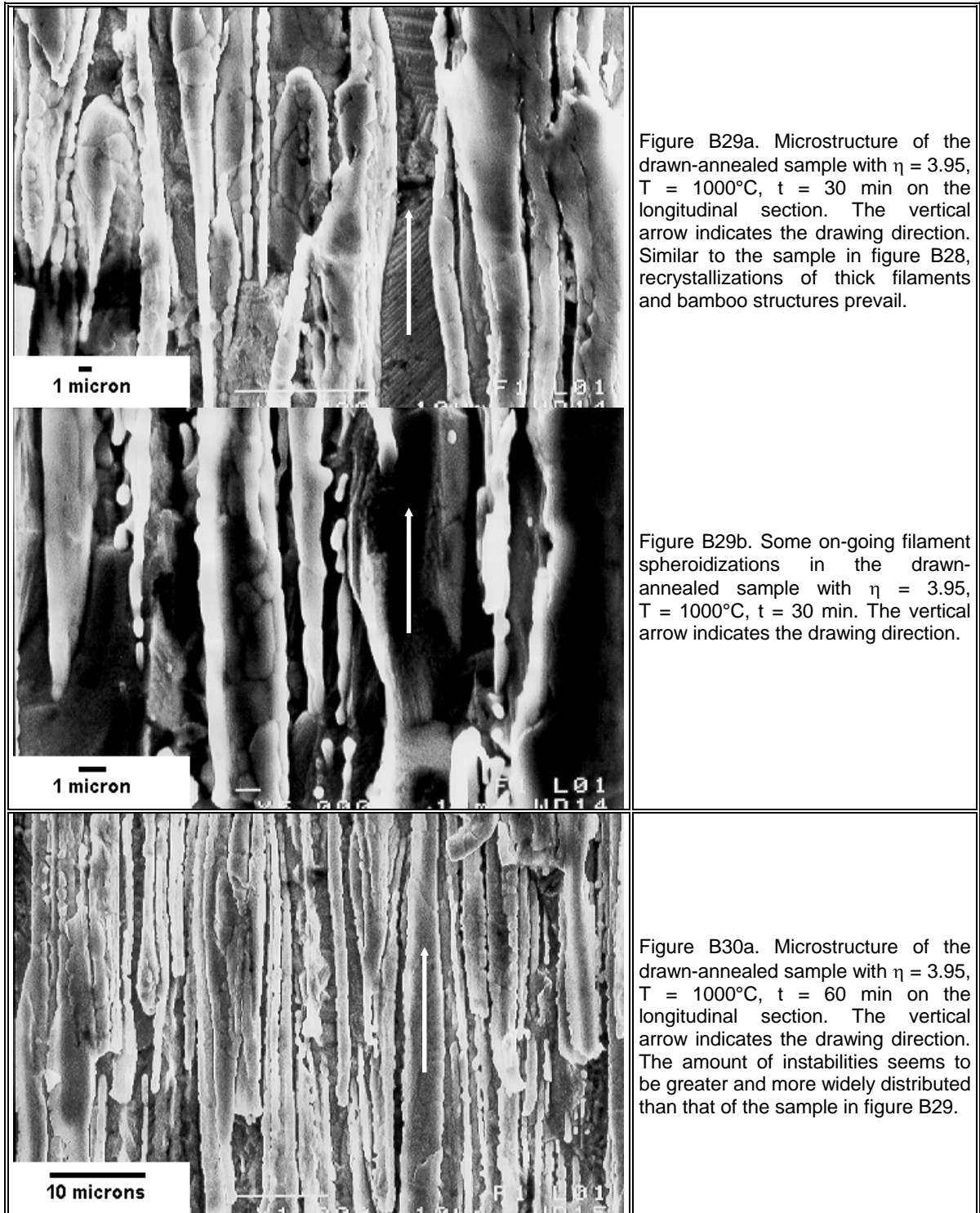


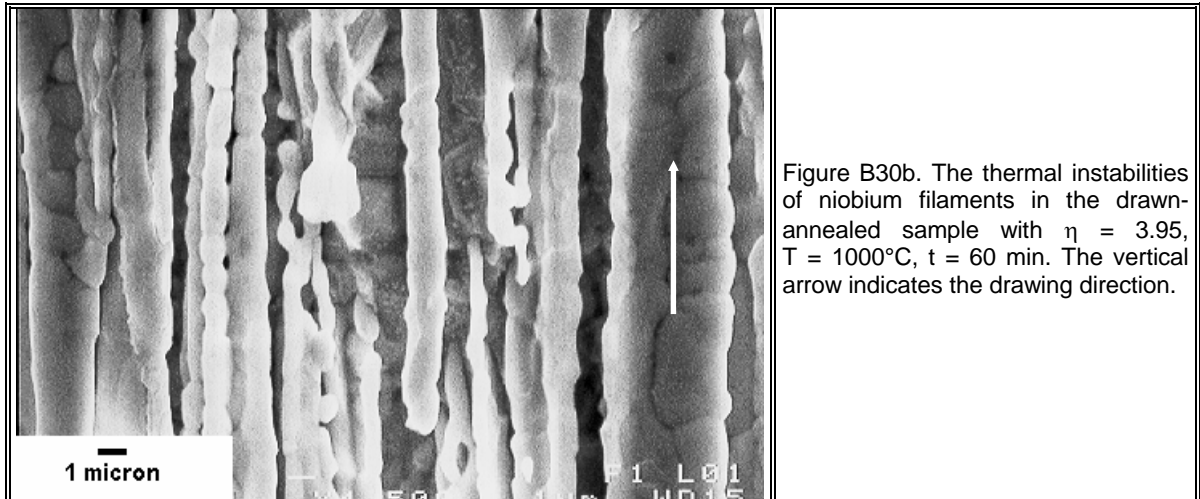


2.3 $\eta = 3.95$

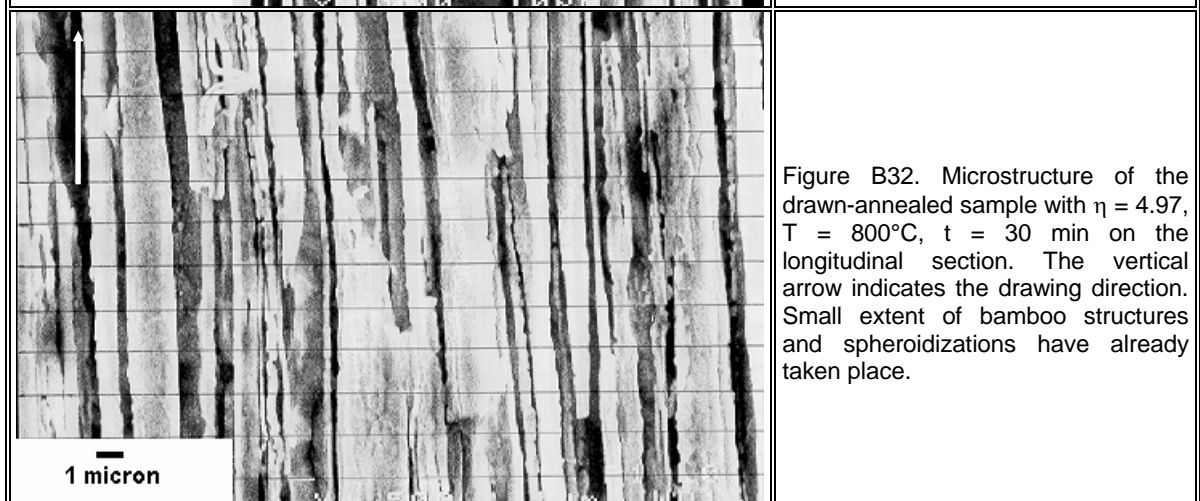
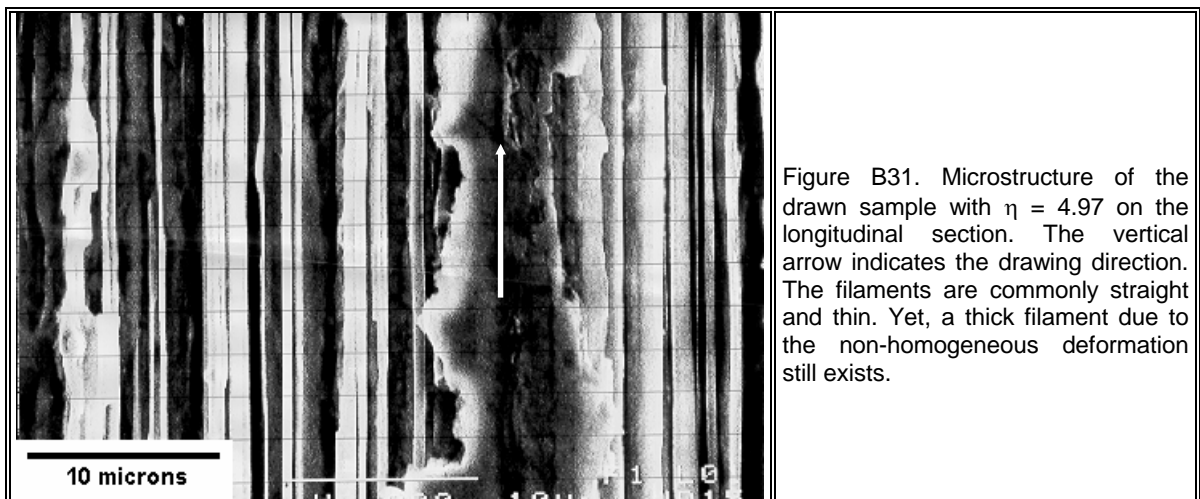
| | |
|--|--|
| | <p>Figure B24. Microstructure of the drawn sample with $\eta = 3.95$ on the longitudinal section. The vertical arrow indicates the drawing direction. In contrast to the sample in figure B17, many filaments are thinner and more closely spaced.</p> |
| | <p>Figure B25. Microstructure of the drawn-annealed sample with $\eta = 3.95$, $T = 800^{\circ}\text{C}$, $t = 60$ sec on the longitudinal section, <i>annealed in salt bath furnace</i>. The vertical arrow indicates the drawing direction. Notice that the interplate diffusion have occurred, resulting in thick filaments.</p> |
| | <p>Figure B26. Microstructure of the drawn-annealed sample with $\eta = 3.95$, $T = 800^{\circ}\text{C}$, $t = 30$ min on the longitudinal section. The vertical arrow indicates the drawing direction. The spacing between filaments is smaller than that of the sample in figure B24.</p> |







2.4 $\eta = 4.97$



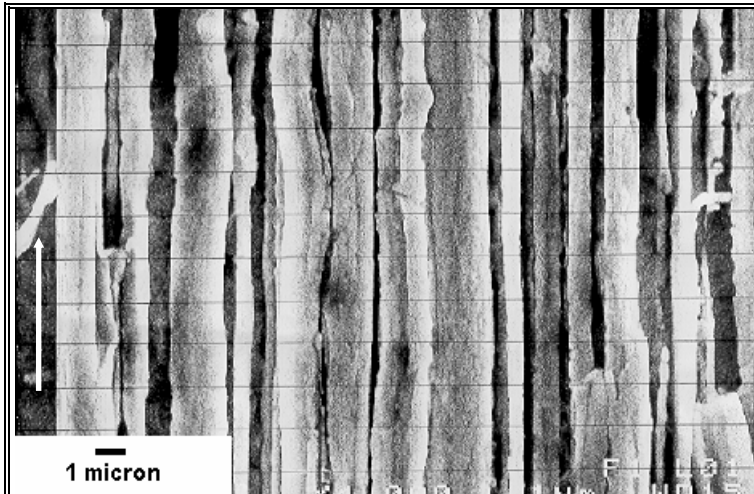


Figure B33a. Microstructure of the drawn-annealed sample with $\eta = 4.97$, $T = 800^{\circ}\text{C}$, $t = 60$ min on the longitudinal section. The vertical arrow indicates the drawing direction. Spheroidizations take place in several places.

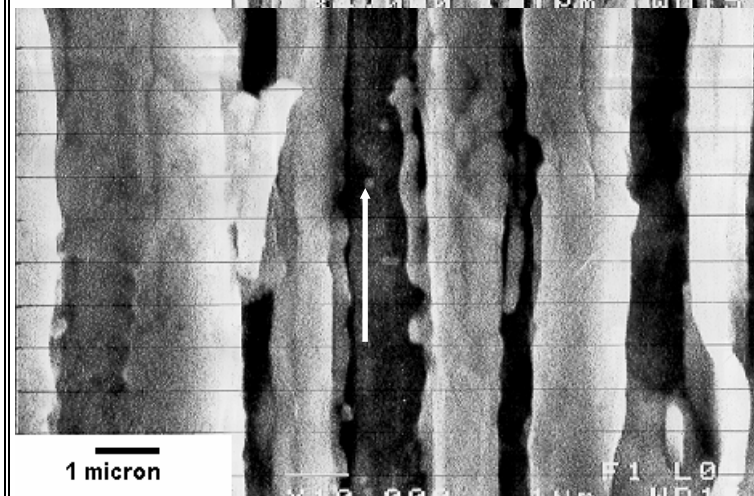


Figure B33b. The instabilities of niobium filaments in the drawn-annealed sample with $\eta = 4.97$, $T = 800^{\circ}\text{C}$, $t = 60$ min. The vertical arrow indicates the drawing direction.

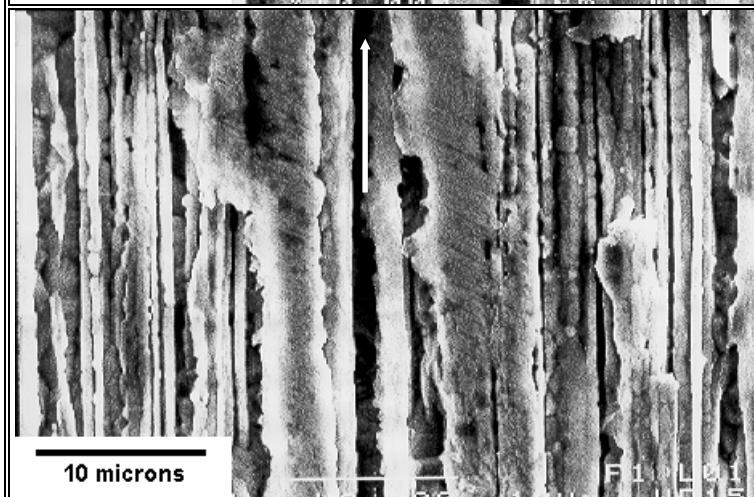
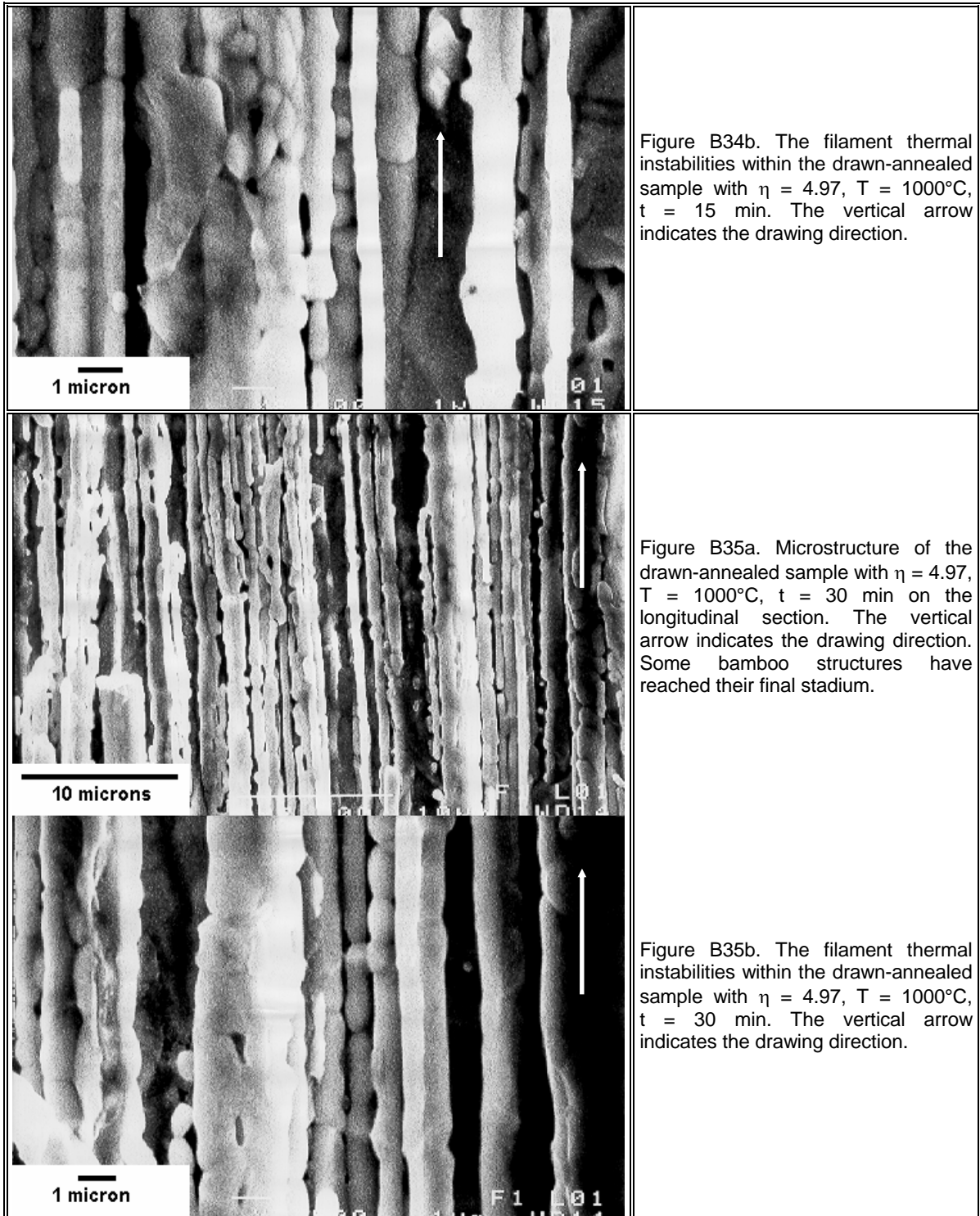
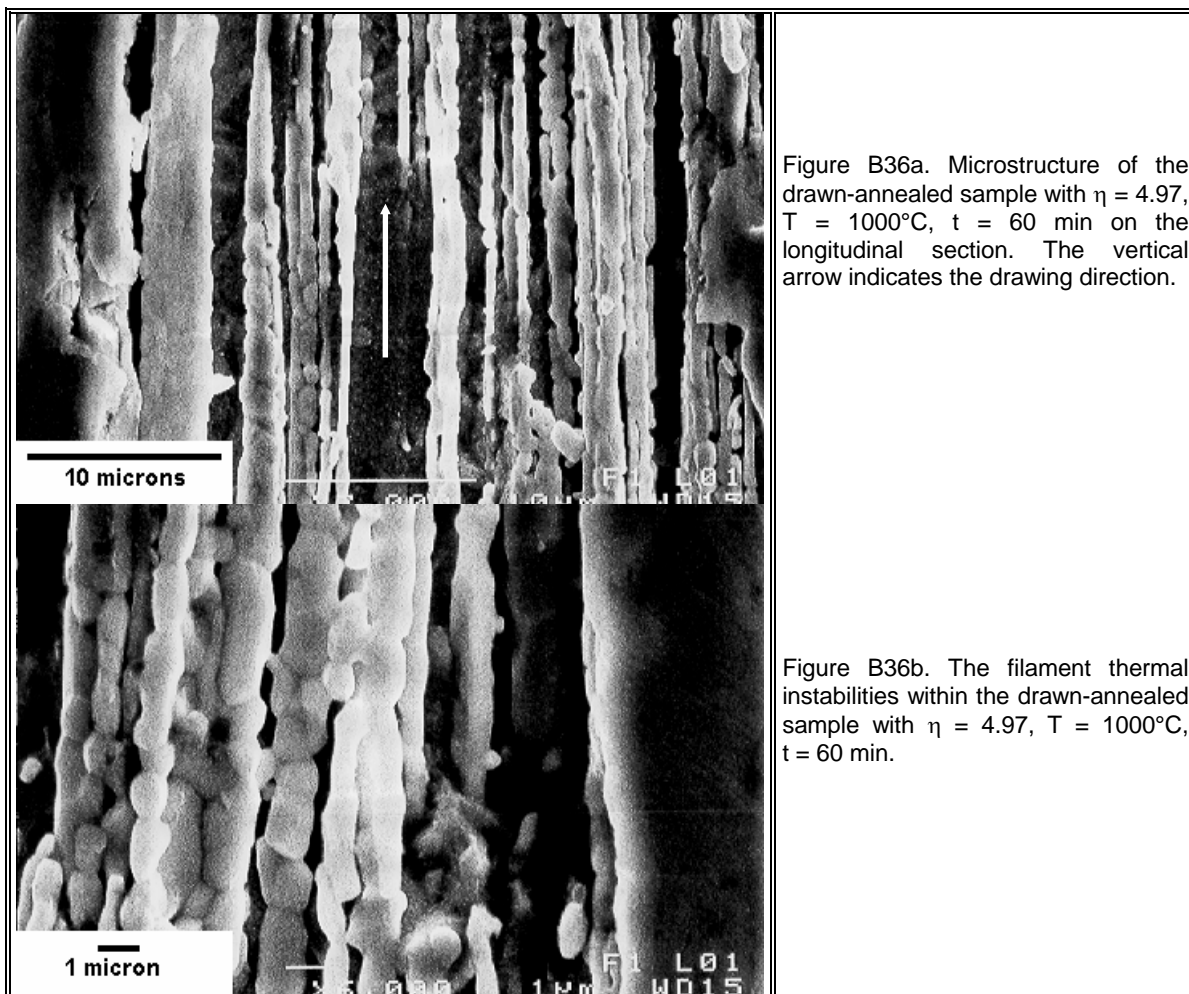


Figure B34a. Microstructure of the drawn-annealed sample with $\eta = 4.97$, $T = 1000^{\circ}\text{C}$, $t = 15$ min on the longitudinal section. The vertical arrow indicates the drawing direction. The instabilities are more extensive than those of the sample in figure B33.





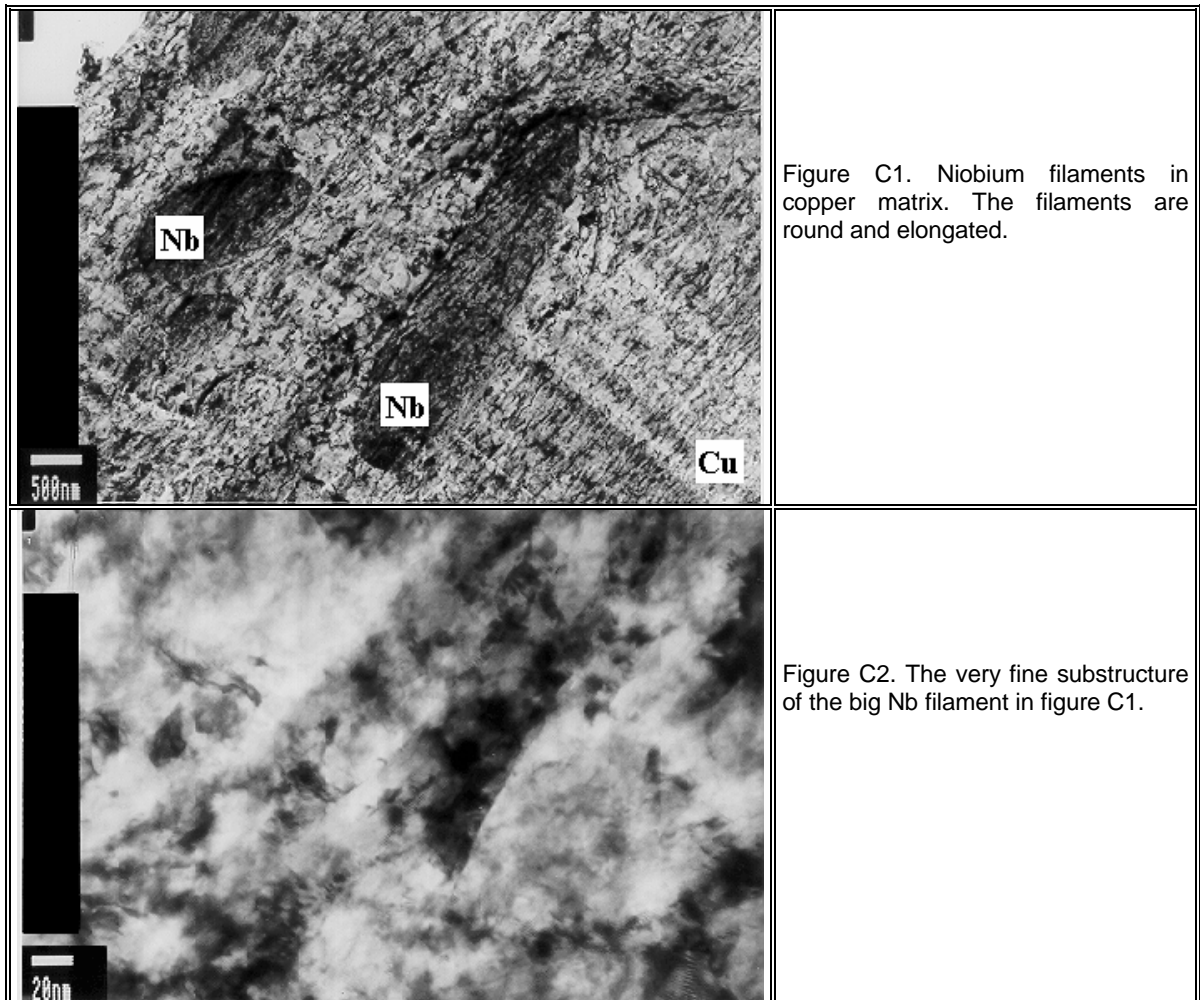
APPENDIX C

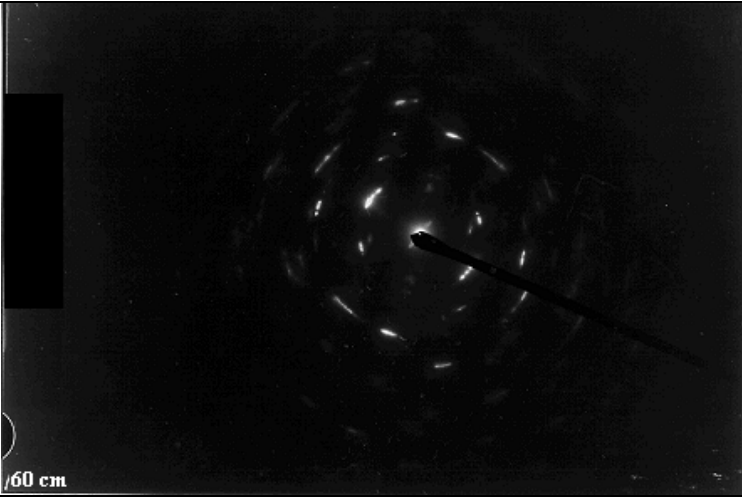
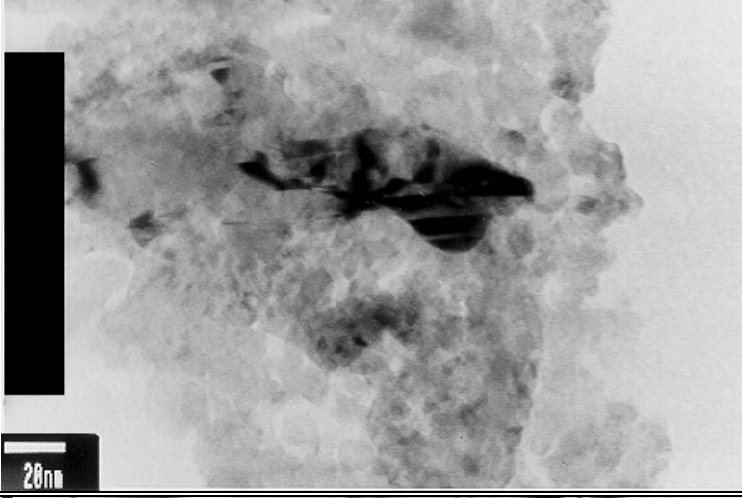
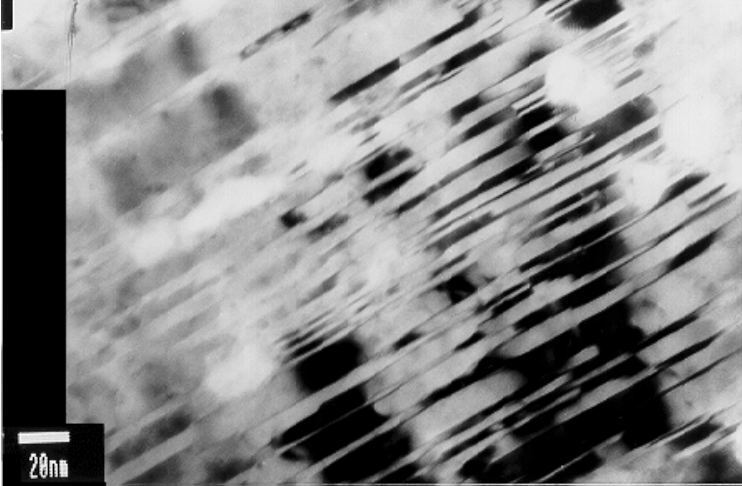
RESULTS OF

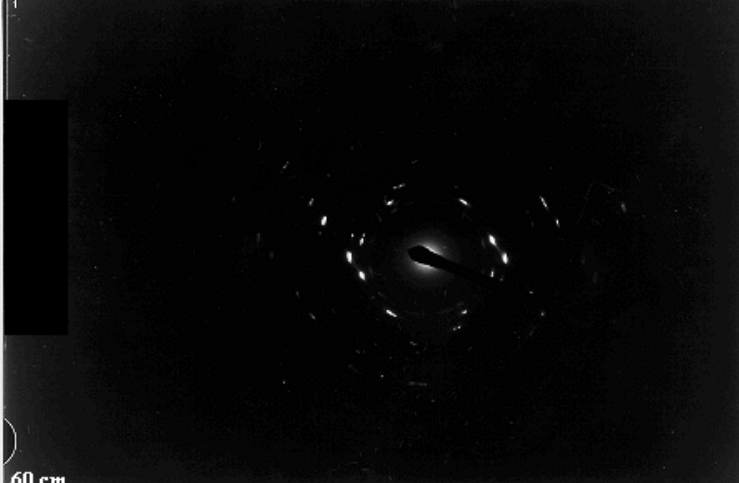
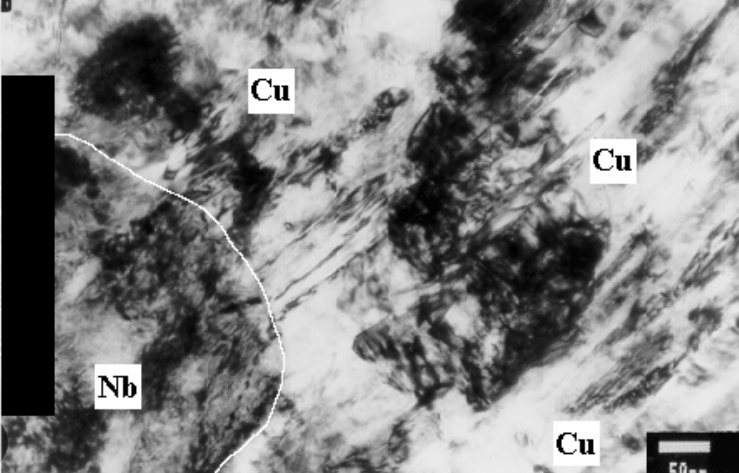
TRANSMISSION ELECTRON

MICROSCOPE

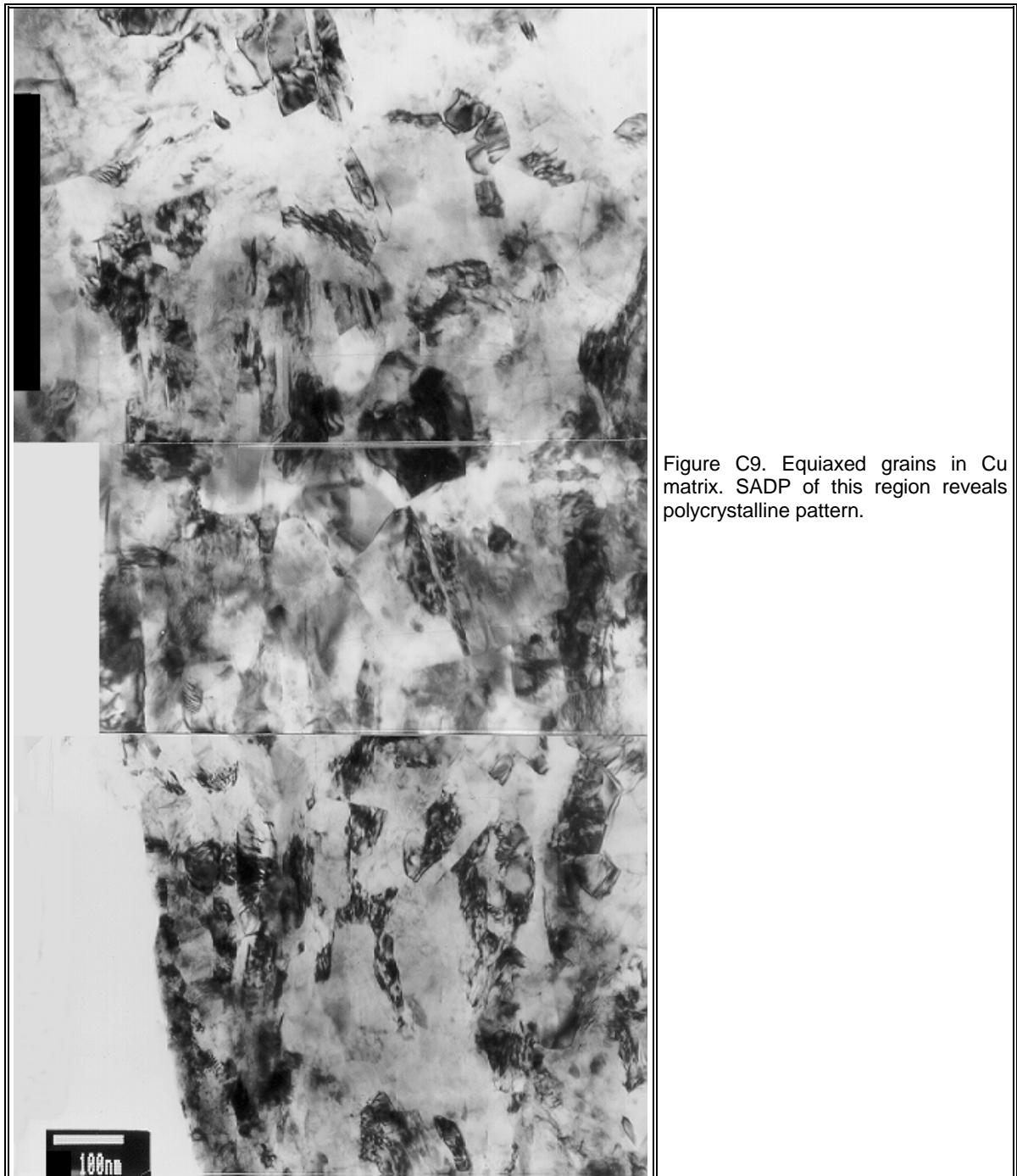
1. As-Drawn Cu-18%Nb with $\eta = 2.08$



| | |
|---|--|
|  <p data-bbox="228 694 295 725">/60 cm</p> | <p data-bbox="994 383 1401 443">Figure C3. SADP of Nb filament in figure C2.</p> |
|  <p data-bbox="228 1182 295 1227">20nm</p> | <p data-bbox="994 880 1401 965">Figure C4. Fine twinings in a small dynamically recrystallized copper grain.</p> |
|  <p data-bbox="228 1673 295 1718">20nm</p> | <p data-bbox="994 1375 1401 1435">Figure C5. Many twinings in copper matrix.</p> |

| | |
|---|--|
|  <p>60 cm</p> | <p>Figure C6. SADP of Cu twinnings in figure C5.</p> |
|  <p>Cu</p> <p>Nb</p> <p>Cu</p> <p>50 nm</p> | <p>Figure C7. The interphase between copper and niobium. Some twinnings are observed in copper matrix.</p> |
|  <p>50 cm</p> | <p>Figure C8. SADP of Cu twinnings in figure C7.</p> |

2. Drawn-Annealed Cu-18%Nb with $\eta = 2.08$, $T = 800^\circ\text{C}$, $t = 60$ sec (Salt Bath Furnace)



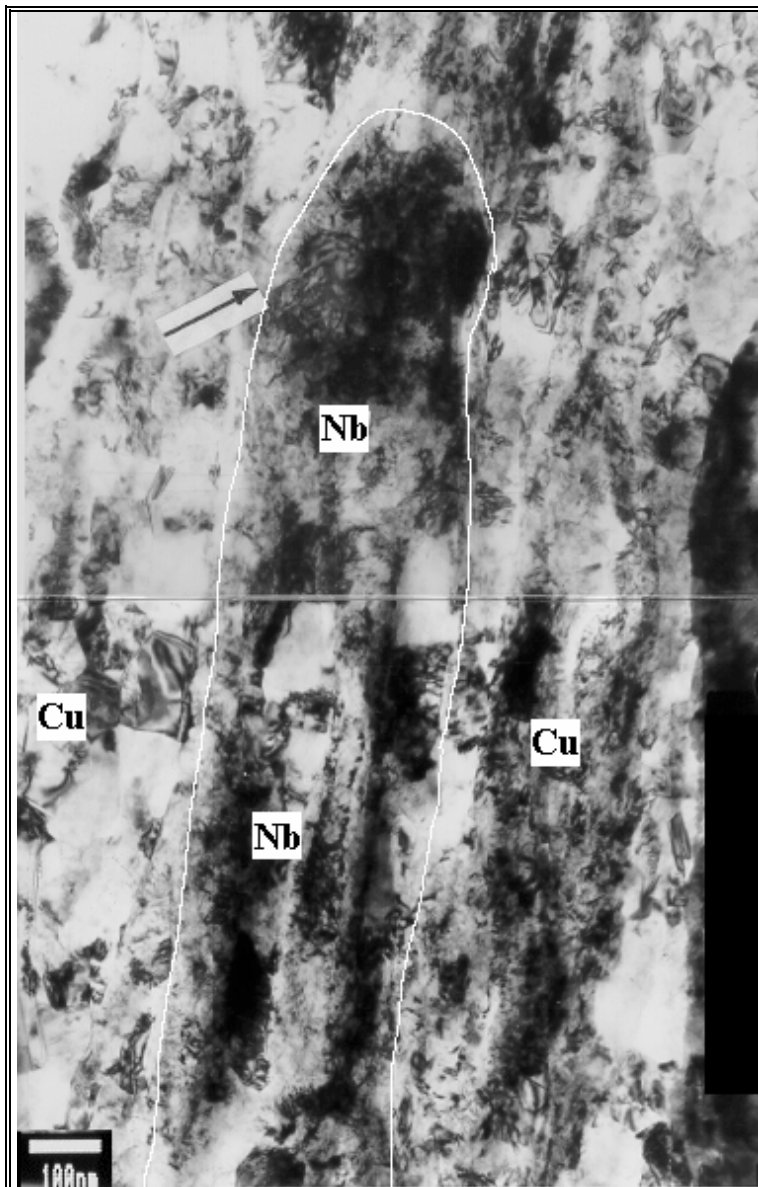


Figure C10. Nb filament in Cu matrix. The interphase region (arrowed) is enlarged in figure C11.

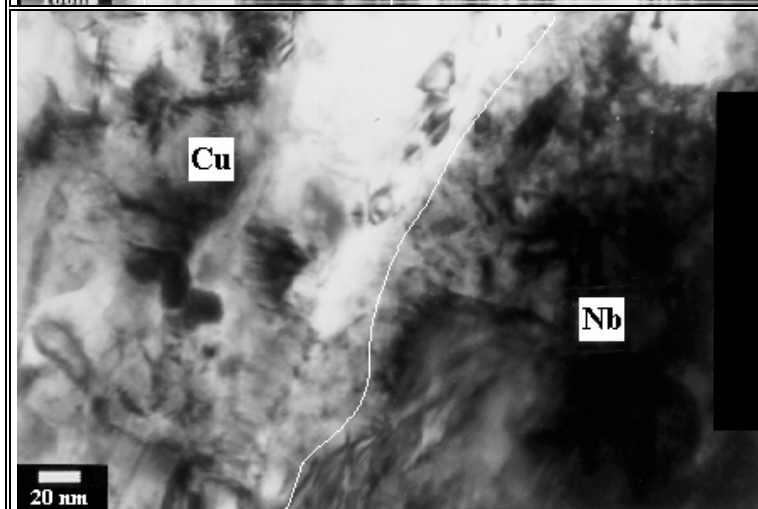
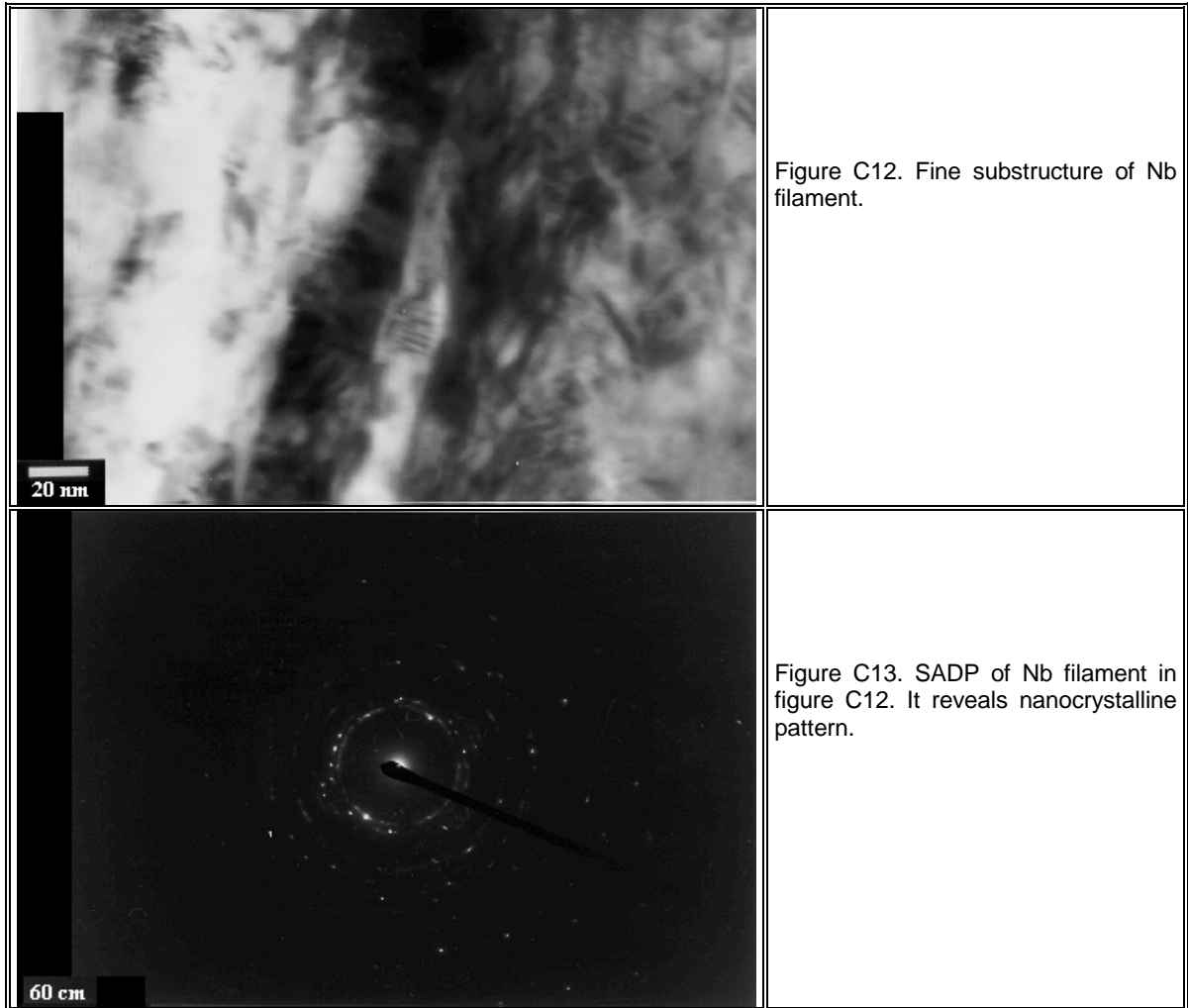
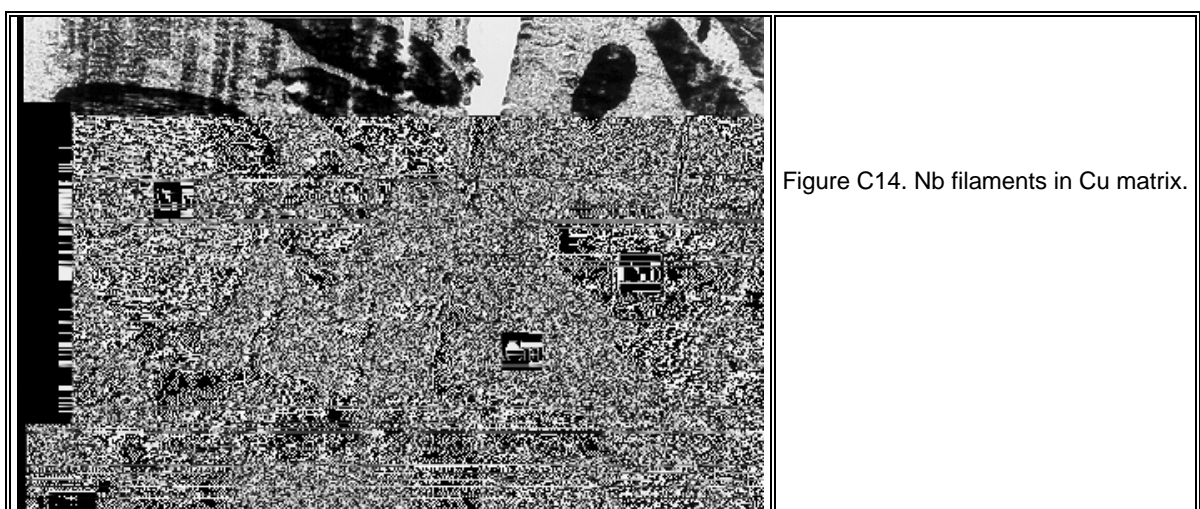


Figure C11. The interphase between copper and niobium. Niobium features a fine substructure.



3. Drawn-Annealed Cu-18%Nb with $\eta = 2.08$, $T = 800^\circ\text{C}$, $t = 30$ min (Vacuum Furnace)



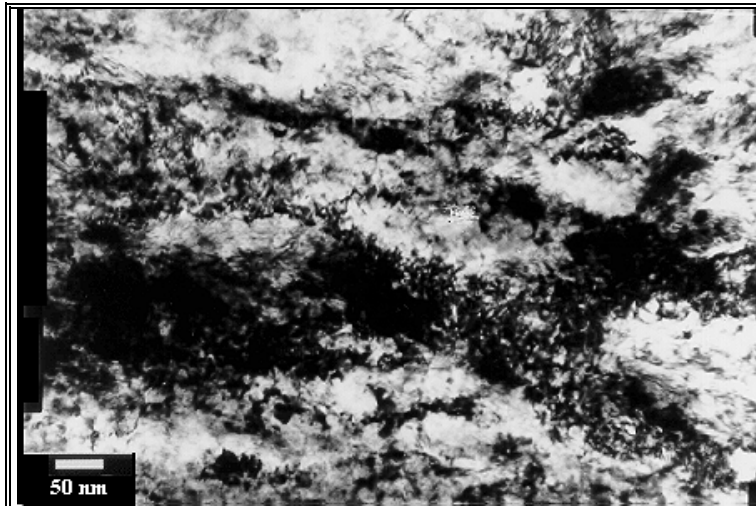


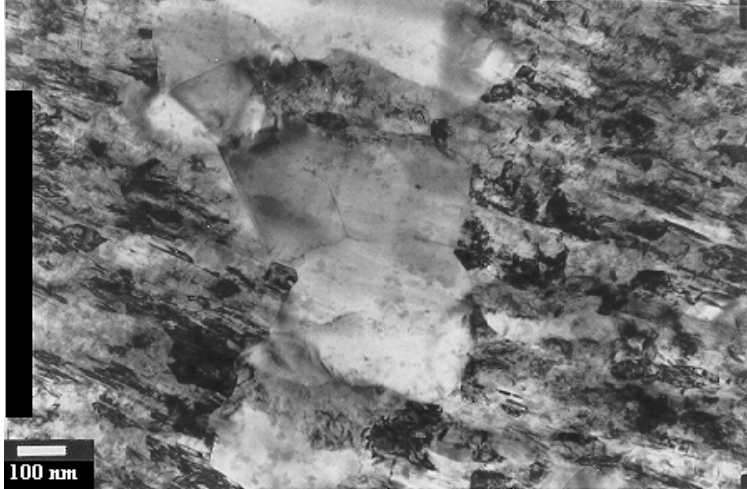
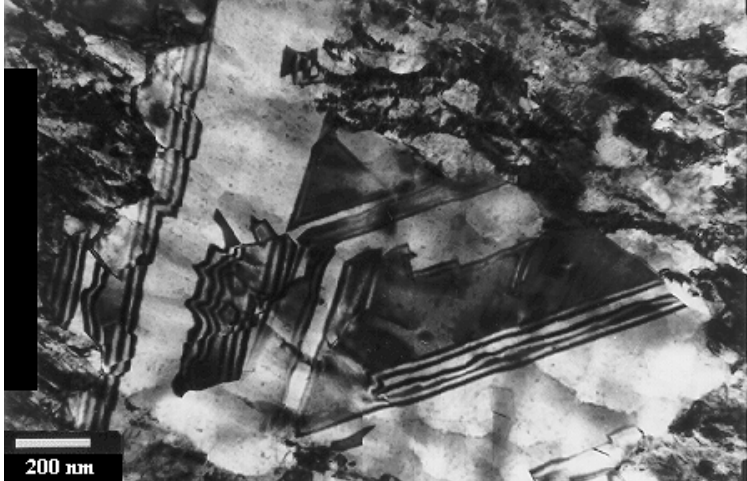
Figure C15. Dislocations in niobium filament.

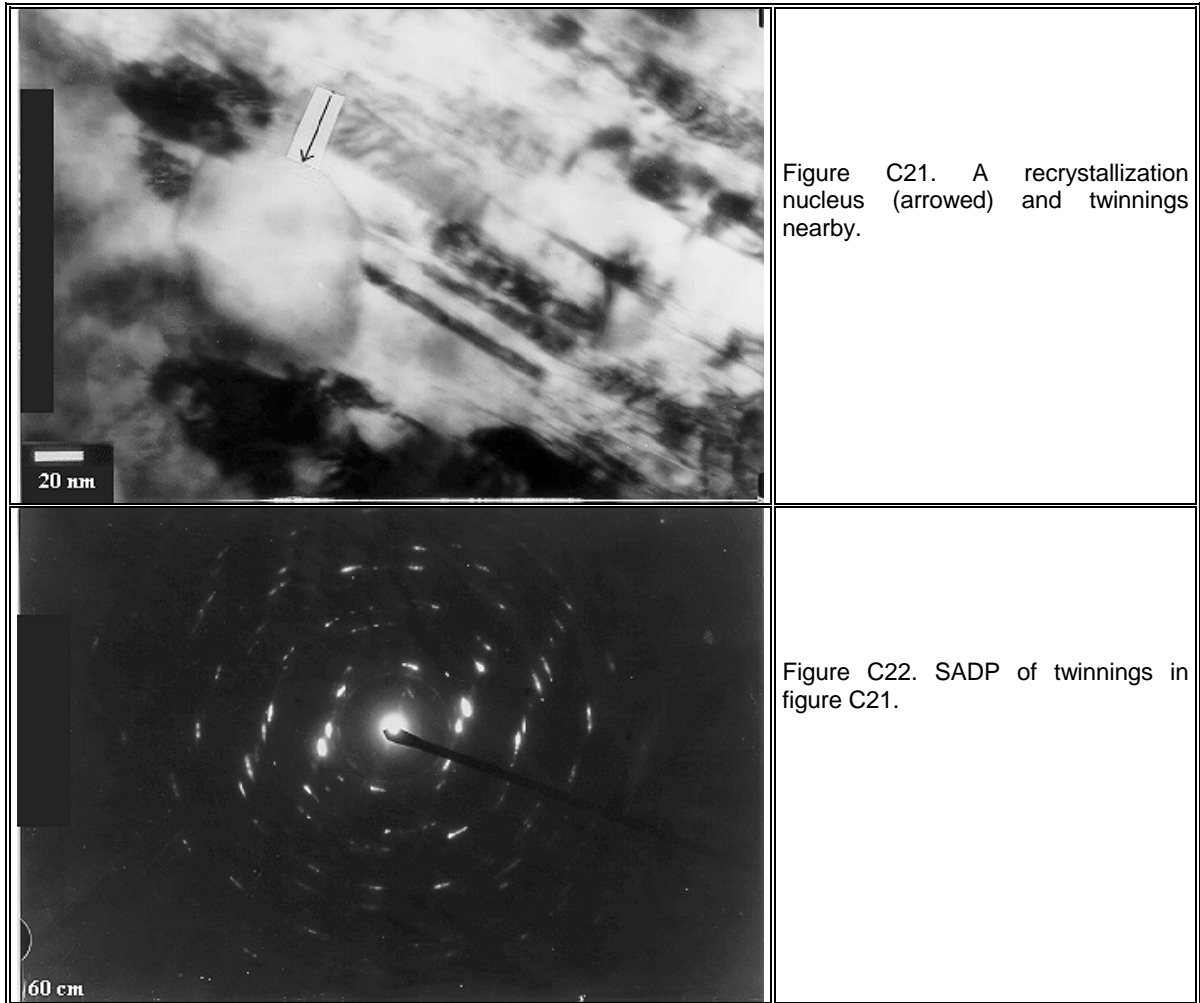


Figure C16. Some dislocations in Nb try to form cell structure (arrowed).

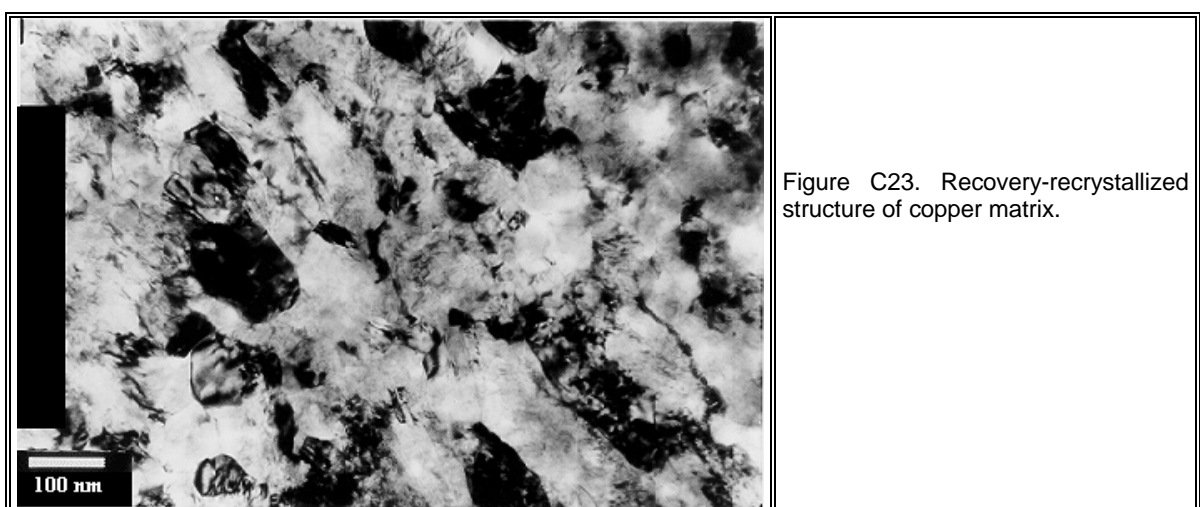


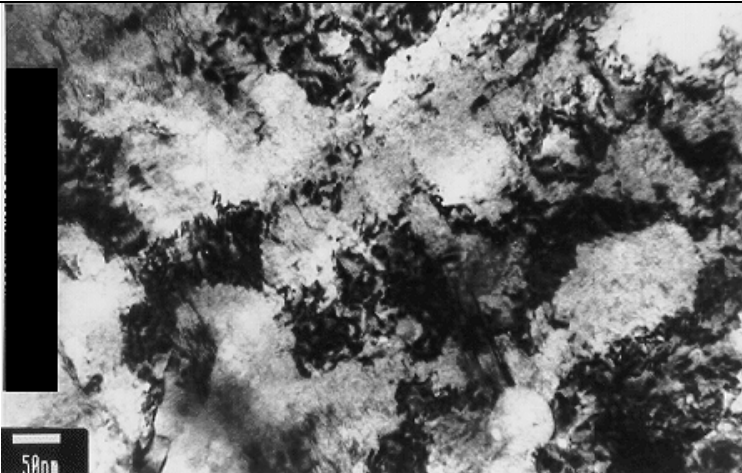
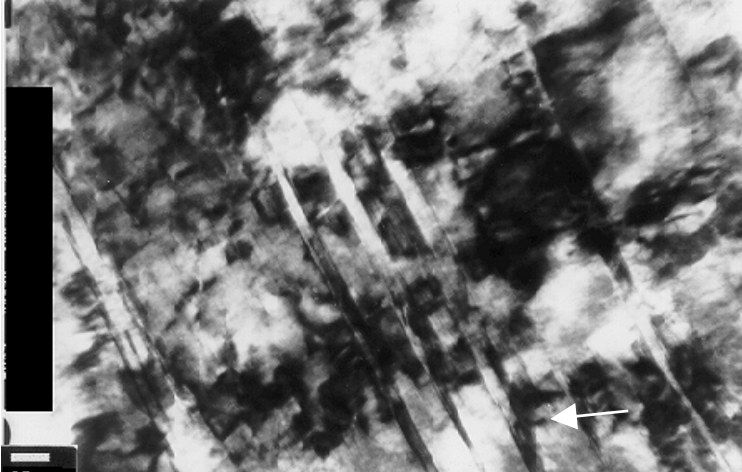
Figure C17. An annealing twinning (arrowed) in a recrystallized Cu grain.

| | |
|---|---|
|  <p>50 μm</p> | <p>Figure C18. Cell structure in copper matrix.</p> |
|  <p>100 μm</p> | <p>Figure C19. The recrystallized copper grains.</p> |
|  <p>200 μm</p> | <p>Figure C20. Recrystallized Cu grains with annealing twinings inside.</p> |

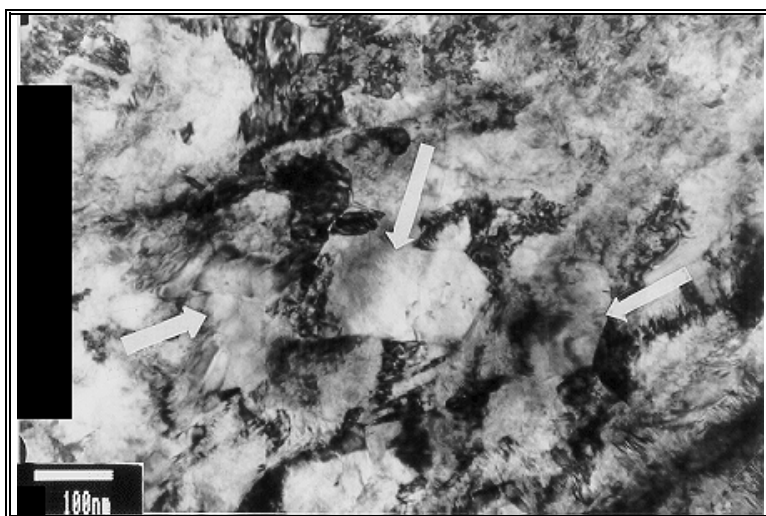


4. Drawn-Annealed Cu-18%Nb with $\eta = 2.08$, $T = 800^{\circ}\text{C}$, $t = 60 \text{ min}$ (Vacuum Furnace)

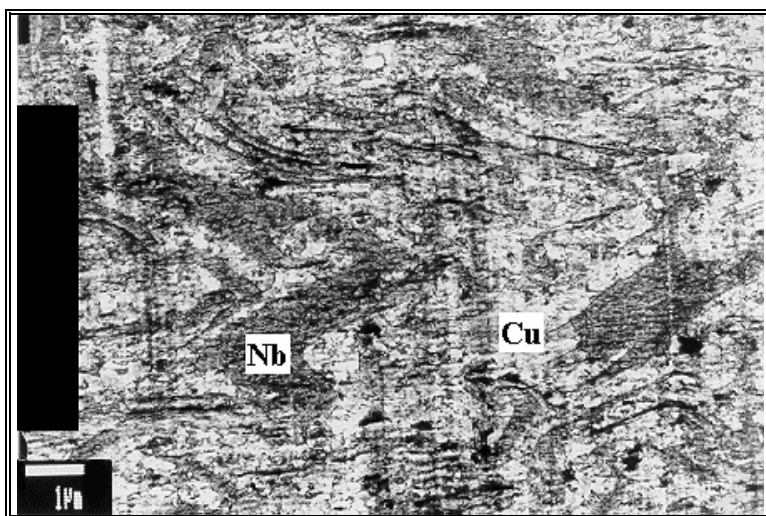
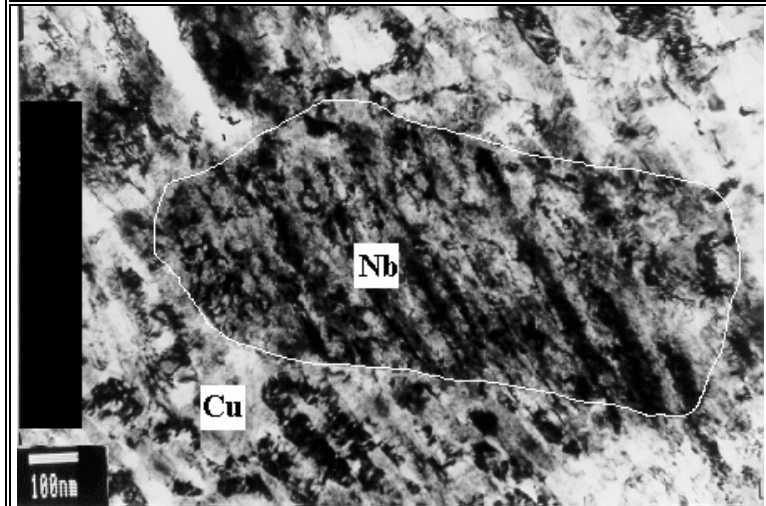
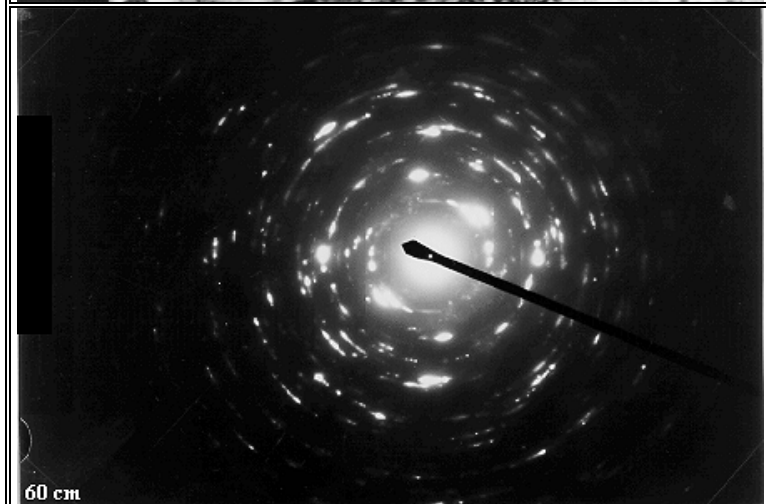


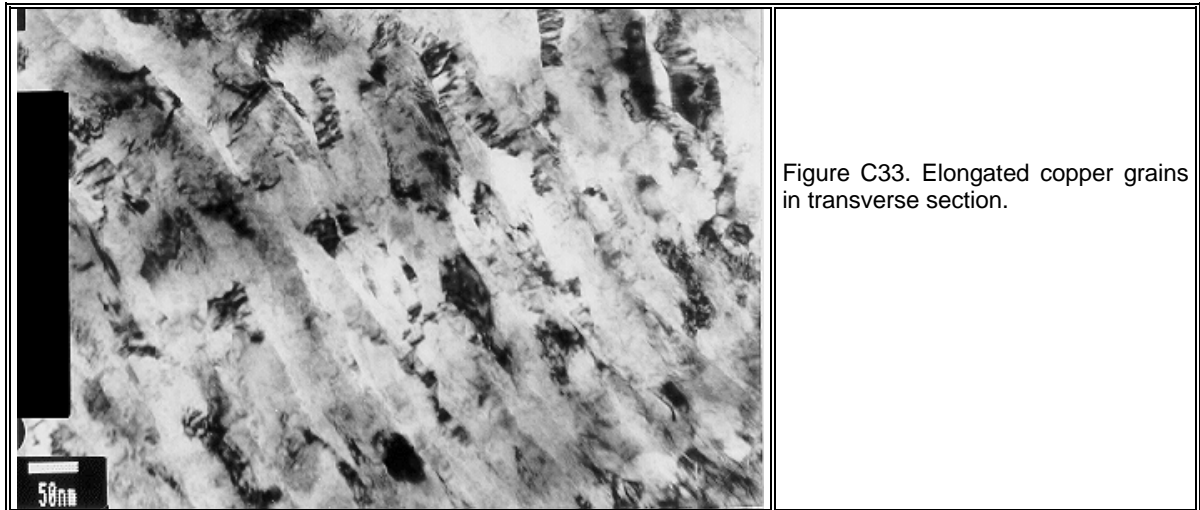
| | |
|---|---|
|  | <p>Figure C24. Cell structure in copper matrix. Arrow indicates a nucleus of recrystallization.</p> |
|  | <p>Figure C25. SADP of copper structure in figure C23. It reveals polycrystalline nature.</p> |
|  | <p>Figure C26. Twinning in copper matrix.</p> |

5. Drawn-Annealed Cu-18%Nb with $\eta = 2.08$, $T = 1000^\circ\text{C}$, $t = 30$ min (Vacuum Furnace)

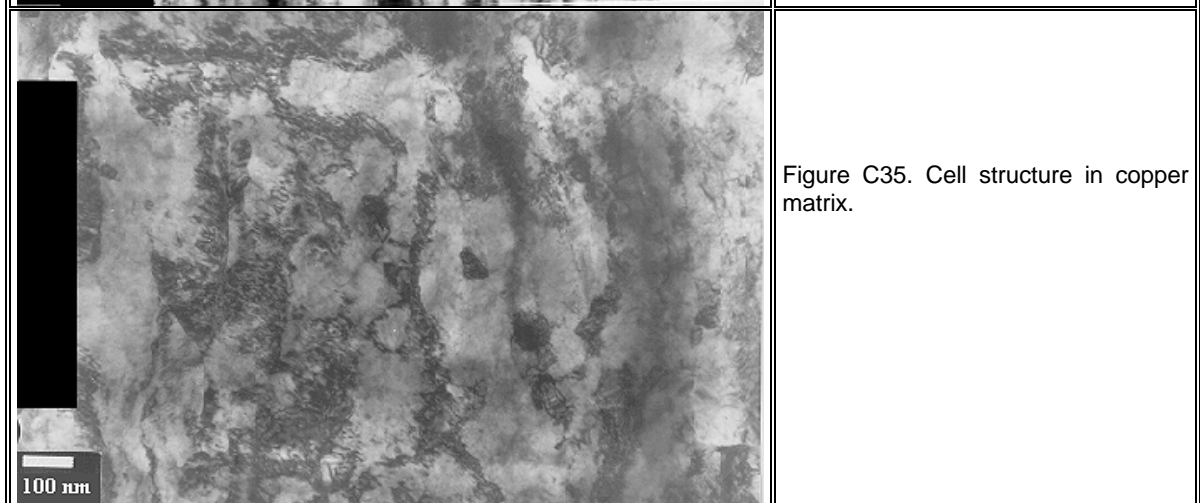
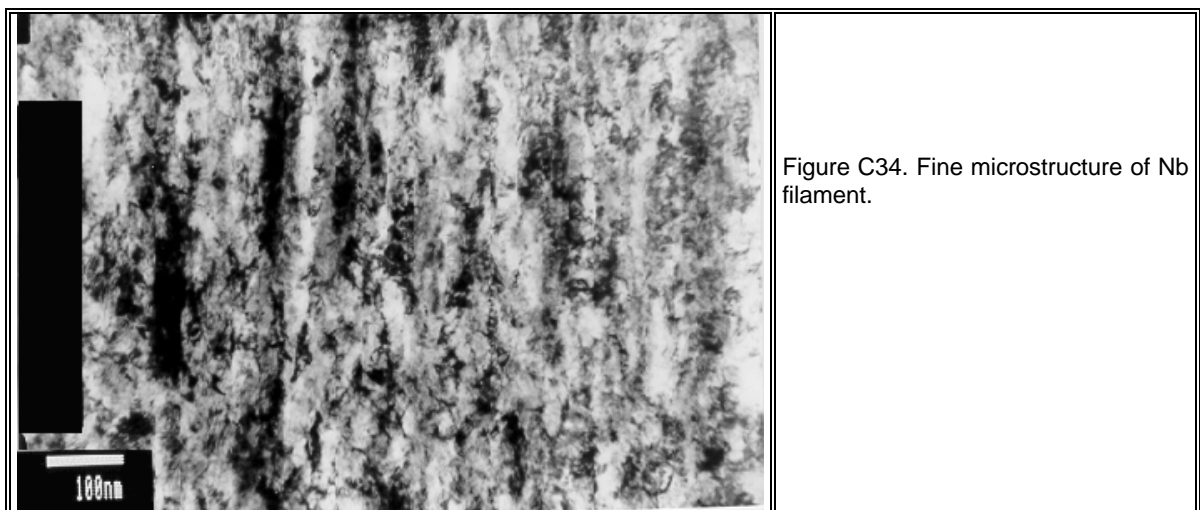
| | |
|---|---|
|  | <p>Figure C27. Recrystallized grains (arrowed) in Cu matrix.</p> |
|  | <p>Figure C28. Large recrystallized grain (bright area) in Cu matrix.</p> |
|  | <p>Figure C29. Twinning still occur in copper matrix.</p> |

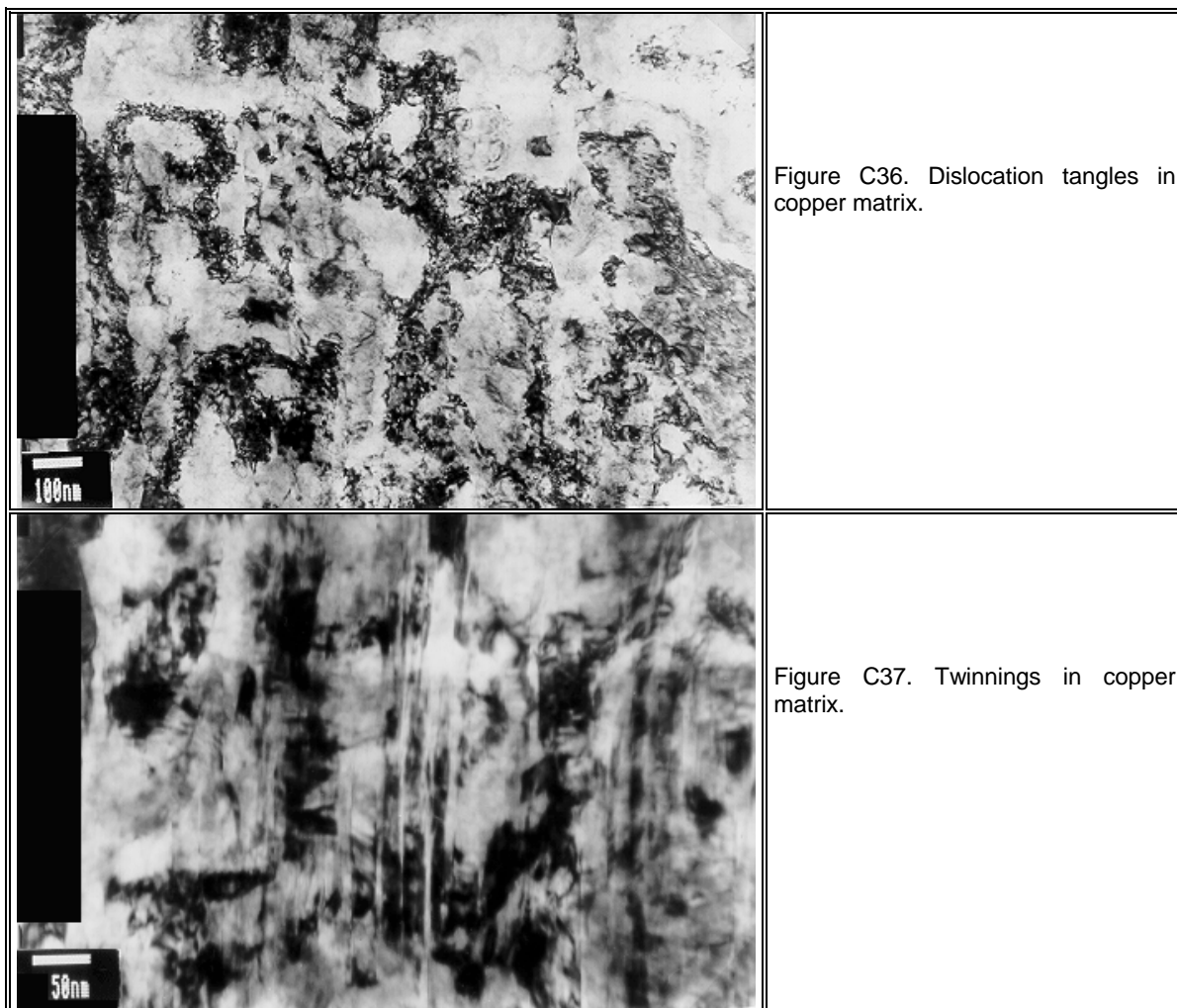
6. As-Drawn Cu-18%Nb with $\eta = 3.95$

| | |
|---|---|
|  | <p>Figure C30. Nb filaments (darker areas) in Cu matrix. In contrast to the drawn sample with $\eta = 2.08$ (figure C1), the filaments are now more curled and flatter in shape.</p> |
|  | <p>Figure C31. A niobium filament with fine substructure.</p> |
|  | <p>Figure C32. SADP of Nb filament in figure C31.</p> |

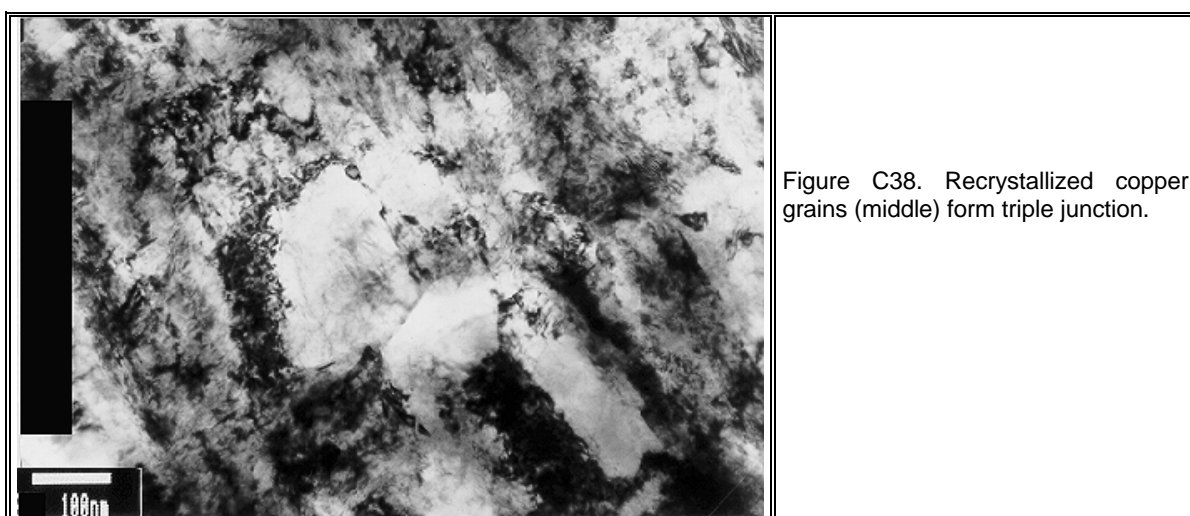


7. Drawn-Annealed Cu-18%Nb with $\eta = 3.95$, $T = 800^\circ\text{C}$, $t = 60$ sec (Salt Bath Furnace)





8. Drawn-Annealed Cu-18%Nb with $\eta = 3.95$, $T = 800^\circ\text{C}$, $t = 30$ min (Vacuum Furnace)



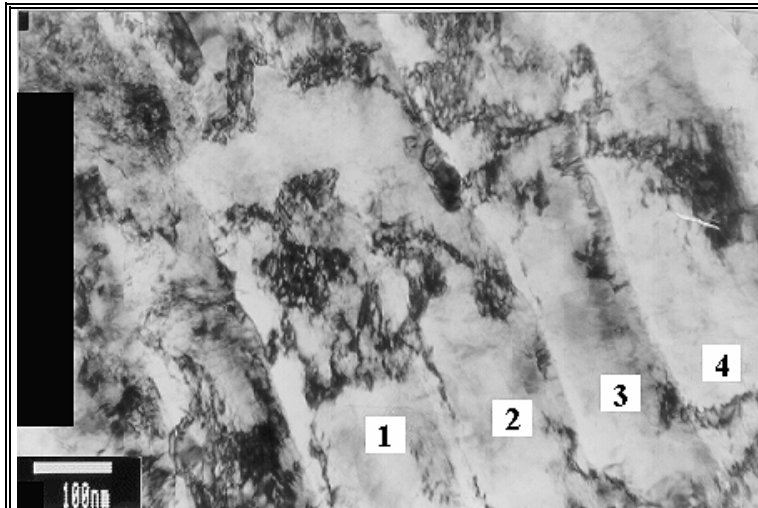


Figure C39. Four neighboring recrystallized copper grains.



Figure C40. A recrystallized copper grain (arrowed).

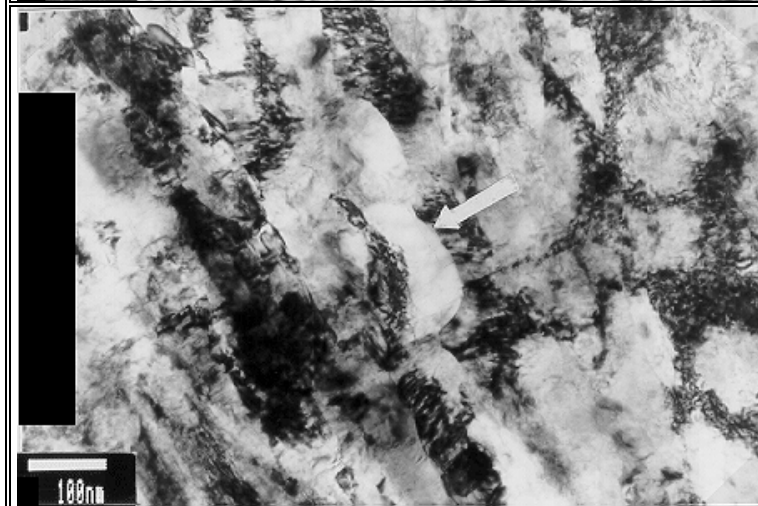


Figure C41. A recrystallized copper grain (arrowed) surrounded by cell structure.

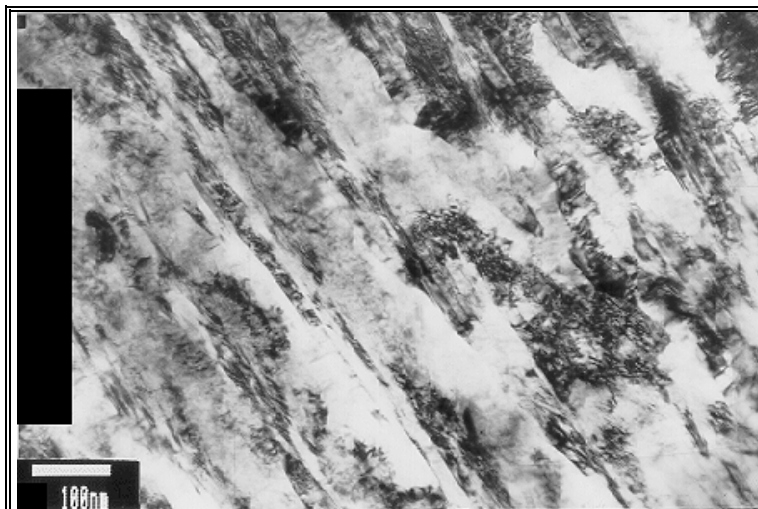


Figure C42. Twinning in copper matrix.

9. Drawn-Annealed Cu-18%Nb with $\eta = 3.95$, $T = 800^\circ\text{C}$, $t = 60$ min (Vacuum Furnace)

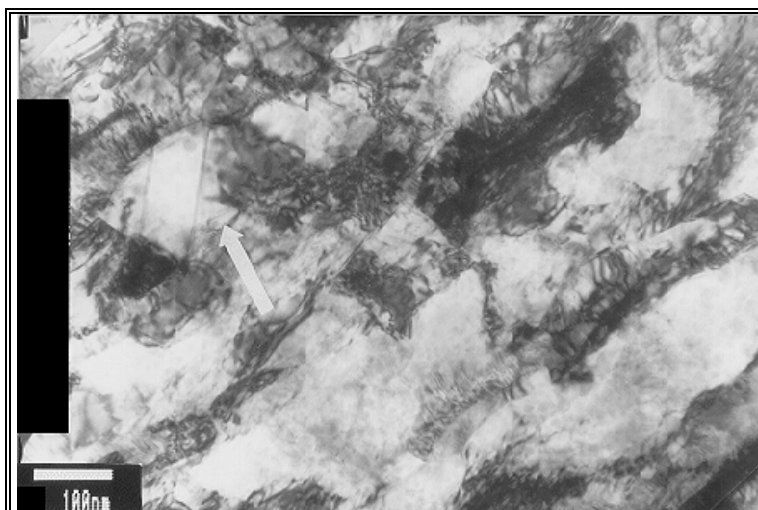


Figure C43. A wide annealing twinning in a recrystallized copper grain is observed (arrowed). Some cell structures still take place.

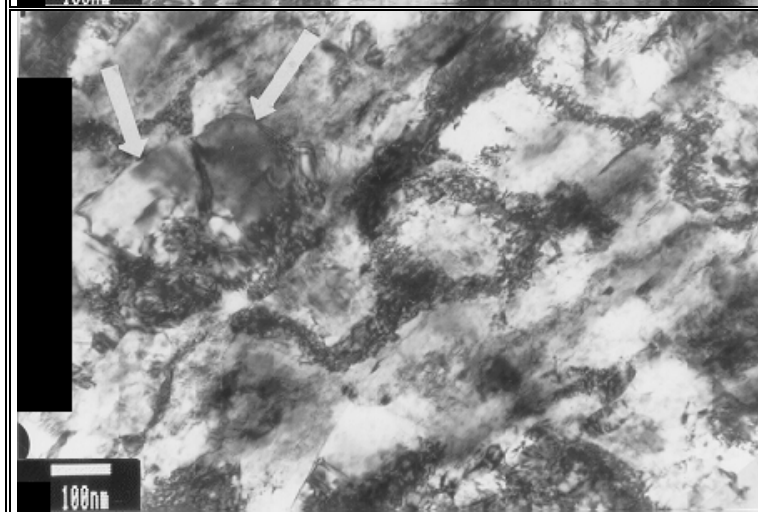


Figure C44. Recovery-recrystallization structure of copper, similar to that of figure C43. Arrows indicate recrystallized grains.

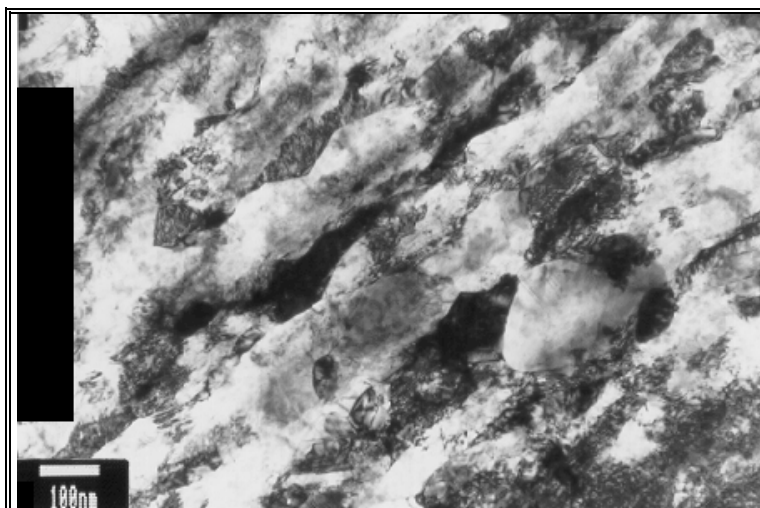


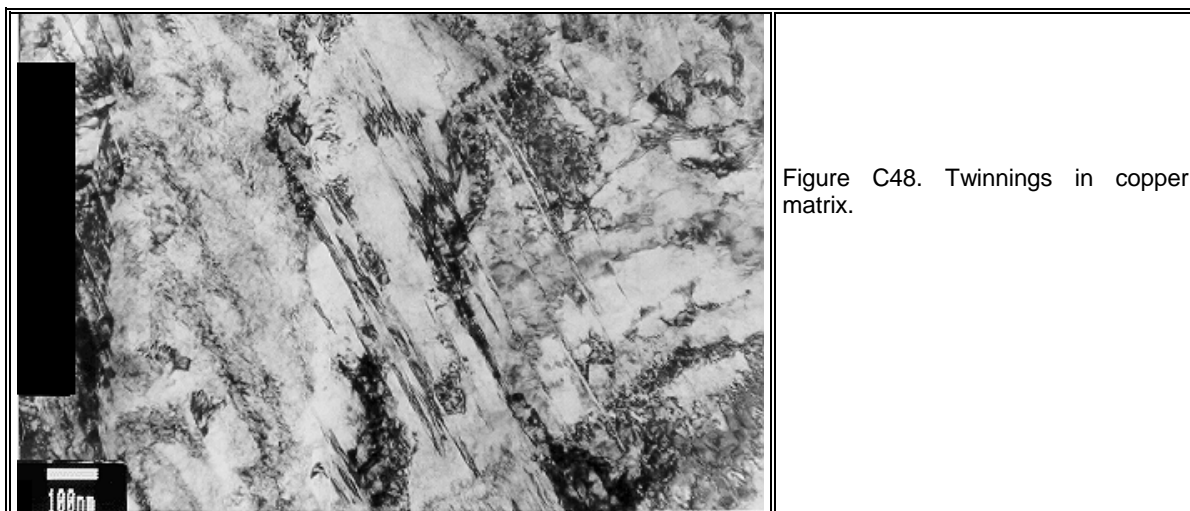
Figure C45. Recovery-recrystallization structure of copper.



Figure C46. An annealing twinning in recrystallized copper grain (arrowed).



Figure C47. A large recrystallized copper grain (dark area), as shown by upper arrow. A neighboring grain is also shown by lower arrow.



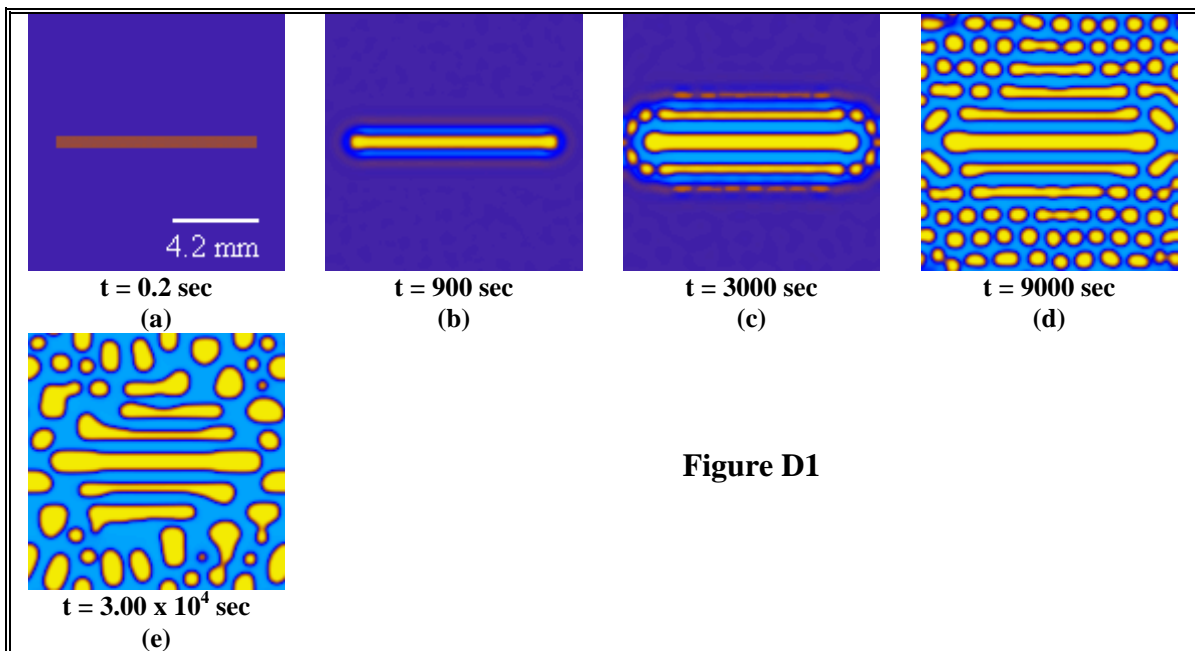
APPENDIX D

RESULTS OF

CAHN-HILLIARD SIMULATION

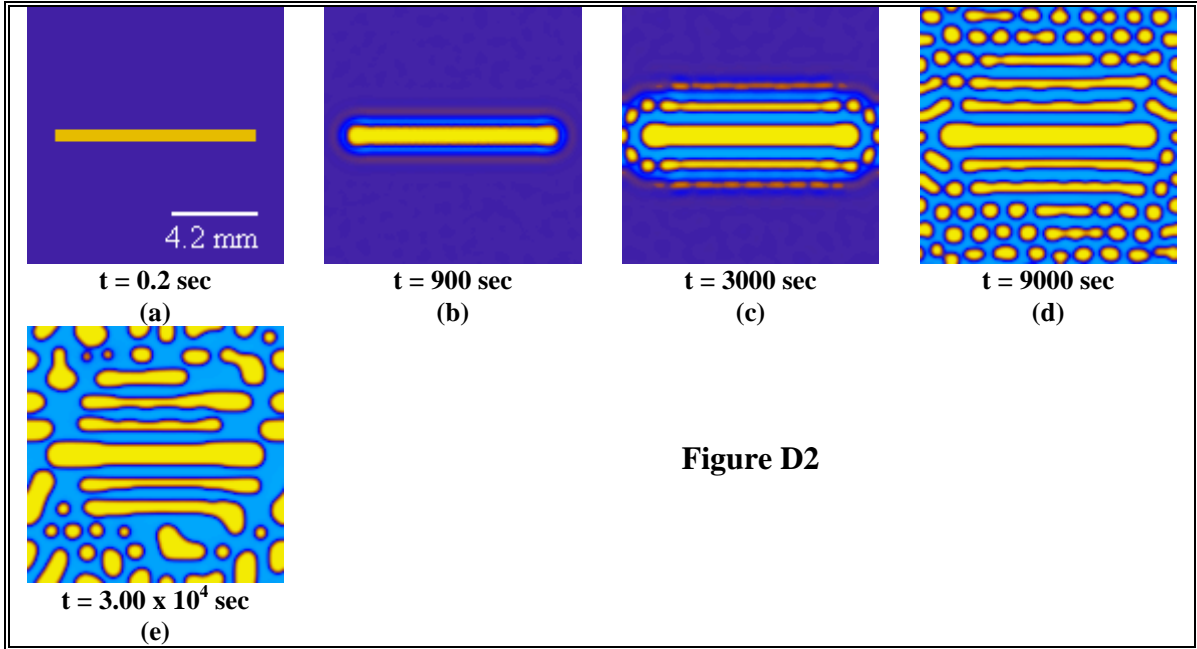
1. Precipitation of Niobium in Copper Phase

| | | |
|--|--------------------------------|------------------------|
| $\Delta x = 1.00 \times 10^{-4}$ m | $C_p^0 = 0.60$ (mole fraction) | Mobility Ratio = 1 : 1 |
| $\Delta c = 3.00 \times 10^{-5}$ (mole fraction) | $\gamma = 100$ J/m | $L = 10$ mm |
| $C_m^0 = 0.40$ (mole fraction) | $T = 1273$ K | $W = 0.60$ mm |

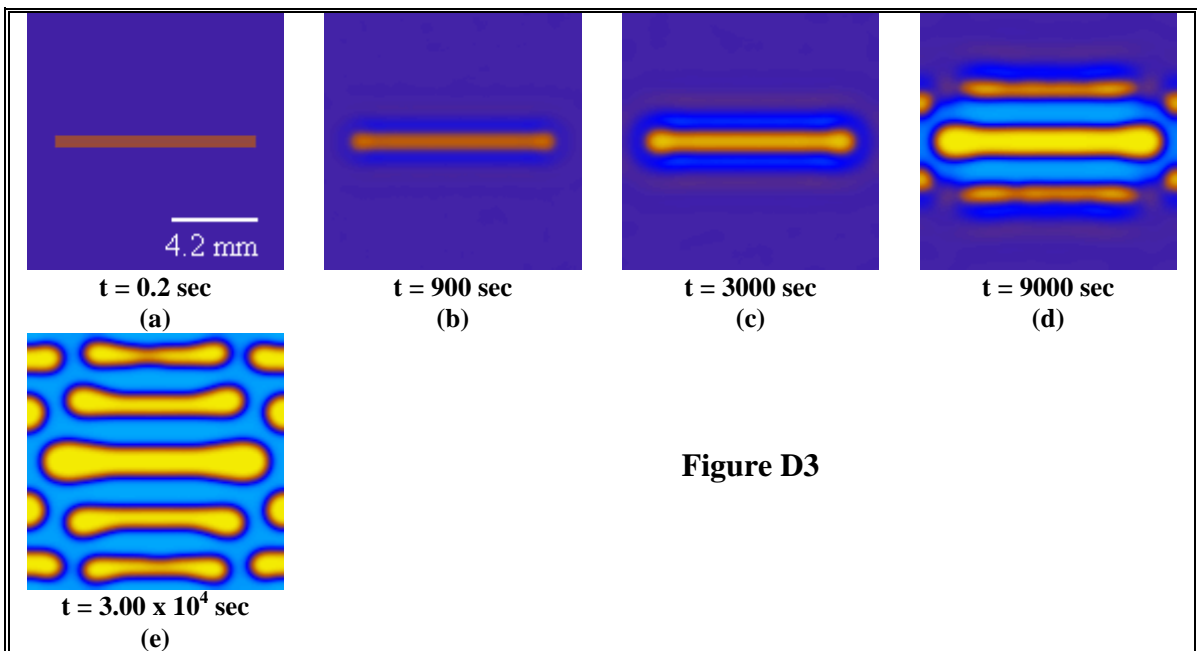




| | | |
|--|--|--|
| $\Delta x = 1.00 \times 10^{-4} \text{ m}$ $\Delta c = 3.00 \times 10^{-5} \text{ (mole fraction)}$ $C_m^0 = 0.40 \text{ (mole fraction)}$ | $C_p^0 = 0.90 \text{ (mole fraction)}$ $\gamma = 100 \text{ J/m}$ $T = 1273 \text{ K}$ | Mobility Ratio = 1 : 1 $L = 10 \text{ mm}$ $W = 0.60 \text{ mm}$ |
|--|--|--|

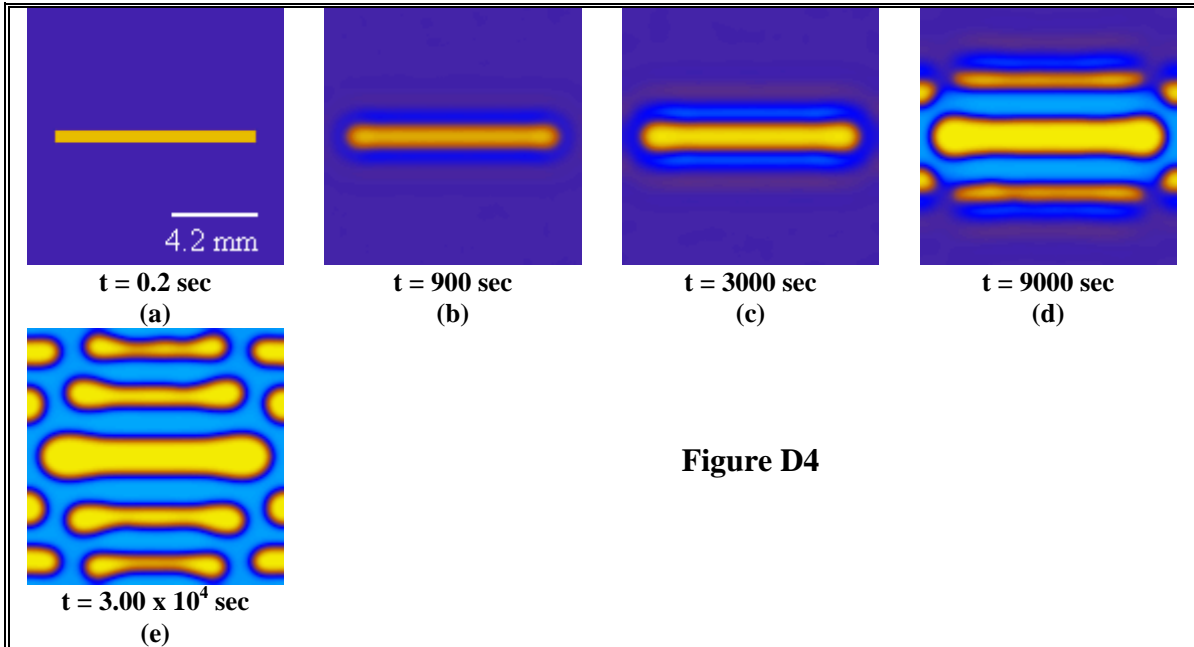


| | | |
|--|--|--|
| $\Delta x = 1.00 \times 10^{-4} \text{ m}$ $\Delta c = 3.00 \times 10^{-5} \text{ (mole fraction)}$ $C_m^0 = 0.40 \text{ (mole fraction)}$ | $C_p^0 = 0.60 \text{ (mole fraction)}$ $\gamma = 500 \text{ J/m}$ $T = 1273 \text{ K}$ | Mobility Ratio = 1 : 1 $L = 10 \text{ mm}$ $W = 0.60 \text{ mm}$ |
|--|--|--|





| | | |
|--|--|--|
| $\Delta x = 1.00 \times 10^{-4} \text{ m}$ $\Delta c = 3.00 \times 10^{-5} \text{ (mole fraction)}$ $C_m^0 = 0.40 \text{ (mole fraction)}$ | $C_p^0 = 0.90 \text{ (mole fraction)}$ $\gamma = 500 \text{ J/m}$ $T = 1273 \text{ K}$ | Mobility Ratio = 1 : 1 $L = 10 \text{ mm}$ $W = 0.60 \text{ mm}$ |
|--|--|--|

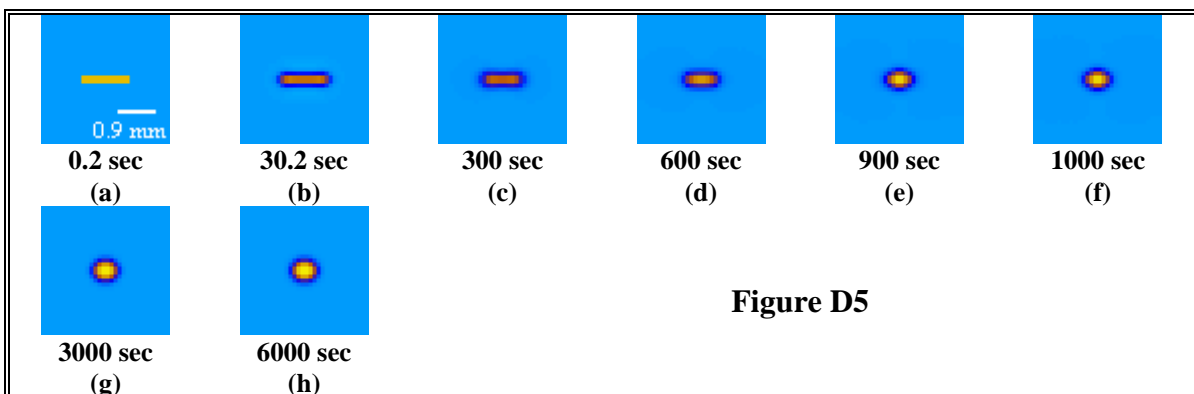


2. Thermal Instability of Niobium in Copper Phase

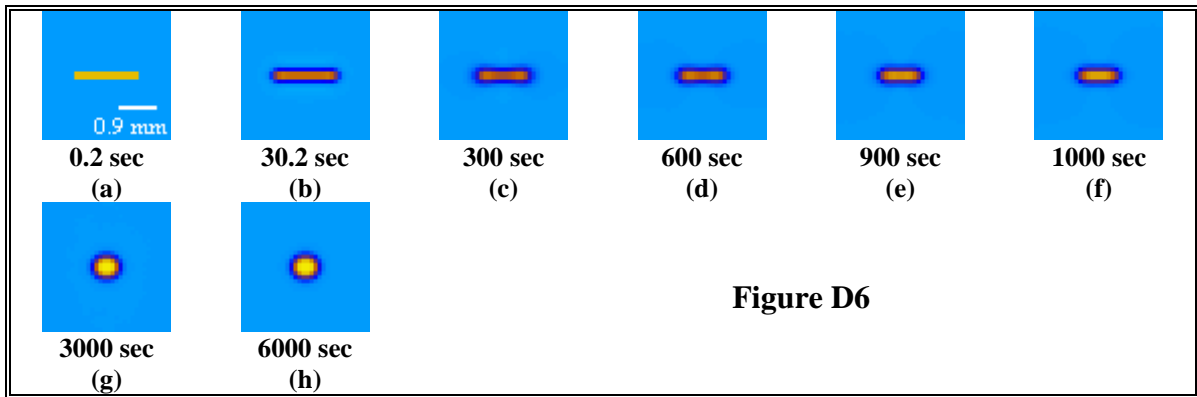
All the thermal instability simulations utilize the following common parameters :

| | | |
|--|---|-------------------------|
| $\Delta x = 1.00 \times 10^{-4} \text{ m}$ $\Delta c = 3.00 \times 10^{-5} \text{ (mole fraction)}$ $C_m^0 = 0.03 \text{ (mole fraction)}$ | $C_p^0 = 0.90 \text{ (mole fraction)}$ $\gamma = 70 \text{ J/m}$ $T = 1273 \text{ K}$ | Mobility Ratio = 10 : 1 |
|--|---|-------------------------|

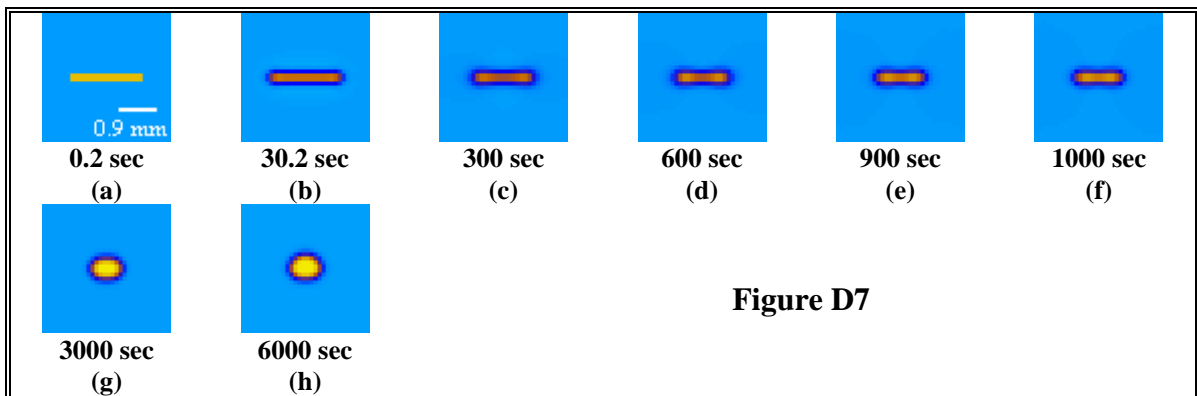
2.1 Aspect Ratio = $L/W = 1.20 \text{ mm}/0.20 \text{ mm} = 6.00$



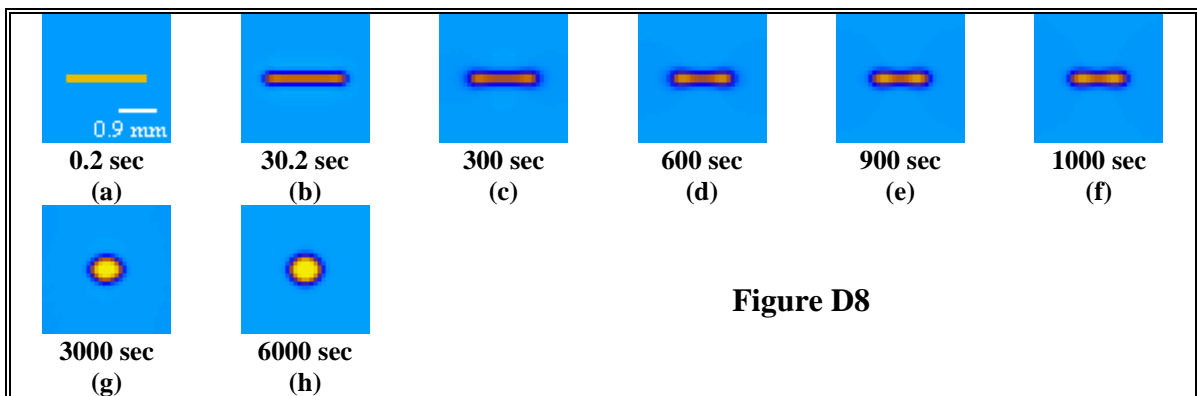
2.2 Aspect Ratio = $L/W = 1.60 \text{ mm}/0.20 \text{ mm} = 8.00$



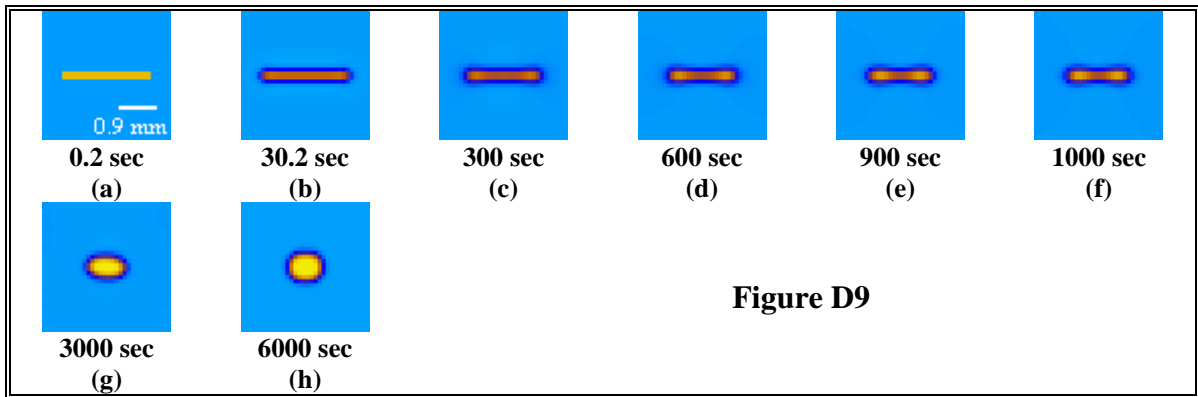
2.3 Aspect Ratio = $L/W = 1.80 \text{ mm}/0.20 \text{ mm} = 9.00$



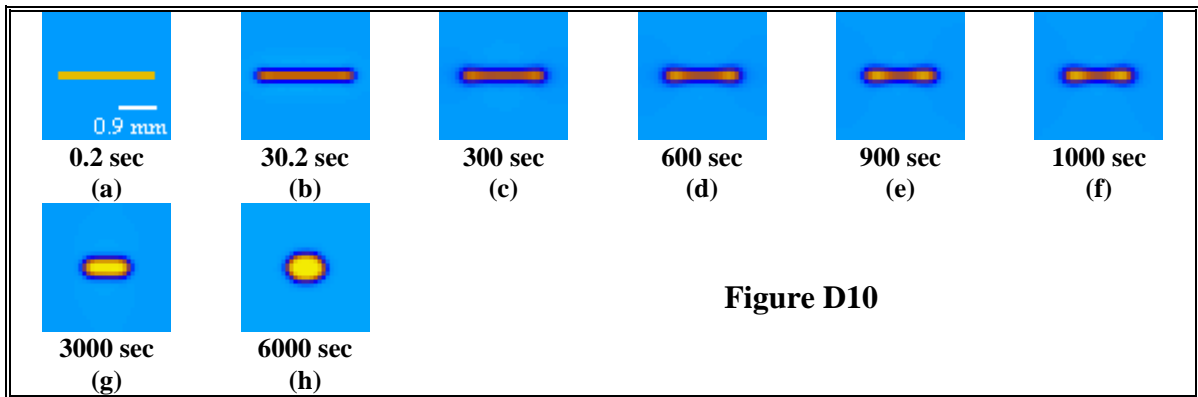
2.4 Aspect Ratio = $L/W = 2.00 \text{ mm}/0.20 \text{ mm} = 10.00$



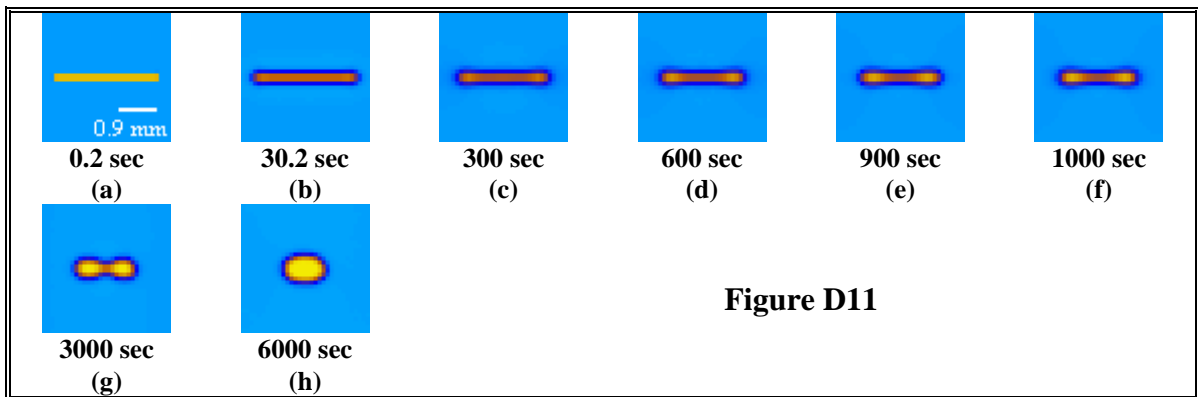
2.5 Aspect Ratio = $L/W = 2.20 \text{ mm}/0.20 \text{ mm} = 11.00$



2.6 Aspect Ratio = $L/W = 2.40 \text{ mm}/0.20 \text{ mm} = 12.00$



2.7 Aspect Ratio = $L/W = 2.60 \text{ mm}/0.20 \text{ mm} = 13.00$



2.8 Aspect Ratio = $L/W = 2.80 \text{ mm}/0.20 \text{ mm} = 14.00$

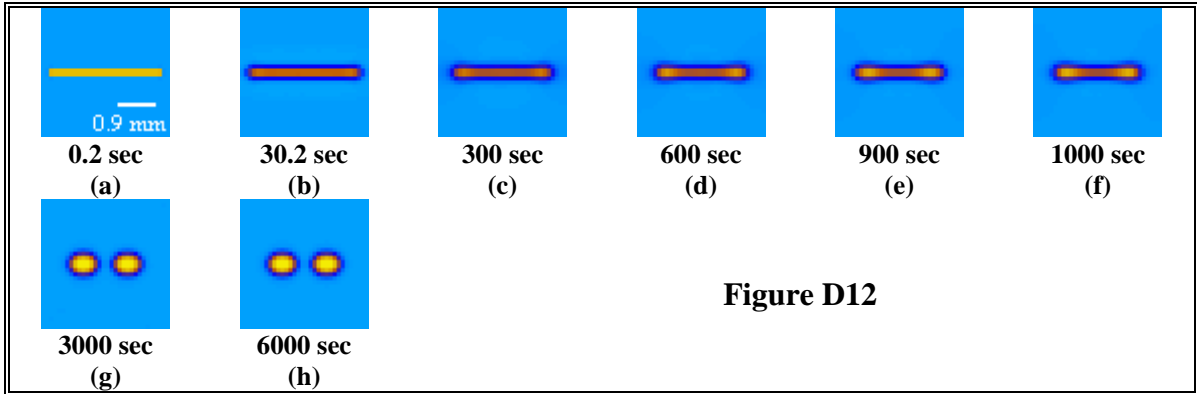


Figure D12

2.9 Aspect Ratio = $L/W = 3.00 \text{ mm}/0.20 \text{ mm} = 15.00$

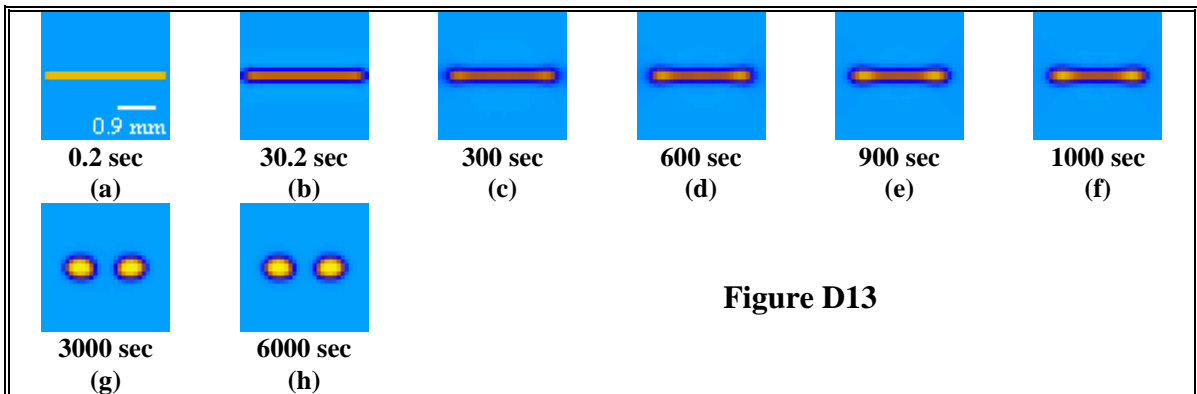


Figure D13

2.10 Aspect Ratio = $L/W = 4.00 \text{ mm}/0.20 \text{ mm} = 20.00$

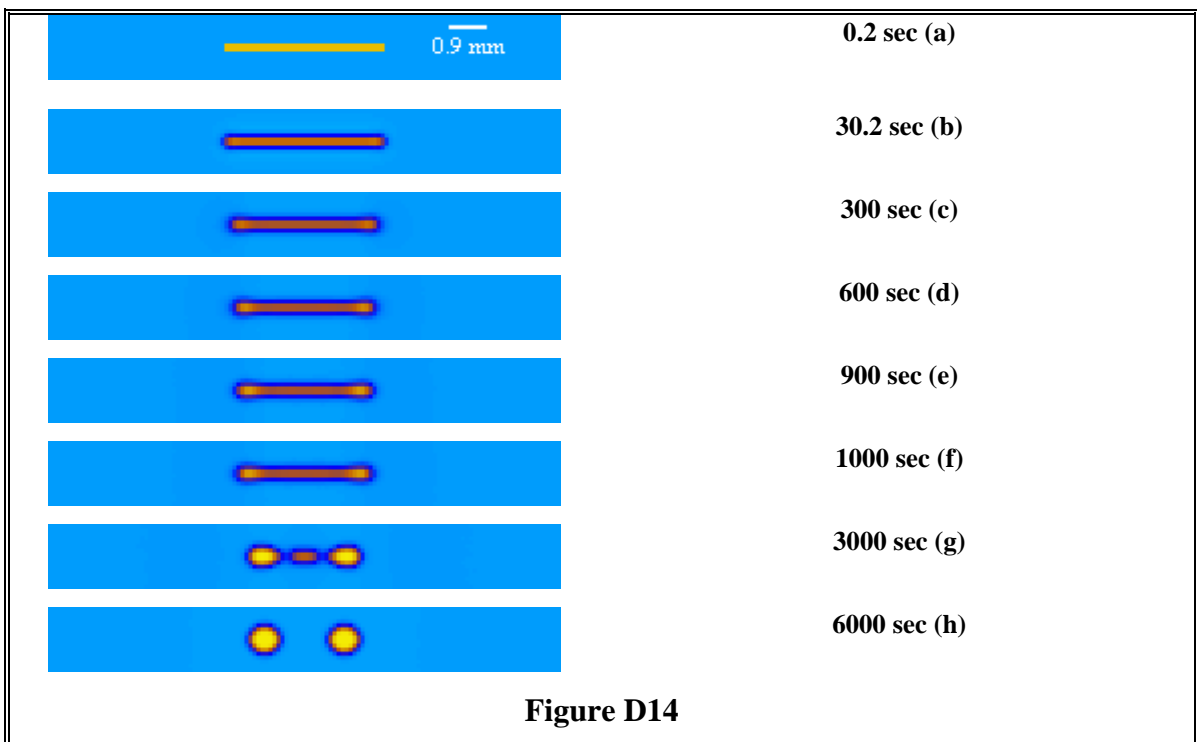
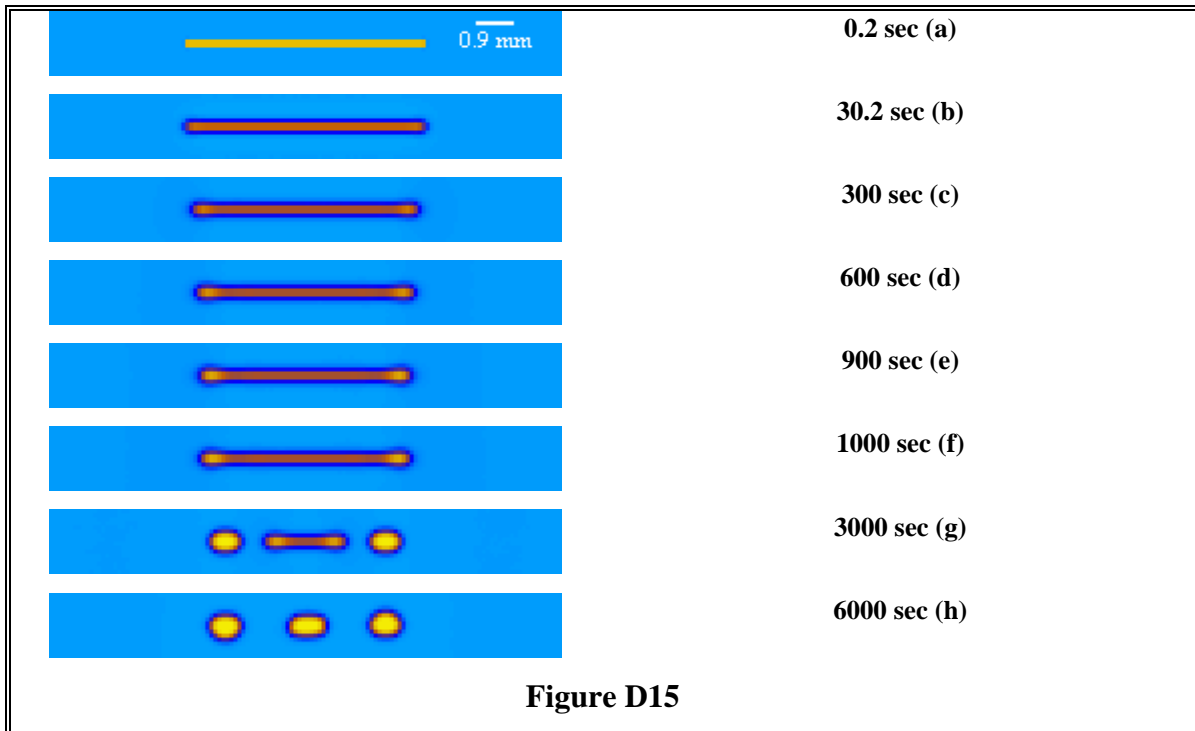
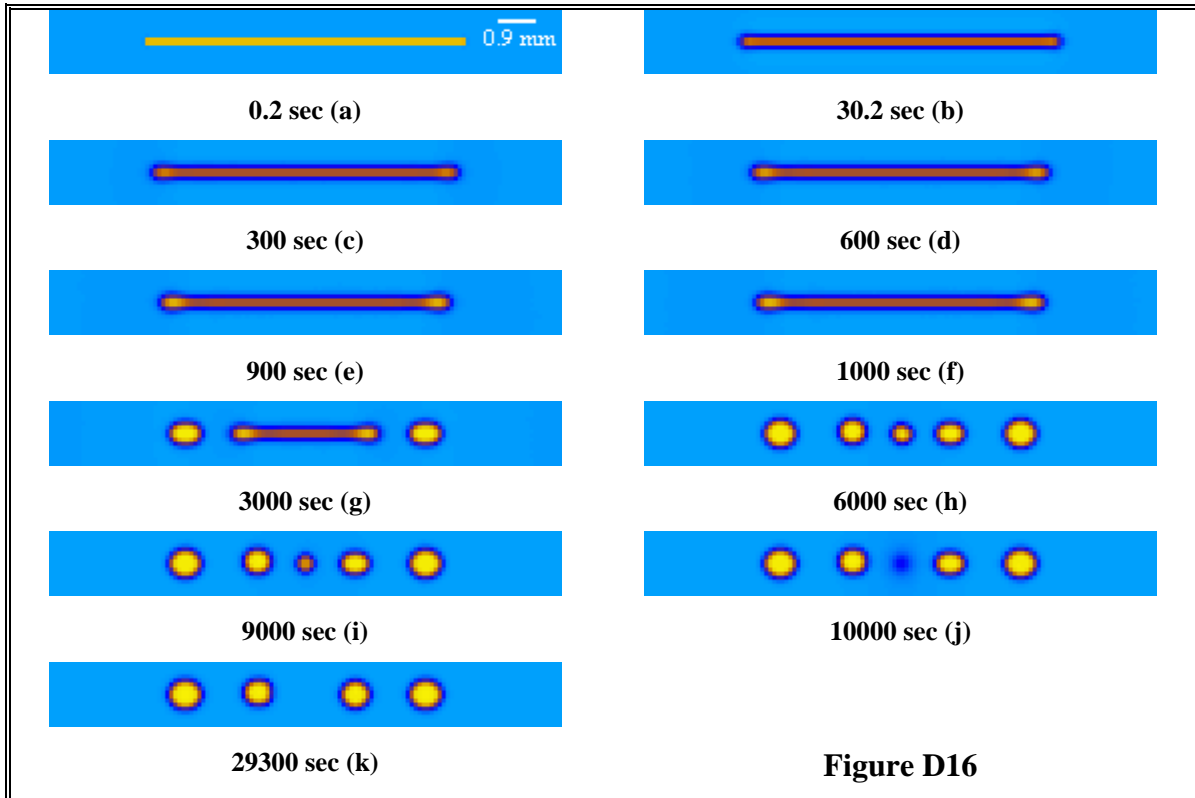


Figure D14

2.11 Aspect Ratio = $L/W = 6.00 \text{ mm}/0.20 \text{ mm} = 30.00$

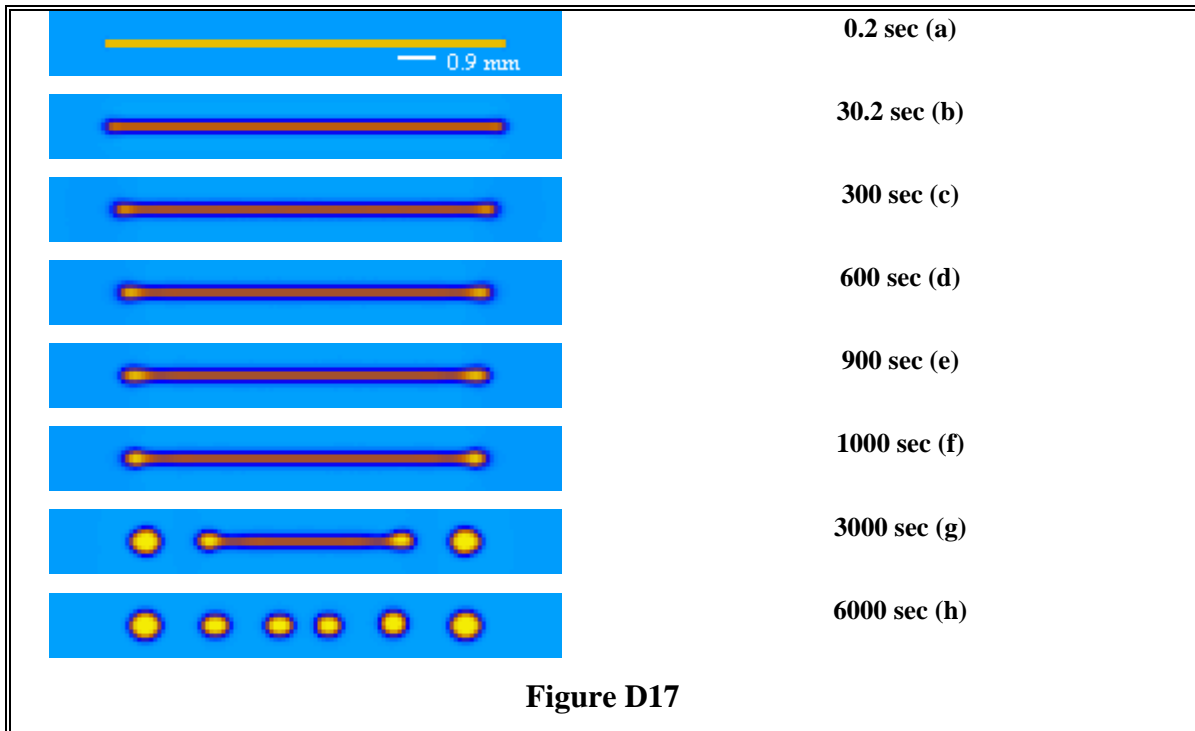


2.12 Aspect Ratio = $L/W = 8.00 \text{ mm}/0.20 \text{ mm} = 40.00$

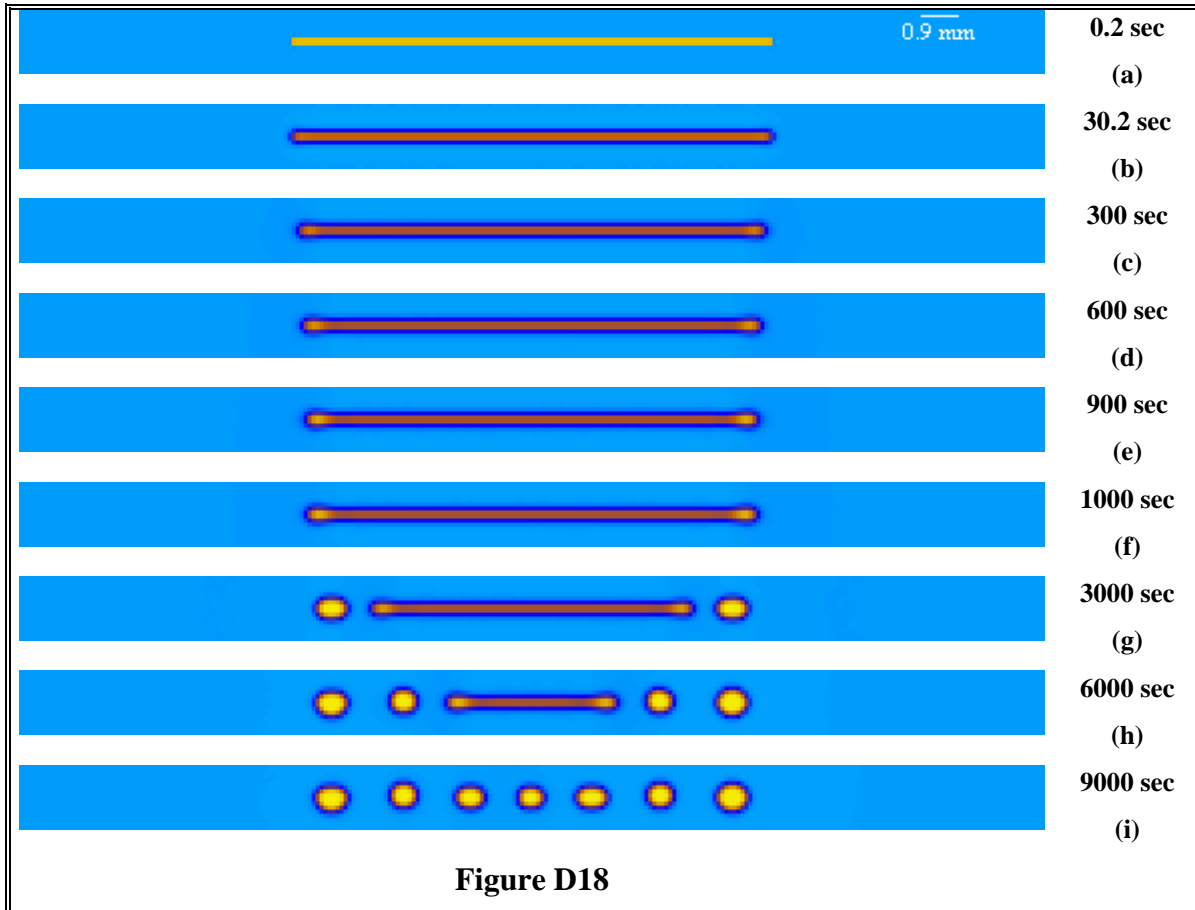




2.13 Aspect Ratio = $L/W = 10.00 \text{ mm}/0.20 \text{ mm} = 50.00$



2.14 Aspect Ratio = $L/W = 12.00 \text{ mm}/0.20 \text{ mm} = 60.00$





2.15 Aspect Ratio = $L/W = 16.00 \text{ mm}/0.20 \text{ mm} = 80.00$

